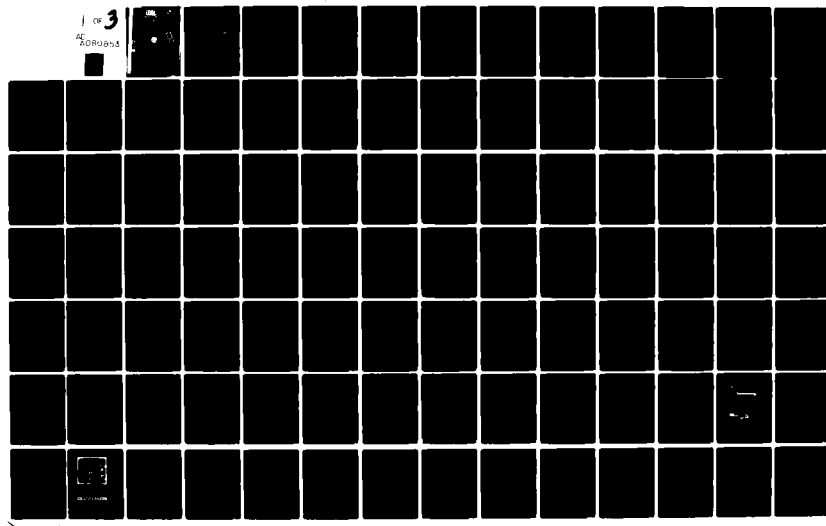


AD-A080 853

ILLINOIS UNIV AT URBANA-CHAMPAIGN DEPT OF CHEMICAL EN--ETC F/8 20/4
IDENTIFICATION OF THE DOMINANT FLOW STRUCTURE IN THE VISCOUS WA--ETC(U)
AUG 79 J H HOGENES, T J HANRATTY N00014-76-C-1034

UNCLASSIFIED TR-2 NL

1 OF 3
AC-A080853



SECURITY CLASSIFICATION OF THIS PAGE (When Data Entered)

REPORT DOCUMENTATION PAGE		READ INSTRUCTIONS BEFORE COMPLETING FORM
1. REPORT NUMBER Report 2	2. GOVT ACCESSION NO.	3. RECIPIENT'S CATALOG NUMBER
4. TITLE (and Subtitle) IDENTIFICATION OF THE DOMINANT FLOW STRUCTURE IN THE VISCOS Wall REGION OF A TURBULENT FLOW		5. TYPE OF REPORT & PERIOD COVERED Technical rept.,
6. AUTHOR(S) Johannes Hubertus Antonius Hogenes and Thomas J. Hanratty Project Supervisor		7. PERFORMING ORGANIZATION NAME AND ADDRESS Department of Chemical Engineering University of Illinois Urbana, Illinois 61801
8. CONTRACT OR GRANT NUMBER(S) NR 062-558 N0004-76-C-1034		9. PERFORMING ORG. REPORT NUMBER 14 TR-2
10. PROGRAM ELEMENT, PROJECT, TASK AREA & WORK UNIT NUMBERS		11. REPORT DATE Aug 1979
12. NUMBER OF PAGES 180		13. SECURITY CLASS. (of this report) Unclassified
14. MONITORING AGENCY NAME & ADDRESS (if different from Controlling Office) 12 192		15. DECLASSIFICATION/DOWNGRADING SCHEDULE N0004-76-C-1934
16. DISTRIBUTION STATEMENT (of this Report) Approved for public release; distribution unlimited		
17. DISTRIBUTION STATEMENT (of the abstract entered in Block 20, if different from Report) 15 N0004-76-C-1934 696 4306		
18. SUPPLEMENTARY NOTES		
19. KEY WORDS (Continue on reverse side if necessary and identify by block number) Turbulence; Turbulence structure; Conditional averaging; Pipe flows.		
20. ABSTRACT (Continue on reverse side if necessary and identify by block number) Simultaneous measurements of the fluctuating velocity have been made at multiple locations in the viscous wall region of a turbulent flow by using electro-chemical probes. Pairs of electrodes flush with the wall in a V configuration allowed for the measurement of the two components of the fluctuating wall velocity gradient, S_x and S_z , at ten wall positions covering a spanwise distance of $z^+ = 150$. A rake of probes arranged along a line perpendicular to the wall was located downstream of the center of		

20. (continued)

the array of wall electrodes. It allowed for the measurement of the x-component of the fluid velocity, u_x , at seven locations covering a distance of $7 < y^+ < 100$. Conditional sampling of the measurements from these probes revealed repetitive structural aspects of the flow. The measurements indicated that S_z had a characteristic wave length in the z^+ direction of $\lambda^+ \approx 100$. Velocity fluctuations in the x-direction, S_x and u_x , are strongly associated with this spanwise velocity component. Patterns of S_z variation showed inflows of high momentum fluid and outflows of low momentum fluid from the wall occurring simultaneously at a distance apart of $S_z^+ \approx 50$. Shear layers could be identified as occurring when outflows of low momentum fluid from the wall displaced fluid of large momentum or when inflows of high momentum fluid displaced low momentum fluid close to the wall.

Accession For

NTIS	Global
DOC TAB	
Unannounced	
Ju	tification
By _____	
FBI - Atlanta	
Availability Codes	
Dist	Avail and/or special
A	

IDENTIFICATION OF THE DOMINANT FLOW STRUCTURE
IN THE VISCOUS WALL REGION
OF A TURBULENT FLOW

Prepared by
Johannes Hubertus Antonius Hogenes
Thomas J. Hanratty, Project Supervisor
for
The Office of Naval Research
Project Number NR 062-558

REPORT 2

Department of Chemical Engineering
University of Illinois
Urbana, Illinois
61801

August 1979

IDENTIFICATION OF THE DOMINANT FLOW STRUCTURE
IN THE VISCOUS WALL REGION OF A TURBULENT FLOW

Johannes Hubertus Antonius Hogenes, Ph.D.
Department of Mechanical Engineering
University of Illinois at Urbana-Champaign, 1979

The coherent eddy structure and the bursting phenomenon were explored in the viscous wall region ($y^+ < 35$) of a fully developed turbulent pipe flow. Multiple wall probes were used to measure the velocity gradients in the axial and spanwise directions at the wall. Also multiple probes were used in the fluid downstream from the wall probes to measure the axial velocities at different radial positions. The measurements were performed in a vertical flow system with an internal diameter of 20 cm and a Reynolds number of approximately 30000.

To explore the viscous wall region the concept of the idealized coherent eddy structure was used. This flow structure consists of pairs of open eddies elongated in the streamwise direction and perpendicular to the direction of mean flow. The elongated eddies carry fluid with high axial momentum to the wall (i.e., inflow). The high momentum fluid exchanges momentum at the wall and then leaves the wall as a momentum deficient flow (i.e., outflow).

Because long-term averages of the turbulence signals disguise the specific features of the coherent boundary layer structure the wall and fluid probe signals were averaged conditionally. The instants from which the conditional average was obtained depended upon the spanwise velocity gradients at the wall for one set of experiments and upon the

fluid probe signals for another set. During inflows and outflows the spanwise velocity gradients form sine wave shaped patterns at the wall and a digital computer was used in the search for these instants in the data set. In another conditional averaging scheme the dynamic behaviour of the velocity at one specific fluid probe was prescribed and in a second case the spatial behaviour of the fluctuating velocities at several fluid probes was specified. Each instant in the data set that met the prescribed condition was used as the centre for purposes of a conditional averaging procedure.

The dominant flow structure in the viscous wall region was found to be a simultaneous flow of high axial momentum fluid towards the wall and low axial momentum away from the wall. The high and low axial momentum fluid flows are separated by a distance of $\Delta z^+ = 50$. The nature of turbulence implies that inflows and outflows are distributed randomly in space and time, inducing inflow-outflow sequences (and vice versa). The common feature of these sequences is a rapid acceleration of the axial velocity fluctuations leading to inflectional velocity profiles. Profile inflexions are a flow phenomenon; they are a consequence of the outflow-inflow sequence (and vice versa), not its impetus.

TABLE OF CONTENTS

CHAPTER	Page
I. INTRODUCTION.....	1
II. LITERATURE SURVEY.....	8
A. <u>Turbulence Properties</u>	8
B. <u>Coherent Structure in the Viscous Wall Region</u>	10
III. EXPERIMENT DESCRIPTION.....	33
A. <u>Measurements</u>	33
B. <u>Eddy Structure in the Viscous Wall Region</u>	35
C. <u>Applied Conditions</u>	37
1. Inflows and outflows.....	37
2. Spatial behaviour of inflows and outflows.....	39
3. Dynamic behaviour of inflows and outflows.....	40
4. Detection of inflows and outflows in the viscous wall region.....	41
5. Spatial behaviour of the velocity fluctuations in the viscous wall region.....	43
6. Dynamic behaviour of the velocity fluctuations at a point in the viscous wall region.....	44
D. <u>Conditional Averaging Procedure</u>	44
IV. THE ELECTROCHEMICAL MEASUREMENT TECHNIQUE.....	50
A. <u>Description of the Electrochemical Technique</u>	50
B. <u>Equations for the Fluid Probes</u>	52
C. <u>Equations for the Wall Probes</u>	59
V. EXPERIMENTAL APPARATUS.....	66
A. <u>Flowloop</u>	66
B. <u>Multi-sensor Fluid Probe</u>	68
C. <u>Wall Electrodes</u>	70
D. <u>Electrode Circuitry and Data Collection</u>	74
VI. RESULTS.....	77
A. <u>Correlations</u>	77
B. <u>Conditional Averaging Criteria Applied to the Spanwise Velocity Gradients of the Wall</u>	84
1. Detection of inflows over a spanwise length of $\Delta z^+ = 153$	84
2. Detection of outflows over a spanwise length of $\Delta z^+ = 153$	86
3. Detection of inflows over a spanwise length of $\Delta z^+ = 102$	89

CHAPTER	Page
4. Detection of outflows over a spanwise length of $\Delta z^+ = 102$	98
5. Spatial coherency of inflows and outflows.....	105
6. Transition of outflows into inflows over time.....	109
7. Transition of inflows into outflows over time.....	115
C. <u>Conditional Averaging Criteria Applied to the Axial Velocity Fluctuations in the Viscous Wall Region</u>	125
1. Detection of inflows with the fluid probes at $y^+ = 8$ and 16.....	125
2. Detection of outflows with the fluid probes at $y^+ = 8$ and 16.....	130
3. Rapid accelerations of the fluctuating velocities in the fluid.....	133
4. Rapid decelerations of the fluctuating velocities in the fluid.....	145
5. Positive slopes in the u_x profiles near the wall.....	155
6. Negative slopes in the u_x profiles near the wall.....	162
7. Time correlations between temporal and spatial u_x fluctuations.....	166
VII. CONCLUSION.....	171
LIST OF REFERENCES.....	173
NOMENCLATURE.....	177
VITA.....	181

Figure		Page
6-10.	Conditionally averaged inflow s_x patterns.....	93
6-11.	Conditionally averaged inflow u_x patterns; $\Delta x^+ = 30$	95
6-12.	Conditionally averaged inflow u_x patterns; $\Delta x^+ = 60$	96
6-13.	Conditionally averaged inflow u_x patterns; $\Delta x^+ = 90$	97
6-14.	Conditionally averaged inflow U_x patterns; $\Delta x^+ = 60$	99
6-15.	Conditionally averaged outflow s_z patterns; $\Delta z^+ = 102$..	100
6-16.	Conditionally averaged outflow s_x patterns.....	101
6-17.	Conditionally averaged outflow u_x patterns; $\Delta x^+ = 30$	103
6-18.	Conditionally averaged outflow u_x patterns; $\Delta x^+ = 60$	104
6-19.	Conditionally averaged outflow u_x patterns; $\Delta x^+ = 90$	106
6-20.	Conditionally averaged outflow U_x patterns; $\Delta x^+ = 60$	107
6-21.	Conditionally averaged inflow-outflow s_z patterns.....	108
6-22.	Conditionally averaged inflow-outflow s_x patterns.....	110
6-23.	Conditionally averaged inflow-outflow U_x patterns; $\Delta x^+ = 90$	111
6-24.	Conditionally averaged transitional outflow-inflow s_z patterns.....	113
6-25.	Conditionally averaged transitional outflow-inflow s_x patterns.....	114
6-26.	Conditionally averaged transitional outflow-inflow u_x patterns; $\Delta x^+ = 60$	116
6-27.	Conditionally averaged transitional outflow-inflow u_x patterns; $\Delta x^+ = 90$	117
6-28.	Conditionally averaged transitional outflow-inflow U_x patterns; $\Delta x^+ = 90$	118
6-29.	Conditionally averaged transitional inflow-outflow s_z patterns.....	119
6-30.	Conditionally averaged transitional inflow-outflow s_x patterns.....	121
6-31.	Conditionally averaged transitional inflow-outflow u_x patterns; $\Delta x^+ = 60$	122

LIST OF FIGURES

Figure		Page
3-1.	Idealized coherent eddy structure.....	36
3-2.	Conditions applied to $s_z(z,t)$ wall pattern.....	38
3-3.	Conditions applied to the velocity fluctuations in the viscous wall region.....	42
3-4.	Conditionally averaged inflow-outflow s_z patterns. $E_D=58$; threshold value=100 k_1	46
3-5.	Conditionally averaged inflow-outflow s_z patterns. $E_D=111$; threshold value=50 k_1	47
3-6.	Conditionally averaged inflow-outflow patterns. $E_D=167$; threshold value=5 k_1	48
4-1.	Polarization curves for a wall electrode and a fluid probe.....	53
4-2.	Dependence of Sherwood number on $g(R_d)$ and $h(\theta)$	56
4-3.	Calibration curves for mass transfer fluid probes.....	58
4-4.	Pair of slanted "V" electrodes.....	63
4-5.	Response of a pair of wall electrodes.....	65
5-1.	Vertical flow system.....	67
5-2.	Multiple-sensor fluid probe.....	69
5-3.	Multiple "V" wall electrodes.....	72
5-4.	Construction sequence of the wall electrodes.....	73
5-5.	Schematic representation of the electrochemical process and the electrode circuit.....	75
6-1.	Time correlation of the axial velocity and the axial velocity gradient at the wall.....	78
6-2.	Spanwise correlations of the velocity gradients s_x and s_z at the wall.....	79
6-3.	Spanwise correlations of the axial velocity and the axial velocity gradient at the wall.....	82
6-4.	Spanwise correlations of the axial velocity and the spanwise velocity gradient at the wall.....	83
6-5.	Conditionally averaged inflow s_z patterns; $\Delta z^+=153$	85
6-6.	Conditionally averaged inflow s_x patterns.....	87
6-7.	Conditionally averaged outflow s_z patterns; $\Delta z^+ = 153$	88
6-8.	Conditionally averaged outflow s_x patterns.....	90
6-9.	Conditionally averaged inflow s_z patterns; $\Delta z^+ = 102$	91

Figure	Page
6-32. Conditionally averaged transitional inflow-outflow u_x patterns; $\Delta x^+=90$	123
6-33. Conditionally averaged transitional inflow-outflow U_x patterns; $\Delta x^+=90$	124
6-34. Conditionally averaged inflow u_x patterns.....	126
6-35. Conditionally averaged inflow U_x patterns.....	127
6-36. Conditionally averaged inflow s_z patterns; $\Delta x^+=90$	128
6-37. Conditionally averaged inflow s_x patterns; $\Delta x^+=90$	129
6-38. Conditionally averaged outflow u_x patterns.....	131
6-39. Conditionally averaged outflow U_x patterns.....	132
6-40. Conditionally averaged outflow s_z patterns; $\Delta x^+=90$	134
6-41. Conditionally averaged outflow s_x patterns; $\Delta x^+=90$	135
6-42. Conditionally averaged acceleration u_x patterns; $y^+=8$	137
6-43. Conditionally averaged acceleration u_x patterns; $y^+=24$	138
6-44. Conditionally averaged acceleration u_x patterns; $y^+=50$	139
6-45. Conditionally averaged acceleration U_x patterns; $y^+=8$	141
6-46. Conditionally averaged acceleration U_x patterns; $y^+=24$	142
6-47. Conditionally averaged acceleration U_x patterns; $y^+=50$	143
6-48. Conditionally averaged acceleration s_z patterns; $\Delta x^+=90$; $y^+=24$	144
6-49. Conditionally averaged acceleration s_x patterns; $\Delta x^+=90$; $y^+=24$	146
6-50. Conditionally averaged deceleration u_x patterns; $y^+=8$	148
6-51. Conditionally averaged deceleration u_x patterns; $y^+=24$	149
6-52. Conditionally averaged deceleration u_x patterns; $y^+=50$	150
6-53. Conditionally averaged deceleration U_x patterns; $y^+=8$	152

Figure	Page
6-54. Conditionally averaged deceleration U_x patterns; $y^+=24$	153
6-55. Conditionally averaged deceleration U_x patterns; $y^+=50$	154
6-56. Conditionally averaged deceleration s_z patterns; $\Delta x^+=90$; $y^+=24$	156
6-57. Conditionally averaged deceleration s_x patterns; $\Delta x^+=90$; $y^+=24$	157
6-58. Conditionally averaged u_x patterns--positively sloped u_x profile.....	159
6-59. Conditionally averaged U_x patterns--positively sloped u_x profile.....	160
6-60. Conditionally averaged s_z patterns--positively sloped u_x profile; $\Delta x^+=90$	161
6-61. Conditionally averaged s_x patterns--positively sloped u_x profile; $\Delta x^+=90$	163
6-62. Conditionally averaged u_x patterns--negatively sloped u_x profile.....	164
6-63. Conditionally averaged U_x patterns--negatively sloped u_x profile.....	165
6-64. Conditionally averaged s_z patterns--negatively sloped u_x profile; $\Delta x^+=90$	167
6-65. Conditionally averaged s_x patterns--negatively sloped u_x profile; $\Delta x^+=90$	168
6-66. Time correlations between spatial derivative and temporal derivative of the axial velocity fluctuations.....	170

I. INTRODUCTION

In the past two decades much research effort has been devoted to studying the turbulent boundary layer in order to predict and control bounded turbulent shear flows. A repetitive and coherent structure (Beatty et al 1956; Kline et al 1967) dominates the viscous wall region ($y^+ < 35$) where viscosity influences momentum transfer. Maxima are reached in the production and dissipation of turbulence kinetic energy (Laufer 1954; Townsend 1976; Wallace et al 1972) in the buffer region ($y^+ \approx 10$) near the wall. Thus an understanding of the flow phenomena in the wall region is essential for describing turbulent processes such as mass transfer, heat transfer and drag reduction.

Turbulence in boundary layer flows is self-sustaining and consists of a random distribution of vorticity. The change in vorticity of a Newtonian fluid is caused by the nonlinear stretching or contraction of vortex tubes and the diffusion and dissipation of vorticity. The wall can be treated as a source of vorticity, induced by pressure gradients, as discussed by Lighthill (1963). This concept provides a framework for understanding bounded turbulent shear flows.

Observations by Tani and Hama (1953) revealed coherent structures in the viscous wall region during boundary layer transition, but these coherent structures were regarded as the result of a transitional state of flow. Studies of turbulent coherent structures in the viscous wall region originated with the experiments of Beatty, Ferrell and Richardson (Corrsin 1956) who pumped a dye solution through a pipe and then observed the formation of residual dye into streamwise filaments at the wall following a flushing with water. The existence of this streaky

structure was confirmed by Hama (Corrsin 1956) who injected dye through wall slots into a turbulent pipe flow. Corrsin interpreted these experiments as the result of a predominance of axial vorticity near the wall which sweeps the dye into long narrow strips.

Because the nature of the streaky structure in the viscous wall region is intermittent, time and space averages of these structures conceal their specific features. Gupta et al (1971) illustrated how long-term averages "smear out" the features of the three-dimensional boundary layer process. Thus far, the only ways by which these coherent structures have been studied experimentally are by visualization techniques and conditional averaging.

The extensive research efforts of Kline et al (1967), Kim et al (1971), Offen and Kline (1974) etc., who used for their visualization experiments hydrogen bubbles and dye to mark the streamlines, revealed the intermittent streaky structure of the turbulent boundary layer. Kline and his co-workers showed also that streaks are regions of low axial velocity which lift away from the wall to interact with the outer flow field. This interaction is called "bursting" because the process is sudden and turbulence is produced instantaneously. Photographic visualization techniques were used by Corino and Brodkey (1969), Nychas et al (1973), and Praturi and Brodkey (1978) to capture the motions of fluid elements in a turbulent boundary layer. Small solid particles were suspended in the flow to trace the fluid motions which were photographed. Grass (1971) studied the turbulent boundary layer structure for different surface roughness conditions using hydrogen bubble tracers and motion picture photography. The burst frequency was studied by Rao et al (1971), and Laufer and Badri Narayanan (1971).

Conditional averaging techniques were used by a number of investigators. In particular Kaplan and Laufer (1969), and Kovasznay et al (1970) took conditional averages in a Lagrangian reference frame. Willmarth and Lu (1972), and Blackwelder and Kaplan (1972) used their conditional averaging technique in an Eulerian reference frame.

Notwithstanding the limitations of the different experimental techniques used to study the viscous wall region, a dimensionless spanwise spacing (made dimensionless with wall parameters) between the low speed streaks was found to be approximately 100. It has been suggested that the mean period between bursts scales with the outer flow variables, the bulk velocity and the boundary layer thickness.

One of the first attempts to describe analytically the structure of the viscous wall region was made by Taylor (1936) who solved the truncated linearized momentum equation and related the velocity field to the pressure field. Linearized analyses were conducted by Sternberg (1962), Schubert and Corcos (1967) and Gurkham and Kader (1970). However, the linearized momentum equations do not take into account the Reynolds stress terms. Omitting of the turbulence production term in the boundary layer calculations made necessary another approach and led to the simplified flow model of Sirkar (1969). This model was used by Fortuna (1971) to explain momentum transfer and drag reduction. Fortuna's approach is based upon the premise that the axial flow fluctuations are controlled by the spanwise velocities of an organized eddy structure elongated in the direction of mean flow. Assuming so, this organized eddy structure brings high momentum fluid from the outer flow to the wall and carries momentum deficient fluid away from the wall, after a momentum exchange occurs with it. In addition, the Fortuna model assumes a pseudo-steady state and homogeneity in the axial direction.

Although this model predicts mean velocities and the axial fluctuations spectrum, its weakness is the time independence of the energy containing eddies.

Hatzivramidis (1978) solved the nonlinear momentum equations in order to describe the most energetic velocity fluctuations in the viscous wall region. His model, an extension of Fortuna's pseudo-steady state model, assumes at values of y^+ less than 40 coherent motions and at values of y^+ greater than 40 a well-mixed flow. The spanwise velocity component in the transition region between the coherent flow and the well-mixed flow is described by a simple function, periodic in time and space. Also assumed is homogeneity of the flow in the axial direction. Even though agreement between calculations and measurements of turbulent properties and bursting features renders strength to this model, its main weakness is the assumption of homogeneity in the axial direction as well as the representation of turbulence as a periodic phenomenon.

The development of methods to measure the velocity gradient at the wall began with the experiments of Reiss and Hanratty (1962), who used a small mass transfer controlled circular electrode to study the viscous sublayer ($y^+ < 7$). Their experiment disclosed a constant mass transfer rate under laminar flow conditions, but a fluctuating mass transfer rate for a turbulent flow. Mass transfer fluctuations were related to velocity fluctuations at the wall by Reiss and Hanratty (1963). A rectangular electrode at the wall was used by Mitchell and Hanratty (1966) at different angles to the mean flow direction to study a fully developed turbulent flow. They discovered that the spanwise velocity fluctuations were much smaller than the longitudinal fluctuations and

found a value of .32 (made dimensionless with the average wall velocity gradient) for the axial velocity intensity at the wall. A pair of rectangular electrodes slanted at small angles to the mean flow direction was used by Sirkar and Hanratty (1969) to measure simultaneously the axial and spanwise wall velocity gradients. A conclusion from their work was that close to the wall the spanwise velocity gradient has a value of .10 (made dimensionless with the average wall velocity gradient).

Sirkar (1969) hypothesized that the flow close to the wall is dominated by a coherent eddy structure in a plane perpendicular to the direction of mean flow as shown in Figure 3-1a. The spanwise velocity gradients at the wall associated with these eddies are assumed to vary harmonically in the spanwise direction and randomly in time. This type of wall pattern is shown in Figure 3-1b. Multiple pairs of rectangular electrodes were used by Eckelman (1971) to study the structure of the wall turbulence and how it relates to eddy transport. Eckelman showed that the axial and spanwise velocity gradients at the wall can be used to detect the coherent eddy structure in the viscous wall region and that this eddy structure is symmetric. From the decomposition of the correlation of the axial velocity fluctuations Bakewell and Lumley (1967) suggested that the coherent structure in the wall region was asymmetric because the inflows were more diffused than the outflows. The work of Eckelman was extended by Lee (1975), who laid the basis for the notion that the axial and spanwise velocity gradients are not independent but form regular eddy patterns during the bursting process. Lee detected a sequence of events from probes flush with the wall. The sequence begins with a change in the spanwise wall velocity gradient pattern while the axial wall velocity gradient pattern remains unchanged.

After a stable sine wave shaped spanwise wall pattern is established the axial velocity gradient changes rapidly until a regular sine wave shaped axial wall pattern is formed. Next, the amplitude of the axial wall pattern increases. According to Lee this is the beginning of the bursting process.

This work explores the coherent eddy structure and the bursting phenomenon in the viscous wall region of a fully developed turbulent pipe flow. Multiple wall probes were used to measure the fluctuating velocity gradients in the axial and spanwise directions at the wall. Also multiple probes were used in the fluid downstream from the wall probes to measure the fluctuating velocity components at different radial positions. Because long-term averages of the turbulent signals disguise the specific features of the coherent boundary layer structure, the wall and the fluid probe signals were averaged conditionally. The instants from which the conditional average was obtained depended upon the spanwise velocity gradients at the wall for one set of experiments and upon the fluid probe signals for another set. The model of the idealized coherent eddy structure in the viscous wall region was applied as the criteria for selecting these instants. This eddy structure induces sine wave shaped axial and spanwise velocity gradient patterns at the wall. A digital computer was used in the search for the sine wave shaped spanwise velocity gradient profiles in the data set which covers a time period (made dimensionless with wall parameters) of approximately 20000. Each spanwise velocity profile that met the prescribed conditions was used as the centre for purposes of a conditional averaging procedure.

In the other conditional averaging scheme the instants from which the conditional average was obtained were determined by the fluid probes.

In one case the dynamic behaviour of the velocity at one specific fluid probe was prescribed and in a second case the spatial behaviour of the fluctuating velocities at several fluid probes was specified. Again each velocity profile that met the prescribed dynamic or spatial behaviour was used as the centre of the averaging scheme. Conditional averages were taken over the fluctuating velocity gradients at the wall as well as over the fluctuating velocities at the fluid probes.

Extensive exploration of the viscous wall region by means of conditional averaging disclosed interesting aspects of the coherent eddy structure. The most remarkable discovery was that the viscous wall region is controlled only by inflows and outflows which are distributed randomly in space and time. Continuity of mass requires that an inflow must be accompanied by an outflow and conditional averaging results showed that inflows and outflows are coupled in space. Because inflows occur randomly in space and time, it is likely that an inflow succeeds an outflow. At the interface of a terminated outflow a large shear layer arises. However the opposite phenomenon may take place in which an inflow is terminated by an outflow or by convected low momentum fluid, and again a large shear layer forms. The process whereby an outflow is followed by an inflow is commonly called the bursting phenomenon.

II. LITERATURE SURVEY

Correlation and spectral measurements indicate that besides fine-scale turbulence a coherent structure exists in bounded turbulent flows (Favre et al 1958). Its presence was evidenced from observations rendered by visualization techniques. In a bounded turbulent shear flow coherent structures can be recognized. These structures are random in space and time, have a statistically definable length and time scale, and exhibit a repetitious physical process. This process has been investigated and described by many researchers; yet no consensus about the nature and behaviour of coherent structures has been reached. In Section A relevant properties of turbulence measurements in the viscous wall region are presented. The various research groups which have investigated the structure of turbulence are described in Section B separately because of the great differences in experimental methodology and in the results obtained.

A. Turbulence Properties

The turbulence properties of a turbulent pipe flow will be described by an orthogonal Cartesian coordinate system. In this coordinate system the x-axis is in the mean flow direction, the y-axis (measured from the wall) in the radial direction and the z-axis in the spanwise direction along the wall. For a fully developed turbulent flow the Reynolds decomposition assumption can be applied, generating the following hydrodynamic quantities,

$$U = \langle U \rangle + u, V = v, W = w, P = \langle P \rangle + p. \quad (2.1)$$

The hydrodynamic quantities in the wall region are made dimensionless with wall parameters, ν , the kinematic viscosity, and u^* , the wall-

friction velocity.

$$\begin{aligned} U^+ &= U/u^*, & y^+ &= yu^*/v, & T^+ &= Tu^2/v, \\ p^+ &= P/\tau_w, & n^+ &= nv/u^{*2}, & S^+ &= Sv/u^{*2}. \end{aligned} \quad (2.2)$$

In the viscous sublayer ($y^+ < 7$) viscosity plays a dominant role in determining the behaviour of the flow. Adjacent to the sublayer is the buffer region ($7 < y^+ < 35$) where inertial effects become increasingly more important relative to the viscous effects. The overlap layer which connects the outer layer and the viscous wall region ($0 < y^+ < 35$) is independent of viscosity. However this region is affected indirectly by the wall through its wall shear stress and the distance from the wall over which the retarded fluid diffuses. Accepted equations for the average velocity for the inner and overlap layers are given by

$$\langle U^+ \rangle = y^+ \quad y^+ < 7 \quad (2.3)$$

and

$$\langle U^+ \rangle = 2.44 \ln y^+ + 5.0. \quad y^+ > 35 \quad (2.4)$$

No agreement exists for the velocity relation in the buffer region ($7 < y^+ < 35$) but the composite law suggested by Spalding (1961) is valid for the viscous sublayer and the buffer layer as well as for the logarithmic overlap region. Thus,

$$y^+ = \langle U^+ \rangle + \exp(-\kappa B) \left[\exp(\kappa \langle U^+ \rangle - 1 - \kappa \langle U^+ \rangle - \frac{(\kappa \langle U^+ \rangle)^2}{2!} - \frac{(\kappa \langle U^+ \rangle)^3}{3!}) \right] \quad (2.5)$$

where $\kappa = .41$ and $B = 5.0$ and so $\exp(-\kappa B) = .1287$.

Turbulence intensities are defined as the root-mean-square of the fluctuating velocities and velocity gradients,

$$\begin{aligned} u' &= \langle u^2 \rangle^{1/2}, & s_x' &= \langle s_x^2 \rangle^{1/2}, \\ v' &= \langle v^2 \rangle^{1/2}, & s_z' &= \langle s_z^2 \rangle^{1/2}. \\ w' &= \langle w^2 \rangle^{1/2}, \end{aligned} \quad (2.6)$$

It has been established that in the viscous wall region $u' > w' > v'$ and that the ratio of the streamwise velocity intensity to the local mean velocity $u'/\langle U \rangle \approx .3$ is greatest in the viscous sublayer. The streamwise intensity u' reaches a maximum at $y^+ \approx 13$ and is zero at the wall. Near the wall the intensities u' and w' vary linearly with the distance y^+ from the wall.

$$\begin{aligned} u'/u^* &= \alpha y^+ && \text{as } y^+ \rightarrow 0 \\ w'/u^* &= \beta y^+ \end{aligned} \quad (2.7)$$

Measurements by Hanratty et al (1977) of s_x' and s_z' at the wall show that

$$s_x'/\langle s_x \rangle = .30 \text{ to } .35$$

and

$$s_x'/s_z' = 3.0.$$

The latter result is supported by measurements of velocity fluctuations close to the wall conducted by Ueda and Hinze (1975).

B. Coherent Structures in the Viscous Wall Region

Flow visualization experiments designed to study the viscous wall region were carried out by Kline and his co-workers. Hydrogen bubbles and dye were used to mark the streamlines and motion pictures were taken of the flow patterns near the wall. The experimental results revealed the streaky structure and the bursting phenomenon discussed in subsections 1, 2, 3 and 4. Brodkey and his co-workers also used a visualization technique to investigate the coherent structure near the wall.

Small solid particles were suspended in the flow and the particle motions were photographed with a camera moving with the flow. A sequence of events was found to occur in the viscous wall region;

this repetitious process is described in subsections 5, 6 and 7.

Multiple hot-film sensors placed in the viscous wall region were used by Blackwelder and Kaplan. Conditional averaging was applied to the instantaneous velocity profiles which showed inflexions and momentum deficient fluid near the wall during the bursting process. This experiment is reviewed in subsection 8. Falco (see subsections 9 and 10) used smoke, hot wire anemometry and motion pictures for his experiments and hypothesized that bounded turbulent flows are controlled by "typical" eddies, large scale motions and flow modules. Flow modules are small disturbed areas in the viscous sublayer which cause ejection of low momentum fluid. Some evidence has been found that the flow modules are induced by the typical eddies. Subsection 11 reviews the work of Grass who conducted a visual study of the viscous wall region for different surface roughness conditions. The work of Grass shows that the roughest boundary layer elicits the most violent ejections of low momentum fluid. The effect of drag reduction upon the coherent structure was investigated by Oldaker and Tiederman. It was found that streaks are formed during a gradual growth stage. By inhibiting the formation of streaks in the viscous sublayer drag reduction was achieved. These findings are summarized in subsection 12.

1. The structure of turbulent boundary layers was explored by Kline et al (1967) using visual techniques for negative, zero, and positive pressure gradients. The experiments were performed in a water channel with a smooth surface. A wire tripped the boundary layer to ensure a fully developed turbulent flow in the test area. In the first experiments dye injected through thin wall slots revealed a streaky structure in the viscous sublayer. For later experiments a thin

platinum wire was used to generate small hydrogen bubbles. The wire was placed parallel to the channel bottom and normal to the flow direction. By pulsing the wire voltage and insulating spanwise portions of the wire, time lines and streaks were formed providing both qualitative and quantitative information. In the viscous sublayer the hydrogen bubbles were swept into long streaks by the spanwise velocity component. These streaks formed a pronounced spanwise spacing, wavered, oscillated and then moved outwards to the edge of the boundary layer.

In the overlap region various scales of motion were present but there was little evidence of streaks, which were clearly visible near the wall. In flows with adverse pressure gradients the streaks tended to be shorter and to waver more violently than in those with favourable pressure gradients. The bursting action of the streaks was suppressed almost totally in flows with strongly favourable pressure gradients and the boundary layer showed signs of returning to a laminar state. In flows with extremely adverse pressure gradients some streaks moved momentarily upstream and then were washed downstream. It has been suggested that the streaks play an integral part in the turbulence production and in the transfer of momentum between the inner and outer regions of the boundary layer. By counting the number of dye streaks per unit of area and per unit of time it was found that the spacing between the streaks scales with wall parameters and has an average spanwise spacing of approximately $\Delta z^+ = 100$. Usually the streaks migrated slowly downstream and away from the wall. When a streak had reached a certain distance ($8 < y^+ < 12$) it began to oscillate. The degree of oscillation increased as the low speed streak moved outwards and then it was broken up abruptly in the region between $10 < y^+ < 30$.

A flow moving towards or away from the wall altered the spanwise vorticity. Vortex tubes were stretched in inflow regions and compressed in outflow regions. The streak lift-up is believed to result from the streamwise vorticity and a sudden instability is thought to cause the breakup leading to the violent bursting process. It was suggested that vortex stretching leads to intermittent formation of intense local shear layers which are a source of dynamic instability in the wall region and cause the breakup of low speed streaks.

2. The boundary layer structure in a water channel with a smooth surface was examined by Kim et al (1971). Of particular interest was the boundary layer in the zone $0 < y^+ < 100$ and the turbulence production process near the wall. Measurements were made with a constant temperature hot wire anemometer in combination with dye injection at the wall. In another set of experiments two hydrogen bubble wires were placed perpendicular to the mean flow in the spanwise and normal directions of the channel. Kim et al found that the intermittent bursting process represents a continuous chain of events starting with quiescent wall flow and ending with chaotic fluctuations during the turbulence production stage.

Near the wall the flow pattern always consisted of low and high speed streaks. The first stage of the bursting process was the gradual lifting of low speed streaks away from the wall. The streamwise vorticity composed of high and low speed streaks was initially very low, resulting in the slow outward motion of low speed streaks. After these streaks had reached a certain distance from the wall, a rapid lift-up of low speed streaks took place. During this lifting process the momentum

deficient fluid particles moved away from the wall. This rapid outward motion of momentum deficient fluid caused an inflection in the instantaneous velocity profile characteristic of the bursting process.

An inflection occurred at a point of maximum vorticity and was unstable when disturbed by certain frequencies. Immediately after an instantaneous inflectional velocity profile was formed a rapid amplification of the oscillatory disturbance took place. The final stage in the bursting process was the breakup of chaotic motion after which the instantaneous velocity profile returned to the mean profile and frequently the low speed streak moved back towards the wall. Breakup of the chaotic motion was caused by local intermittent instability. In general an instantaneous inflectional velocity profile led to growing oscillation and a breakup. Nearly all the turbulence production in the zone $0 < y^+ < 100$ occurred during bursting and in particular throughout the oscillatory growth stage.

Three different oscillatory growth modes were observed. The most frequent one was the streamwise vortex motion in which the vortex size and its strength grew as the motion proceeded. This mode accounted for approximately 65 percent of the growth stages. The two less common modes of oscillatory growth were the spanwise vortex mode and the repeated oscillation (wavy motion) mode.

3. Two dye injectors and a normal hydrogen bubble wire were used by Offen and Kline (1974) to investigate the turbulent boundary layer over a smooth plate. The objective of this study was to improve understanding of the relationship between the bursting process and the flow field farther away from the wall. One dye injector was a standard wall slot and the other was a small flattened pitot tube which could be

placed anywhere in the flow. The boundary layer was developed on a flat vertical lucite wall. A thick turbulent boundary layer was obtained by a trip rod at the channel entrance.

When the movable dye injector was placed at $y^+ \approx 100$ upstream from the wall dye slot, it was found that if the outer stream lines moved towards the wall (i.e. a sweep), the wall stream lines lifted up. On the other hand, if the outer stream lines were straight and moved parallel to the wall, no lift-up occurred. Thus each lift-up was associated with a sweep originating in the logarithmic region.

Sweeps were generated by the interaction of a burst from farther upstream and the fluid in the logarithmic region. The state of the logarithmic region alternated between periods of relative quiescence and periods of significant turbulence. Many of these disturbances had large velocity components towards the wall. Limited by the two-dimensional nature of the motion pictures, Offen and Kline obtained no information about the spanwise relationship between bursts and sweeps. Frequently lift-ups were succeeded by sweeps which seemed to terminate the ejection process (called cleansing sweeps). All the sweeps contained a fluid element for which the streamwise velocity was different from that of its surroundings. If this difference was significant the sweep grew rapidly.

Two types of vortical motions were seen frequently--the spanwise vortex which brought fluid down towards the wall and the upward tilted streamwise vortex (vortex with a large component normal to the wall). Simultaneously with the appearance of the first oscillations in the wall streamlines a high shear layer was created between the outward moving fluid and the outer flow. Although the ejections probably were induced

by wallward moving disturbances the bursting fluid appeared to be drawn away from the wall by vortices created in the high shear zone between the momentum deficient wall fluid and the high speed sweep. At the end of the burst's growth stage large vortex-like structures were formed by the interaction of the bursting fluid and the fluid in the logarithmic region.

4. A quasi-cyclical model of the bursting process in a turbulent boundary layer in a Lagrangian reference frame was developed by Offen and Kline (1975). In this model low speed streaks with a three-dimensional structure were treated as a sub-boundary layer within the conventionally defined boundary layer. When the sub-boundary layer grew it was convected downstream by the mean flow. Lift-up of the wall streaks (lifting module) was akin to separation caused by local adverse pressure gradients. The lifting module consisted of the ejected fluid and a re-circulation cell which was formed below the lifted fluid. A pressure fluctuation near the wall caused by the arrival of a sweep imposed the lifting module on the low speed streak.

Sweeps were associated with spanwise vortices which caused a pressure gradient at the wall beneath them. Some fluid from both the burst and its associated sweep returned to the wall along the downstream edge of the re-circulation cell. When this fluid arrived at the wall it spread out sideways and was retarded rapidly, forming a new low speed streak farther downstream. Since the wall streak was a fluid element of finite volume, the sub-boundary layer disappeared quickly during lift-up and the re-circulation cell was swept away by the new in-moving fluid. This replacement fluid was the cleansing sweep which terminated the ejection stage of the burst. The lift-up was a consequence of vortex

roll-up which occurred when the vortex of an upstream burst passed over the vortex associated with a wall streak.

In the proposed model the fluid motions associated with the lift-up induced a vortex. When fluid was lifted away from the wall other fluid had to move into the vacant burst region. Fluid from the adjacent spanwise and streamwise (downstream) directions replaced the bursting fluid. The circulatory pattern that resulted from this combination of motions rotated in the direction of vorticity caused by the mean flow field. Streamwise and spanwise vortices represented the different sections of this newly formed vortex which was stretched and lifted during the oscillatory growth stage. At this point the horseshoe vortex as proposed by Theodorsen (1952) and the stretched and lifted vortex as proposed by Kline et al (1967) bore a striking resemblance.

5. To gain insight into the generation of turbulence and transport processes, a visual investigation of the wall region in a turbulent pipe flow ($R_e \approx 20,000$) was conducted by Corino and Brodkey (1969). High speed motion pictures were taken of a magnified wall region ($x^+ = 56$, $y^+ = 40(16)$ and $z^+ = 16(40)$). Colloidal sized particles were suspended in the fluid and these tracers followed the turbulent motions which were photographed in the Lagrangian reference frame.

A cyclic process random in time and space was discovered by Corino and Brodkey. The first event was the deceleration of the axial fluid velocity within a local region near the wall ($0 < y^+ < 30$). Fluid from upstream with a velocity lower than the average mean velocity gradually replaced the field of view. The actual size of the decelerated region varied greatly but in general it covered a rather small area of the pipewall. Individual particle velocities which were representative for

the decelerated region had deficiencies as great as 50 percent of the local mean velocity. After the deceleration a fluid mass from upstream with an axial velocity of approximately that of the local mean velocity began to accelerate the retarded fluid. This high momentum fluid usually entered at about $y^+=15$ and most often the fluid motion was nearly parallel to the pipe wall or at a slight angle toward it. Occasionally the fluid entered with a large radial velocity component at an angle of 5 to 15 degrees towards the wall. The entry of the high speed fluid into the retarded field often resulted in an immediate interaction between the two velocity fields. On other occasions the high momentum fluid entered the retarded field but the high speed fluid seemed to be on a different spanwise plane than the low momentum fluid (i.e., the two layer velocity effect). Total acceleration of the retarded fluid occurred above a particular y^+ position but below this position the retarded fluid was affected gradually. During acceleration there was often a sharp interface between the accelerated and retarded fluid, creating a high shear layer. Frequently as the high speed fluid was proceeding wallwards there was a simultaneous ejection of low momentum fluid. Thus two opposing flows occurred at the same time but did not interact with each other. This specific sequence involving a wallward movement of the accelerating fluid occurred occasionally; more often the accelerating fluid's direction was nearly parallel to the pipe wall.

When two large fluid masses, each possessing a distinct velocity occupy the same radial or y^+ position but do not interact with each other, a two layer velocity is said to occur. Thus in a two layer velocity two opposing fluid masses are separated in the spanwise direction.

After the acceleration of the low momentum fluid had begun discrete fluid elements were ejected outwards from the wall but sometimes ejections occurred just as the accelerating fluid entered the field of view. These ejections were local events, random in space and time. Their development proceeded rapidly to the fully developed stage. Ejected fluid elements measured axially $x^+=20$ to 40 and in the spanwise direction $z^+=15$ to 20. At times ejections appeared to be correlated but at others no correlation existed between simultaneous ejections within the same field. Ejections started generally at $5 < y^+ < 15$ (some at $y^+=2.5$); those starting at distances from the wall of $y^+=2.5$ showed a slight outward movement which appeared as an axial flow at a slight angle toward the wall (low speed streak).

The hypothesis that the shear layer between the high speed fluid and the retarded fluid might be unstable and bring about ejections by some instability mechanism was not substantiated. No oscillatory motions were detected during the shear layer formation nor was tight rotation of fluid elements observed. It has been suggested that the ejection event begins with the oscillatory motion as described by Kim and Kline (1971). As the ejected fluid moved outward at an average angle of 8.5 degrees, it was accelerated axially to a small extent. At a certain distance from the wall the ejection encountered fluid with high axial velocity where upon a violent interaction and chaotic turbulence production occurred. The chaotic motions spread out in all directions and the more violent ones reached even the sublayer and the wall. In this manner the inner parts of the viscous sublayer were disturbed by ejections. The large eddies originating in the outer flow contributed little to the turbulence production. The conjecture of Kline et al (1967) that

the wall layer streak break-up (ejection event) plays a dominant role in determining the structure of the entire turbulent boundary layer was supported. Most commonly the interaction zone occurred over the region $7 < y^+ < 30$ (Kline: $10 < y^+ < 30$). The ejection phase ended with the sweep which was fluid moving at the average local velocity in the axial direction. This fluid swept the velocity field of retarded flow and re-established a semblance of the normal velocity profile.

6. The outer region of a turbulent boundary layer along a flat plate was investigated by Nychas et al (1973). In addition, they made a limited study of the wall area. The visualization technique employed involved suspending small solid particles in the turbulent flow. The fluctuating particle motions were photographed with a high speed camera moving with the flow. The dimensions of the field of view were $x^+=1400$, $y^+=700$ and $z^+=150$ and the Reynolds number specified for the experiments was $R_\theta=900$. The wall and the outer regions were both in view and the events and relations of both regions could be identified easily.

A feature of both the wall ($0 < y^+ < 70$) and the outer region ($y^+ > 70$) of a turbulent boundary layer is the existence of a number of discrete events occurring in sequence but randomly in space and time. The nature and scales of these events are different for the wall area and the outer flow. The first event observed was the appearance in the field of view of a decelerated region moving with a streamwise velocity smaller than the mean. Frequently the decelerated flow extended from the wall to a y^+ of approximately 500. This decelerated fluid moved as a plug flow with very little turbulence or violent interactions. It was observed that the pluglike decelerated flow extended inside the wall region. A

large scale fluid motion entered from upstream while the low speed fluid was still in view. Most of the time this high speed fluid moved with a velocity greater than the local mean velocity and appeared in the outer region at approximately $150 < y^+ < 400$. A sharp interface between the decelerated region and the entering high speed fluid was found not to exist, but a sharper demarcation line did evolve as the wall was approached. As the high speed fluid moved downstream it gradually displaced both the decelerated fluid near the wall and the fluid in the outer region. A region of high shear was formed between the low speed fluid (adjacent to the wall) and the high speed fluid next to it. The high speed fluid moved at an angle towards the wall but the size of this angle decreased as the wall area was approached. The next event was a small scale ejection that originated ($0 < y^+ < 50$) in the low speed region. The ejected fluid often interacted violently with the surrounding low speed fluid. Most of the ejected fluid particles reached a y^+ of 80 to 100 while some particles reached values as high as 200, and were swept downstream by the incoming high speed fluid. Several times, ejected fluid particles originating in the decelerated region passed fluid particles in the accelerated region. Apparently they were in different x-y planes separated in the spanwise (z) direction (the two layer velocity effect). In a few cases ejected fluid elements turned back towards the wall after travelling over a y^+ distance of 30 to 40 and finally were swept downstream by the advancing high speed fluid. The ejected fluid became part of the accelerated region which interacted with the ejected fluid particles and swept them downstream.

Spanwise vortices were found to exist in the outer region and were formed as follows. The interface of the advancing high speed fluid

front formed an angle with the wall, resulting in a region composed of two large scale streams of fluid. Immediately after such a flow configuration was established a rotational large scale motion developed. A problem with the experimental technique used was the difficulty of distinguishing between the rotational and irrotational regions. The interface between high and low speed fluid regions was unstable and induced a Helmholtz instability and a spanwise vortex. This vortex was transported downstream at a small angle with respect to the wall and its scale changed slightly during its downstream movement. Such a vortex has a scale of approximately $200 y^+$ units with the centre of rotation located in a range of y^+ from 200 to 400. Both forward and reverse spanwise vortices were formed depending on the angle of the entering high speed fluid. The high speed fluid region was responsible for the vortex formation and the only active region in the decelerated flow was the wall area where the ejections originated.

Another event observed was a large scale inflow which usually dominated the entire outer region and sometimes even penetrated the wall area. An inflow is a large region of fluid moving towards the wall with a small wallward angle and a streamwise velocity component close to the local mean velocity. The motion was continuous from a y^+ of approximately 100 to 500 and covered a streamwise x^+ length of about 1500. Usually an inflow followed an outflow (or vice versa) or an inflow occurred after a spanwise vortex. Also the inflows and outflows were independent of the accelerated and decelerated flow field and were rarely associated with wall area ejections. The inflows and outflows appeared to have a laminar nature and no violent interactions inside these flows were observed. Most outflows originated from a region at y^+ of 150 to 200 and extended as far as y^+ of 500 to 600. In contrast

to the inflows which often penetrated the wall area the outflows were found to occur in the outer region only.

7. A stereoscopic visual study of coherent structures along a flat plate turbulent boundary layer was conducted by Praturi and Brodkey (1978). The main advantage of the stereoscopic approach was that observation of axial vortex motions was made possible. Small particles were suspended in the flow (in some experiments dye) and the motions of these particles were photographed with a stereoscopic medium-speed camera moving with the flow. Three regions characterized the flow, namely, the wall region ($0 < y^+ < 100$), the outer region of the boundary layer ($100 < y^+ < 450$) and the irrotational region ($450 < y^+$) beyond the edge of the boundary layer. The camera's field of view was approximately 950 x^+ units in the streamwise direction, 850 y^+ units in the transverse direction and 1000 z^+ units in the spanwise direction. Most of the films were taken with an axial camera speed equal to the velocity at $y^+ = 60$ (approximately 70 percent of the free stream velocity). The Reynolds number R_θ for this work was approximately 900.

The decelerated fluid behaved as a plug flow with a laminarlike structure across the entire boundary layer except close to the wall where turbulence prevailed. The demarcation line between advancing high speed fluid and decelerated fluid was sharper in the wall region than in the outer region. At approximately $y^+ = 200$ the high speed fluid entered the boundary layer and gradually replaced the decelerated fluid. There was always decelerated fluid between the wall and the high speed fluid which was directed at a small angle towards the wall. Immediately preceding and during periods of intense turbulent activity in the boundary layer, inflows were observed. Inflows originating in the irrotational

region of the flow field occurred in combination with outflows which were less coherent and always originated in the boundary layer's outer region. The turbulent-nonturbulent interface at the edge of the boundary layer was contorted by inflows which extended from 300 to 700 y^+ units in the transverse direction and from 100 to 300 x^+ units in the streamwise direction. In general spanwise vortex motions were observed in the outer region of the boundary layer and these vortices were created by inflows and high speed fluid fronts that were slightly delayed.

The motions most frequently observed in the outer boundary layer were spanwise vortices. Spanwise vortices originated at y^+ of 100 to 300 and had a diameter of approximately 150 to 200 y^+ units. Other but less common motions were the streamwise and the tilted vortices. After an inflow had occurred the vortices were formed by a Helmholtz instability between the high speed and low speed fluid. The spanwise vortices moved with the mean flow, were highly coherent, and moved slightly away from the wall. As they moved they grew weaker and larger and then became gentle circulations. Immediately after the appearance of spanwise vortices in the outer region of the boundary layer, ejections occurred as rapid outward movements of fluid from the decelerated wall region. Ejections originated at a y^+ of about 5 to 30 and travelled as small scale straight line motions to a y^+ of 100 where they interacted with the high speed front.

In the wall region streamwise and spanwise vortices were observed. The former were found in the decelerated wall region; some of these vortices were initiated by ejections. However most streamwise vortices resulted from interactions between high speed fluid and retarded fluid near the wall. These vortices had a diameter of about 50 z^+ units and a

length of $100 x^+$ units. Frequently these streamwise vortices changed their axes of rotation and became spanwise vortices. The spanwise vortices in the wall region also were formed by ejections and high shear layers. Vortex structures in the wall region were more intense than those in the outer region and rarely made more than three complete rotations around their axes.

8. The wall region of a turbulent boundary layer was investigated with a conditional averaging method by Blackwelder and Kaplan (1976). To detect the coherent structure and the bursting phenomenon the variable interval time averaging technique (VITA) was employed. With this technique the localized VITA variance of the streamwise velocity fluctuations at $y^+=15$ was determined so that localized measures of the turbulent energy were obtained. Detection was triggered by rapid changes in the velocity profile. After applying a threshold level to this localized variance signal the instants in the data set were obtained around which the conditional averages were taken. With this conditional averaging method the bursting phenomenon was detected. During this bursting process the wall region ($y^+ < 40$) had momentum deficient fluid which later was swept away by high momentum fluid. The outer region ($y^+ > 40$), however, contained fluid with a momentum excess throughout the entire bursting process. The conditionally averaged Reynolds stress was found to be an order of magnitude greater than its conventionally averaged value, indicating that most of the Reynolds stress was produced during the bursting process. Conditionally averaged velocity profiles showed that the fluid moved away from the wall in areas of fluid with great momentum deficiencies and towards the wall in fluid regions of high axial momentum. During the bursting process

inflections were found in the conditionally averaged velocity profiles. However it is not clear if the inflectional profile was the cause or the result of the bursting phenomenon. In addition, no conclusion could be reached about whether the bursting process is driven by the outer flow or the burst drives the outer turbulence. Furthermore, the relationship, if any, between the bursting process and the intermittent nature of the outer part of the boundary layer remains unknown.

9. Falco (1977) studied the coherent motions in the outer region of a turbulent boundary layer. Anemometry and flow visualization in combination with motion pictures were used to determine the characteristics of "typical" eddy motions and large scale motions. The experiments were performed in the Lagrangian reference frame at a Reynolds number of $R_g=1000$. Typical eddies were observed at the upstream boundary of the large scale motions. These eddies were found to be highly coherent and three dimensional. They appeared in every turbulent flow and were Reynolds number dependent. At low Reynolds numbers the eddy size was on the order of the boundary layer thickness. As the Reynolds number increased typical eddies continued to be observed but their scales decreased. The Reynolds stress produced by these eddies was measured conditionally and the results were made dimensionless with the wall parameters. The contribution to the Reynolds stress by typical eddies was large, leading Falco to conclude that these eddies were important parts of the boundary layer motions. As the Reynolds number increased ($R_g>1000$) the typical eddies decreased in size and the bulges in the outer boundary layer could then be identified. These bulges are the large scale motions; they evolve slowly in time and are independent of the Reynolds number. Two hot wires at $y^+=67$ and 343 were used to detect

these motions. The large scale motions do not exhibit burstlike features at high Reynolds numbers. High streamwise velocities were found at the back of the bulges. Conditional averaging of the large scale motions showed that approximately 50 percent of these motions had a zone average velocity greater than the local mean velocity. The others had a zone average velocity smaller than the local mean velocity. Contributions to the Reynolds stress were measured in the momentum deficient zones but in the momentum excess zones shear stress production was less than that of the local long-term average Reynolds stress value. It could not be ascertained whether the typical eddies were formed by sublayer bursts or resulted from a redistribution of the vorticity in the logarithmic region caused by the large scale flow field. Because these eddies appear to be sweep events (Offen and Kline 1974) and their scales are 100 y^+ units, it is contended that typical eddies in the logarithmic region produce sublayer ejections. Typical eddies become sweep motions when they move towards the wall and their scales ($y^+=100$, $z^+=100$) are constant over a wide range of Reynolds numbers. These eddies may be responsible for the spanwise scale in the viscous sublayer and if so, for the sublayer bursts as well.

10. Instabilities in a laminar boundary layer forced upon by a wake were studied by Falco (1978). The experiments were performed in a tunnel equipped for flow visualization measurements. A laminar boundary layer was formed on the test wall of the flow tunnel and a cylinder was placed across the tunnel. A low Reynolds number ($R_D=770$) wake formed inducing interactions between the turbulent wake and the laminar boundary layer. Smoke was oozed into the cylinder wake and hot wire anemometers were used in the laminar boundary layer. Motion pictures

showed the following sequence of events. Fluid from the turbulent wake moved towards the wall and created a pocket (flow module) in the laminar boundary layer. This pocket was a response to a disturbance which was convected towards the wall. Such a disturbance was either a vortex or a wallward moving flow module (commonly called a sweep). The length scales of the outer layer vortices were roughly 100 wall layer units which corresponds to the typical eddy flow module scale (Falco 1977). After the pocket formation, fluid was ejected from the boundary layer. These ejections occurred at the downstream end of the pocket. The rapid fluid ejection was clearly independent of the low speed streaks because the boundary layer was a laminar one and no streamwise vorticity was present to produce low speed streaks. Both visual and anemometry data suggested that the ejections were a direct result of a boundary layer instability which in turn was caused by the interaction of the sweeps with the wall. Also the sweep and ejections resulted in significant Reynolds stress contributions. If the cylinder Reynolds number was increased the size of the pocket decreased. This behaviour suggests that coherent motions which are Reynolds number dependent, such as the typical eddy (Falco 1977), interact with the laminar boundary layer. Other experiments showed that in the sublayer of a turbulent boundary layer a double structure exists, namely the well known streaky structure and a very energetic flow module. During its evolution, a flow module exhibits a short pair of streaks which are joined to form an upstream apex. It is suggested that the bursting sequence is associated with the formation of flow modules. These modules cause an instability in the instantaneous velocity profile and lead to ejections of sublayer fluid.

11. The structural features of a turbulent flow over boundaries with different roughness conditions was experimentally studied by Grass (1971). Three experiments with different boundary conditions--hydraulically smooth, transitional and rough--were performed in an open channel with a Reynolds number (R_h) of 7000. Hydrogen bubbles and motion picture photography were used to obtain an instantaneous visual and quantitative description of the flow field. An increase in the wall roughness was obtained by placing 2 mm sand grains and 9 mm pebbles on the channel bottom. Relative to the smooth wall the shear stress was increased by 40 percent by the sand and by 90 percent by the pebbles. The results of this study suggest that the fluid inrush phase plays an important role in the momentum transfer mechanism near the wall. Large lateral flow velocities were produced along the sides of the high velocity inflows (high speed streaks) as the fluid was turned and spread out over the surface. Such a stagnated flow pattern was accompanied by vortex stretching as suggested by Lighthill (1963). The spanwise fluid flow along the adjacent sides of the high speed streaks was swept together and this low momentum fluid was lifted and ejected from the boundary. If this momentum deficient fluid travelled outwards it obstructed the high momentum outer flow which then had to pass over and around it. According to Grass the shear layer between the ejected fluid and the outer flow produces inflexions in the longitudinal velocity profiles. It was also surmised that the inflow phase as well as the outflow phase plays a dominant role in the turbulence production process. Differences in the inflow and outflow sequences between the smooth and rough boundary flows were associated mainly with the detailed mechanics of low momentum fluid entrained at the wall surface following inflow

phases. The fluid trapped between the roughness elements formed a reservoir of low momentum fluid which was drawn during the ejection phase. In the case of the rough boundary the ejection of fluid was extremely violent and rose almost vertically from between the roughness elements. During an inflow phase the fluid with high streamwise velocity very close to the wall was slowed by viscous shear stress in the case of a smooth wall flow. In contrast, the fluid in the rough boundary was decelerated quickly by the drag-inducing obstacles. The latter case resulted in a more localized inflow for rough boundaries and an increase in Reynolds stress production. It is postulated that as the boundary roughness scale increases the overall scale of the inflow and outflow eddies also increases.

12. The effect of dilute long chain polymer solutions upon the spatial structure of the viscous sublayer was investigated by Oldaker and Tiederman (1977). A fully developed turbulent channel flow ($R_h=10000$), together with dye injection through wall slots and motion pictures were used to study the streak formation process. For a Newtonian flow the streak spacing (Δz^+) is constant for $y^+=8$. For inflows with up to approximately 30 percent drag reductions, Δz^+ increased linearly with the percentage of drag reduction. For flows with a drag reduction higher than 30 percent Δz^+ increased linearly in the wall region for y^+ greater than 2 but at values of y^+ less than 2, Δz^+ increased more rapidly. Some streaks that would have occurred in a Newtonian flow were suppressed from forming in a drag reduced flow. In particular the number of streaks that were separated by a Δz^+ value less than 50 decreased in the 24 percent drag reducing flow and there were no streaks so close together in the 57 percent drag reducing flow. It has been hypothesized that the

Increased streak spacing in drag reducing flows is caused by the resistance of the dilute polymer solution to vortex stretching which inhibits the formation of streaks.

A sequence of events was found to be associated with the formation, growth and breakdown of the low speed streaks in a drag reducing flow. A similar phenomenon occurs in water flows suggesting that the streak formation process could be the same for drag reducing and non-drag reducing flows. The sequence began with a local deceleration of fluid in the wall region. Next the viscous sublayer became distorted by a small crater-like depression. Sweep events were associated with these wall disturbances. The axis of this oval shaped crater-like depression was stretched in the mean flow direction and the longitudinal sides (streaks) along this crater were lifted. The elongation continued, forming a valley between the growing streaks. Similar depressions occurred within the valleys between the initial streaks. The streaks grew, more depressions occurred, new streaks were formed and merged together. During this growing process the streaks were convected downstream slowly. Hardly any streamwise vorticity arose until the streak lifted away from the wall and burst. The strength of the rotation of the high speed streak was low and seldom were more than two revolutions observed.

Drag reducing flows exhibited long and thick single streaks. The average length of the drag reducing streak was much longer than the average streak length in water flow at equal u^* . Streak lengths increased with both the percentage of drag reduction and the solution viscosity. The streaks swept periodically with a small spanwise amplitude. However the drag reducing streaks showed an attenuation of this wavy motion when

compared with a water flow streak at the same u^* . For water and drag reducing flows 15 percent of the streaks merged to a single streak and all the water flow streaks burst within the field of view. However in the drag reducing flow 63 percent of the streaks burst, 14 percent did not burst and 23 percent lost their identity without bursting. Also a large portion of the drag reducing streaks were left as a residual after bursting. The work of Oldaker and Tiederman showed that drag reduction is achieved by inhibiting the formation of streaks by dilute polymer solutions. At equal flow rates the number of streaks in the drag reducing flow was smaller and the spatially averaged bursting rate lower. Consequently less turbulence was produced and less momentum transport achieved which in turn led to reduced production of wall shear stress.

III. EXPERIMENT DESCRIPTION

The coherent eddy structure and the bursting phenomenon in the viscous wall region of a turbulent pipe flow were examined with multiple probes and by means of conditional averaging. Ten pairs of wall probes equally spaced were placed at the wall of the test section. The wall probes were used to measure the axial and spanwise components of the fluctuating velocity gradient at the wall. An eight sensor fluid probe (i.e. rake) with fixed distances between its sensors was placed downstream from the wall probes. The rake was used to measure the average and the fluctuating axial velocity components at seven positions in the fluid and the radial velocity component at one position. The measurements were performed with a fully developed turbulent pipe flow at a Reynolds number of 29625 and are described in Section A. In Section B the model of the coherent eddy structure which serves as the theoretical basis for this work is presented. Conditional averaging criteria applied to the wall and fluid probes are discussed in Section C. Finally the way in which the conditional averages were calculated from the selected events in the data set is the subject of Section D.

A. Measurements

Three separate data sets were obtained using different rake positions relative to the wall probes. The rake was placed in the centre and at dimensionless downstream distances from the wall probes of 30, 60 and 90. For this work the length and time scales were made dimensionless with the wall parameters of kinematic viscosity (ν) and wall friction (u^*) unless otherwise specified. During each run the rake was placed at a different distance from the wall. Table 1 presents the dimensionless

distances of the fluid probes from the wall along with the downstream distances of the rake from the wall probes. The total dimensionless spanwise length covered by the wall electrodes was 153, which accounts for a dimensionless spanwise spacing of 17 between each adjacent electrode pair.

Table 1

Rake position Δx^+	Dimensionless distance (y^+) of the fluid probes (1,2,...,7) from the wall						
	1	2	3	4	5	6	7
30	14	22	30	39	56	75	106
60	11	19	27	36	53	72	103
90	8	16	24	33	50	69	100

The rake positions for purposes of data collection were chosen after several test runs were made. If the rake was placed too close to the wall probes, probe interference occurred and the spanwise wall intensities were affected, while the axial wall and fluid probe intensities remained nearly unchanged. Test runs indicated that the dimensionless distance--not the absolute distance--between the rake and the wall probes is critical to probe interference. Reliable measurements were obtained when the rake was placed at $x^+ (= \frac{xu^*}{v}) = 90$ downstream from the wall probes, independent of the $y^+ (= \frac{yu^*}{v})$ distance of the fluid probes from the wall. It was found that if the rake was placed at $x^+=0$ (same position as the wall probes) the first fluid probe had to be at a distance of at least $y^+=20$ from the wall to avoid probe interference. For each of the runs indicated in Table 1, 28 signals were processed. The analog signals of the fluid and wall probes were digitalized simultaneously with a sample frequency of 30 Hz for approximately 5.5 minutes until 10000 data

were obtained from each of the 28 channels. These data were transferred to a Cyber-175 digital computer as described in Chapter 5. A summary of the parameters used in this experiment is given in Table 2.

Table 2

$R_D = 29625$	$v = .00886 \text{ cm}^2/\text{s}$
$D = 19.37 \text{ cm}$	$C_b = 6.28 \times 10^{-6} \text{ moles/cm}^3$
$U_b = 13.553 \text{ cm/sec}$	$F_s = 30 \text{ sec}^{-1}$
$\langle S \rangle = 63.361 \text{ sec}^{-1}$	$N_D = 10000$
$\langle s_x^2 \rangle^{1/2} = 22.754 \text{ sec}^{-1}$	$T_D^+ = 20000$
$\langle s_z^2 \rangle^{1/2} = 7.430 \text{ sec}^{-1}$	$E_D = 100$

B. Eddy structure in the Viscous Wall Region

To explore the viscous wall region ($y^+ < 35$) the concept of the coherent eddy structure as introduced by Bakewell and Lumley (1967) and Sirkar (1969) was accepted. This structure consists of pairs of open eddies elongated in the streamwise direction and perpendicular to the direction of mean flow as depicted in Figure 3-1a. The elongated eddies carry fluid with high axial momentum to the wall (i.e. inflow) as indicated by point A of Figure 3-1a. The high momentum fluid exchanges momentum at the wall and then leaves the wall (i.e. outflow) at point B as a momentum deficient flow. The spanwise velocity component associated with the eddies is assumed to be homogeneous in the mean flow direction, harmonically variable in the spanwise direction and random in time,

$$w_z(y^+, z^+; t) = \hat{w}(t) y^+ \sin(2\pi z^+ / \lambda^+). \quad (3.1)$$

This type of flow pattern indicates a variation in the spanwise wall velocity gradient ($s_z(z, t)$) of the form shown in Figure 3-1b. The axial wall velocity gradient pattern ($s_x(z, t)$) which satisfies the conditions

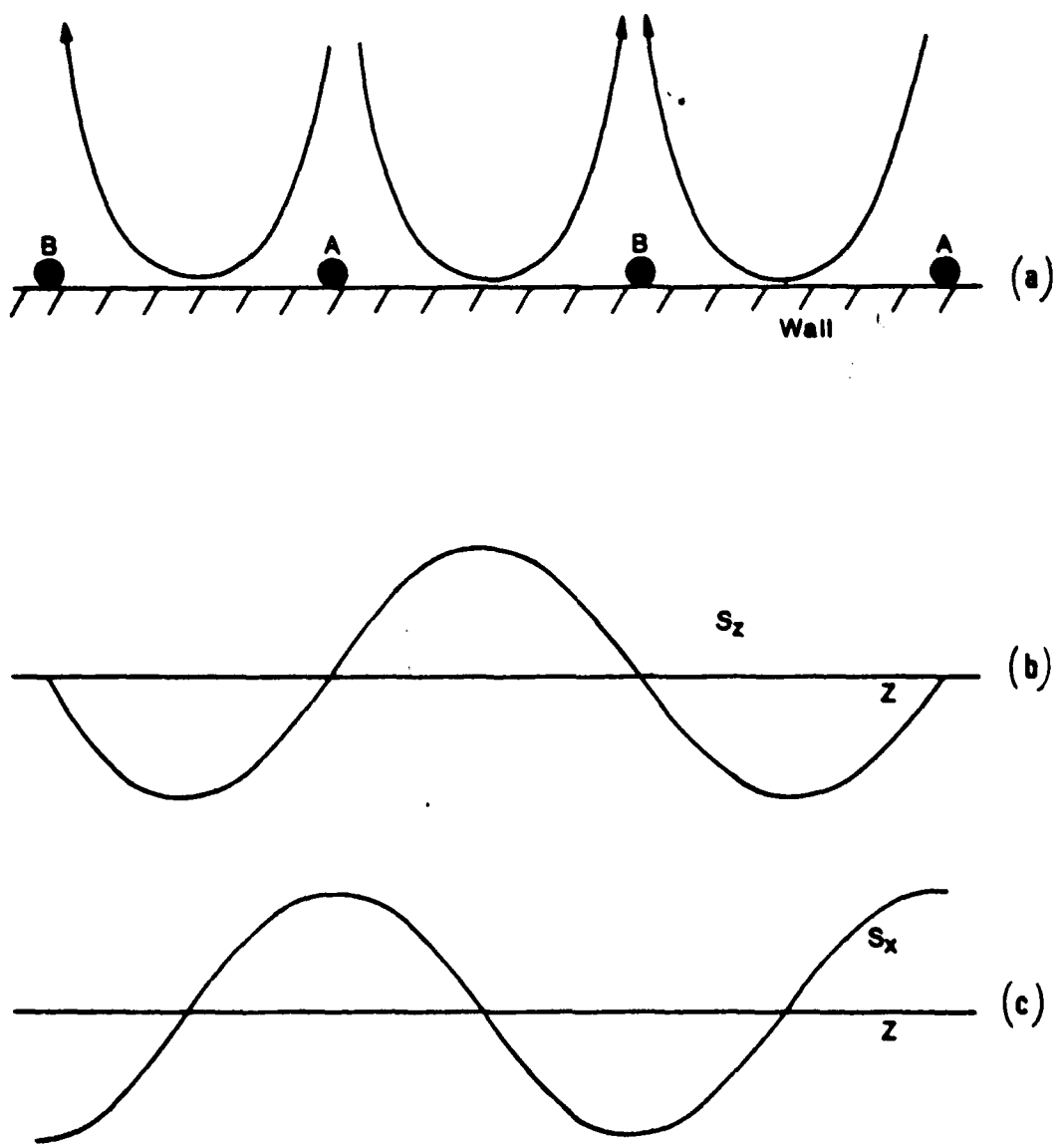


Figure 3-1. Idealized coherent eddy structure.

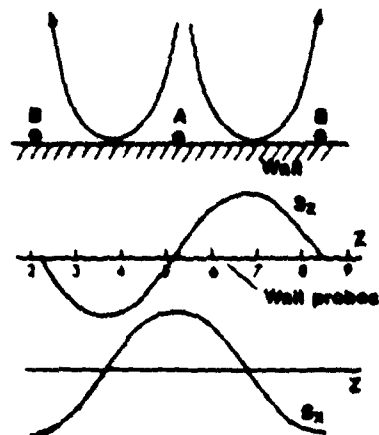
of inflows, outflows and a momentum exchange at the wall is shown in Figure 3-1c.

C. Applied Conditions

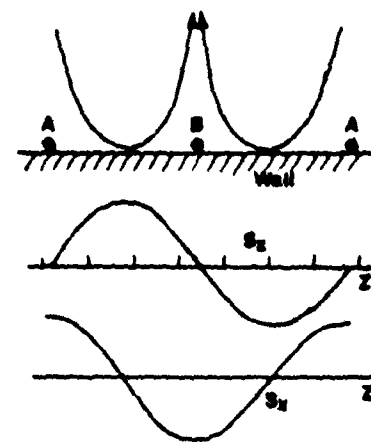
Conditional averaging was used to investigate the coherent eddy structure in the viscous wall region. To do so, conditions were applied to wall probe signals and fluid probe signals in order to determine events in the data set over which an average was to be taken. No theory exists for determining the proper conditions to be applied to the fluid and wall probes. The criteria used in this study were that the constraints placed upon the signals be few and simple and that the averaging procedure be easily repeated.

1. Inflows and outflows.

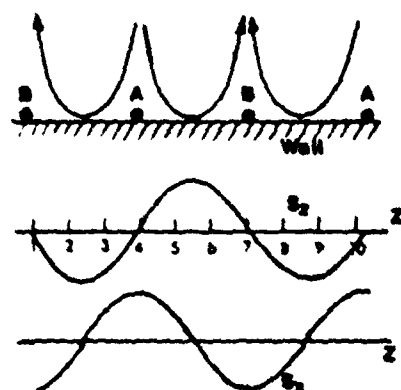
To detect inflows (fluid with high axial momentum moving towards the wall) and outflows (fluid with low axial momentum moving away from the wall) the idealized eddy model described in Section B was employed. Figure 3-2a shows that an inflow is accompanied by a zero crossing, a positive tangent in the $s_z(z,t)$ pattern and a maximum value in the $s_x(z,t)$ pattern. An outflow occurs at the point where the $s_z(z,t)$ pattern has a zero crossing and a negative tangent while the $s_x(z,t)$ pattern exhibits a minimum. As a conditional averaging criterion, only the $s_z(z,t)$ pattern was used. The $s_z(z,t)$ pattern is anti-symmetric around the zero crossing, thus multiplication of its values at equal distances from the zero crossing results in a negative number. For the search of the sine wave shaped $s_z(z,t)$ patterns in the data set, the spanwise velocity gradients at the wall (at equal distances from the multiple wall probe centre) were multiplied and added together. If this summation yielded a positive value then the instant in the data set was



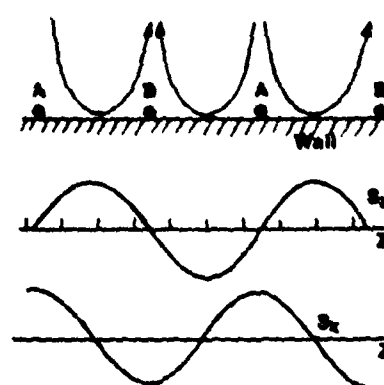
(a-1) Inflow pattern.



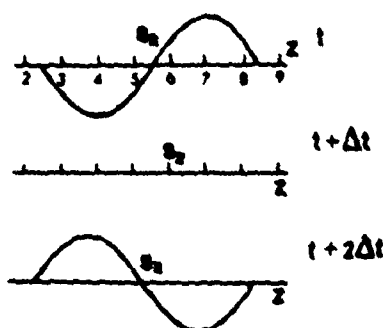
(a-2) Outflow pattern.



(b-1) Counter-clockwise rotating open eddy.



(b-2) Clockwise rotating open eddy.

(c) Change of the s_z pattern over time.Figure 3-2. Conditions applied to $s_z(x, t)$ wall pattern.

rejected as possible inflow (or outflow) event. The detection process is described by the following expression,

$$C_1(t) = \frac{\sum_{i=1}^3 s_z(6-i,t) - s_z(5+i,t)}{\left| \sum_{i=1}^3 s_z(6-i,t) - s_z(5+i,t) \right|} \sum_{i=1}^N s_z(6-i,t) s_z(5+i,t). \quad (3.2)$$

In this equation the spanwise velocity gradient $s_z(q,t)$ is expressed as a function of the wall electrode pair q , where q is numbered from 1 to 10. The multiple wall probe centre is between probes 5 and 6 and the assumed anti-symmetry of the $s_z(z,t)$ pattern between these probes causes the inflows and outflows to be near this multiple probe centre as shown in Figure 3-2a. A strong inflow at the multiple probe centre (that is, a sine wave shaped $s_z(z,t)$ pattern with large amplitudes) generates a large positive value for $C_1(t)$. Inflows and outflows were distinguished by the coefficient of equation (3.2); its value is plus unity for outflows and minus unity for inflows. Thus a violent outflow was known to occur near the multiple wall probe centre if $C_1(t)$ was negative with a large absolute value.

2. Spatial behaviour of inflows and outflows.

By studying another part of the idealized eddy structure the spatial behaviour of inflows and outflows was examined. Figure 3-2b shows the idealized $s_z(z,t)$ and $s_x(z,t)$ patterns when inflows and outflows are coupled in space. For a counter-clockwise rotating open eddy the $s_z(z,t)$ pattern has a maximum at the point where the $s_x(z,t)$ pattern has a zero crossing and a negative tangent. A clockwise rotating open eddy exhibits the same features but of opposite sign. Symmetry exists around the maximum and minimum of the spanwise velocity gradient pattern as shown in Figure 3-2b. To obtain the instants in the data set for the conditional average the spanwise velocity gradients at the wall

(at equal distances from the multiple wall probe centre) were multiplied and added together. This condition is described by the following equation,

$$C_2(t) = \frac{\sum_{i=1}^4 s_z(3+i, t)}{\left| \sum_{i=1}^4 s_z(3+i, t) \right|} \sum_{i=1}^4 s_z(6-i, t) s_z(5+i, t). \quad (3.3)$$

The positions of the inflow and outflow determined the rotation of the open wall eddy which is specified by the coefficient in equation (3.3). A positive coefficient indicates a counter-clockwise rotating eddy and a negative coefficient a clockwise rotating one. Those instants which yielded large positive or negative values for $C_2(t)$ were included as events for the conditional average.

3. Dynamic behaviour of inflows and outflows.

The dynamic behaviour of the coherent eddy structure was studied by examining inflows and outflows as functions of time. Because inflows and outflows occur randomly in space and time, it is likely that an outflow is followed by an inflow and vice versa. If a sine wave shaped $s_z(z, t)$ pattern was found in the data set, the change of this $s_z(z, t)$ pattern over time was examined. The following equations detect the $s_z(z, t)$ pattern change,

$$C_3(t) = \sum_{j=1}^K \frac{\sum_{i=1}^3 s_z(6-i, t-j) - s_z(5+i, t-j)}{\left| \sum_{i=1}^3 s_z(6-i, t-j) - s_z(5+i, t-j) \right|} \sum_{i=1}^N s_z(6-i, t-j) s_z(5+i, t-j) \\ \frac{\sum_{i=1}^3 s_z(6-i, t+j) - s_z(5+i, t+j)}{\left| \sum_{i=1}^3 s_z(6-i, t+j) - s_z(5+i, t+j) \right|} \sum_{i=1}^N s_z(6-i, t+j) s_z(5+i, t+j) \quad (3.4)$$

and

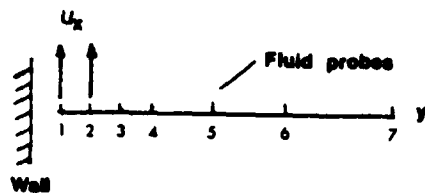
$$C_4(t) = \frac{\sum_{i=1}^3 s_z(6-i, t+K) - s_z(6-i, t-K) + s_z(5+i, t-K) - s_z(5+i, t+K)}{\left| \sum_{i=1}^3 s_z(6-i, t+K) - s_z(6-i, t-K) + s_z(5+i, t-K) - s_z(5+i, t+K) \right|}. \quad (3.5)$$

A negative value for $C_3(t)$ indicates that the $s_z(z, t)$ pattern changed sign over time which means the flow direction of the coherent eddies near the wall reversed, as indicated in Figure 3-2c. In essence equation (3.4) is the same as equation (3.2) but was applied simultaneously at several times in the data set. Only those instants for which $C_3(t)$ was a large negative value were considered for the conditional averaging scheme. The parameter $C_4(t)$ indicates the sequence of the detected $s_z(z, t)$ patterns at the wall. If $C_4(t)$ was positive then it was known that an inflow was followed by an outflow whereas for a negative value the opposite phenomenon took place.

4. Detection of inflows and outflows in the viscous wall region.

If inflows and outflows can be detected with the fluid probes then the spanwise and axial velocity gradient patterns at the wall can be predicted. To do so, two fluid probes were placed at distances from the wall of approximately y^+ equal to 8 and 16. At each instant the fluctuating velocity signals of the two probes were multiplied. Only those instants at which both velocity fluctuations were positive (see Figure 3-3a) or negative were considered, resulting in a positive product. If both velocity signals were positive an inflow was indicated and if negative an outflow. Inflows and outflows in the viscous wall region were selected on the basis of

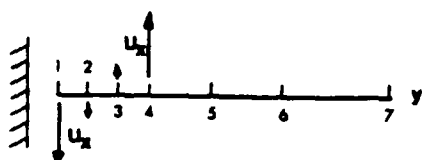
$$C_5(t) = \frac{u_x(y(1), t) + u_x(y(2), t)}{|u_x(y(1), t) + u_x(y(2), t)|} u_x(y(1), t) u_x(y(2), t). \quad (3.6)$$



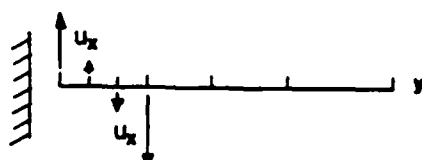
(a-1) Detection of inflows.



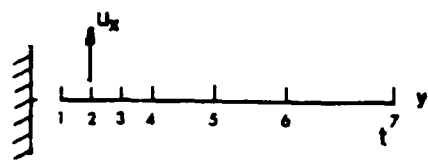
(a-2) Detection of outflows.



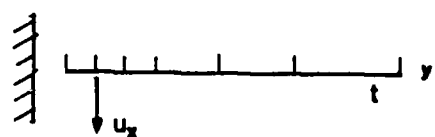
(b-1) Shear layer with positive slope.



(b-2) Shear layer with negative slope.



(c-1) Deceleration of fluid near the wall.



(c-2) Acceleration of fluid near the wall.

Figure 3-3. Conditions applied to the velocity fluctuations in the viscous wall region.

In this equation the axial velocity fluctuation $u_x(y(q), t)$ is expressed as a function of the fluid probe number q . Table 1 presents the relation between this fluid probe and its distance from the wall. Only those instants in time for which the absolute value of $C_5(t)$ was large were selected for the conditional averaging scheme. If the coefficient of equation (3.6) was positive an inflow took place whereas for a negative value an outflow occurred.

5. Spatial behaviour of the velocity fluctuations in the viscous wall region.

Four fluid probes at distances y^+ from the wall of approximately 8, 16, 24 and 33 were used to study the spatial behaviour of the turbulent velocities. Figure 3-3b shows the instantaneous turbulent velocity profile at fluid probes 1 to 4. If the fluctuating velocity profile shows a momentum deficiency at probes 1 and 2 but a momentum excess at probes 3 and 4 a positive shear layer forms. Thus rapid changes in the velocity fluctuations with respect to distance give rise to strong shear layers in the fluid which were detected by

$$C_6(t) = \frac{\sum_{j=1}^2 u_x(y(j), t) - u_x(y(2+j), t)}{\left| \sum_{j=1}^2 u_x(y(j), t) - u_x(y(2+j), t) \right|} \sum_{j=1}^2 u_x(y(3-j), t) u_x(y(2+j), t). \quad (3.7)$$

The instants for which large positive or negative values for $C_6(t)$ were obtained were used in the conditional averaging procedure. Distinction between the two types of shear layers (see Figure 3-3e) was made with the coefficient of equation (3.7). A positive coefficient indicates high momentum fluid near the wall and momentum deficient fluid farther away from it. Thus a positive value for $C_6(t)$ suggests a shear layer with a positive slope in the fluid near the wall and a negative value indicates a shear layer with opposite sign.

6. Dynamic behaviour of the velocity fluctuations at a point in the viscous wall region.

The change in turbulent fluctuations as a function of time was studied at several points in the viscous wall region. Of interest were the large fluctuating velocity changes as shown in Figure 3-3c. The data set was searched for rapid changes from large positive amplitudes to large negative ones and vice versa. These strong accelerations and decelerations were selected with

$$C_7(t) = \frac{\sum_{j=1}^K u_x(y(i), t-j) - u_x(y(i), t+j)}{\left| \sum_{j=1}^K u_x(y(i), t-j) - u_x(y(i), t+j) \right|} \sum_{j=1}^K u_x(y(i), t-j) u_x(y(i), t+j). \quad (3.8)$$

The magnitude of the change of a turbulent velocity fluctuation over time varied directly with the value $C_7(t)$. Positive and negative accelerations were distinguished by the coefficient of equation (3.8) which changes sign as a change in acceleration occurs. For the conditional averaging procedure only strong events were selected. Thus a strong acceleration is represented by a large value of $C_7(t)$ and a strong deceleration occurred when $C_7(t)$ was negative with a large absolute value.

D. Conditional Averaging Procedure.

All the investigated patterns described in Section C appeared many times in the data set but to different degrees as expressed by solutions to equations (3.2) to (3.8). Crucial to the conditional averaging procedure was the threshold level that was applied to the $C_i(t)$ values (where $i=1, 2, \dots, 7$) of equations (3.2) to (3.8) to determine the events

in the data set. In this study the conditionally averaged results were found to be insensitive to the applied threshold value, as can be seen in Figures 3-4, 3-5 and 3-6. These figures show the conditionally averaged spanwise velocity gradients at the wall for the condition described by equation (3.3). This condition is representative of all the conditions described in Section C. The applied threshold levels in Figures 3-4, 3-5 and 3-6 are from $100k_1$ to $5k_1$ (where k_1 is an arbitrary calculation constant) while the number of events over which the average was taken varied from 58 to 167. Thus a twentyfold decrease in threshold level resulted in approximately a threefold increase in the number of detected events. Figures 3-4, 3-5 and 3-6 show that lower threshold levels effected a decrease in the amplitudes of the $s_z(z,t)$ patterns but the specific features of these patterns remained unchanged. To avoid controversy about the threshold level value, one percent of the data set time was chosen as the event time. For example in a data set of 10000 data approximately 100 events were selected for the conditional averaging procedure. An explanation of why 100 is an acceptable number for the averaging procedure follows. To detect the coherent eddy structure different intervals of the $s_z(z,t)$ pattern were focussed upon as discussed in Section C. Equally spaced intervals can be denoted around four characteristic points of the sine wave shaped $s_z(z,t)$ pattern. These points are: (1) a maximum, (2) a minimum, (3) a positive slope with a zero crossing and (4) a negative slope with a zero crossing. Because the $s_z(z,t)$ pattern is random in space the chance (α) of focussing upon a specified interval of the $s_z(z,t)$ pattern is 25 percent. The data set has a dimensionless time period of $T_D^+ = 20000$. From Figures 3-4, 3-5 and 3-6 the conditionally averaged duration of the event is found to

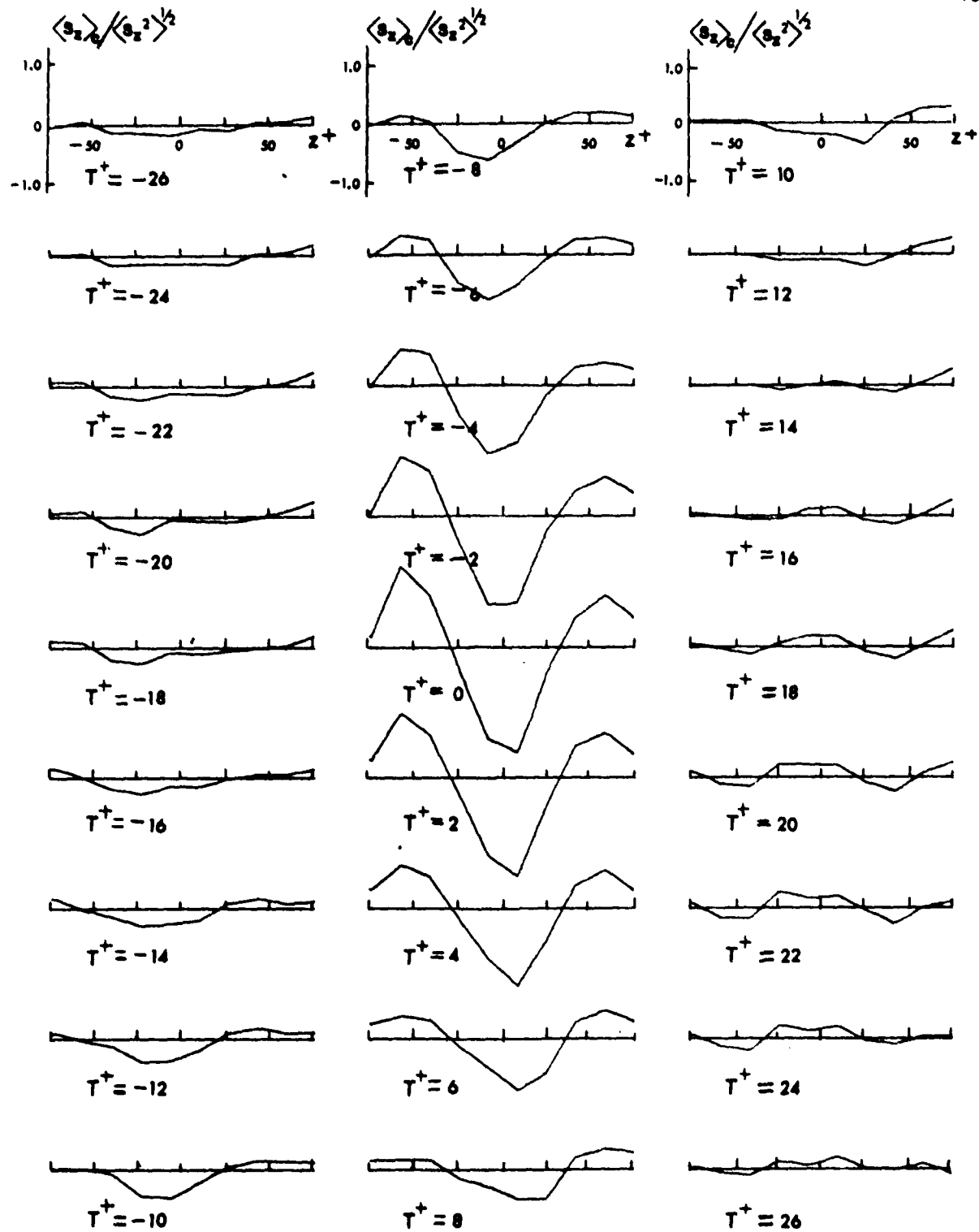


Figure 3-4. Conditionally averaged inflow-outflow s_z patterns. Equation (3.3) applied to s_z gradients; $E_D = 58$; z threshold value = $100 k_1$.

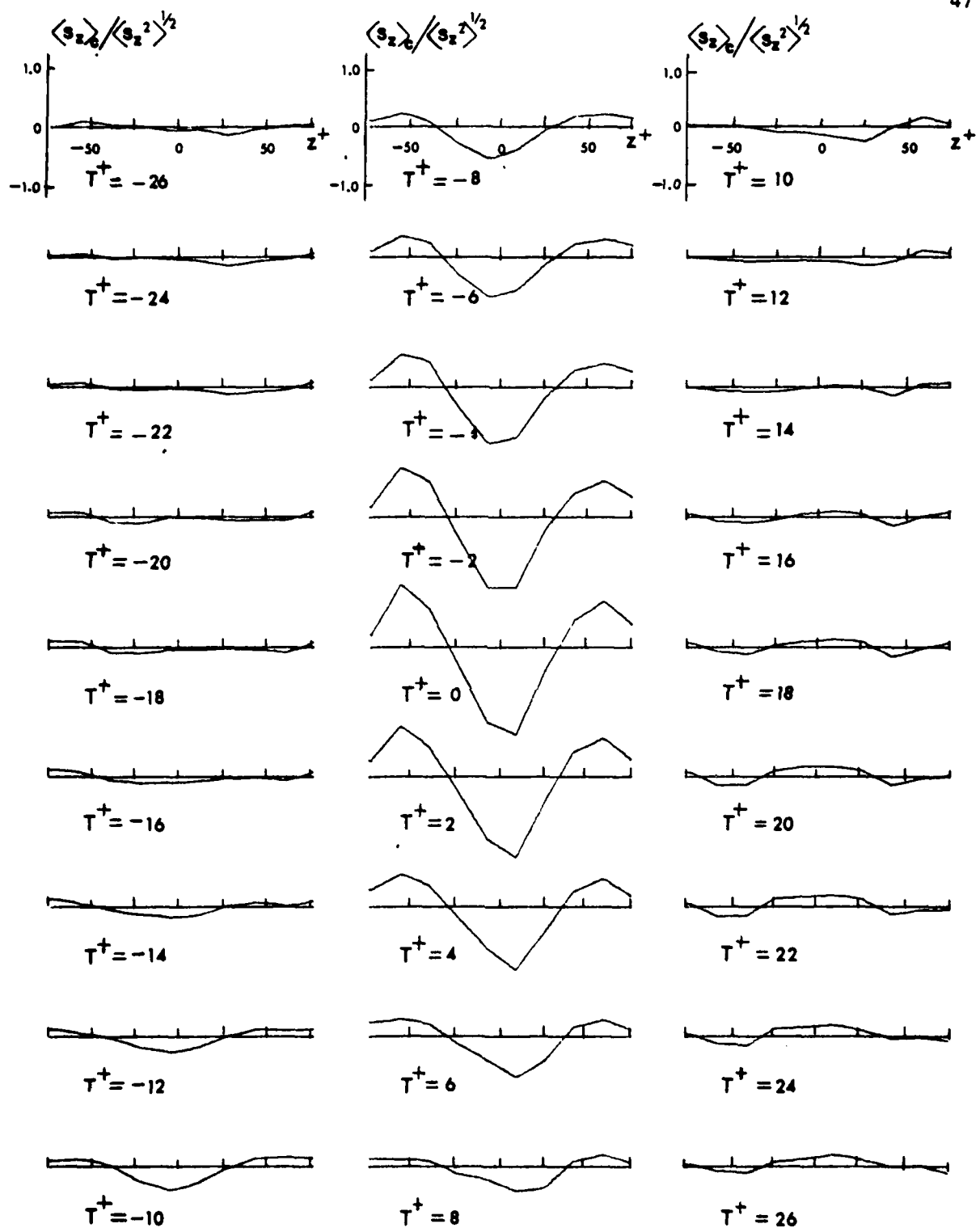


Figure 3-5. Conditionally averaged inflow-outflow s_z patterns. Equation (3.3) applied to s_z gradients; $E_D = 111$; threshold value = $50 k_1$.

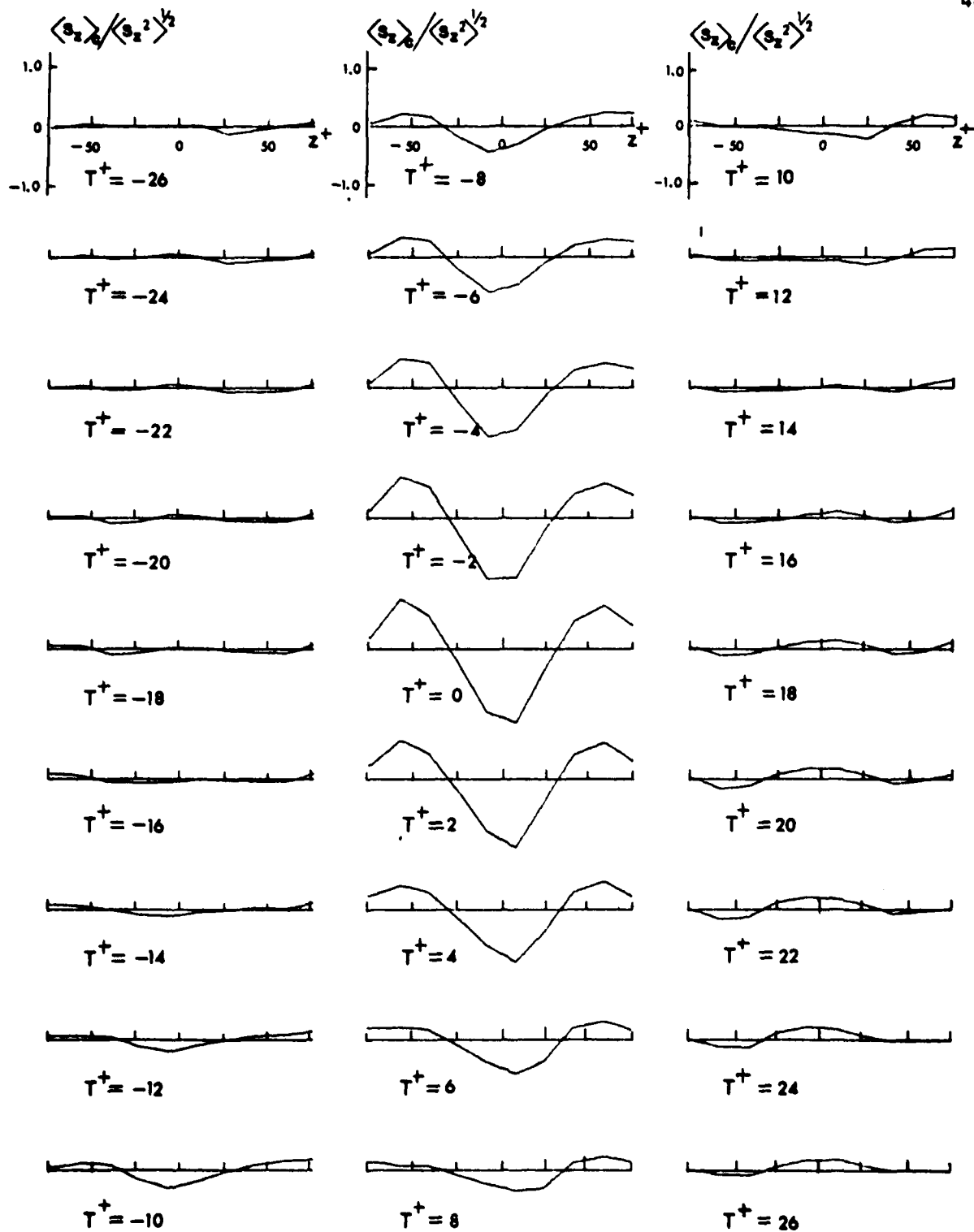


Figure 3-6. Conditionally averaged inflow-outflow s_z patterns. Equation (3.3) applied to s_z gradients; $E_D = 167$; threshold value = $5 k_1$.

be approximately $T_E^+ \approx 50$. Thus the number of events (E_D) in the data set for a given condition can be estimated from

$$E_D = \frac{T_D^+}{\alpha T_E^+} \approx 100.$$

All the instants at which the selected events occurred were labeled $T^+=0$. To avoid averaging over the same event more than once the minimum dimensionless time between each of two consecutive events was longer than $\Delta T^+=50$. Counting from these $T^+=0$ points back and forward in time the $T^+=-26, -24, -22, \dots, 24, 26$ points were denoted. The dimensionless time $T^+=2$ between adjacent points in the data set is equal to the frequency at which the analog signals were digitalized. The conditional average of a given event was obtained by taking averages over all the dimensionless time points in the data set of the same numerical value. Thus the conditional averages of the fluctuating and instantaneous velocities are given by

$$\langle u_x(y(j); T^+ \pm \Delta T^+) | C_i(t) \rangle \quad (3.10)$$

and

$$\langle U_x(y(j); T^+ \pm \Delta T^+) | C_i(t) \rangle \quad (3.11)$$

where $j=1, \dots, 8$ (the fluid probe number) and $C_i(t)$ (where $i=1, 2, \dots, 7$) are the conditions described in Section D. The conditionally averaged axial and spanwise wall velocity gradients for conditions $C_i(t)$ are described by

$$\langle s_x(z(k); T^+ \pm \Delta T^+) | C_i(t) \rangle \quad (3.12)$$

and

$$\langle s_z(z(k); T^+ \pm \Delta T^+) | C_i(t) \rangle \quad (3.13)$$

where $k(=1, \dots, 10)$ is the number of the wall electrode pair.

IV. THE ELECTROCHEMICAL MEASUREMENT TECHNIQUE

Many authors have presented mathematical analyses of diffusion controlled electrochemical systems. Reiss and Hanratty (1962, 1963) and Mitchell and Hanratty (1966) developed a technique for measuring velocity and laid the mathematical framework required to study turbulence near a solid boundary. Fortuna and Hanratty (1971) presented a boundary layer analysis of the frequency response of electrochemical wall probes and McConaghay (1974) described the iodine potassium-iodide electrochemical system.

A. Description of the Electrochemical Technique

The wall probes as well as the fluid probes are electrodes. An electrochemical probe (the mass transfer analog of the hot film anemometer) measures fluctuations in the flow indirectly through fluctuations in the concentration gradient at the probe surface. The operation of such a probe is based upon a reduction-oxidation reaction for which the rate is limited by mass transfer. The electrolyte used was composed of iodine and potassium-iodide; the iodine primarily exists as the tri-iodide ion I_3^- ,



The reaction in this electrochemical system is the reduction of iodine ions on a small platinum electrode (cathode) in combination with oxidation on a large anode, downstream from the cathode. The surface area of the anode was made many orders of magnitude larger than that of the cathode so that the reverse reaction to I_3^- was complete. The reaction at the cathode is



and at the anode



The experiments were performed with an iodine (I_2) concentration of approximately .005 M and a potassium iodide (KI) concentration of approximately .10 M. Excessive iodide is necessary to keep the electrolyte electrically neutral. Neutrality of the flow medium prevents the electric field from affecting the migration of the charged I_3^- ions to the electrode. The I_3^- concentration was determined by titration with .01 N sodium thiosulfate, $Na_2S_2O_3$.

The mass transfer rate can be related to the fluctuating velocity field near the cathode if the following assumptions are valid:

- a. The scales of the turbulent eddies are large with respect to the electrode size.
- b. The concentration boundary layer thickness is smaller than the viscous sublayer thickness.
- c. The fluid properties of density, viscosity and diffusivity are constant.

Assuming the electrode size is smaller than the scales of the turbulence implies uniform flow over the electrode, so that at any instant the velocity over all segments of the electrode is the same. Thus the smallest electrode is least affected by nonuniform flow. The thickness of the concentration boundary layer may be approximated from the Nernst diffusion layer equation,

$$y_c = \frac{\theta}{\langle K \rangle} . \quad (4.4)$$

Raiss and Hanratty (1963) showed that for Reynolds numbers in the range of 2×10^3 to 50×10^3 the concentration boundary layer is less than one-tenth

of the viscous sublayer thickness. The electrolyte temperature was maintained carefully at 25. \pm .1 degrees Celsius and the iodine-iodide concentration was made low, in order to keep variations in density, viscosity and diffusivity caused by temperature and concentration variations small.

The local rate of mass transfer was studied by measuring the average current and current fluctuations at the probe. An electric potential was applied between the probe and a downstream anode, and then the voltage in this circuit was measured. If after applying a certain voltage at the probe a limiting circuit voltage (current= $V_o - V_i / R_f$) was obtained, the probe was mass transfer controlled. The probes were operated at the plateau region of the polarization curve as shown in Figure 4-1. In this operation region the current was controlled by the mass transfer rate rather than by the reaction kinetics. The concentration of the reacting species was zero at the probe surface. In this study the electric potential applied at the probes was about -.50 volts, which approximates the middle of the plateau region of the polarization curve.

B. Equations for the Fluid Probes

For this research the mass transfer fluid probes were used successfully to measure turbulence at low Reynolds numbers. Also accurate intensities were measured and long-term stability of the signals was achieved. Use of a mass transfer probe has several advantages over use of a heat transfer probe. The time response of the mass transfer probe is negligible because the charge capacity of this probe is very small. In the mass transfer mode cooling effects of the probe supports do not exist. By measuring close to a wall a heat transfer probe may

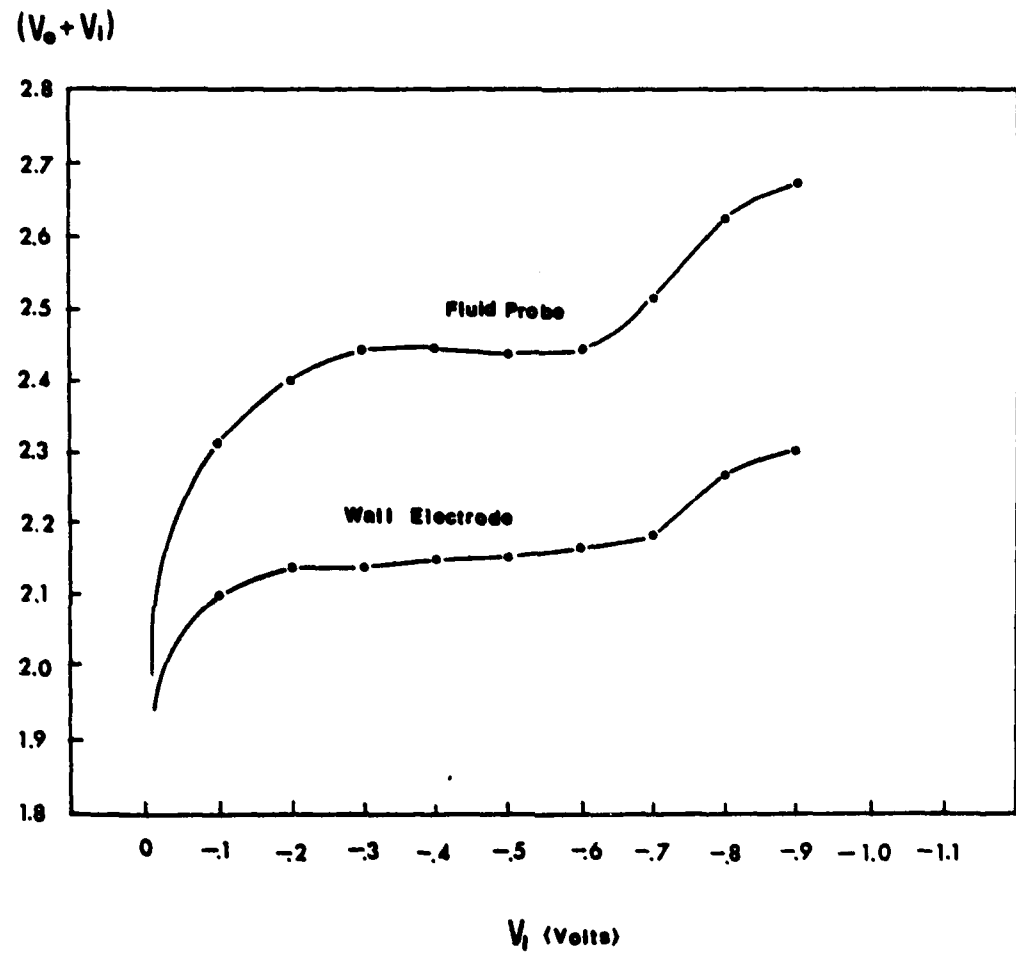


Figure 4-1. Polarization curves for a wall electrode and a fluid probe.

interfere with the wall by heat conduction and convection. A mass transfer probe does not cause this problem because the wall is inert to the electrochemical reaction. The electronics to measure the mass transfer are simple and inexpensive. However, the mass transfer probe is not without disadvantages. The sensitivity of the probe decreases rapidly if dirt accumulates around the probe wire. In addition the harsh electrolytic environment in which the probe operates may limit the lifetime of the probe wire.

A diffusion controlled electrochemical reaction occurs at the probe surface, and the mass transfer rate of this reaction can be related to the velocity gradient at the probe. The mass balance at the probe surface for the tri-iodide ion was solved by Dimopoulos and Hanratty (1968) for high Schmidt numbers by using a similarity transformation of Acrivos (1960). For nonseparated flow the local mass transfer coefficient k can be expressed as a function of the Sherwood number in the following dimensionless equation,

$$\frac{S_h}{(R_d S_c)^{1/3}} = \frac{\delta^{1/2}}{9^{1/3} \Gamma(4/3) \left(\int_0^x \delta^{1/2} dx \right)^{1/3}} \quad (4.5)$$

where $S_h (=kd/\theta)$ is the Sherwood number and δ is the streamwise wall velocity gradient made dimensionless with the velocity of the approaching stream and the characteristic length of the sensor. Shaw (1976) presented an empirical correlation for the molecular diffusivity as a function of kinematic viscosity for the iodine potassium-iodide electrochemical system,

$$\log \theta = -1.054 \log \nu - 7.128. \quad (4.6)$$

According to Rosenhead (1963), for Reynolds numbers on the order of one, the stream function for a flow near a probe wire is given approximately by

$$\psi = \frac{d}{2} U \sin \theta \left[\frac{1}{2S} \left(\frac{2r}{d} \left(2 \ln \frac{2r}{d} - 1 \right) + \frac{d}{2r} \right) \right] \quad (4.7)$$

where d is the diameter of the wire and $S=1/2-\gamma+\ln(8/R_d)$ in which γ is Euler's constant. The dimensionless streamwise wall velocity gradient can be calculated from equation (4.7) and is

$$\beta = \frac{d}{U} \frac{\partial^2 \psi}{\partial r^2}. \quad (4.8)$$

When (4.8) is substituted into (4.5) an expression for the local Sherwood number is obtained,

$$\frac{S_h}{(R_d S_c)^{1/3}} = \frac{1.0762 (\sin \theta)^{1/2}}{S^{1/3} \left(\int_0^\theta (\sin \theta)^{1/2} d\theta \right)^{1/3}}. \quad (4.9)$$

The local mass transfer coefficient k as given in expression (4.9) is a function of the Reynolds number and angle θ . If the Schmidt number ($S_c=805$) is substituted into (4.9) a simple expression can be obtained for the Sherwood number,

$$S_h = 10.011 g(R_d) h(\theta) \quad (4.10)$$

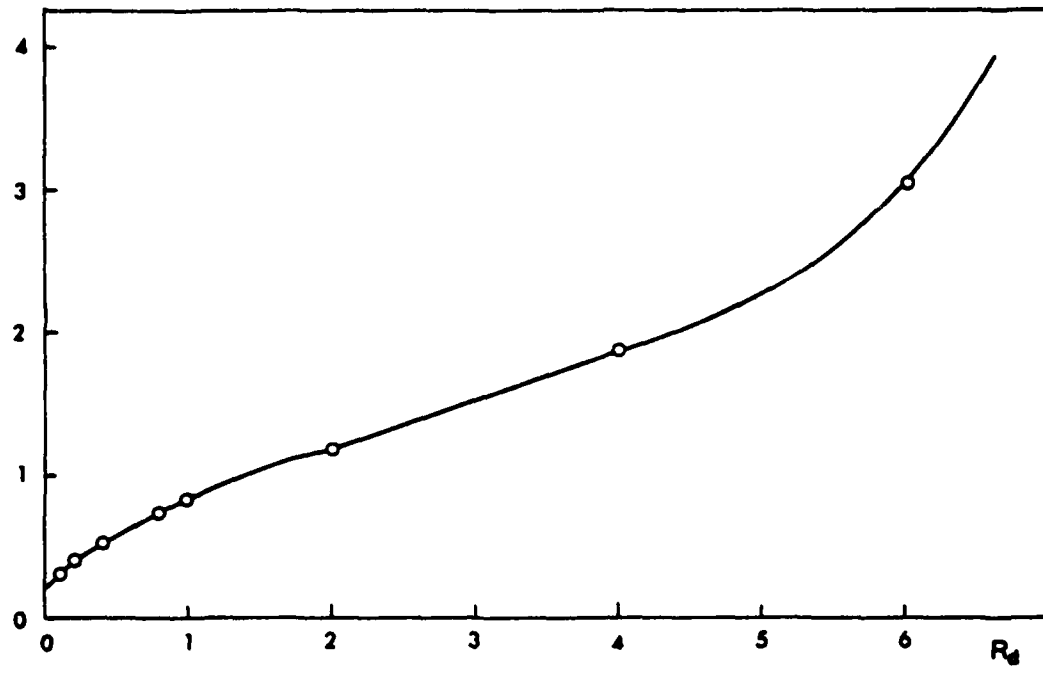
where

$$g(R_d) = \left[\frac{R_d}{(-.0772 + \ln(8/R_d))} \right]^{1/3}$$

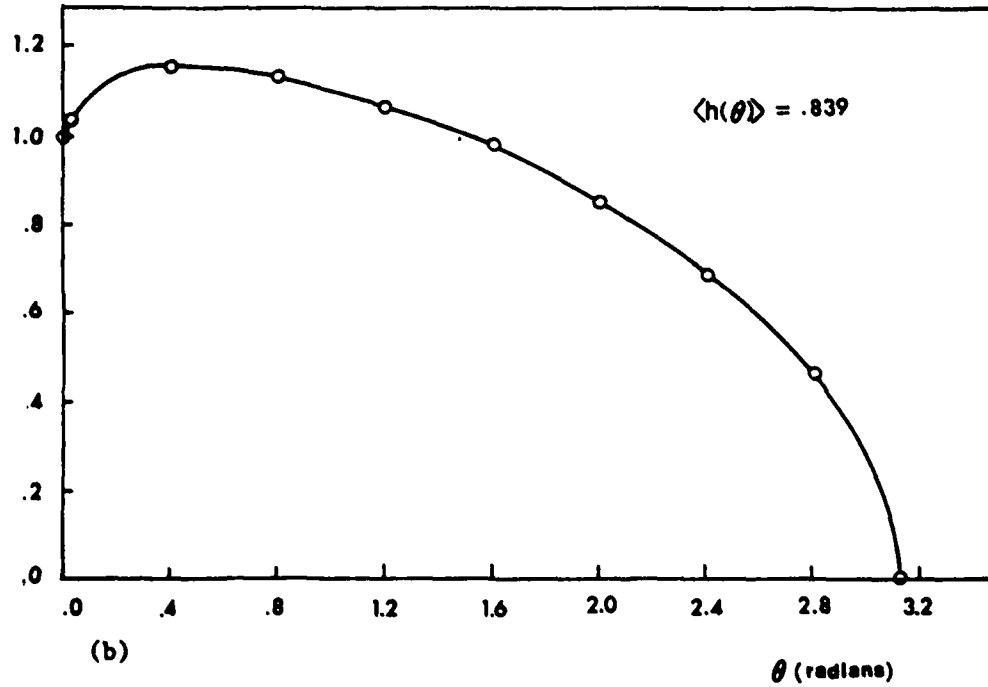
and

$$h(\theta) = \frac{(\sin \theta)^{1/2}}{\left(\int_0^\theta (\sin \theta)^{1/2} d\theta \right)^{1/3}}$$

The function $g(R_d)$, shown in Figure 4-2a, indicates an approximately linear region for Reynolds numbers smaller than one, based on wire diameter. The local mass transfer at the probe depends on the function $h(\theta)$ which is plotted in Figure 4-2b. By integrating $h(\theta)$ from zero to

$g(R_d)$ 

(a)

 $h(\theta)$ 

(b)

Figure 4-2. Dependence of Sherwood number on $g(R_d)$ and $h(\theta)$.

π , the average value of $h(\theta)$ is found to be $\langle h(\theta) \rangle = .83923$. Thus the average mass transfer coefficient for the cylindrical element is given as

$$\frac{\langle K \rangle d}{\partial} = \int_0^{\pi} S_h d\theta = 8.4017 g(R_d) . \quad (4.11)$$

Figure 4-3 shows the theoretical curve for the average mass transfer of the sensor as a function of the Reynolds number. Because the fluid probes were operated over a large Reynolds number range, the theoretical approach could not be used. The fluid probes were calibrated using the empirical formula

$$E = BU^n \quad (4.12)$$

where the velocity U is related to the cathode current caused by the mass transfer. Typical calibration curves, from data taken in this work, are given in Figure 4-3 along with the constants B and n . The constants B and n for the theoretical mass transfer curve, as shown in Figure 4-3, are 2.397 and 4.191 respectively. Calibration curves of Zilker (1977), also shown in Figure 4-3, agree with the calibration curves taken in this experiment. It is to be noted that the theoretical and the calibrated curves show agreement over a wide range of Reynolds numbers.

For calibration the fluid probes were transferred to the centre of the flow loop. The maximum centre line velocity can be related to the bulk mean velocity by the following expression,

$$\frac{U_b}{\langle U_m \rangle} = \frac{2n^2}{(n+1)(2n+1)} . \quad (4.13)$$

Isakof and Drew (1951) correlated the data of several pipe flow investigations and found the exponent n to have the following equation,

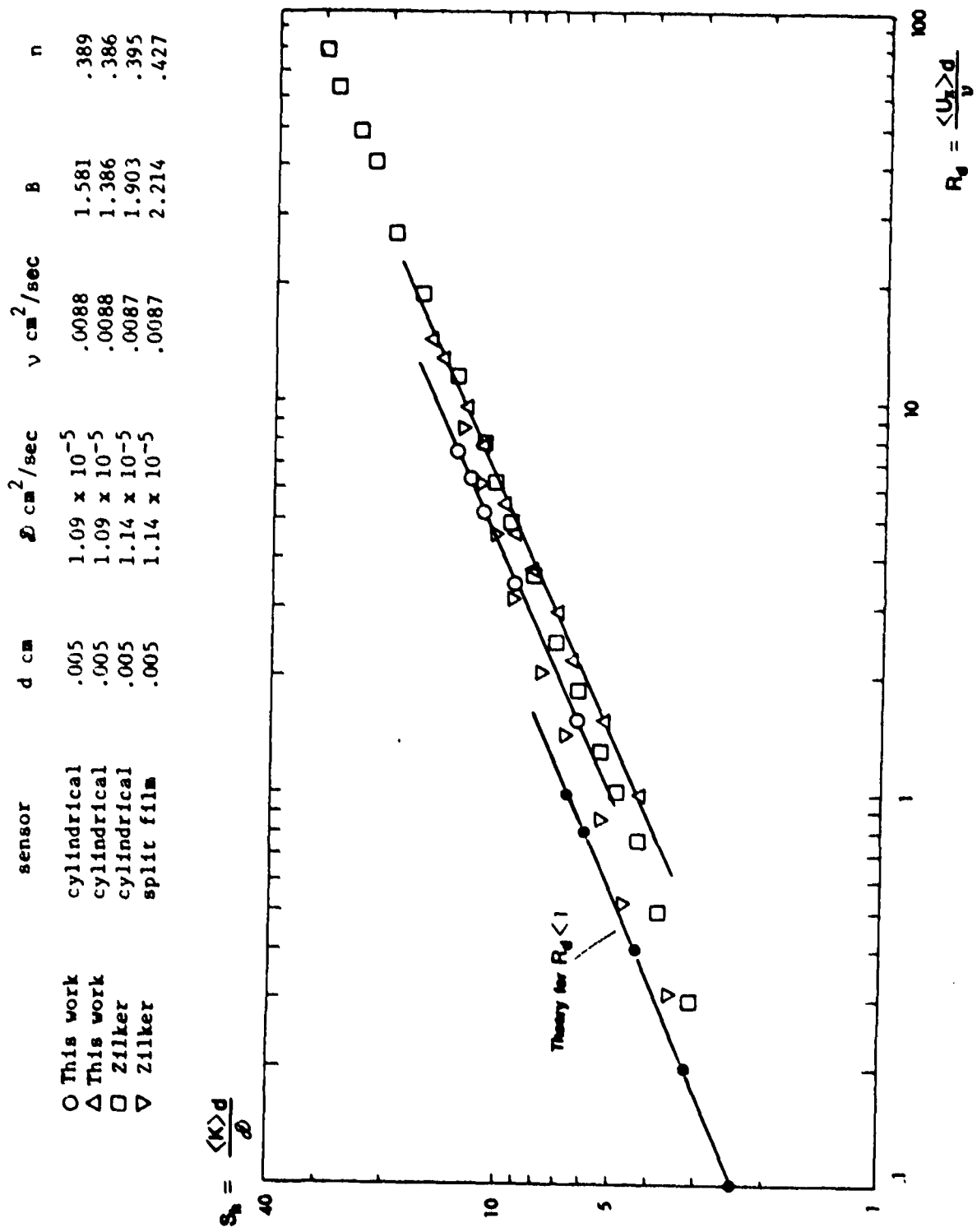


Figure 4-3. Calibration curves for mass transfer fluid probes.

$$\frac{1}{H} = 0.2679 - 0.02725 \log R_D \quad (4.14)$$

Equations (4.13) and (4.14) were used to calculate the average velocity at the fluid probes under calibration conditions.

Radial velocity fluctuations were measured with a two sensor fluid probe. Suppose the sensors S_a and S_b of the two sensor probe form an angle of α degrees and the instantaneous velocity forms an angle of β degrees with sensor S_b . The instantaneous axial and radial velocities at the two sensor mass transfer probe can be calculated by

$$\langle U \rangle + u = U_1 \cos(\alpha - \beta) \quad (4.15a)$$

and

$$v = U_1 \sin(\alpha - \beta) \quad (4.15b)$$

The effective mass transfer velocities for wires S_a and S_b respectively are given as

$$N_a = U_1 \cos \beta \quad (4.16a)$$

and

$$N_b = U_1 \sin \beta \quad (4.16b)$$

From equations (4.15) and (4.16) the average velocity and instantaneous turbulent velocities in the axial and radial directions are determined.

C. Equations for the Wall Electrodes

Mitchell (1965) experimented with rectangular wall electrodes and found that velocity fluctuations perpendicular to the mean flow direction can be measured if the electrode length is parallel to the flow direction. A rectangular wall electrode at an angle to the mean flow is sensitive to flow fluctuations in both the longitudinal and spanwise direction. Sirkar and Hanratty (1969) studied the axial and spanwise sensitivity of rectangular electrodes for different angles of this electrode to the

mean flow direction. A pair of electrodes slanted at angles of ± 15 degrees to the flow direction gave the best result for measuring simultaneously the longitudinal and spanwise velocity gradients at the wall. For this work multiple pairs of rectangular electrodes were used.

The flux of the tri-iodide ion to the surface of such a rectangular electrode (cathode) with area A_e is related to the cell current I by the relationship

$$N = \frac{I(1-T)}{n_e A_e F} \quad (4.17)$$

where F is Faraday's constant and n_e is the number of electrons transferred in the reaction. The transference number T is approximately .001 and can be neglected. Consequently the current was determined by mass transfer rather than charge transfer. The mass transfer coefficient K is defined as

$$K = \frac{N}{C_b - C_w} \quad (4.18)$$

where C_b is the bulk concentration of the reacting species, C_w is the concentration of that species at the surface of the electrode, and $C_w=0$ if the reaction is diffusion controlled. Using equation (4.17) the mass transfer coefficient in equation (4.18) can be rewritten as

$$K = \frac{I}{n_e A_e F C_b} \quad (4.19)$$

Because the Schmidt number is much greater than one, the concentration boundary layer is very thin, so the average velocity and the fluctuating velocities can be represented as first terms of a Taylor series expansions around $y=0$,

$$\langle U \rangle = \langle S_x \rangle y$$

$$u = s_x y$$

$$w = s_{zy} .$$

Conservation of mass requires the fluctuating velocity perpendicular to the wall to be given as

$$v = -\frac{1}{2} \left(\frac{\partial s_x}{\partial x} + \frac{\partial s_z}{\partial z} \right) y^2 .$$

The measured mass transfer rates can be related to the velocity field after certain simplifications have been made. The simplifications are justified due to the thinness of the concentration boundary layer. If the pseudo-steady state approximation of Mitchell and Hanratty (1966) is accepted, the average concentration field is described by

$$\langle S_y \rangle \frac{\partial \langle C \rangle}{\partial x} = \frac{\partial^2 \langle C \rangle}{\partial y^2} \quad (4.20)$$

and the boundary conditions are

$$\langle C(0, y) \rangle = \langle C(x, \infty) \rangle = C_b$$

$$\langle C(x, 0) \rangle = 0 .$$

The solution of equation (4.20) is

$$\frac{\langle C(x, y) \rangle}{C_b} = \frac{1}{\Gamma(\frac{4}{3})} \int_0^\eta e^{-\eta^3} d\eta \quad (4.21)$$

where

$$\eta = y \left(\frac{\langle S_y \rangle}{9 \partial_x} \right)^{1/3} .$$

Values of the integral of equation (4.21) were tabulated by Abramowitz (1951) and the average mass transfer over the electrode surface is given as

$$\langle K \rangle = \frac{1.5}{\Gamma(\frac{4}{3})} \left(\frac{\partial^2 \langle S_y \rangle}{9 L} \right)^{1/3} = \sigma \left(\frac{\langle S_y \rangle}{L} \right)^{1/3} . \quad (4.22)$$

The term L is the effective length of the electrode for a given path of the flow. Consider the rectangular electrode of length L and width W at an angle ϕ to the direction of mean flow as shown in Figure 4-4. Assume a uniform flow over the electrode surface. The direction of flow at any instant forms an angle θ with the direction of mean flow,

$$\tan\theta = \frac{s_z}{\langle s_x \rangle + s_x}$$

Divide the electrode into a number of strips of length w parallel to the instantaneous flow direction. As demonstrated in Figure 4-4, the value of w is less near the edges of the electrode than in the central region. If $\phi-\theta=\psi$, where $\psi=\tan^{-1}(L/W)$ then the mass transfer coefficient for each of these strips equals

$$K_w = \sigma \left(\frac{S_w}{w} \right)^{1/3}$$

The average instantaneous mass transfer coefficients of two electrodes in the "V" arrangement (shown in Figure 4-4) slanted at angles ϕ to the direction of mean flow are

$$K_1 = \sigma \left[\frac{S \sin(\phi-\theta)}{L} \right]^{1/3} [1+\tau \cot(\phi-\theta)] \quad (4.23)$$

and

$$K_2 = \sigma \left[\frac{S \sin(\phi+\theta)}{L} \right]^{1/3} [1+\tau \cot(\phi+\theta)] \quad (4.24)$$

where

$$\tau = \frac{L}{5W}$$

The time averaged mass transfer coefficient is then given as

$$\langle K \rangle = \sigma \left(\frac{\langle S \rangle \sin \phi}{L} \right)^{1/3} (1+\tau \cot \phi) \quad (4.25)$$

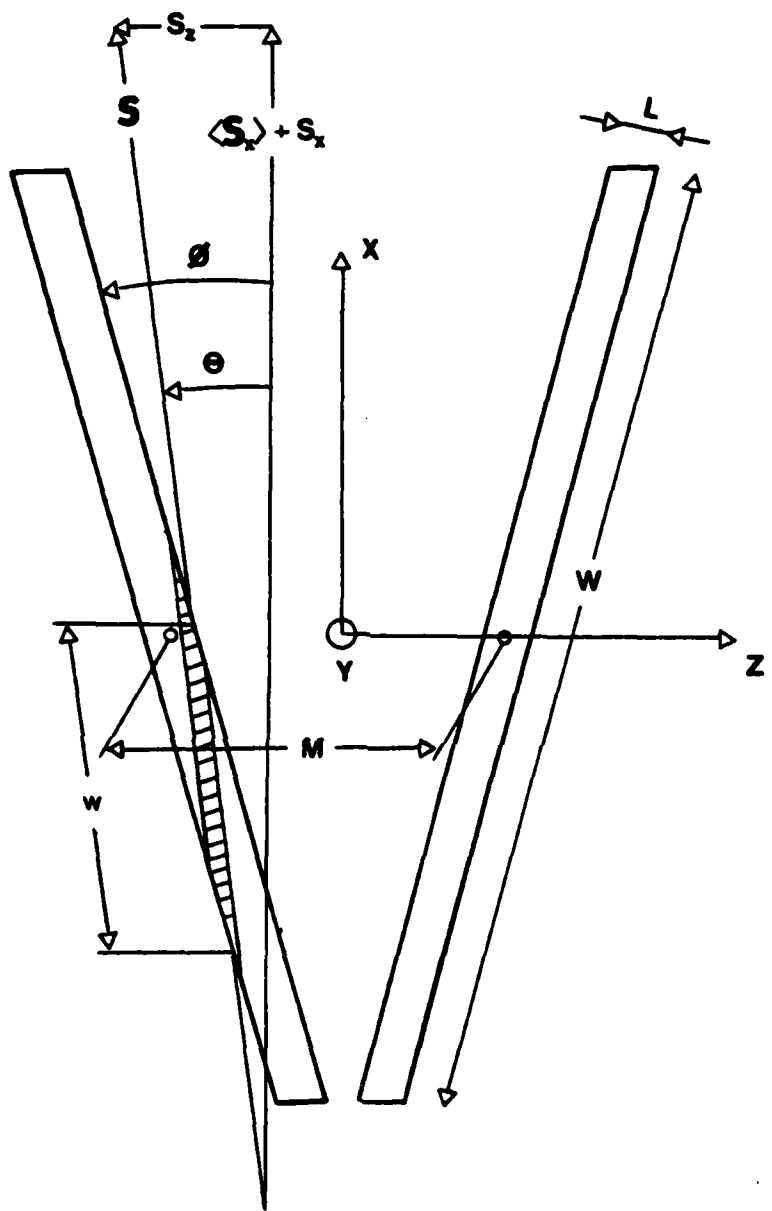


Figure 4-4. Pair of slanted "V" electrodes.

By virtue of equations (4.23) and (4.24) it follows that

$$\frac{K_1 - K_2}{K_1 + K_2} = \frac{f_1 - f_2 + \tau(f_1 f_3 - f_2 f_4)}{f_1 + f_2 + \tau(f_1 f_3 + f_2 f_4)} \quad (4.26)$$

where

$$\begin{aligned} f_1 &= [\sin(\phi-\theta)]^{1/3}, & f_3 &= \cot(\phi-\theta), \\ f_2 &= [\sin(\phi+\theta)]^{1/3}, & f_4 &= \cot(\phi+\theta). \end{aligned}$$

Equation (4.26) is a function of θ only. Figure 4-5 shows the relationship between K_1 , K_2 and θ with $\theta < 14$ for which equation (4.26) is valid.

The instantaneous magnitude of the velocity vector is determined by

$$S = \frac{L}{\sigma^3} \left[\frac{K_1 + K_2}{f_1 + f_2 + \tau(f_1 f_3 + f_2 f_4)} \right]^3. \quad (4.27)$$

The axial and spanwise velocity gradients at the wall are then calculated as

$$\begin{aligned} \langle s_x \rangle + s_x &= S \cos \theta \\ s_z &= -S \sin \theta. \end{aligned}$$

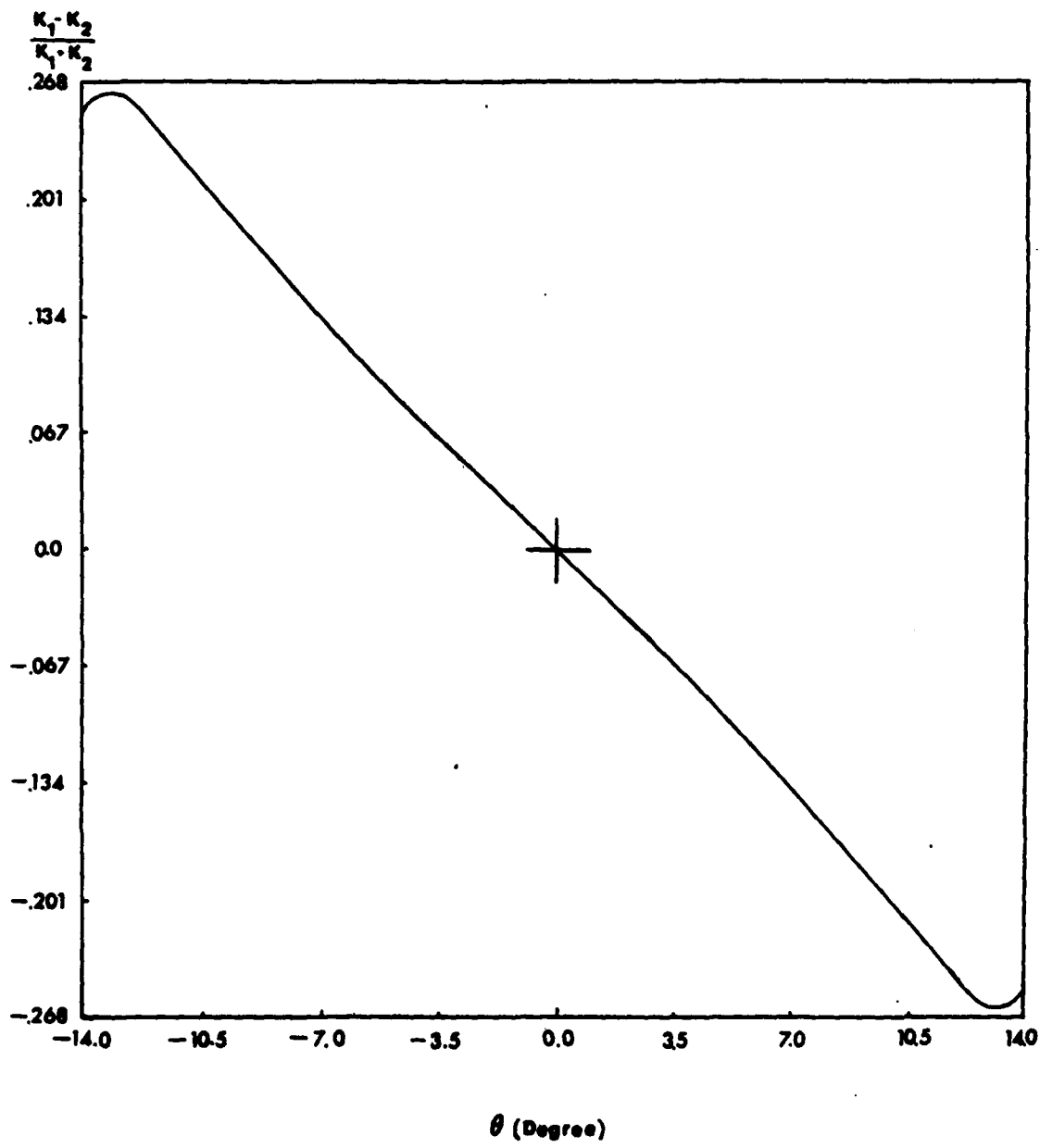


Figure 4-5. Response of a pair of wall electrodes.

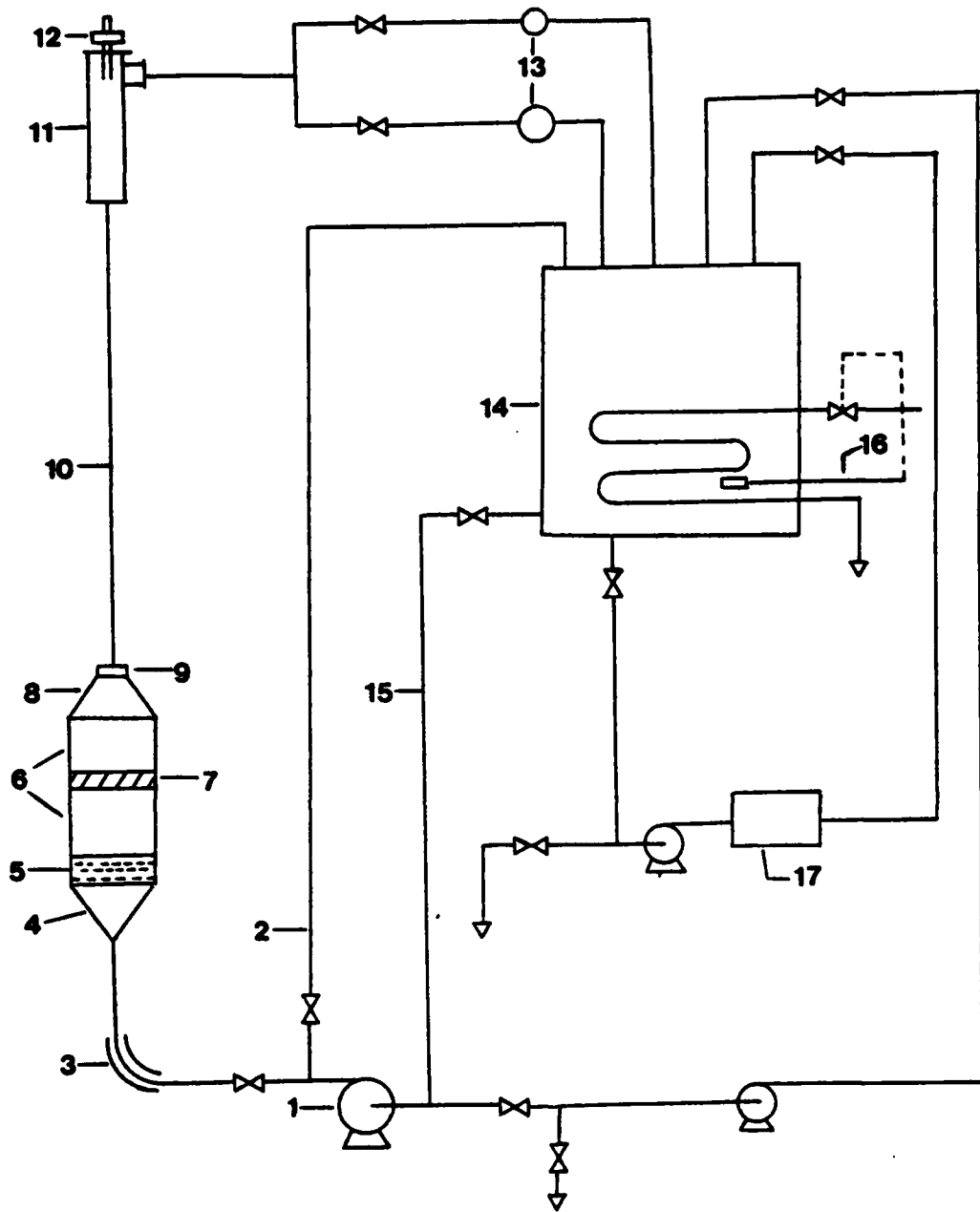
V. EXPERIMENTAL APPARATUS

A. Flow Loop

The experiments were conducted with a fully developed turbulent flow in a vertical, five level high, flow system schematically shown in Figure 5-1. The test section of the flow system has an internal diameter of 20 cm and a straight entrance length of 15 m (i.e. 75 pipe diameters). Operation of the flow loop is possible in the Reynolds number range of 2400 to 140,000 for bulk flows of 1.0 to 62 cm per second in the test section. Because the iodine-iodide flow medium has a corrosive nature, only stainless steel and Van-Cor UPVC were used as building materials for the flow loop.

The test fluid discharges from a 2500 liter storage tank on the top level via a 10 cm pipe to a centrifugal pump on the ground level. This pump, with an output pressure of 140 kilo Pascal, has a capacity of 20 liters per second. Past the pump the test fluid flows through respectively, a 90 degree elbow with turning vanes, a 1 m diffuser with a 55 cm square downstream section, a 20 cm honeycomb with square cells, a 25 cm settling chamber, a 20-mesh wire screen, another 25 cm settling chamber and a 55 cm nozzle with an outlet diameter of 20 cm. The uniform flow that emerges from the nozzle is tripped by a 1.5 cm ring consisting of a series of 1 cm equilateral triangles around the circumference of the adjacent pipe. Beyond this calming section the fluid flows through a 13 m vertical entrance section, which has a 20 cm internal diameter, and next through a 2 m acrylic test section also with a 20 cm internal diameter.

The wall electrodes are located near the downstream end of the test section. At the top of the test section is a three-dimensional traversing mechanism, operated by three Bodine adjustable speed, torque



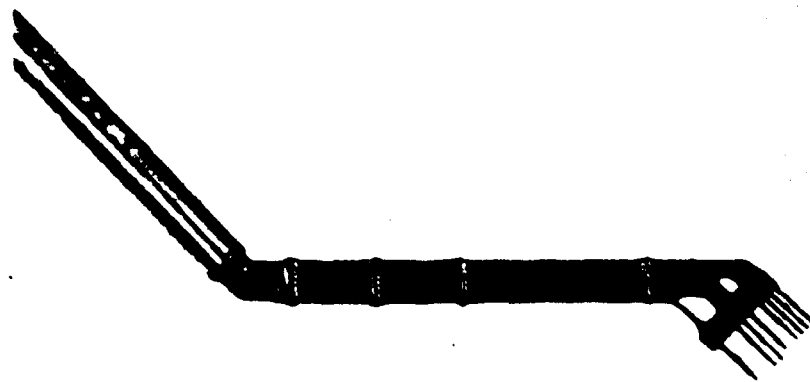
(1) main pump; (2) pump bypass; (3) 90 degree elbow with turning vanes; (4) diffuser; (5) honeycomb; (6) settling chamber; (7) gauge screen; (8) contraction nozzle; (9) turbulence trip; (10) upflow with a length of 13 m and ID of 20 cm; (11) 2 m long test section with 20 cm ID; (12) traversing mechanism; (13) vortex shedding flow meters; (14) storage tank; (15) down flow; (16) temperature control flow medium; and (17) filter section.

Figure 5-1. Vertical flow system.

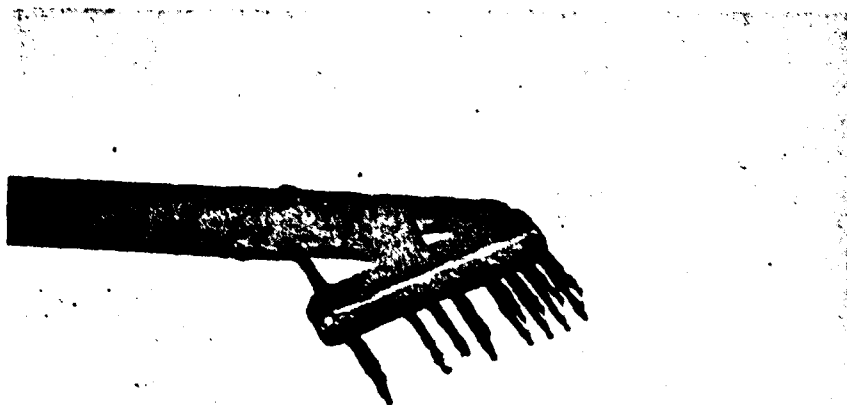
motors, which permit placement of the fluid probes at any position desired in the test section. The radial and axial displacements of the fluid probe are obtained from linear transducers with a readout accuracy of 0.125 mm. The circumferential readout is obtained with a 40 cm diameter high accuracy protractor. Downstream from the test section is the anode, composed of a 2 m pipe with a diameter of 20 cm inside of which nickel plates are positioned parallel to each other. The flow rate in the loop is measured with two Neptune-Eastech flow transmitters with an accuracy of 0.5 per cent covering the flow range from 0.333 to 20.0 liters per second. Cooling coils placed in the storage tank maintain the temperature of the electrolyte at 25.0 ± 1 degrees Celsius. Twelve filters, brand Pall MCY 1001 YC 98%-5 micron, were placed in an independent filter loop connected to the storage tank. The electrolyte was pumped through the filter loop at a rate of 13 liters per second.

B. Multi-sensor Fluid Probe

A multi-sensor electrochemical operated fluid probe, custom made by Thermo Systems Inc., was used to measure the turbulence and the average velocity in the fluid. Figure 5-2a shows the fluid probe and its stem, a 6 mm thick shaft which was mounted in the traversing mechanism. Also shown are the long probe needles designed to minimize the blockage effect created by the multi-probe. The bulk flow is parallel to the probe needles which are kept at a distance of 7 cm from the probe stem by a slender probe body to minimize possible flow disturbances in the measuring area caused by the stem or the traversing mechanism. The instantaneous axial velocity was measured at seven different radial positions and the instantaneous radial velocity at one position. Probe wire one is defined as the extreme righthand side wire shown in Figure



(a) Actual size



(b) Three times actual size

Figure 5-2. Multiple-sensor fluid probe.

5-2b. The distance between probe wires one and two is 1 mm as is the distance between probe wires two and three, and three and four. Between probe wires four and five the distance is 2 mm, between five and six it is 2.25 mm and between six and seven it is 3.75 mm. (Note: Probe wire six consists of the cross wires.) The dimensionless distance between the multi-probe wires is a function of the Reynolds number and is obtained from the following equation,

$$d_p^+ = 2.0 \frac{d_p}{D} R_D^{7/8} \quad (5.1)$$

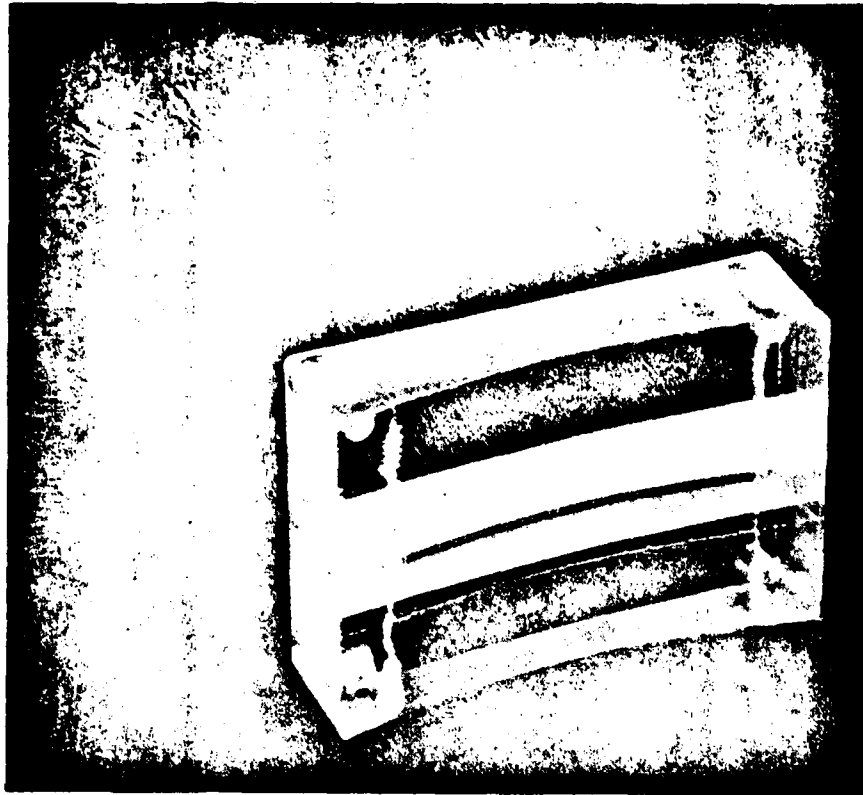
where d_p is the distance between the wires and D is the test section diameter. All the wire diameters are .05 mm and the sensing lengths 1.0 mm; thus the length-diameter ratio is 20. High purity platinum was used as wire material and the gold-plated needle supports were coated with conothane for electrical insulation. The Reynolds numbers based on the sensor diameter, for maximum and minimum flow in the test section are 34 and .6 respectively and are below the Reynolds number where vortex shedding begins ($R_d=44$).

C. Wall Electrodes

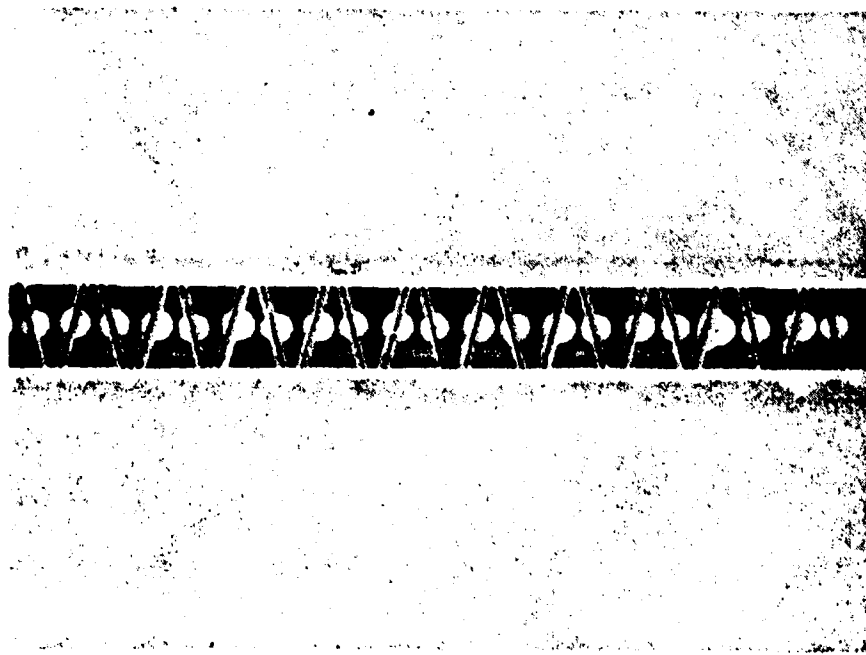
The wall electrodes used in this experiment were multiple pairs of rectangular electrodes ("V" electrodes) operated by the electrochemical technique. They are shown in Figure 5-3. These electrodes measure the axial and spanwise velocity gradient at the wall of the test section. Figure 5-3a shows a plug with 40 pairs of "V" electrodes and Figure 5-3b depicts an elevenfold magnification of the sensing lengths of the electrodes. The total spanwise length covered by the 40 pairs of electrodes is 3.6 cm. Thus the desired range of dimensionless spanwise length could be covered over a wide range of Reynolds numbers by using

the appropriate number of "V" electrodes. The electrodes have a sensing length W of 1.0 mm, a width L of .05 mm and form an angle of 15 degrees to the direction of mean flow.

For construction of the wall electrodes an acrylic block, 6x4x1.2 cm was machined so that a 6x.6x.6 cm strip extended from the centre on the upperside of the block in the lengthwise direction as shown in Figure 5-4. Exactly under this strip a trough of 4.9x.4x.5 cm was cut in the lengthwise direction over the bottomside of the block. Forty holes of .10 mm were drilled in the strip at a separating distance of .9 mm. Next, slots with widths of .076 mm were cut over the drilled holes at a 15 degree angle. Platinum blades of 6x3x.05 mm (to which copper wires were spot-welded) were glued into the slots with an epoxy resin, to which seven per cent by weight catalyst was added. After heating for three hours at 66 degrees Celsius, the epoxy was cured and the strip with the electrodes was machined to the desired width of 1.0 mm. Next the machined surfaces were polished and acrylic pieces were glued on each side of this 1.0 mm thick strip. The procedure described above was then repeated. Holes of .1 mm were drilled between the existing ones and slots were cut at a 15 degree angle in the opposite direction to form a total angle of 30 degrees between electrode pairs. Electrodes were glued in the slots, the strip was machined to the correct width, polished and new pieces of acrylic material were glued on each side of the 1.0 mm long electrodes. Finally the probe surfaces were milled to the curvature of the test section. An illustration of the finished probe is provided by Figure 5-3a. This plug was glued in the wall of the test section with the dividing line of the "V" electrodes parallel to the flow direction. After insertion in the test



(a) Actual size



(b) Eleven times magnification

Figure 5-3. Multiple "V" wall electrodes.

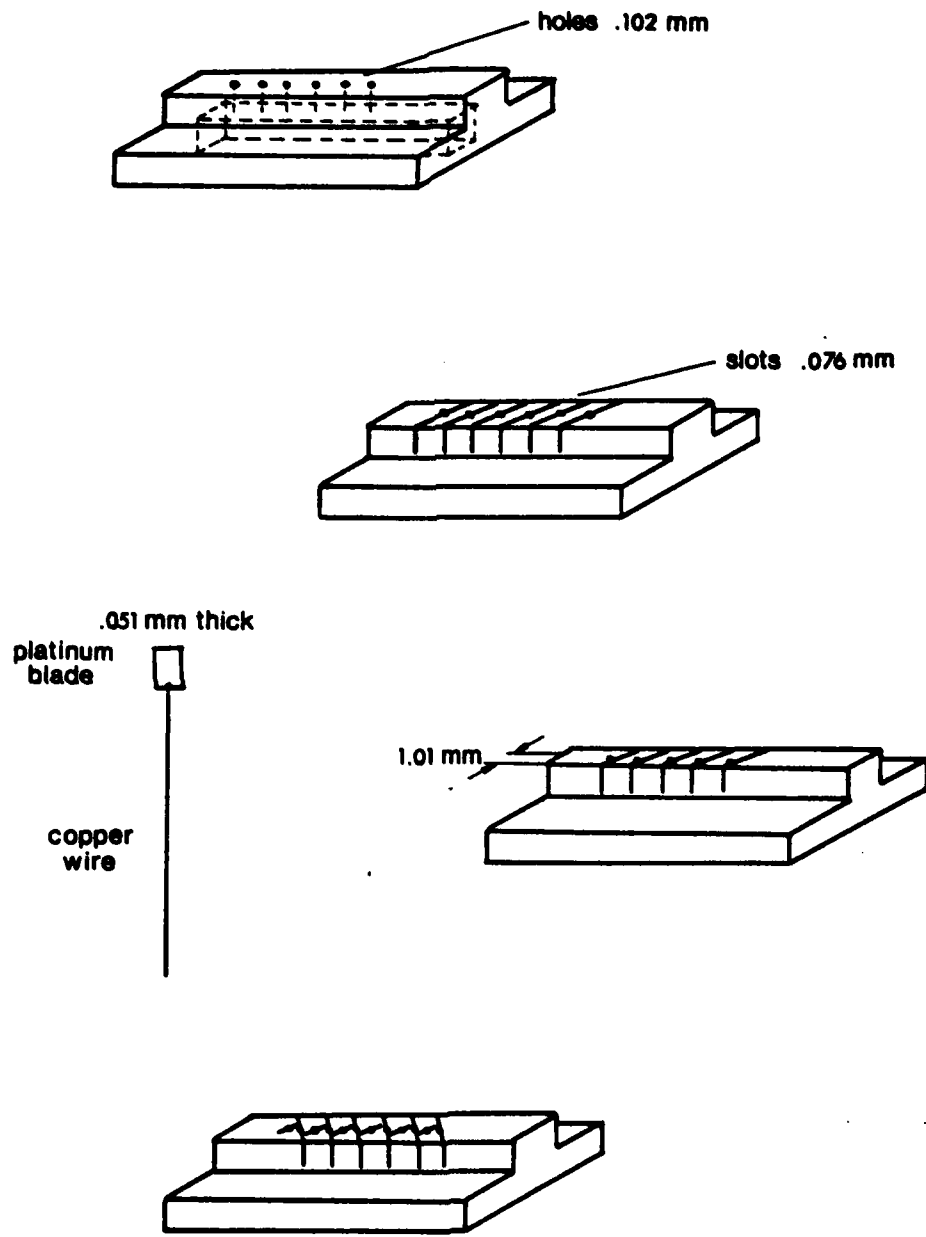


Figure 5-4. Construction sequence of the wall electrodes.

section the plug was polished with progressively finer grades of emery paper and rubbing compounds until the plug was an integrated part of the test section, smooth and flush with the pipe wall.

D. Electrode Circuitry and Data Collection

The electrode circuit used to operate the wall electrodes and fluid probes was a voltage follower with gain and is schematically shown in Figure 5-5. A description of this circuitry is given by Eckelman (1971). The applied voltage at the cathode is determined by the adjusting of the 1K-ohm helipot. An input voltage at the cathode of approximately -.50 volts is appropriate because it permits operation in the plateau region of the polarization curve. The current flow at the cathode is a function of the mass transfer and can be calculated readily from input and output voltage and the feedback resistor as given by

$$I_c = \frac{1}{R_f} (V_o - V_i) . \quad (5.2)$$

By varying the feedback resistor R_f , the gain of the amplifier was changed to values between ± 5.0 volts, a condition imposed upon the output voltage so as to be accepted by the IBM-1800 computer. Beyond the electrode circuit the analog signal was filtered by a fourth order low pass Butterworth filter with a cut-off frequency of 15 Hz. An IBM-1800 computer was used for digitalization of the 28 analog signals and for data collection. The signals were connected to a 64 input multiplexer, sampled simultaneously with a sample frequency of 30 Hz and digitalized with a resolution of 16 bits. The digitalized data were transferred to the IBM-1800 disk with a storage capacity of approximately 400,000 words. Next the data on the disk were transferred to a magnetic tape, suitable for use on the Cyber-175 computer. This computer

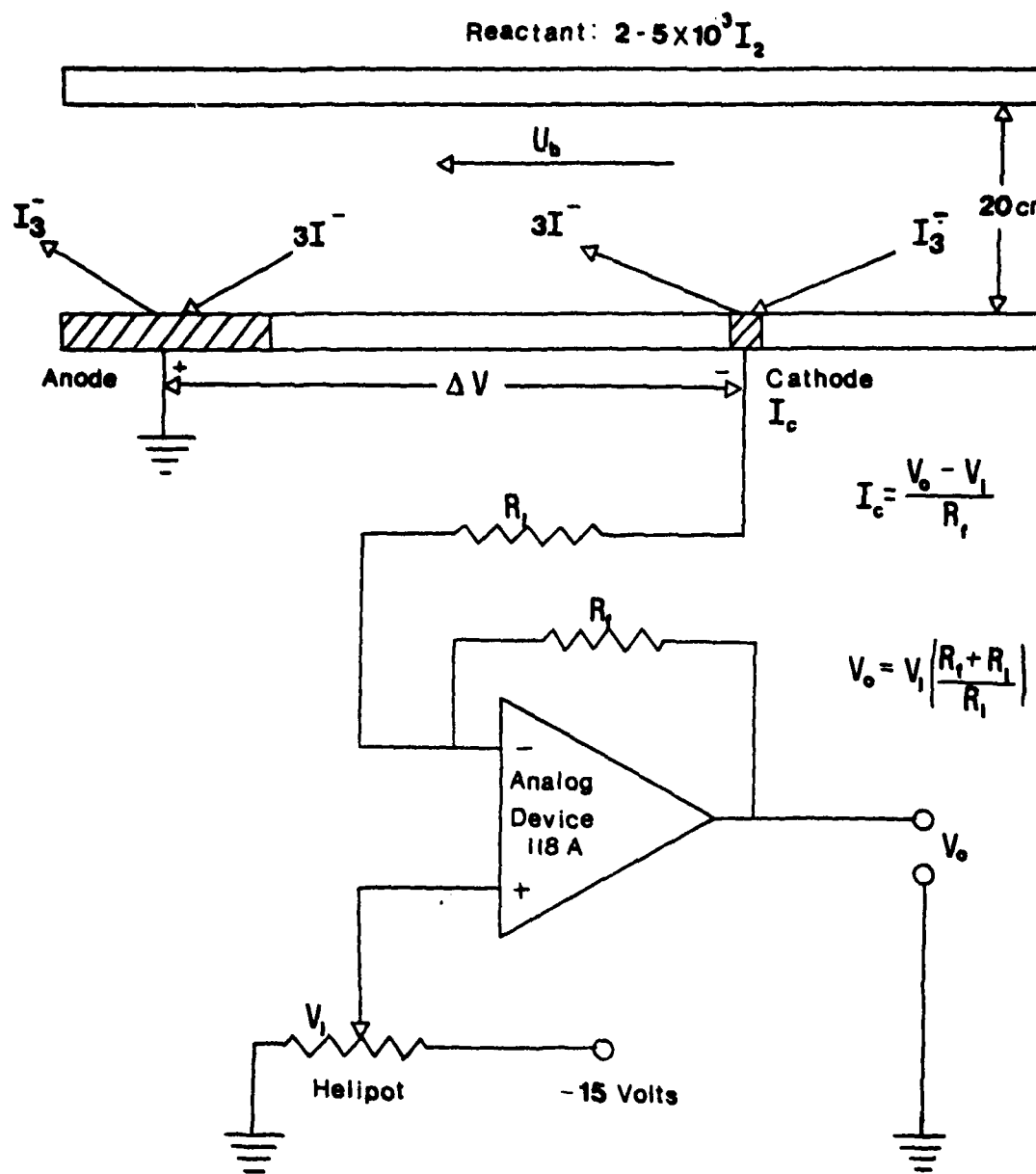


Figure 5-5. Schematic representation of the electrochemical process and the electrode circuit.

was used for the conversion of the mass transfer signals to the turbulence signals as well as for the statistics and operations concerning the turbulence signals in this work.

VI. RESULTS

A. Correlations

Time correlations between the axial velocity and the axial velocity gradient at the wall ($R_{s_x u_x}(\tau^+)$) were calculated for different positions of the fluid probe in relation to the wall probe. The fluid probe was placed at three downstream locations. For the calculations the wall signals were delayed with respect to the fluid signals. For zero time delay the correlations have nearly the same values, as shown in Figure 6-1. The high correlation value for the probes, streamwise separated, indicates coherency of the flow in the axial direction. This high correlation is consistent with the streaky structure observed in the viscous wall region. These streaks are elongated in the flow direction and extend over a dimensionless length Δx^+ of approximately 1000. For time delays of $\tau^+=3$ and $\tau^+=2$ maximum correlations were reached with the fluid probes at $\Delta x^+=90$ and $\Delta x^+=60$, respectively. No calculations were made for $\tau^+=1$ but it is expected that the probe at $\Delta x^+=30$ reaches its maximum correlation at that instant. Consequently an estimate of the dimensionless convection velocity for these correlations is $U_c^+=30$. Figure 6-1 shows also that the farther the fluid probe is placed from the wall, the faster the correlation value declines as a function of time delay.

Spanwise correlations of the spanwise and axial velocity gradients at the wall (s_z, s_x) are presented in Figure 6-2. The spanwise correlation of the axial wall velocity gradients ($R_{s_x s_x}(\Delta z^+)$) reaches a minimum value of .014 at $\Delta z^+=68$ but has no zero crossing, as shown in Figure 6-2. This result differs from those of Fortuna (1971), Kreplin and Eckelmann (1972) and Blackwelder and Eckelmann (1978) who found a zero crossing for

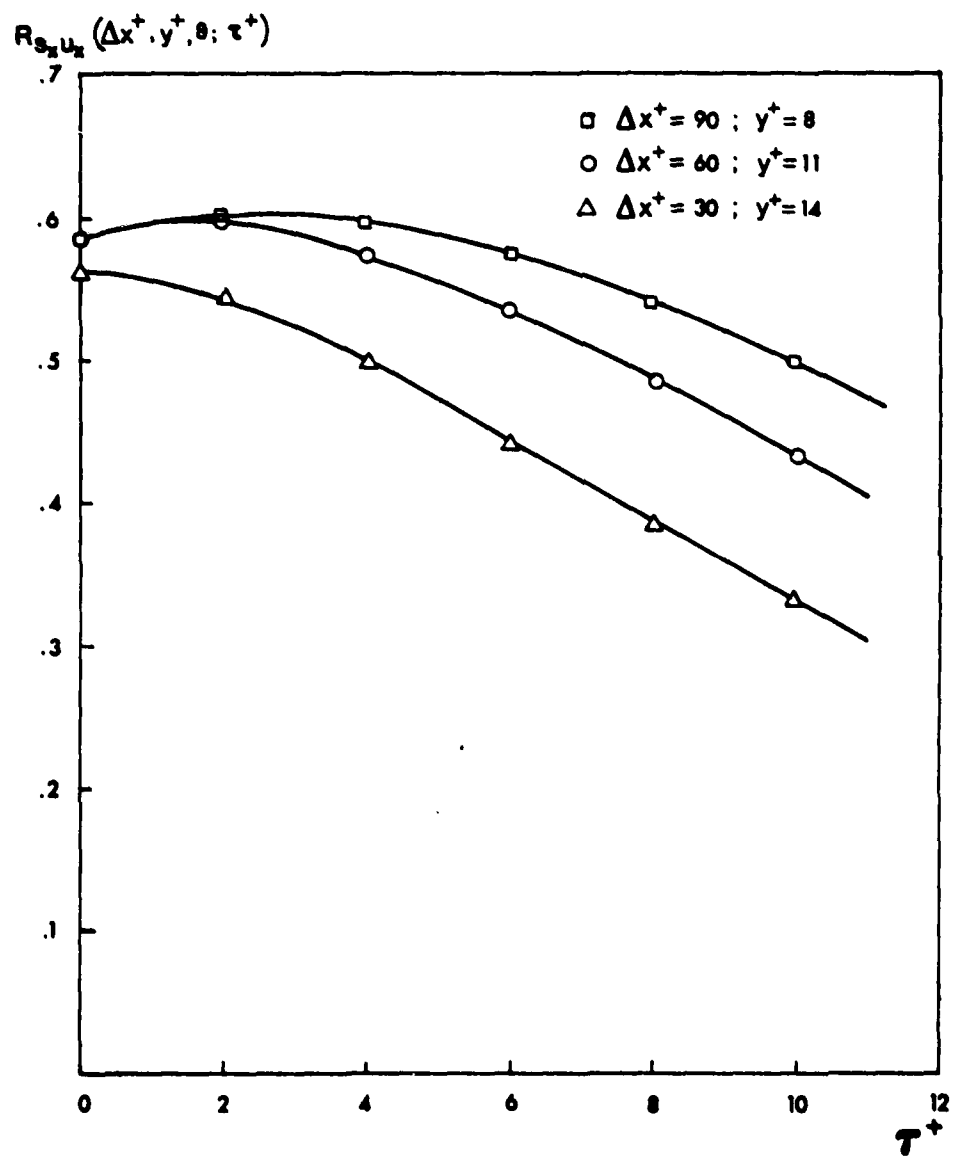


Figure 6-1. Time correlation of the axial velocity and the axial velocity gradient at the wall.

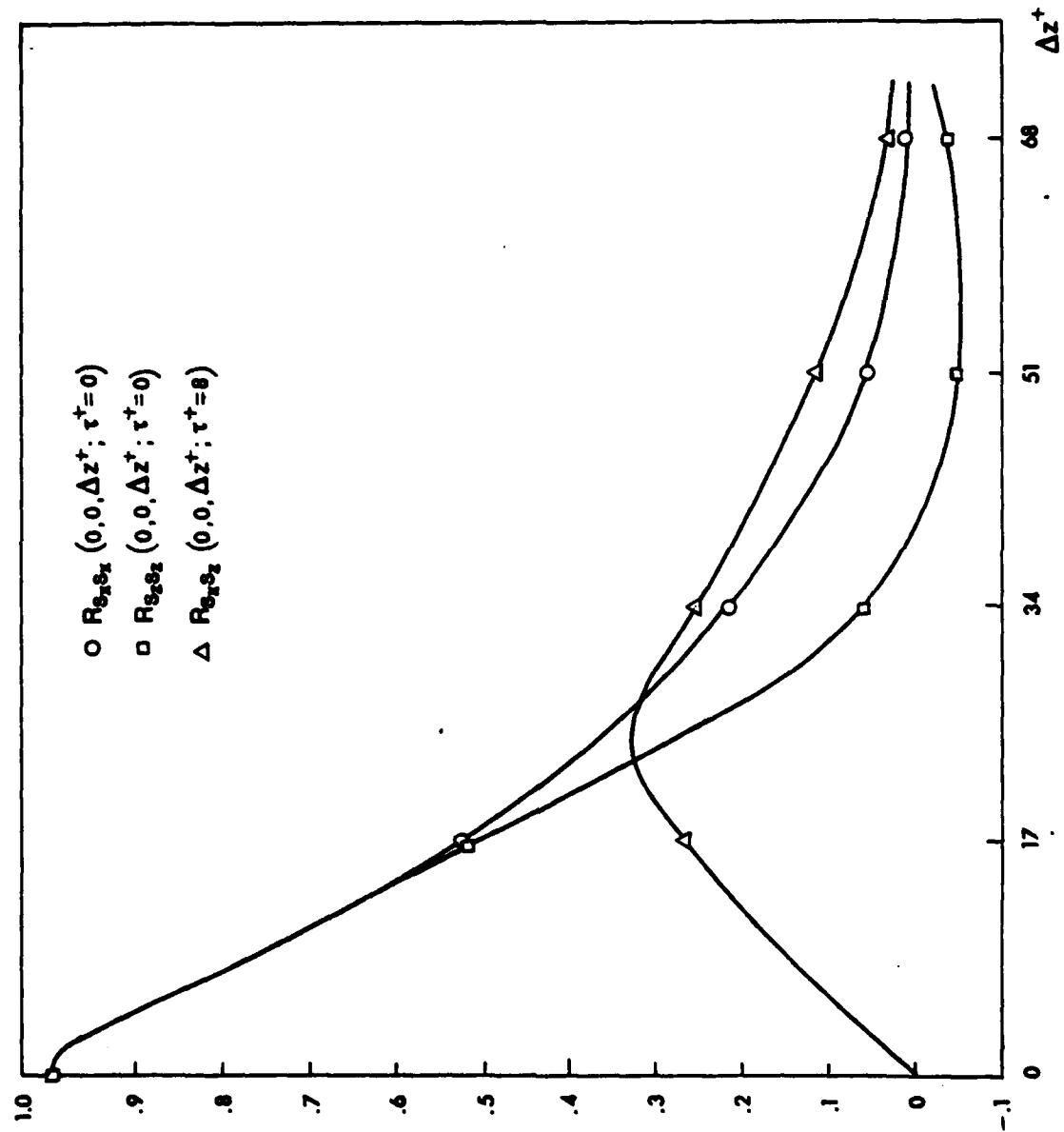


Figure 6-2. Spanwise correlations of the velocity gradients s_x and s_z at the wall; s_z delayed in time.

$Rs_x s_x(\Delta z^+)$ at $\Delta z^+=36$. The $Rs_x s_x(\Delta z^+)$ correlation of this work is similar to the correlation measurements of Eckelman (1971), who used the same flow loop but different wall electrodes. According to Eckelman, absence of a zero crossing in the correlation curve is caused by a low frequency signal unrelated to the turbulence. However the spanwise correlation between the streamwise fluctuating velocity gradient at the wall and the streamwise fluctuations in the fluid at $\Delta x^+=60$ and $y^+=11$ (figure 6-3) does exhibit a zero crossing at $\Delta z^+=53$.

The spanwise correlation of the spanwise fluctuations ($Rs_z s_z(\Delta z^+)$), shown in Figure 6-2, was found to have a zero crossing at $\Delta z^+=40$. This correlation was also measured by Lee, Eckelman and Hanratty (1974), Kreplin and Eckelmann (1978) and Blackwelder and Eckelmann (1978). The $Rs_z s_z(\Delta z^+)$ correlation found in this work exhibits the same behaviour as the correlation measured by Lee who discovered a zero crossing at $\Delta z^+=38$ at a Reynolds number of approximately 30000. Kreplin found a zero crossing at $\Delta z^+=30$ at a Reynolds number of 7700. Unlike these results, the measurements of Blackwelder show a zero crossing at $\Delta z^+=18$ and a large negative correlation of -.2 at $\Delta z^+=30$.

The spanwise correlations between the axial and spanwise velocity gradients at the wall ($Rs_x s_z(\Delta z^+)$) exhibits a maximum of .33 at $\Delta z^+=25$ (Figure 6-2). This correlation, with its maximum and minimum values separated by a half wavelength ($\Delta z^+=50$), agrees with that hypothesized under the idealized coherent eddy structure (see Figure 3-1). Lee et al found for the $Rs_x s_z(\Delta z^+)$ correlation a maximum value of .35 for $\Delta z^+=25$ while Blackwelder and Eckelmann's results indicate a maximum correlation value of .5 at $\Delta z^+=18$.

Spanwise correlations between the axial velocity and the axial velocity gradient at the wall ($R_{sx}u_x(\Delta z^+)$) are shown in Figure 6-3. Correlations were obtained for five fluid probe positions at distances between $y^+=11$ and $y^+=53$ (and for each case $\Delta x^+=60$). The $R_{sx}u_x(\Delta z^+)$ correlation curves have the same shape as the $R_{sx}s_x(\Delta z^+)$ correlation curve at the wall (Figure 6-2), suggesting that the coherent eddy structure extends into the viscous wall region. If the fluid probe is placed farther away from the wall (for example at $y^+>36$) the maximum correlation value decreases rapidly and the curve becomes flatter. Therefore coherency between the different parts of the open eddy structure is slight when the distance from the wall is large.

Spanwise correlations of the axial velocity and the spanwise velocity gradient at the wall ($R_{sz}u_x(\Delta z^+)$) are presented in Figure 6-4. These correlations show the same behaviour as the spanwise correlation of the axial and spanwise velocity gradients at the wall (Figure 6-2). The shapes of the $R_{sz}u_x(\Delta z^+)$ curves indicate that the idealized coherent eddy structure as depicted in Figure 3-1 does exist in the viscous wall region. This eddy structure contrasts with the eddy model for the viscous wall region proposed by Gupta (1970), Lee (1975), Lau (1977) and Hanratty et al (1977) under which a phase change occurs at $y^+\approx 12$. Their model is based upon closed counter-rotating eddies with an extent of $\Delta z^+=50$ and $y^+\approx 12$ near the wall and an open eddy structure from $y^+>12$ into the viscous wall region. Under this model the momentum deficient fluid ejected from the wall meets the high momentum fluid moving towards the wall at $y^+\approx 12$, causing a phase change in the fluid velocity components in the spanwise and axial directions. If a phase change of the fluctuating velocities does occur in the viscous wall region then the spanwise correlations between the axial and spanwise fluctuations change signs

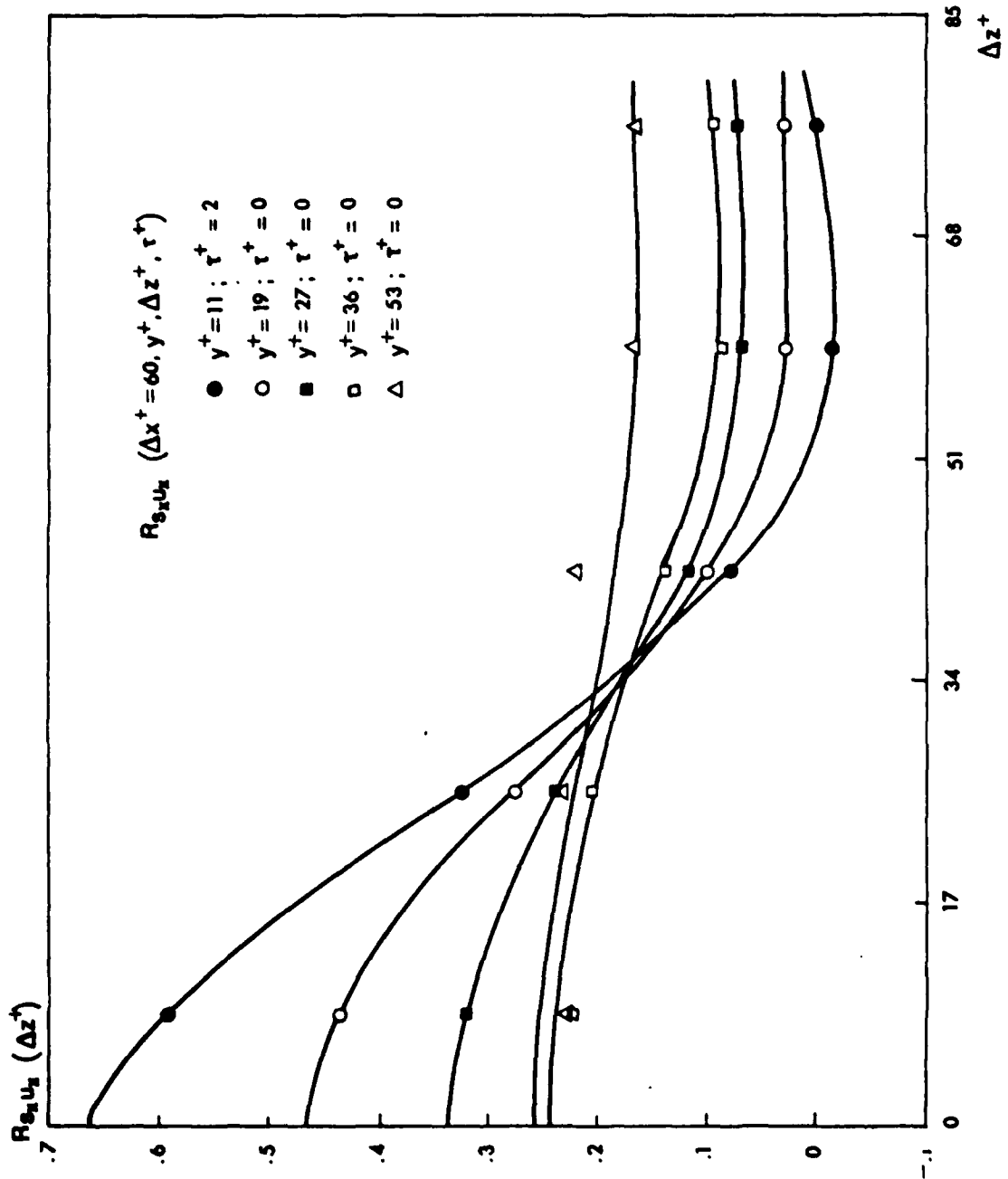


Figure 6-3. Spanwise correlations of the axial velocity and the axial velocity gradient at the wall; s_x delayed in time.

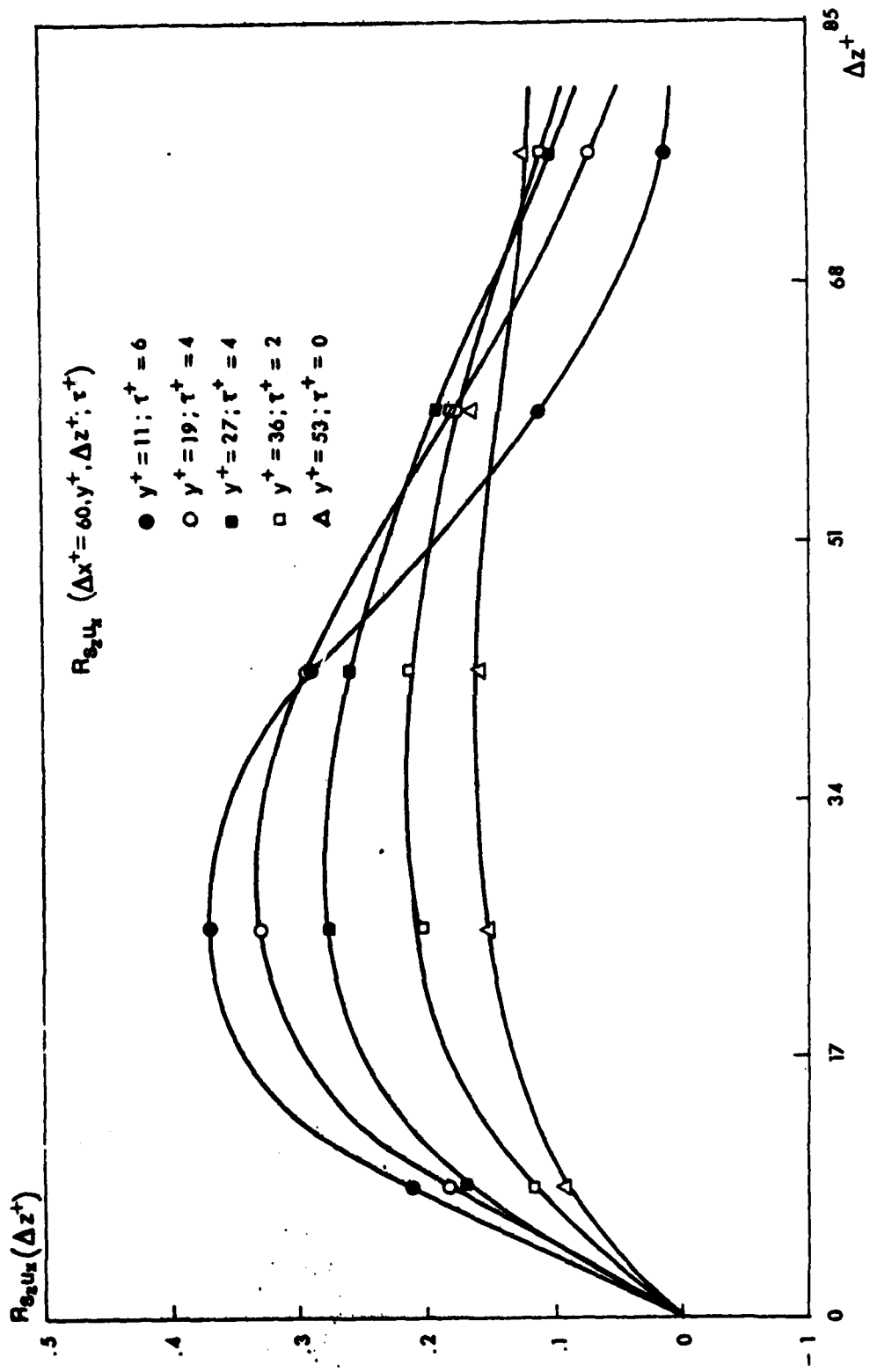


Figure 6-4. Spanwise correlations of the axial velocity and the spanwise velocity gradient at the wall; s_z delayed in time.

for $y^+ > 12$. The correlations, as shown in Figures 6-2, 6-3 and 6-4, do not change signs; thus, it appears no phase change occurs. At a distance from the wall of $y^+ = 40$ the inflows and outflows become diffused and as a consequence the degree of correlation diminishes.

B. Conditional Averaging Criteria Applied to the Spanwise Velocity

Gradients at the Wall

1. Detection of inflows over a spanwise length of $\Delta z^+ = 153$.

To detect the coherent eddy structure in the viscous wall region the condition as represented by equation (3.2) was applied to the spanwise velocity gradients ($s_z(z,t)$) at the wall. The constant N in this equation was set equal to 5, so at every instant ten spanwise velocity gradients were used for the search of the sine wave shaped $s_z(z,t)$ patterns in the data set. These ten spanwise velocity gradients were equally spaced over a dimensionless spanwise length of $\Delta z^+ = 153$. Ninety-five events with positive slope in the s_z patterns were selected from the data set. At the event times a conditional average was taken over the s_z velocity gradients as described in Chapter III-D. Figure 6-5 shows the conditionally averaged s_z patterns. This figure exhibits clearly the build-up and the breakdown of the s_z patterns as a function of dimensionless time. From $T^+ = -26$ to $T^+ = -10$ the plots do not show any identifiable pattern but after $T^+ = -10$ a spanwise velocity gradient pattern emerges, that increases in amplitude. At $T^+ = 0$ a well defined sine wave shaped s_z pattern appears. For time points greater than $T^+ = 0$ the amplitude of the sine wave shaped pattern decreases gradually and at $T^+ = 18$ the shape of this pattern disintegrates. The s_z pattern has a maximum amplitude equal to 90 percent of the spapwise turbulence intensity, a dimensionless distance between its peaks of $\Delta z^+ = 50$ and an overall wavelength of

AD-A080 853

ILLINOIS UNIV AT URBANA-CHAMPAIGN DEPT OF CHEMICAL EN--ETC F/6 20/4
IDENTIFICATION OF THE DOMINANT FLOW STRUCTURE IN THE VISCOUS WA--ETC(U)

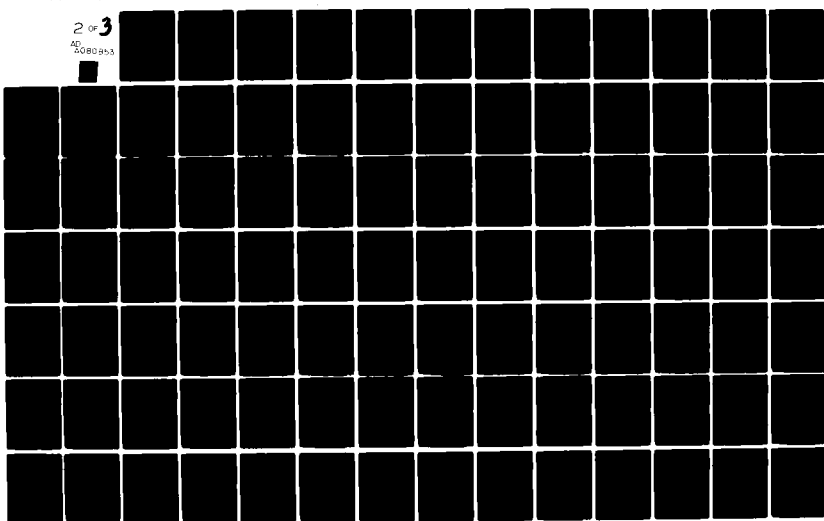
AUG 79 J H HOGENES, T J HANRATTY N00014-76-C-1034

NL

UNCLASSIFIED

TR=2

2 of 3
AD-A080 853



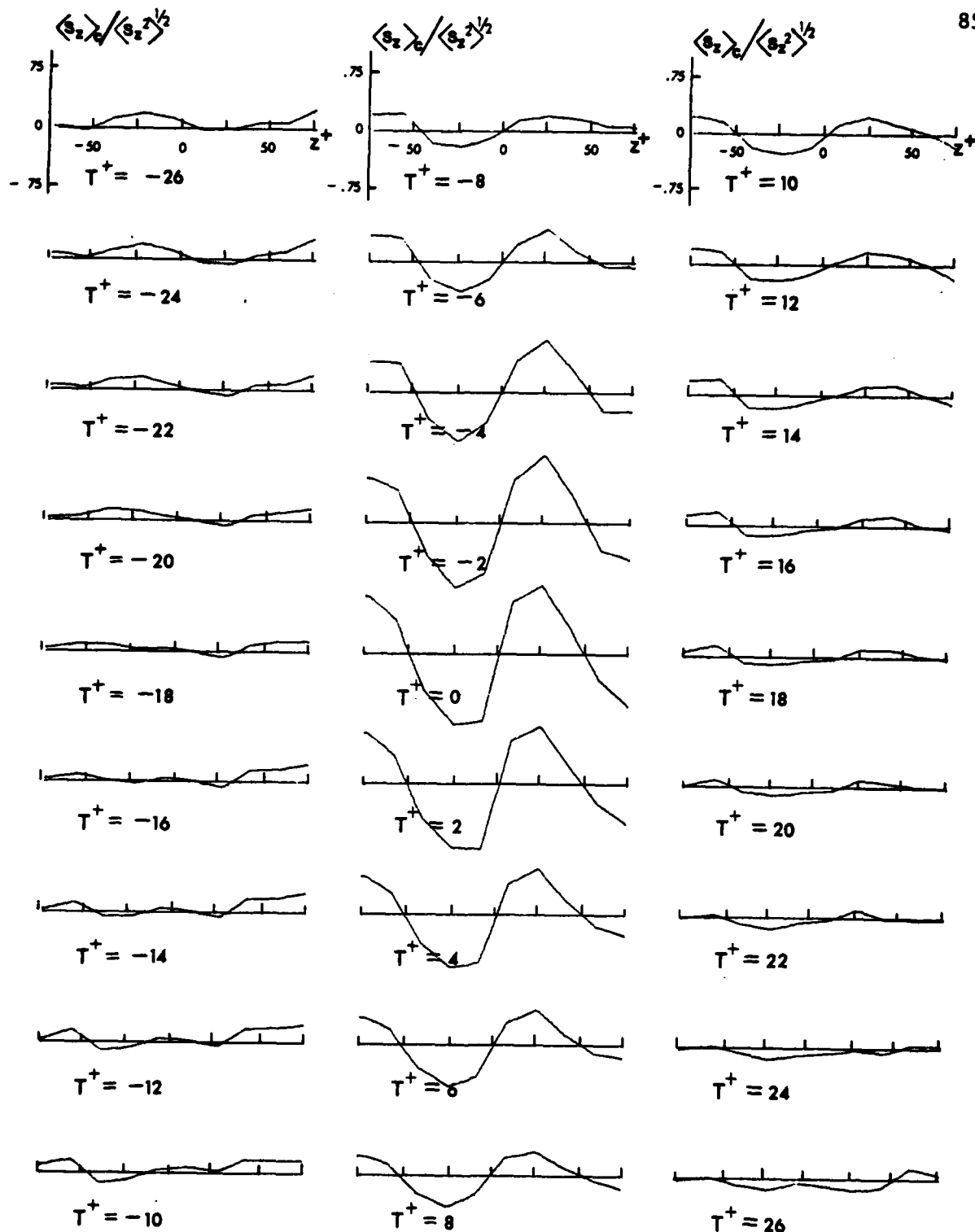


Figure 6-5. Conditionally averaged inflow s_z patterns. Equation (3.2) where $N = 5$ applied to s_z^2 gradients: $E_D = 95$.

$\Delta z^+ = 100$. Noteworthy is that this pattern bears a strong resemblance to the s_z pattern of the coherent eddy structure shown in Figure 3-1b.

Conditionally averaged s_x patterns were obtained during the same 95 instants and are shown in Figure 6-6. These plots exhibit the growth sequence for inflows. From $T^+ = -26$ to $T^+ = -18$ no pattern is identifiable but at $T^+ = -16$ a valley appears in the centre of the profile which indicates the development of an outflow. The presence of an outflow is also evidenced by the s_z plots which show signs of negatively sloped patterns from $T^+ = -26$ to $T^+ = -20$ (see Figure 6-5). After $T^+ = -6$ the amplitude of the s_x pattern increases and by $T^+ = 4$ a regular inflow pattern develops with a maximum peak of 65 percent of the axial turbulence intensity. At the peak's sides are valleys, separated by a distance of $\Delta z^+ = 100$. The peaks in the s_x patterns are caused by the high momentum fluid that moved at that position towards the wall. At the valley locations low momentum fluid moved away from the wall after exchanging momentum with it. It is to be noted that the highest peak in the s_x pattern emerges after a dimensionless time period of $\Delta T^+ = 3$ had elapsed since the maximum s_z profile was established.

2. Detection of outflows over a spanwise length of $\Delta z^+ = 153$.

Conditionally averaged s_z patterns as shown in Figure 6-7 were obtained from those instants in the data set for which equation (3.2) had a large negative value. These patterns have the same features as those shown in Figure 6-5, differing only with respect to the slope in the centre of the profiles. According to the idealized eddy structure (see Figure 3-1) a negative slope in the s_z pattern characterized an outflow. A maximum amplitude for the outflow pattern is reached at $T^+ = 0$ and is approximately 90 percent of the spanwise turbulence intensity.

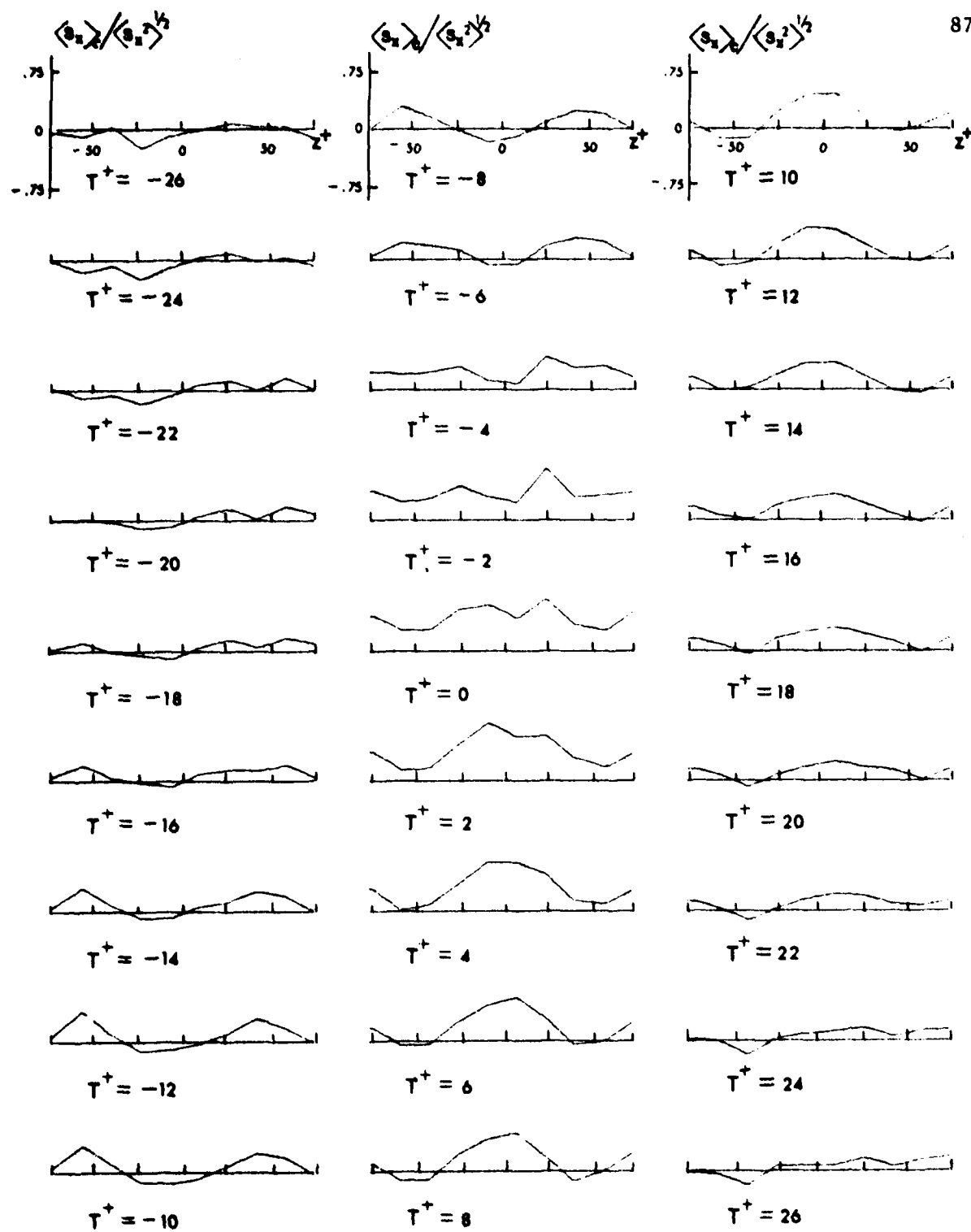


Figure 6-6. Conditionally averaged inflow s_x patterns. Equation (3.2) where $N = 5$ applied to s_z gradients; $E_D = 95$.

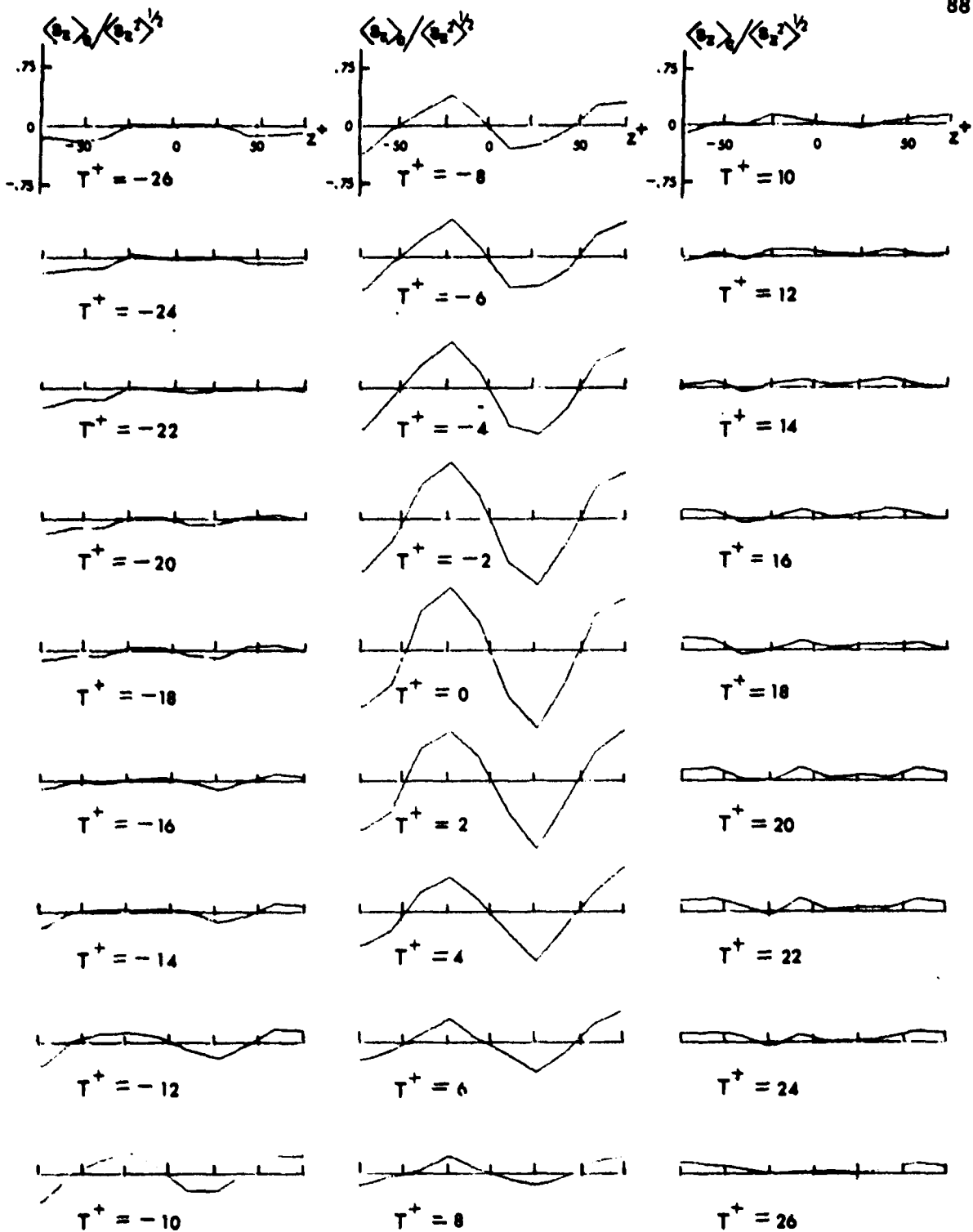


Figure 6-7. Conditionally averaged outflow s_z patterns. Equation (3.2) where $N = 5$ applied to s_z gradients; $E_D = 96$.

The dimensionless distance between the maximum peaks is $\Delta z^+ = 50$ and the overall wavelength at that instant is $\Delta z^+ = 100$. Axial velocity gradient outflow patterns as shown in Figure 6-8 are associated with the s_z patterns of Figure 6-7. At $T^+ = -2$ the s_x pattern develops a valley in its centre and maxima at its sides. The maximum outflow pattern with a wavelength of $\Delta z^+ = 100$ is reached at $T^+ = 4$. Outflows take place in the valleys and at the peaks inflows occur. The time delay between both the maximum s_z pattern and the maximum s_x pattern is $T^+ = 4$ indicating that the s_z pattern is established before a strong ejection of low momentum fluid takes place.

3. Detection of inflows over a spanwise length of $\Delta z^+ = 102$.

For the applied detection criteria discussed in subsection 1 (equation (3.2) with $N=5$) the inflow had to take place in the centre of the wall electrodes before it was possibly characterized as an inflow event. Because the chance that an inflow occurs exactly in the centre of the wall electrodes is small the most spectacular inflows were not identified with this conditional averaging scheme. To identify inflows in the data set equation (3.2) was again applied to the spanwise velocity gradients at the wall but this time for $N=3$ and a new set of inflow events was found. From this set 100 strong inflows were selected. At the instants of the selected inflow events the spanwise velocity gradients were averaged conditionally. The results obtained are shown in Figure 6-9. These plots are similar to those presented in Figure 6-5 but have larger amplitudes, larger overall wavelengths and a longer total inflow time, starting at $T^+ = -14$ and ending at $T^+ = 14$. Development of an identifiable s_z pattern starts at $T^+ = -14$ and its amplitude increases until $T^+ = 0$. At $T^+ = 0$ the plot has a dimensionless distance between its

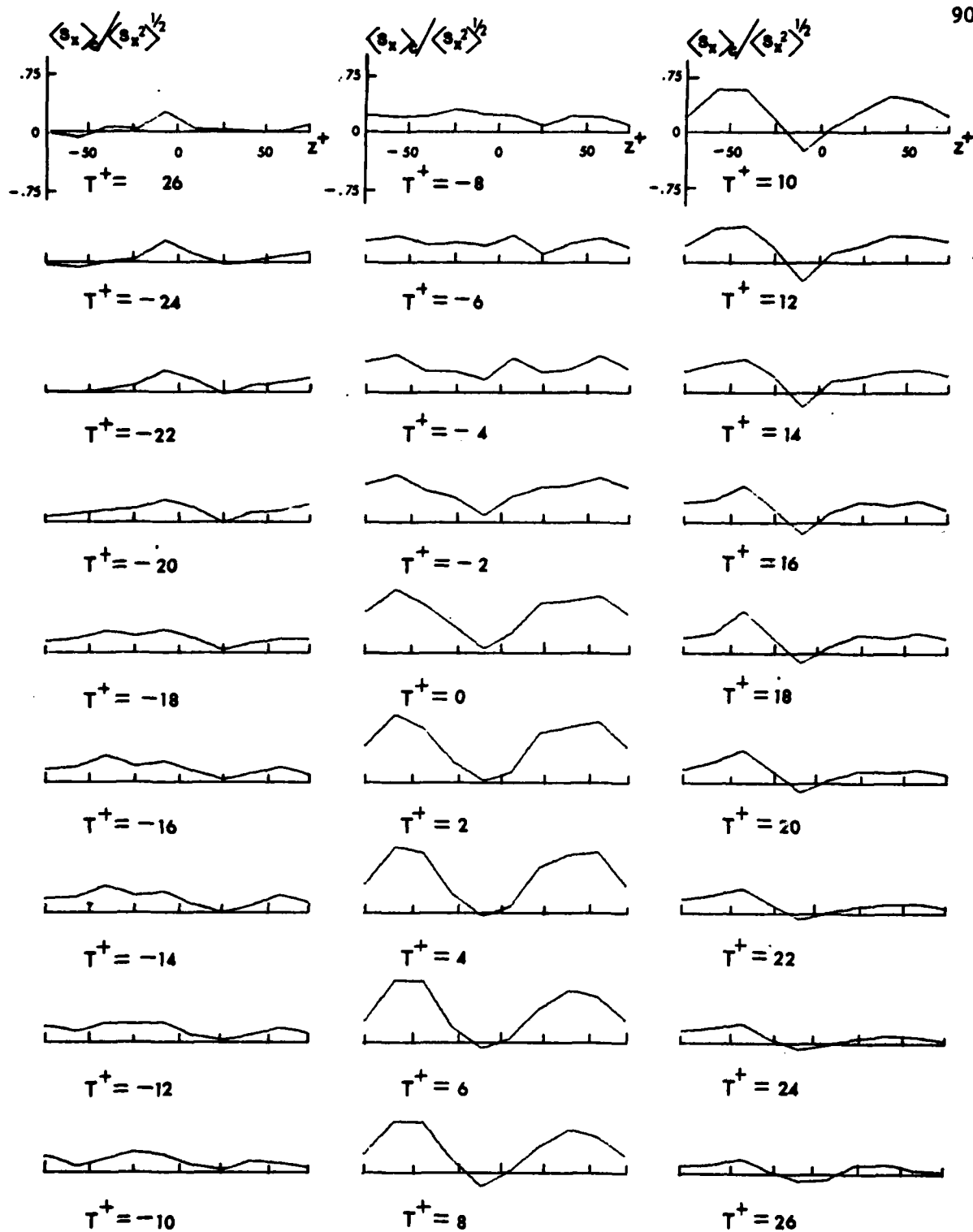


Figure 6-8. Conditionally averaged outflow s_x patterns. Equation (3.2) where $N = 5$ applied to s_z gradients; $E_D = 96$.

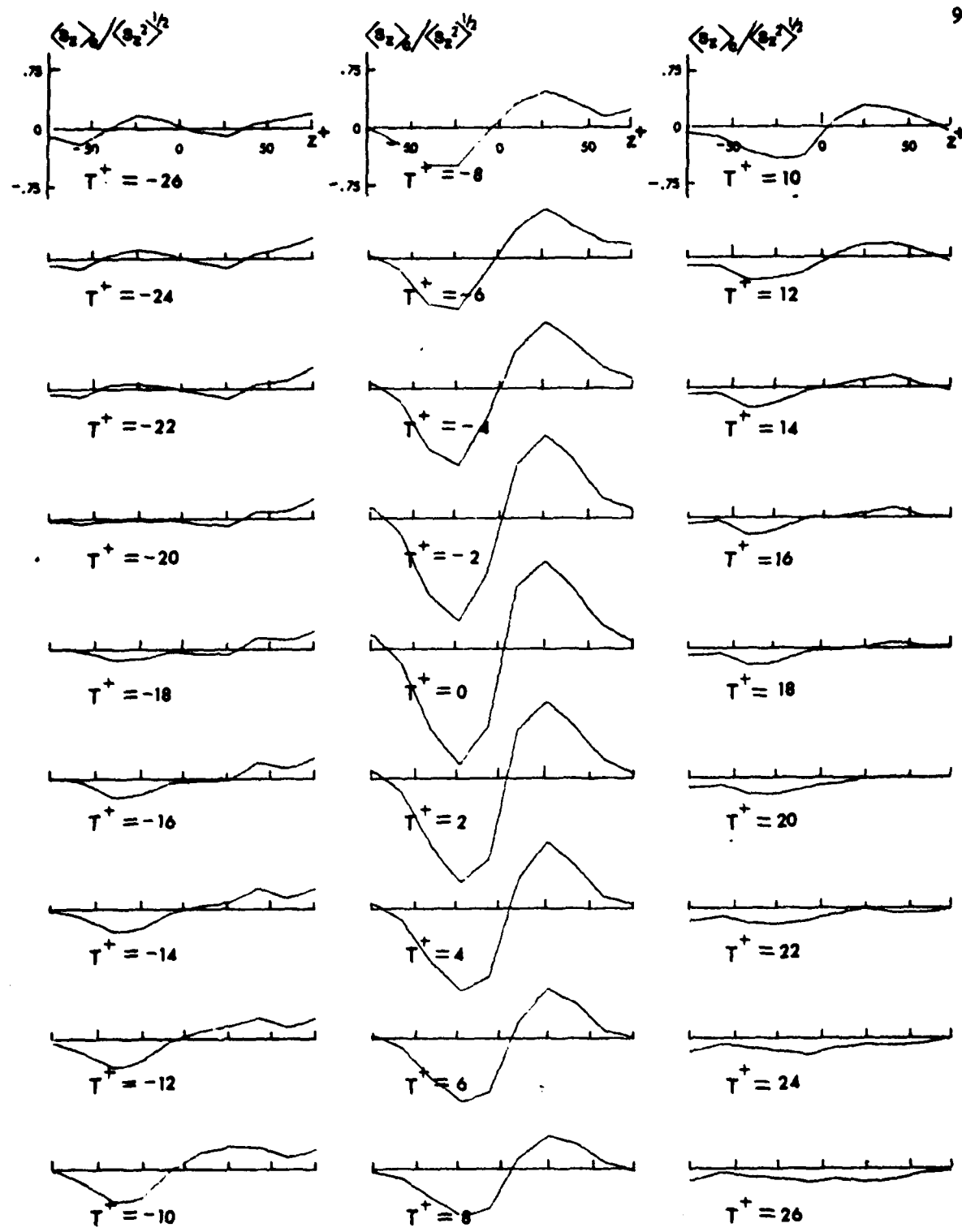


Figure 6-9. Conditionally averaged inflow s_z patterns. Equation (3.2) where $N = 3$ applied to s_z gradients; $E_D = 97$.

peaks of $\Delta z^+=50$, an overall wavelength slightly larger than $\Delta z^+=100$ and a maximum amplitude of 1.5 times the spanwise turbulence intensity. Because N was set equal to 3 in equation (3.2) the total spanwise length covered by the detection electrodes was $\Delta z^+=102$. For a detection criterion based upon this spanwise length the s_z patterns become less well defined beyond the peaks resulting in an overall wavelength larger than 100. Clearly this criterion is less restrictive than the one used in subsection 1 where $N=5$ in equation (3.2). Beyond $T^+=0$ the amplitude of the s_z pattern decreases gradually and after $T^+=16$ the conditionally averaged spanwise fluctuations are close to zero.

Axial inflow patterns which are associated with the spanwise patterns are shown in Figure 6-10. Development of the inflow pattern starts at approximately $T^+=-8$ and culminates at $T^+=4$. During this instant of strong inflow, a maximum appears in the centre of the plot which is 1.05 times the axial turbulence intensity and 1.6 times the peak value shown in Figure 6-6. After the maximum inflow pattern appears the s_x pattern becomes slender and valleys develop on its sides. Low momentum fluid is ejected from these valleys which are separated by a distance of $\Delta z^+=100$. The amplitude of the s_x pattern decreases gradually and after $T^+=18$ no well defined inflow pattern is observed.

Fluid probes were placed downstream from the wall probes at distances of $\Delta x^+=30$, 60 and 90. Conditional averages were obtained for the velocity fluctuations at these probes during the selected inflow events. Figure 6-11 shows the averages for a dimensionless downstream distance of $\Delta x^+=30$. At $T^+=-26$ a small momentum excess is present at the fluid probes that increases gradually as time elapses. The fluid probes at time $T^+=0$ exhibit a large momentum excess and one of them, the

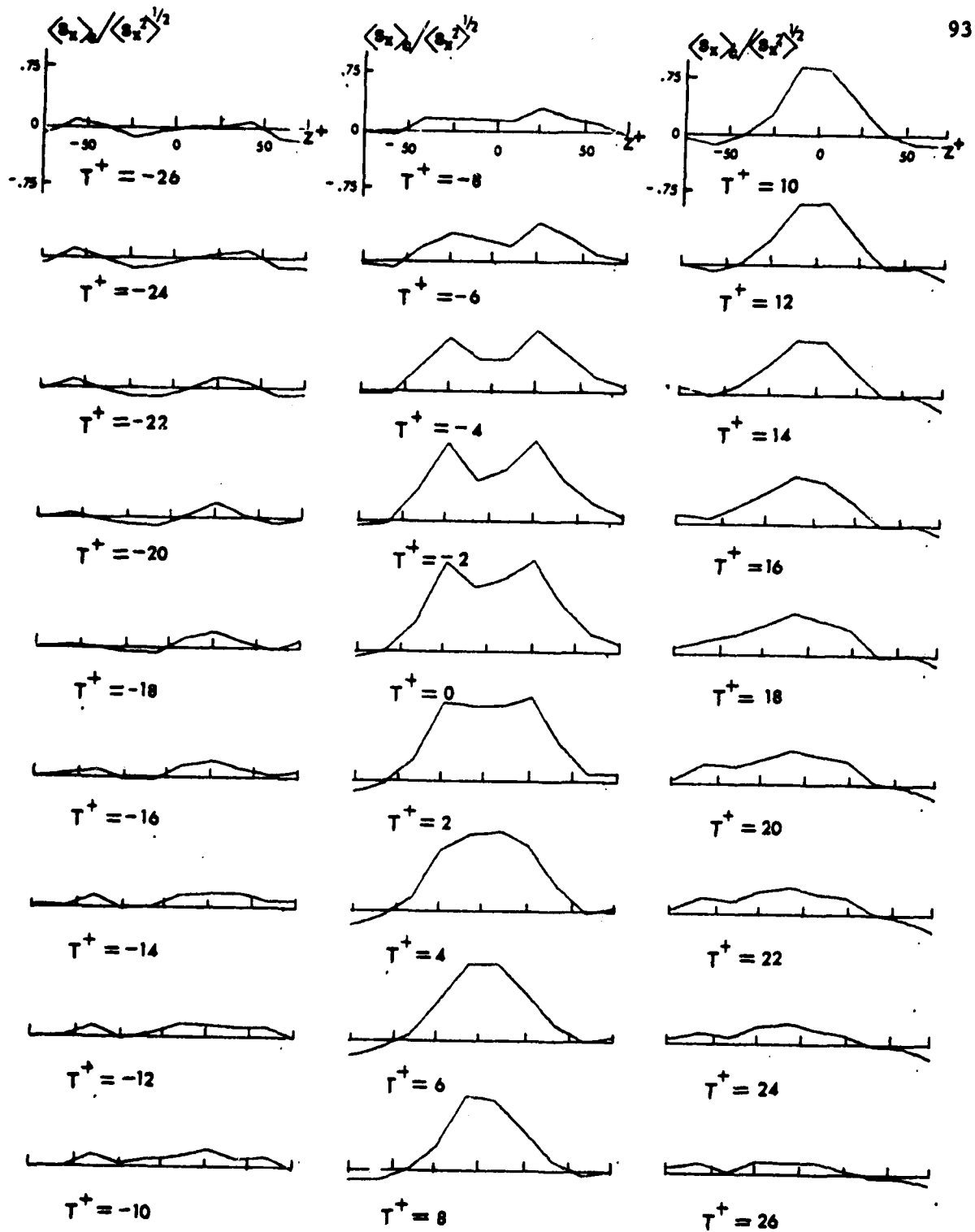


Figure 6-10. Conditionally averaged inflow s_x patterns. Equation (3.2) where $N = 3$ applied to s_z gradients; $E_D = 97$.

probe at $y^+=14$, has a momentum excess equal to 18 percent of the bulk velocity. At time points greater than zero there is a decrease in momentum of the fluid farthest away from the wall and then a decrease in momentum of the fluid closest to the wall. At $T^+=22$ hardly any high momentum fluid was detected by the probes and at $T^+=26$ a zero fluctuation profile was reached. Placement of the fluid probes at $\Delta x^+=60$ (see Figure 6-12) yielded inflow patterns that developed in a similar manner to those obtained when probes were placed at a distance of $\Delta x^+=30$. The high momentum fluid enters the viscous wall region from distances larger than $y^+=100$ and the u_x velocity profile shows a gradual increase in momentum excess. When this high momentum fluid reaches the wall region, it appears as a peak in the u_x profile because this immoving fluid creates a proportionately larger velocity increase near the wall than say at $y^+>30$. It takes the fluid a finite time period to reach a location farther downstream. Thus the maximum u_x fluctuation profile is reached later than in the case where $\Delta x^+=30$ --namely, at a dimensionless time of $\Delta T^+=4$. This maximum u_x profile shows a momentum excess of 18 percent of the bulk velocity at the position of $y^+=11$. After $T^+=4$ the high momentum fluid decreases in the region where $y^+>35$ and subsequently in the viscous wall region until the mean velocity profile is reached at $T^+=24$. Figure 6-13 shows the plots of the conditionally averaged velocity fluctuations for the fluid probes at $\Delta x^+=90$. These plots have the same features as the ones previously discussed for the fluid probes at $\Delta x^+=30$ and 60. In this case it takes the fluid still more time to reach the probes because the maximum fluctuating u_x profile is obtained at $T^+=6$. Also the inflow of high momentum fluid takes place later, namely at $T^+=18$. High momentum fluid is still present at the probes at $T^+=26$.

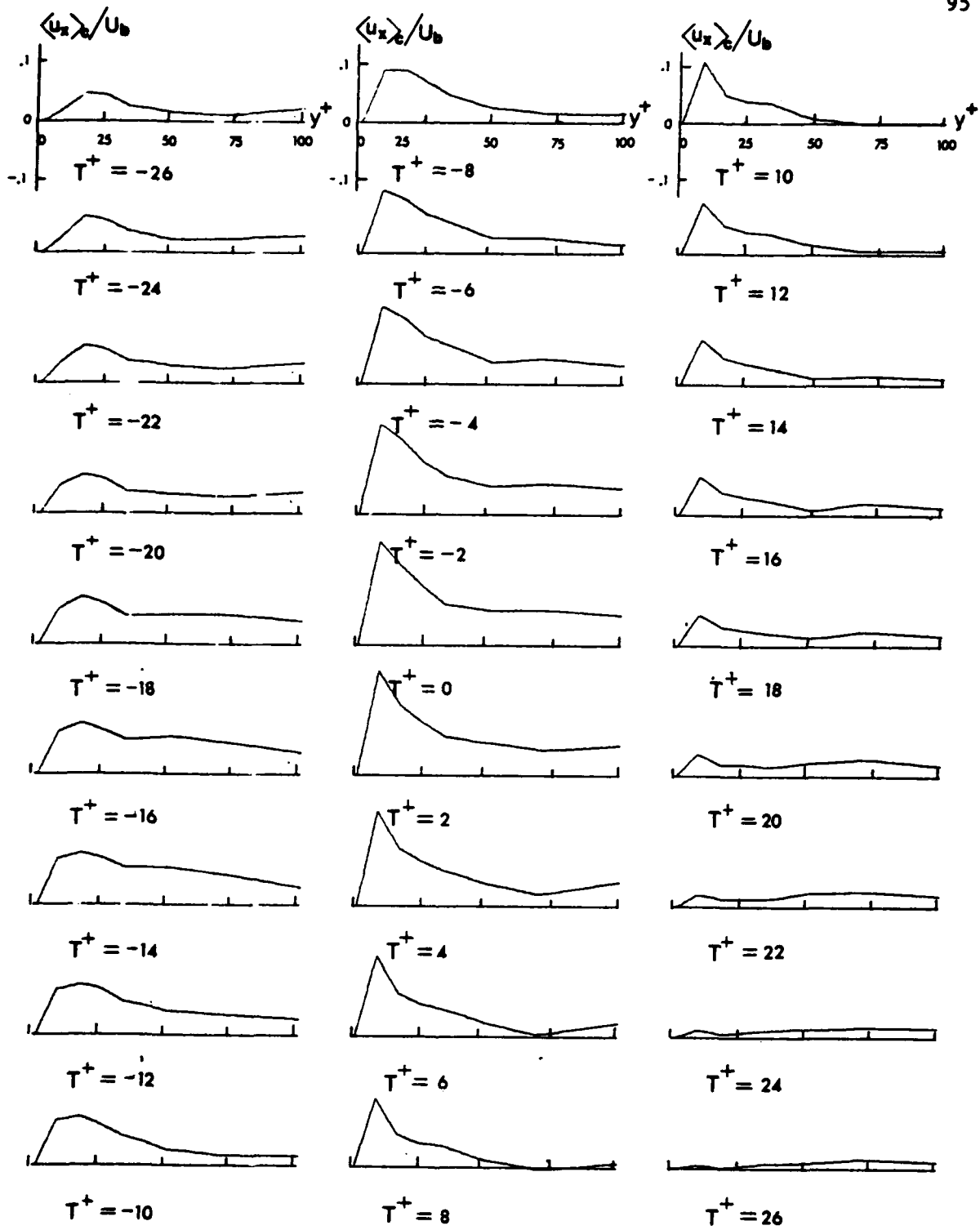


Figure 6-11. Conditionally averaged inflow u_x patterns. Equation (3.2) where $N = 3$ applied to s_z gradients; $E_D = 91$; fluid probes at $\Delta x^+ = 30$.

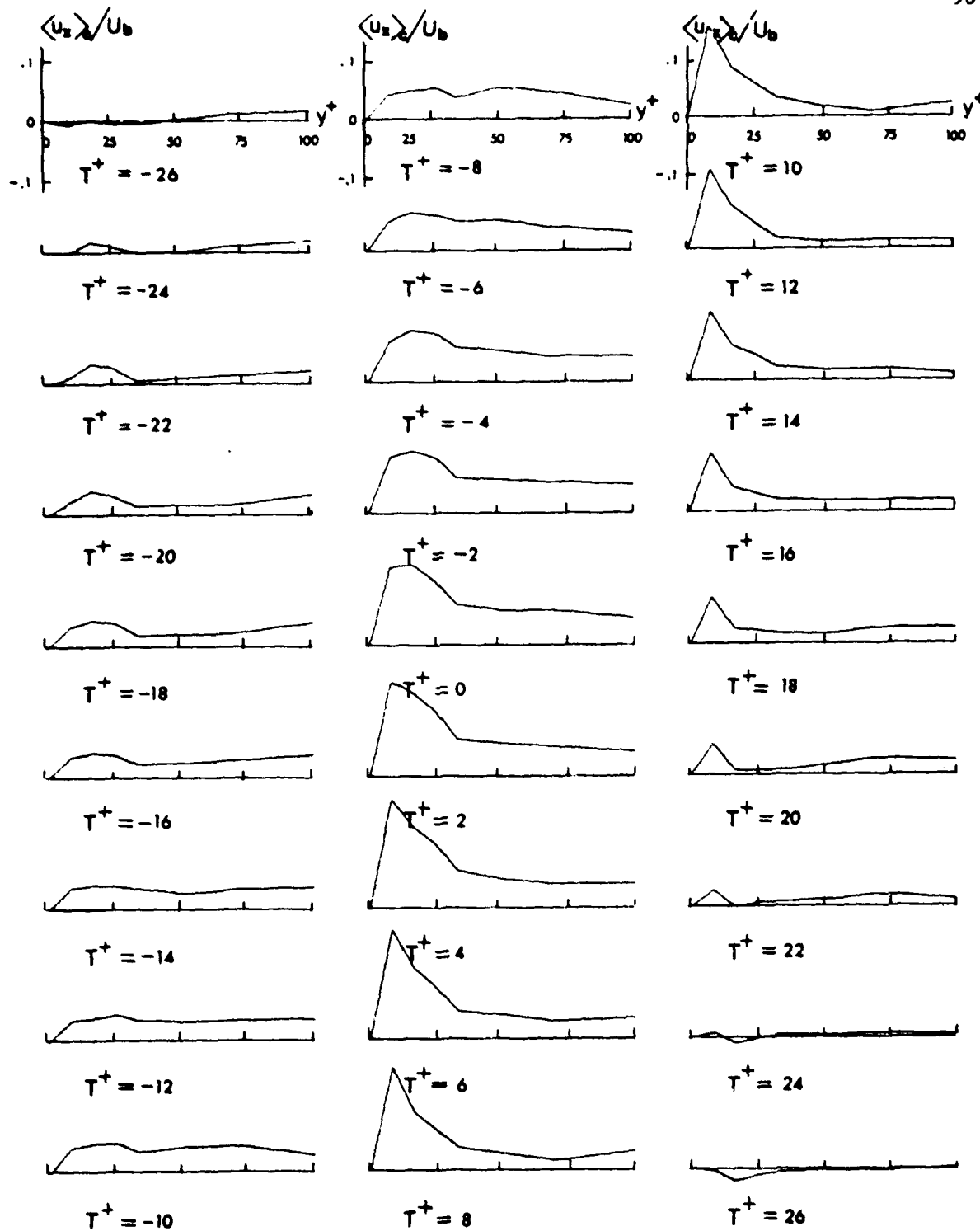


Figure 6-12. Conditionally averaged inflow u_x patterns. Equation (3.2) where $N = 3$ applied to s_z gradients; $E_D = 97$; fluid probes at $\Delta x^+ = 60$.

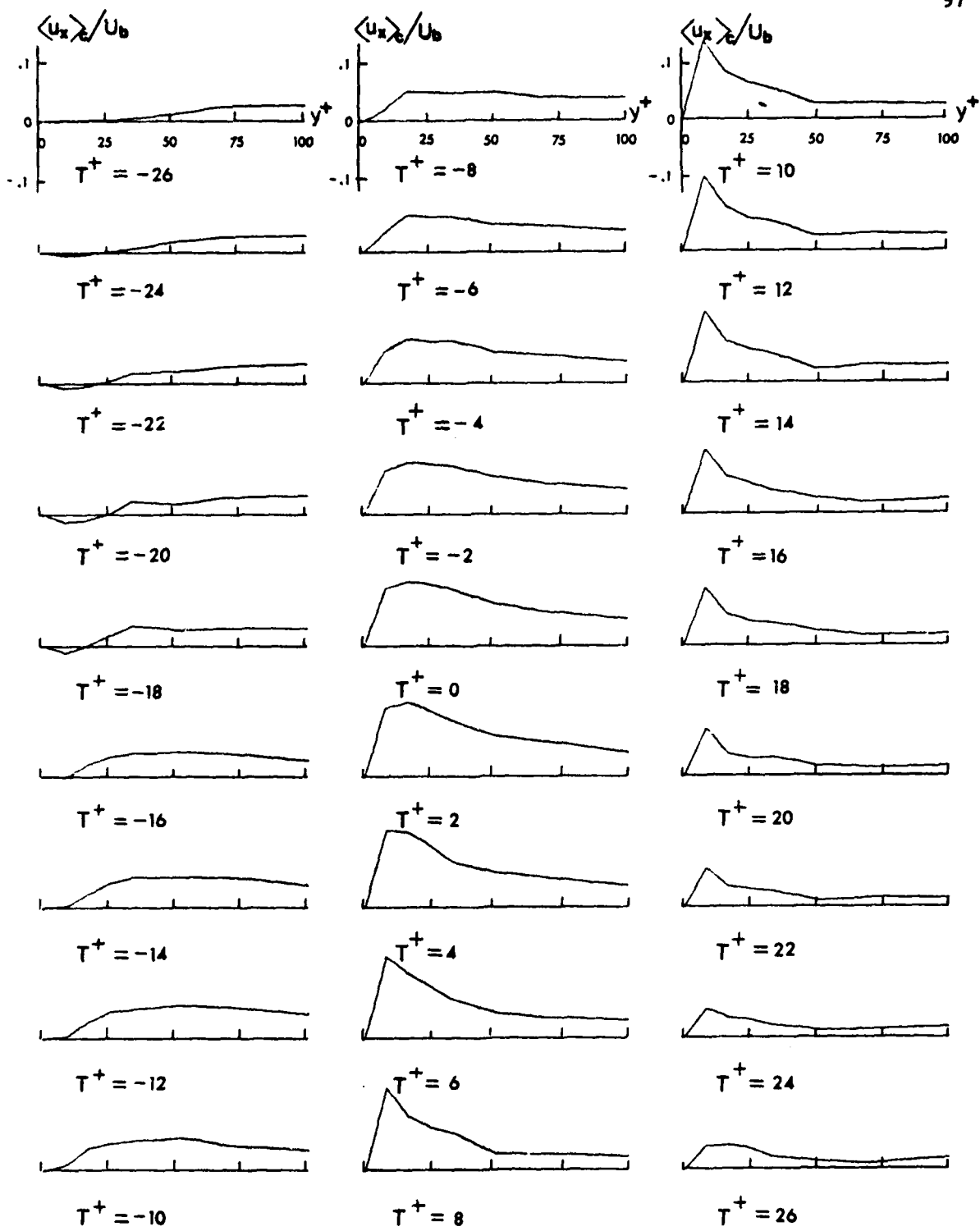


Figure 6-13. Conditionally averaged inflow u_x patterns. Equation (3.2) where $N = 3$ applied to s_z gradients; $E_D = 100$; fluid probes at $\Delta x^+ = 90$.

Summing the conditionally averaged velocity fluctuations and the mean velocity profile yields Figure 6-14. The solid lines represent the conditionally averaged velocity profiles and the dashed lines represent the mean profiles. Starting at $T^+ = -20$, high momentum fluid gradually accumulates until a maximum momentum excess is attained at $T^+ = 4$. After this dimensionless time period the conditionally averaged velocity profiles revert back to the mean profile.

4. Detection of outflows over a spanwise length of $\Delta z^+ = 102$.

Besides inflows (discussed in subsection 3) outflows were detected with equation (3.2) where $N=3$. A total of 98 outflow events were selected. At the instants of these events conditionally averaged outflow profiles were calculated. Figure 6-15 shows the conditionally averaged s_z plots which are characterized by negative slopes in the centre. At $T^+ = -10$ a negatively sloped s_z pattern is first identifiable. As a function of time this pattern increases in amplitude and reaches a maximum sine wave shaped s_z profile at $T^+ = 0$. At this instant the distance between its maximum and minimum is $\Delta z^+ = 50$, its dimensionless overall wavelength is slightly larger than 100 and its amplitudes are approximately 1.3 times the spanwise turbulence intensity. These amplitudes are 1.45 times larger than those shown in Figure 6-7 for $N=5$. Because the total spanwise length covered by the detection electrodes was $\Delta z^+ = 102$, the s_z patterns become less well defined beyond the peaks resulting in an overall wavelength larger than 100. Beyond $T^+ = 0$ the s_z pattern diminishes slowly and at $T^+ = 12$ the final spanwise outflow pattern can be identified.

For the 98 outflow instants the conditionally averaged s_x patterns were calculated and are presented in Figure 6-16. The s_x patterns show for $T^+ = -20$ to $T^+ = -10$ a small inflow profile. Outflow of low momentum

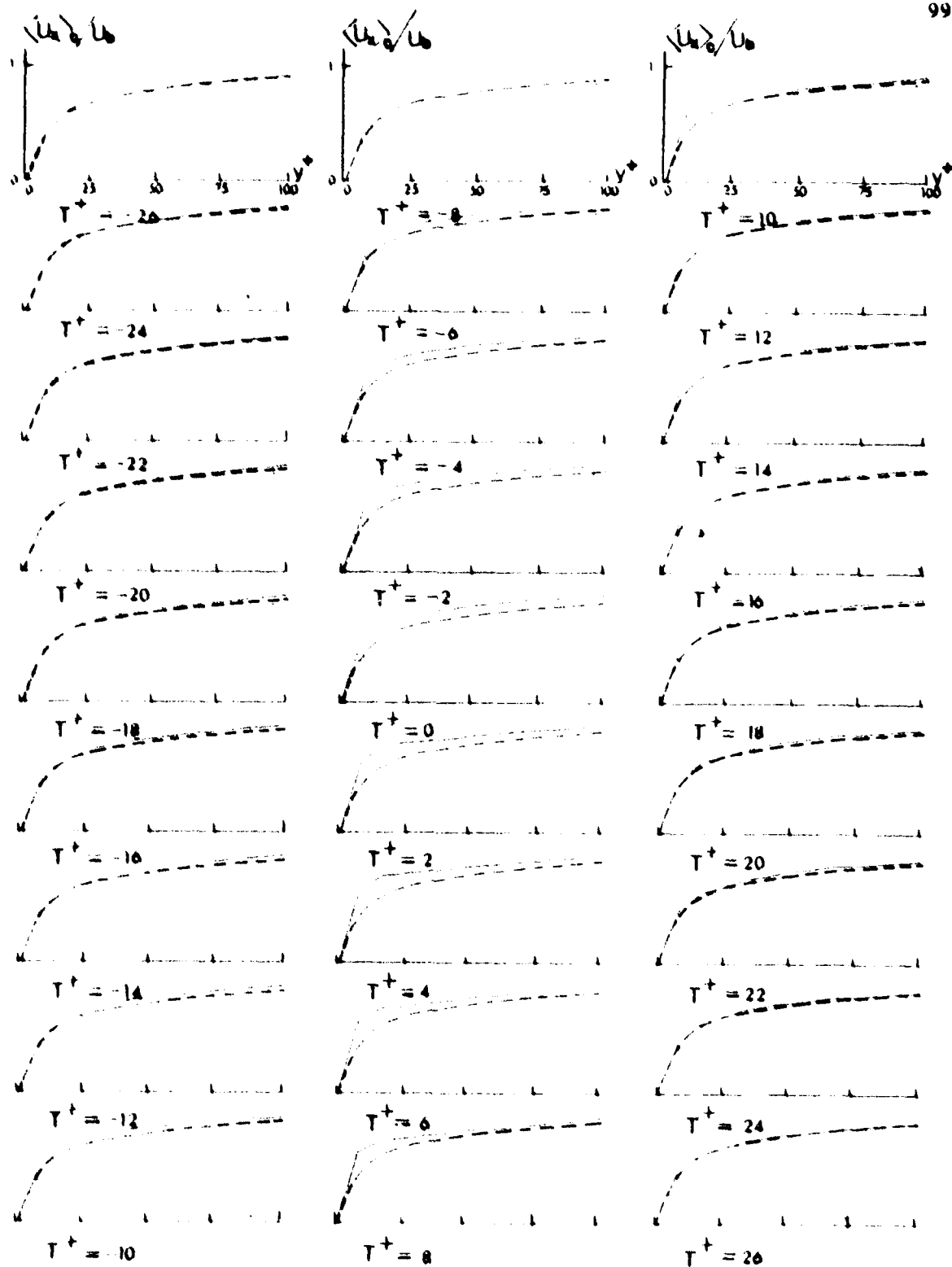


Figure 6-14. Conditionally averaged inflow U_x patterns. Equation (3.2) where $N = 3$ applied to s_z gradients; $\delta p = 9\%$; fluid probe at $Ax^+ = 60$; dashed line--mean velocity profile; solid line--conditionally averaged pattern.

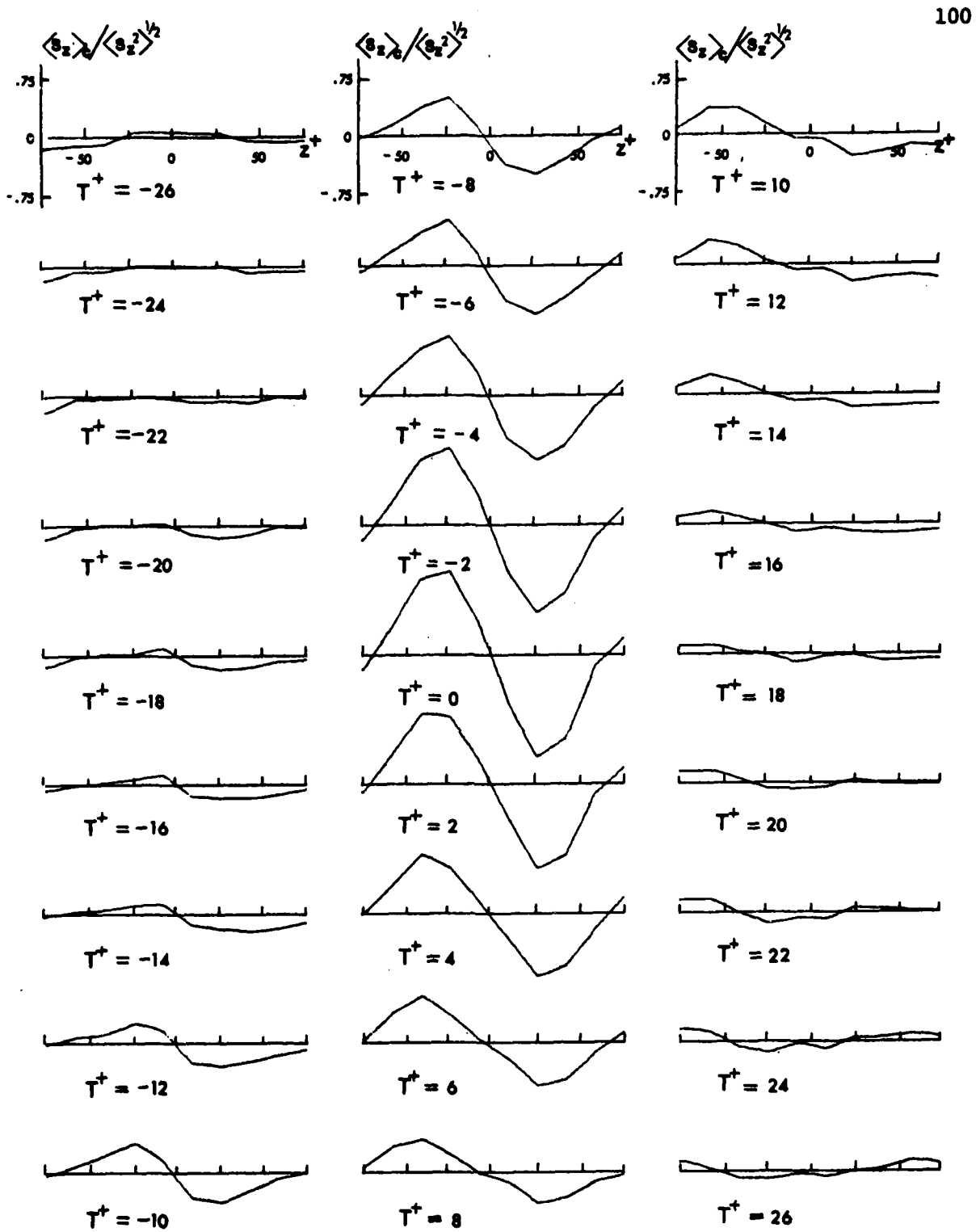


Figure 6-15. Conditionally averaged outflow s_z patterns. Equation (3.2) where $N = 3$ applied to s_z gradients; $E_D = 98$.

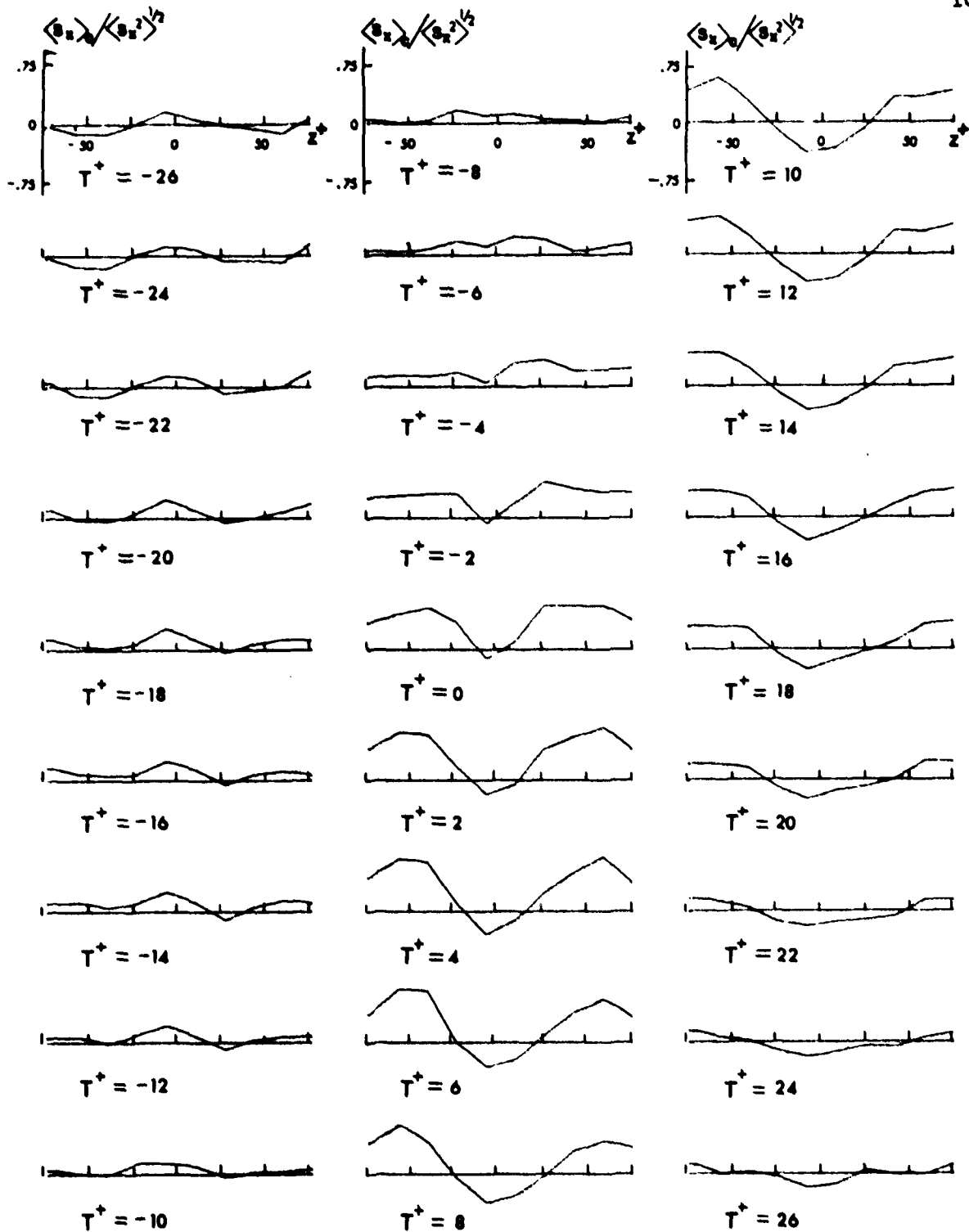


Figure 6-16. Conditionally averaged outflow s_x patterns. Equation (3.2) where $N = 3$ applied to s_z gradients; $E_D = 98$.

fluid is known to start at $T^+ = -4$ because the s_x pattern exhibits a small trough at that time point. The trough enlarges gradually and at $T^+ = 6$ a sine wave shaped outflow pattern is established. The wavelength of this outflow profile is $\Delta z^+ \approx 100$ and its valley is deeper than the one shown in Figure 6-8. A time interval of $\Delta T^+ = 6$ occurs between the appearance of the maximum s_z pattern (Figure 6-15) and that of the maximum s_x pattern. After $T^+ = 6$ the amplitudes of the s_x pattern decrease slowly and at $T^+ = 22$ no axial outflow profile can be identified.

Outflows were detected also with the fluid probes which were placed at three different downstream positions, $\Delta x^+ = 30, 60$ and 90 . Figure 6-17 illustrates the conditionally averaged u_x profiles for the fluid probes at $\Delta x^+ = 30$. These u_x profiles have momentum deficient fluid near the wall for $T^+ = -26$ to $T^+ = -18$. High momentum fluid is present from $T^+ = -26$ to $T^+ = -2$ at distances larger than approximately $y^+ = 50$. In contrast to these u_x profiles no low momentum fluid is observed in the s_x patterns (Figure 6-16) for $T^+ < -2$, leading to the conclusion that the fluid probe signals might have been disturbed. At approximately $T^+ = 0$ the region of momentum deficient fluid extends all the way to $y^+ = 70$ and at $y^+ = 25$ the momentum deficiency is 10 percent of the bulk velocity. This low momentum fluid is gradually replaced by fluid with the local mean velocity until at $T^+ = 18$ a profile with neither momentum excess nor deficiency is established. By placing the fluid probes at $\Delta x^+ = 60$, the low momentum fluid reaches the probes at $T^+ = -20$ at a distance from the wall of $y^+ = 50$, as shown in Figure 6-18. Apparently the low momentum fluid migrates away from the wall as it moves downstream. At $T^+ = 6$ momentum deficient fluid is present in the region where $y^+ < 75$, and at $y^+ = 19$ the momentum deficiency is 17 percent of the bulk velocity. Beyond the instant when

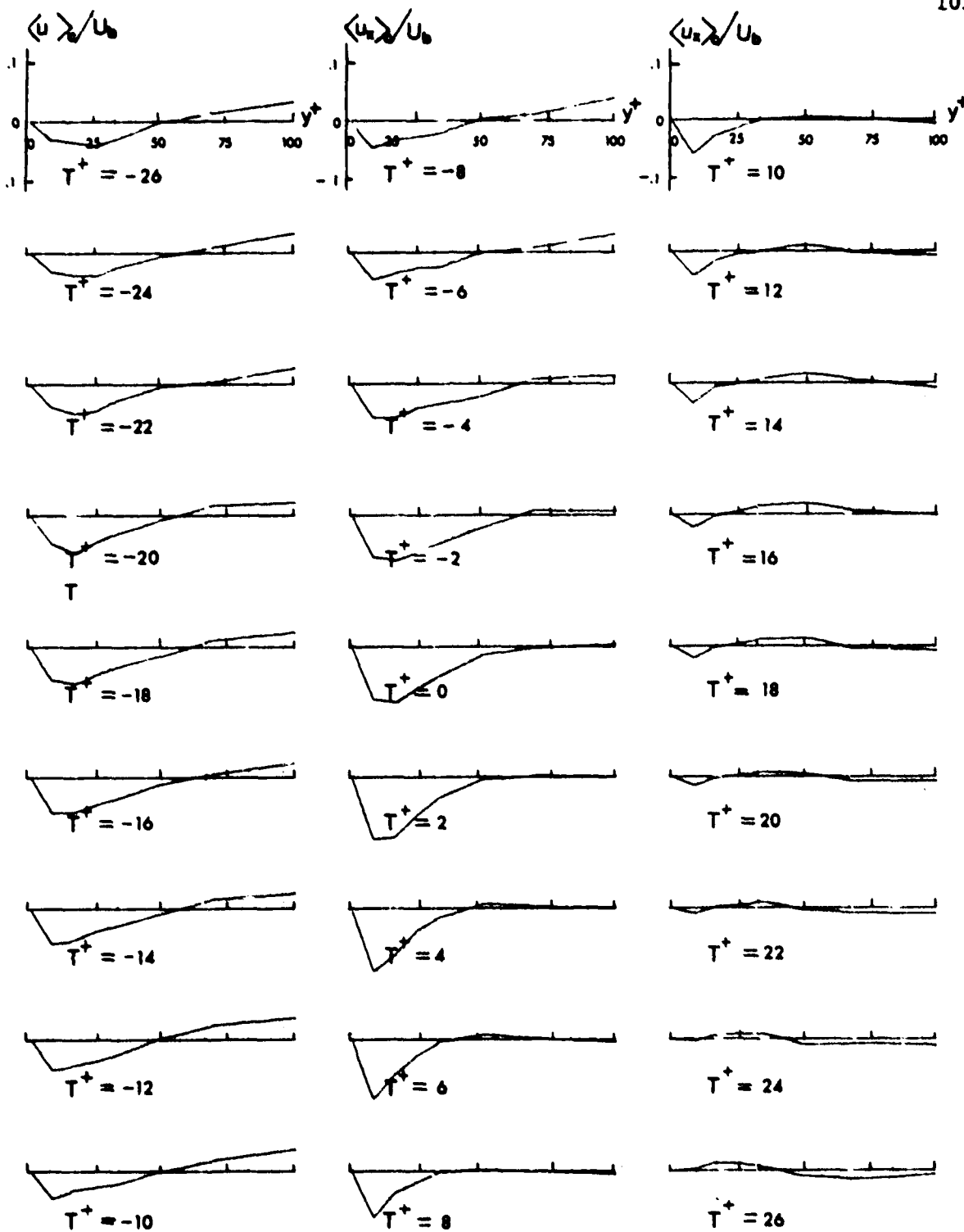


Figure 6-17. Conditionally averaged outflow u_x patterns. Equation (3.2) where $N = 3$ applied to s_z gradients; $E_D = 89$; fluid probes at $\Delta x^+ = 30$.

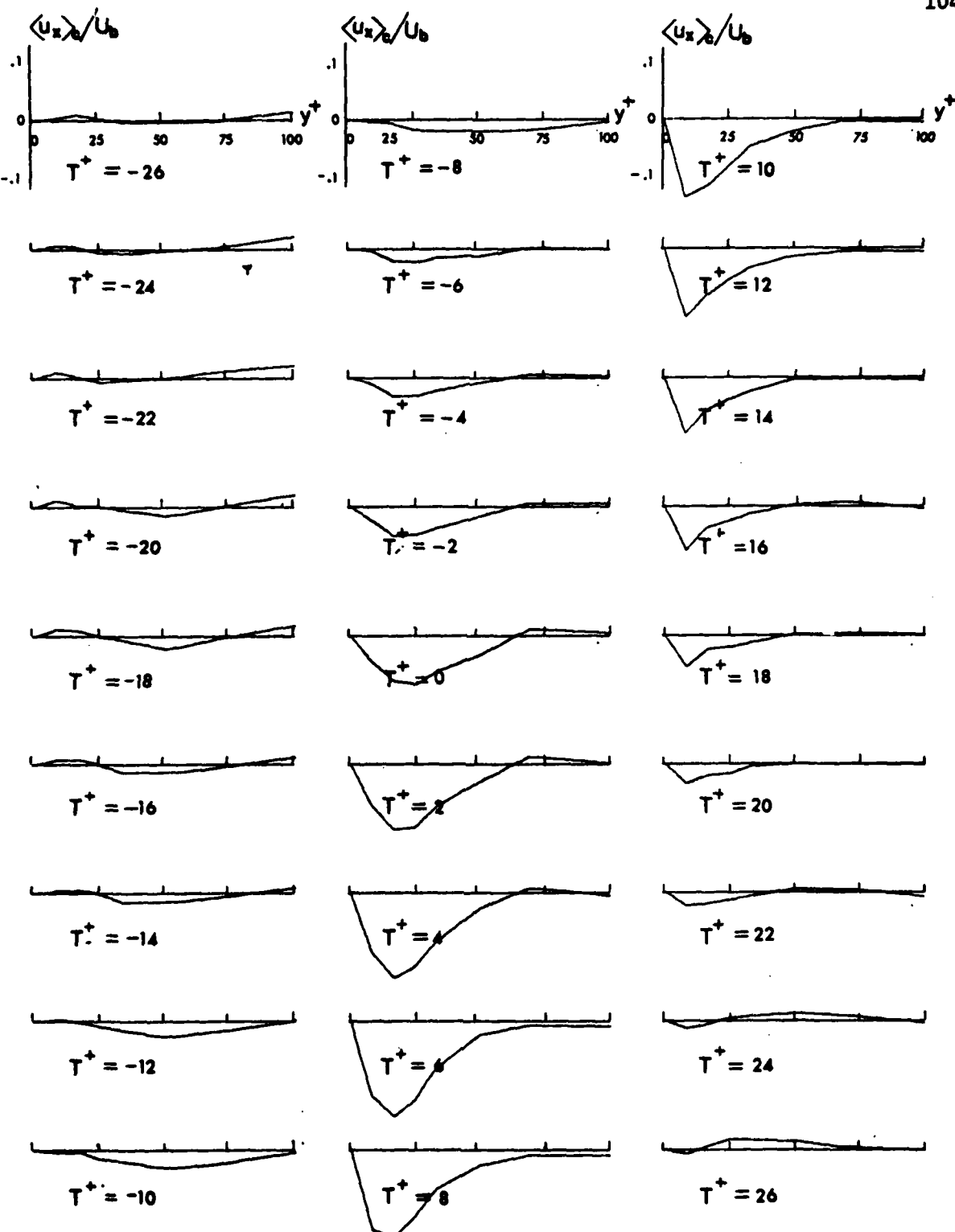


Figure 6-18. Conditionally averaged outflow u_x patterns. Equation (3.2) where $N = 3$ applied to s_z gradients; $E_D = 98$; fluid probes at $\Delta x^+ = 60$.

the fluid has its maximum momentum deficiency the u_x fluctuation profile relaxes gradually into a profile with only negligible momentum deficiency. Figure 6-19 shows the outflow profiles for the fluid probes at $\Delta x^+=90$ and indicates that it takes the low momentum fluid longer to reach probes placed farther downstream. Low momentum fluid is first visible at $T^+=-2$ where $y^+=35$. Over time the momentum of the fluid in the viscous wall region becomes increasingly more deficient. A maximum outflow of low momentum fluid is established at $T^+=8$ with a maximum momentum deficiency of 15 percent of the bulk velocity. After this instant the conditionally averaged fluctuation profile relaxes to zero as a function of time.

Figure 6-20 resulted from adding the conditionally averaged fluctuating velocities of Figure 6-18 to the local mean velocities. A solid line represents a conditionally averaged velocity pattern and a dashed line represents the mean velocity profile. From $T^+=-26$ to $T^+=-8$ the conditionally averaged velocity is nearly the same as the local mean velocity. Inflexions in the conditionally averaged profiles are indicated from $T^+=-4$ to $T^+=8$. Although these inflexions are very small they demonstrate that they do form during strong outflows. For $T^+>14$ the conditionally averaged profile returns rapidly to the average mean velocity profile.

5. Spatial coherency of inflows and outflows.

The spatial coherency of inflows and outflows was studied by applying equation (3.3) with $N=4$ to the spanwise velocity gradients at the wall. A total of 100 events representing clockwise rotating open eddies were selected from the data set. During the instants of these events conditional averages were calculated from the spanwise velocity gradients. Plots of these wall patterns are shown in Figure 6-21. At $T^+=-14$ a s_z pattern with a valley in the centre and small bulges on each

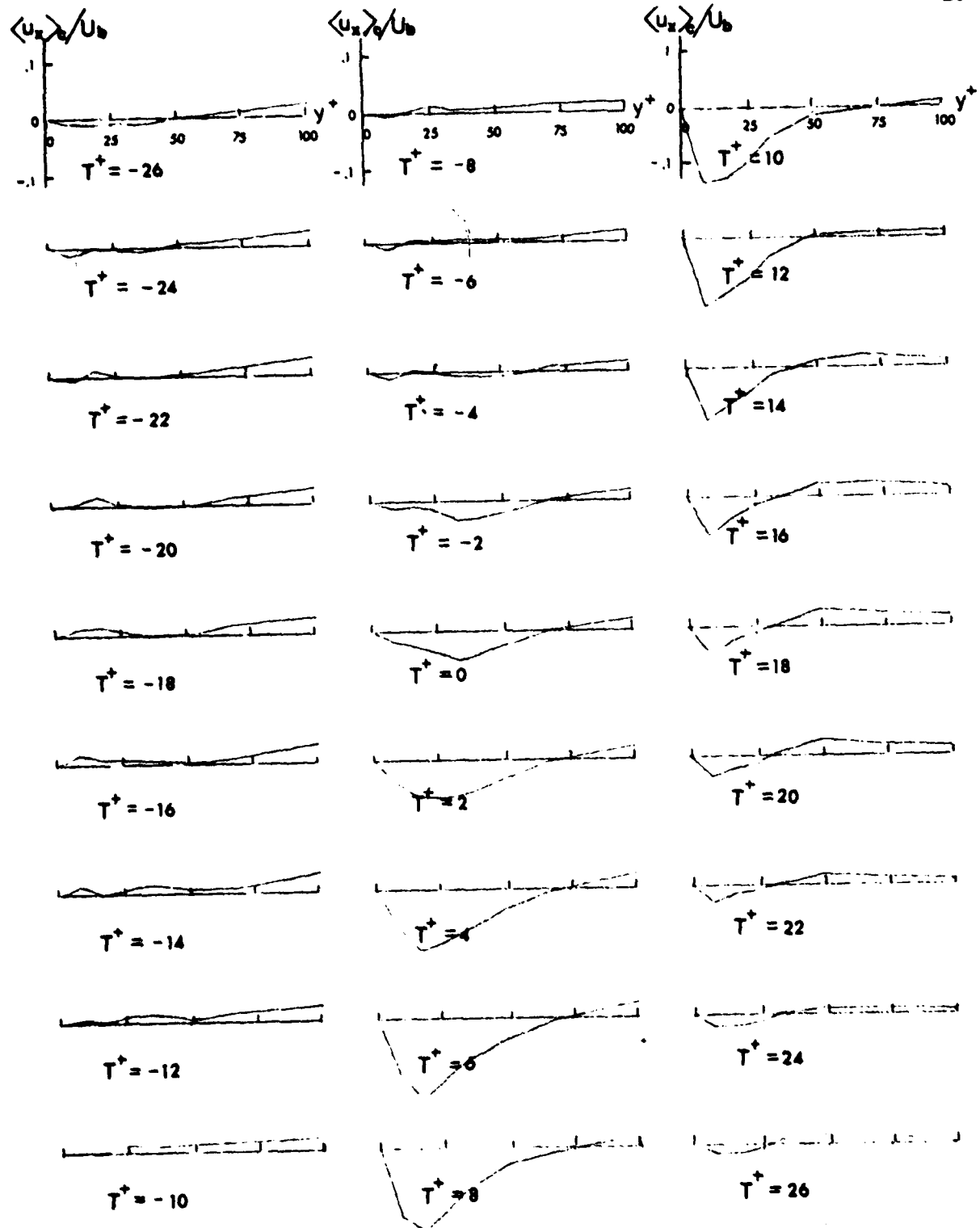


Figure 6-19. Conditionally averaged outflow u_x patterns. Equation (3.2) where $N = 3$ applied to s_z gradients; $E_D = 97$; fluid probes at $\Delta x^+ = 90$.

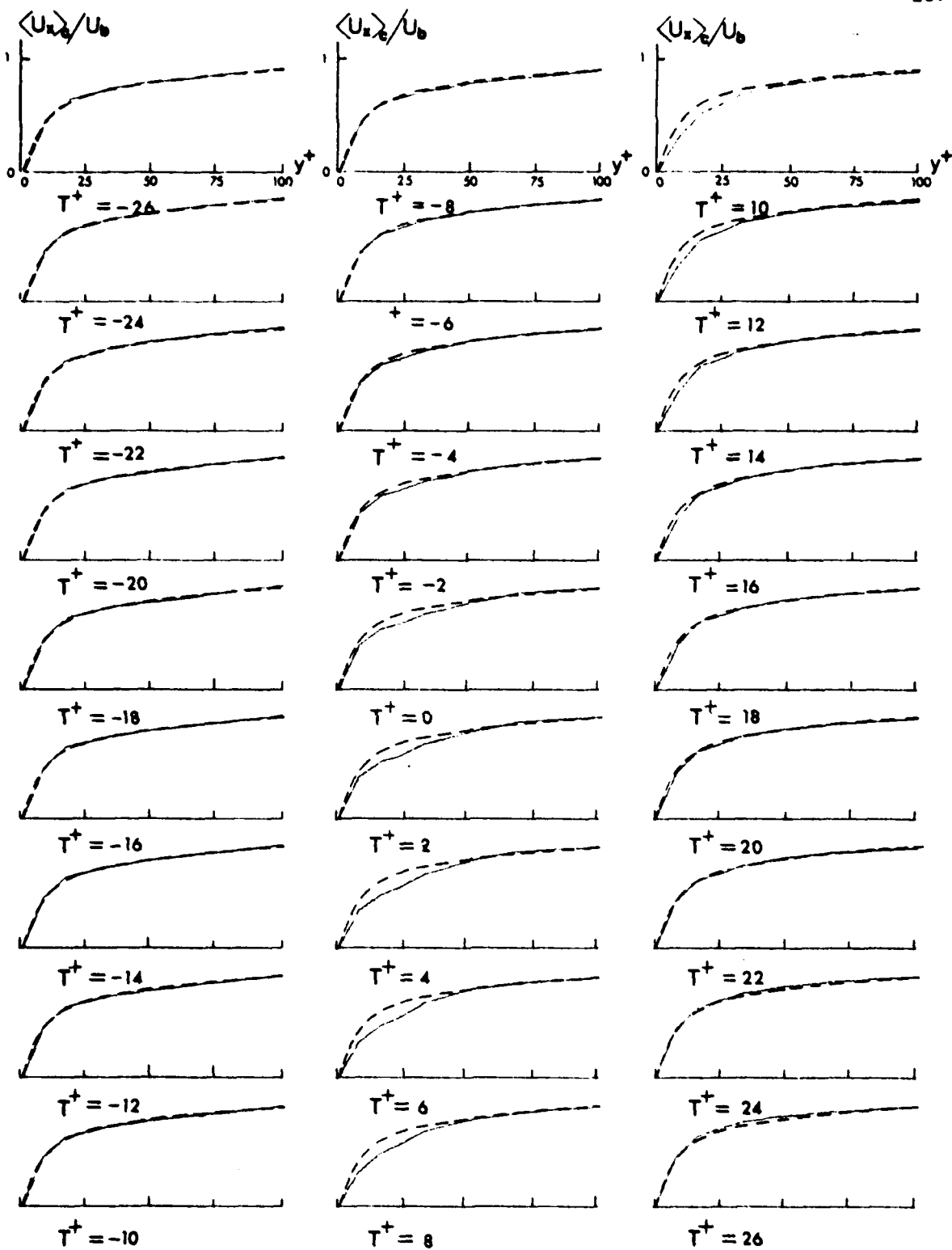


Figure 6-20. Conditionally averaged outflow U_x patterns. Equation (3.2) where $N = 3$ applied to s_z gradients; $E_D = 98$; fluid probes at $\Delta x^+ = 60$; dashed line--mean velocity profile; solid line--conditionally averaged pattern.

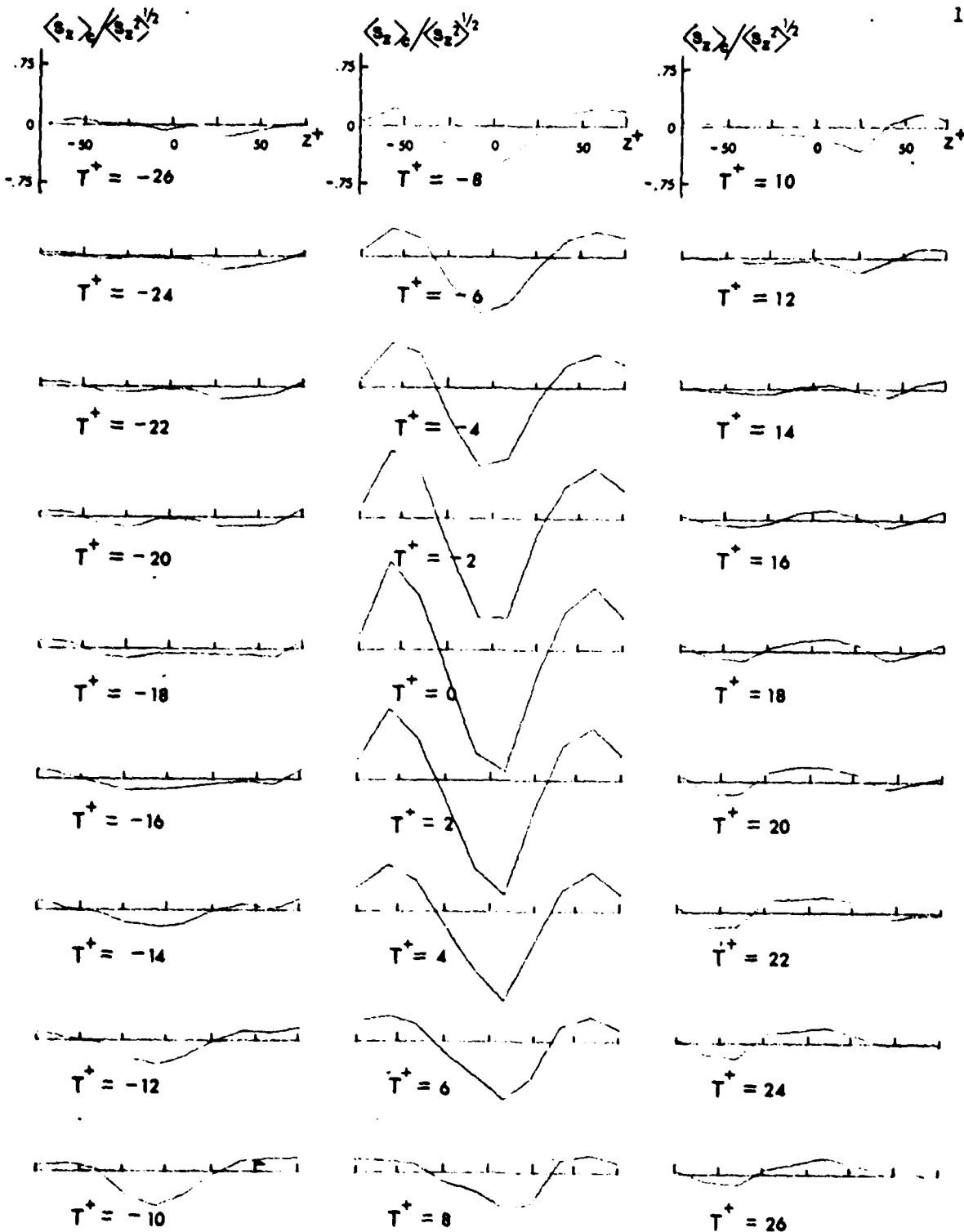


Figure 6-21. Conditionally averaged inflow-outflow s_z patterns. Equation (3.3) applied to s_z gradients; $E_D = 100$.

side is identifiable. Further in time this pattern develops very rapidly until $T^+=0$ when a sine wave shaped profile with a large amplitude is reached. The maximum amplitude at this instant is 1.5 times the spanwise turbulence intensity and the dimensionless wavelength between its two peaks is approximately 100. Further in time this pattern diminishes in amplitude until at $T^+=12$ a conditionally averaged fluctuation profile close to zero is attained.

The conditionally averaged s_x patterns which were determined for the same event set are shown in Figure 6-22. Development of an s_x inflow-outflow pattern starts at $T^+=-4$, a time delay of about $\Delta T^+=7$ after the start of the development of the s_z pattern. At time $T^+=6$ a sine wave shaped s_x profile is established. At the bulge an inflow takes place and in the valley an outflow. Forward in time this s_x profile slowly decreases in amplitude. Only the patterns for a clockwise rotating open eddy are shown; results for a counter-clockwise rotating open eddy are the same but of opposite sign for both the s_x and s_z profiles.

Fluid probes which were placed in the centre of the wall probes at a downstream location of $\Delta x^+=90$ did not detect fluid with either high or low momentum, as illustrated in Figure 6-23. This result is hardly surprising since the s_x patterns have their zero crossings in the centre of the wall probes and consequently only fluid on the order of the local mean velocity passes over the fluid probes.

6. Transition of outflows into inflows over time.

The random nature of turbulence suggests that inflows and outflows occur randomly both in space and time. To study the outflow-inflow

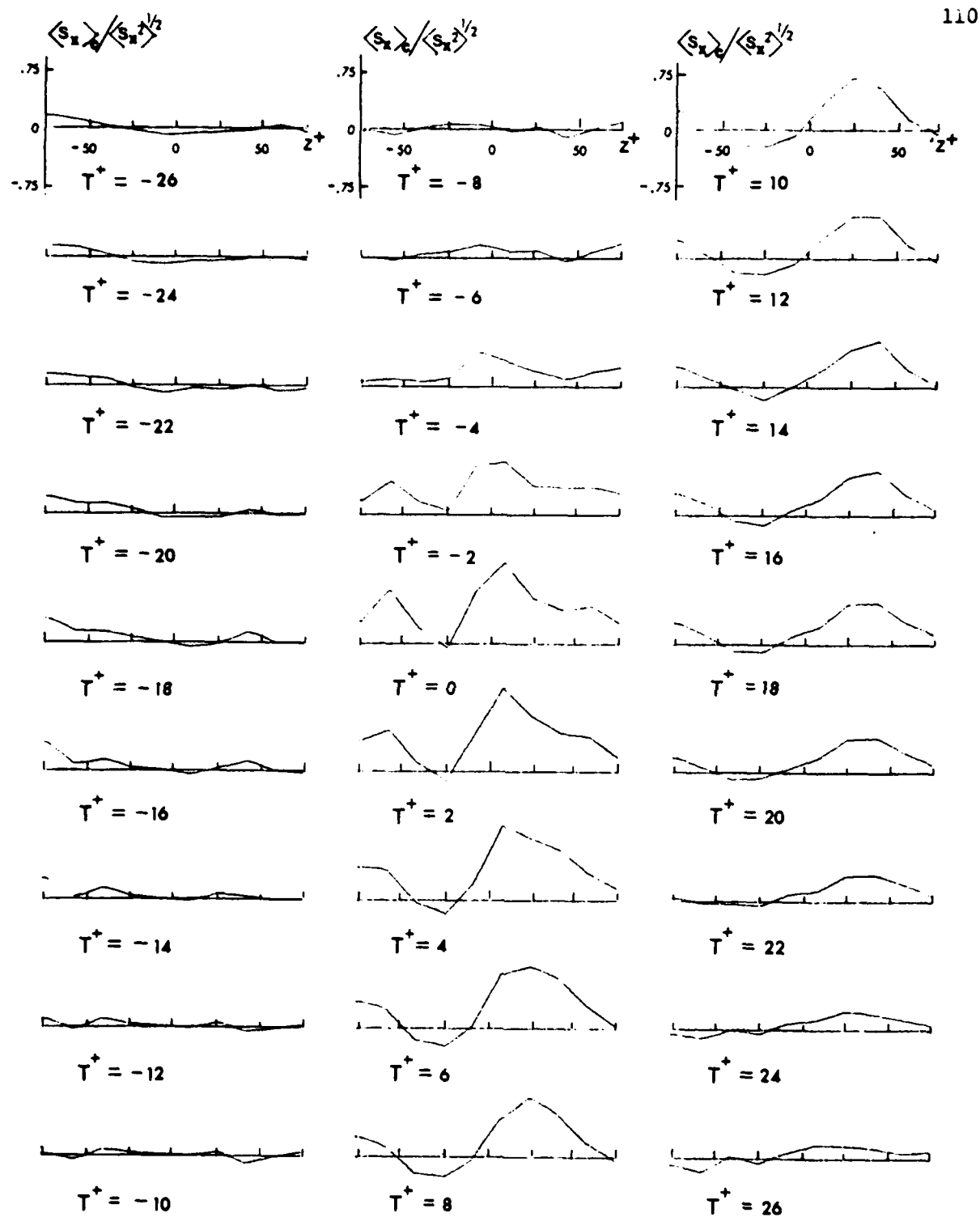


Figure 6-22. Conditionally averaged inflow-outflow s_x patterns. Equation (3.3) applied to s_z gradients; $E_D = 100$.

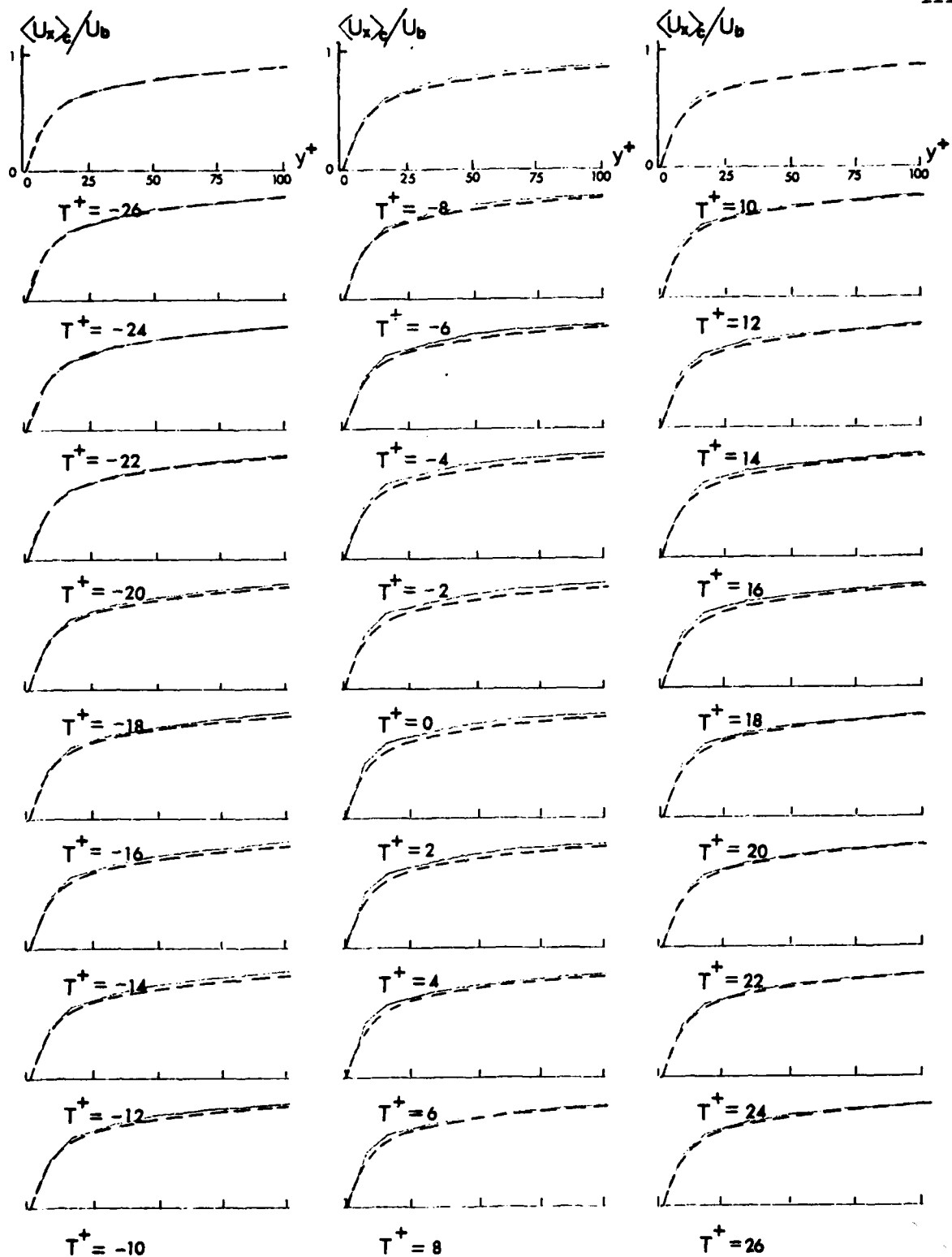


Figure 6-23. Conditionally averaged inflow-outflow U_x patterns. Equation (3.3) applied to s_z gradients; $E_D = 100$; fluid probes at $\Delta x^+ = 90$; dashed line--mean velocity profile; solid line--conditionally averaged pattern.

sequence over time, equation (3.4) with $N=3$ and $K=4$ was applied to the spanwise velocity gradients. Rapid changes of an outflow s_z pattern into an inflow s_z pattern were found in the data set. Seventy of these events were selected and used to calculate the conditionally averaged s_z patterns which are shown in Figure 6-24. At $T^+=-18$ an outflow pattern (with negative slope) appears that grows steadily until $T^+=-8$ when a large amplitude sine wave shaped pattern is obtained with a wavelength of approximately $\Delta z^+=100$. Forward in time this pattern decreases in amplitude and from $T^+=-2$ to $T^+=2$ the outflow pattern changes to an inflow pattern which has a positive slope. The inflow s_z pattern develops until $T^+=8$ when the pattern's amplitude begins to decrease slowly. At $T^+=8$ the inflow sine wave shaped s_z pattern is established with an amplitude of 68 percent of the spanwise turbulence intensity and a wavelength of approximately $\Delta z^+=100$.

Also calculated for the outflow-inflow sequence were the s_x plots shown in Figure 6-25. An outflow s_x pattern is observable from $T^+=-12$ to $T^+=8$. At $T^+=0$ a sine wave shaped s_x pattern was obtained with a time delay of $\Delta T^+=8$ after the maximum s_z pattern was reached. During the period of $T^+=8$ to $T^+=12$ the s_x pattern changed rapidly from an outflow profile to an inflow profile. This change took place at a dimensionless time of approximately $\Delta T^+=10$ after the s_z pattern changed. The inflows are not as strongly evident as the outflows, possibly because the axial momentum of the former is more diffused than that of the latter.

The outflow-inflow sequence was measured also with the fluid probes. Two data sets were obtained, one with the probes at $\Delta x^+=60$ and the other with the probes at $\Delta x^+=90$. The results of these two runs are depicted

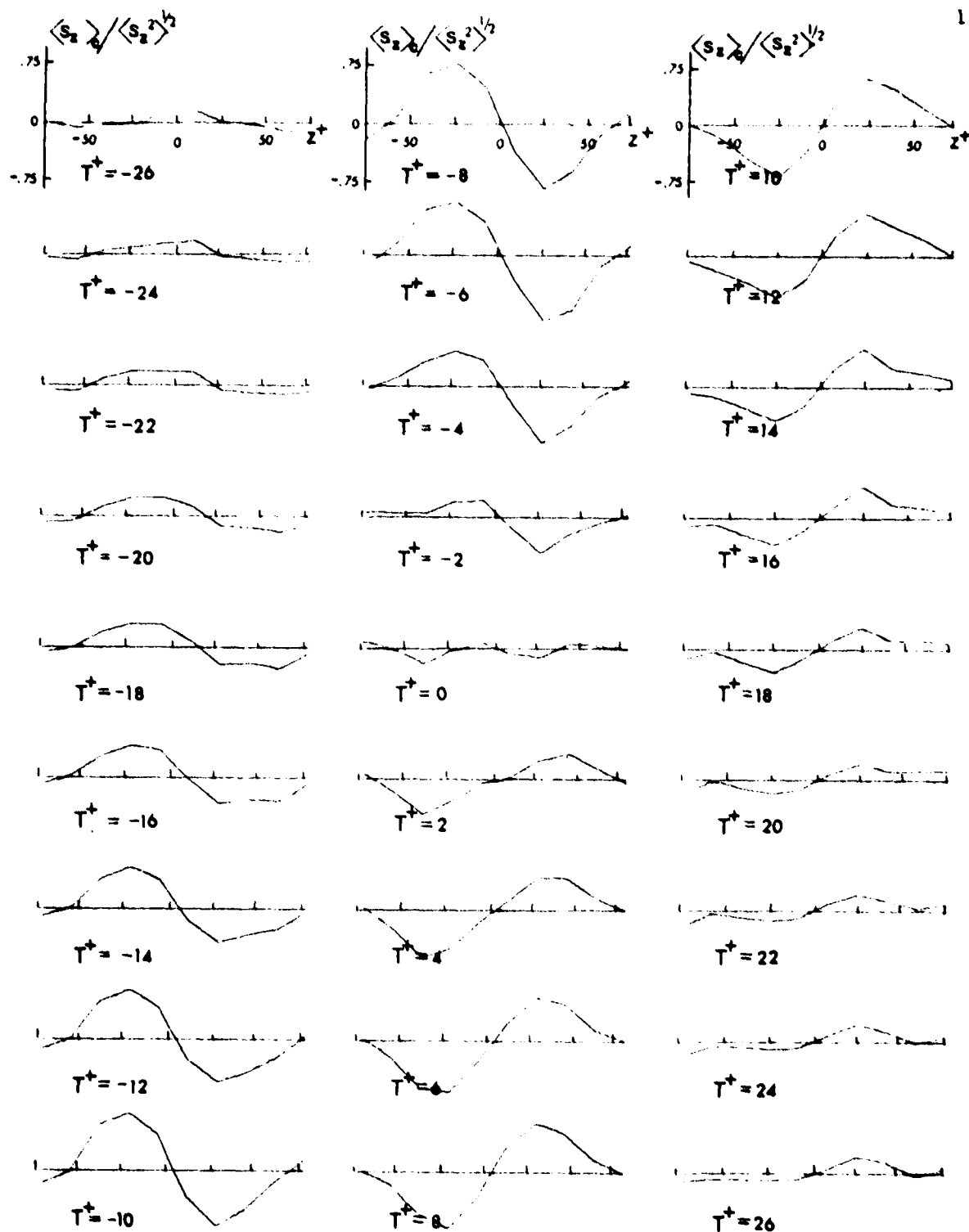


Figure 6-24. Conditionally averaged transitional outflow-inflow s_z patterns. Equation (3.4) applied to s_z gradients; $E_D^2 = 70$.

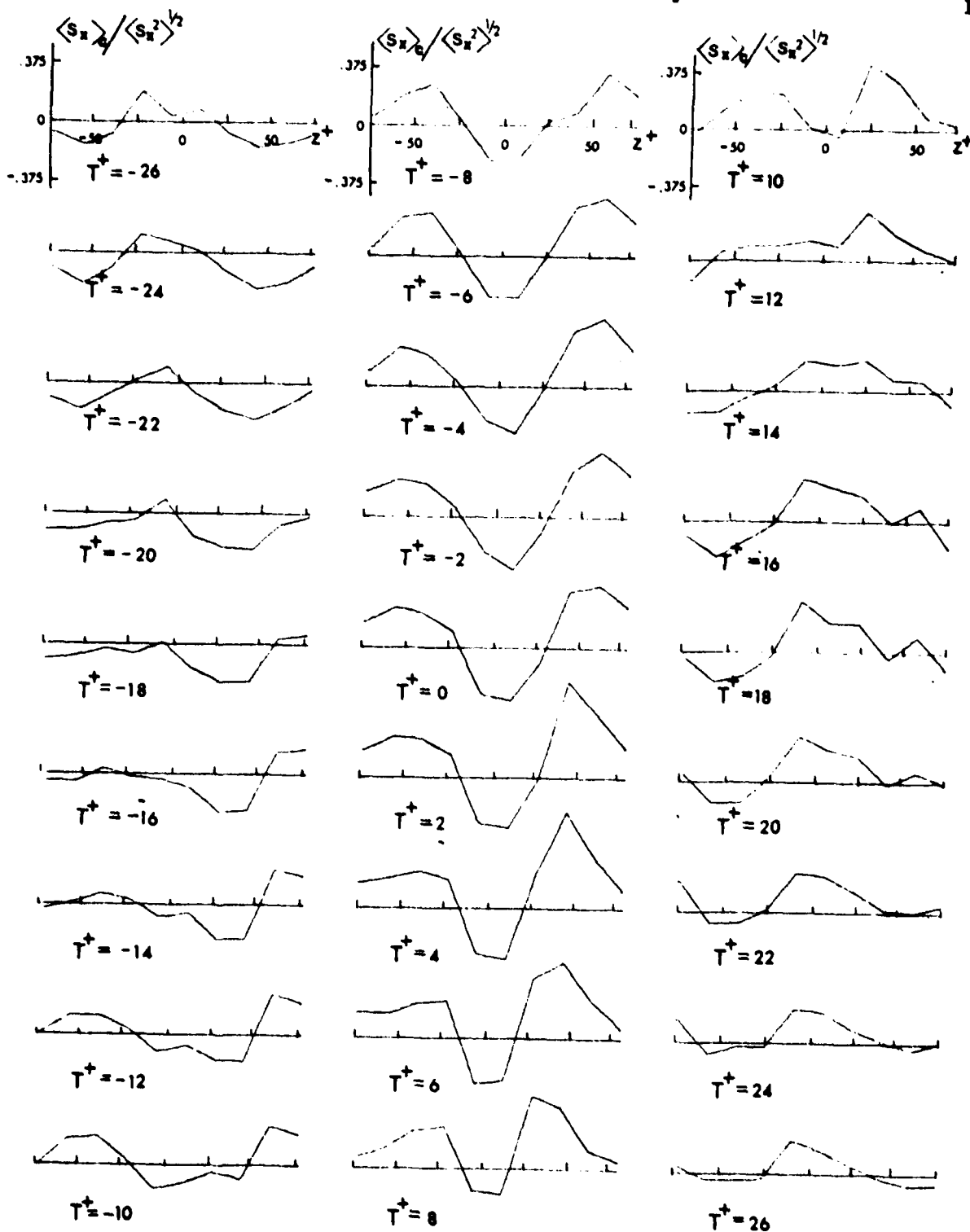


Figure 6-25. Conditionally averaged transitional outflow-inflow s_z patterns. Equation (3.4) applied to s_z gradients; $E_D = 70$.

in Figures 6-26 and 6-27. The major difference between the figures is that the low momentum fluid was replaced totally by high momentum fluid at $T^+ = 8$ for the probes at $\Delta x^+ = 60$ but not until $T^+ = 12$ for the probes at $\Delta x^+ = 90$. The rapid change of low momentum fluid into high momentum fluid in the viscous wall region takes a time period of about $\Delta T^+ = 6$.

The conditionally averaged fluctuating velocities of Figure 6-27 were added to the mean velocities and the results are presented by the solid lines in Figure 6-28. These plots show that starting at $T^+ = -22$ low momentum fluid slowly accumulates. At $T^+ = -6$ the first signs of in-moving high momentum fluid originating at the outer edge of the boundary layer becomes visible. This inflowing high momentum fluid caused inflexions in the conditionally averaged velocity profile. Inflexions occur in the viscous wall region from $T^+ = -6$ to $T^+ = 2$. After $T^+ = 2$ the high momentum fluid pushes the momentum deficient fluid rapidly away and at $T^+ = 12$ the entire conditionally averaged velocity profile shows a momentum excess. Then this profile changes only slightly over time until $T^+ = 26$.

7. Transition of inflows into outflows over time.

Another finding of this work was that inflows are succeeded by outflows. In order to detect this sequence of events equation (3.4) was applied (with $N=3$ and $K=4$) to the spanwise velocity gradients. Sixty-six of these inflow-outflow events were selected and at the instants of these events the s_z patterns were conditionally averaged. Figure 6-29 shows the calculated s_z patterns as a function of time. At $T^+ = -18$ an inflow pattern, positively sloped, is clearly identifiable. This pattern grows in amplitude until $T^+ = -8$ when the maximum inflow pattern is reached which has a wavelength of $\Delta z^+ = 100$ and a large amplitude. Gradually this pattern decreases in amplitude and between $T^+ = -2$ and

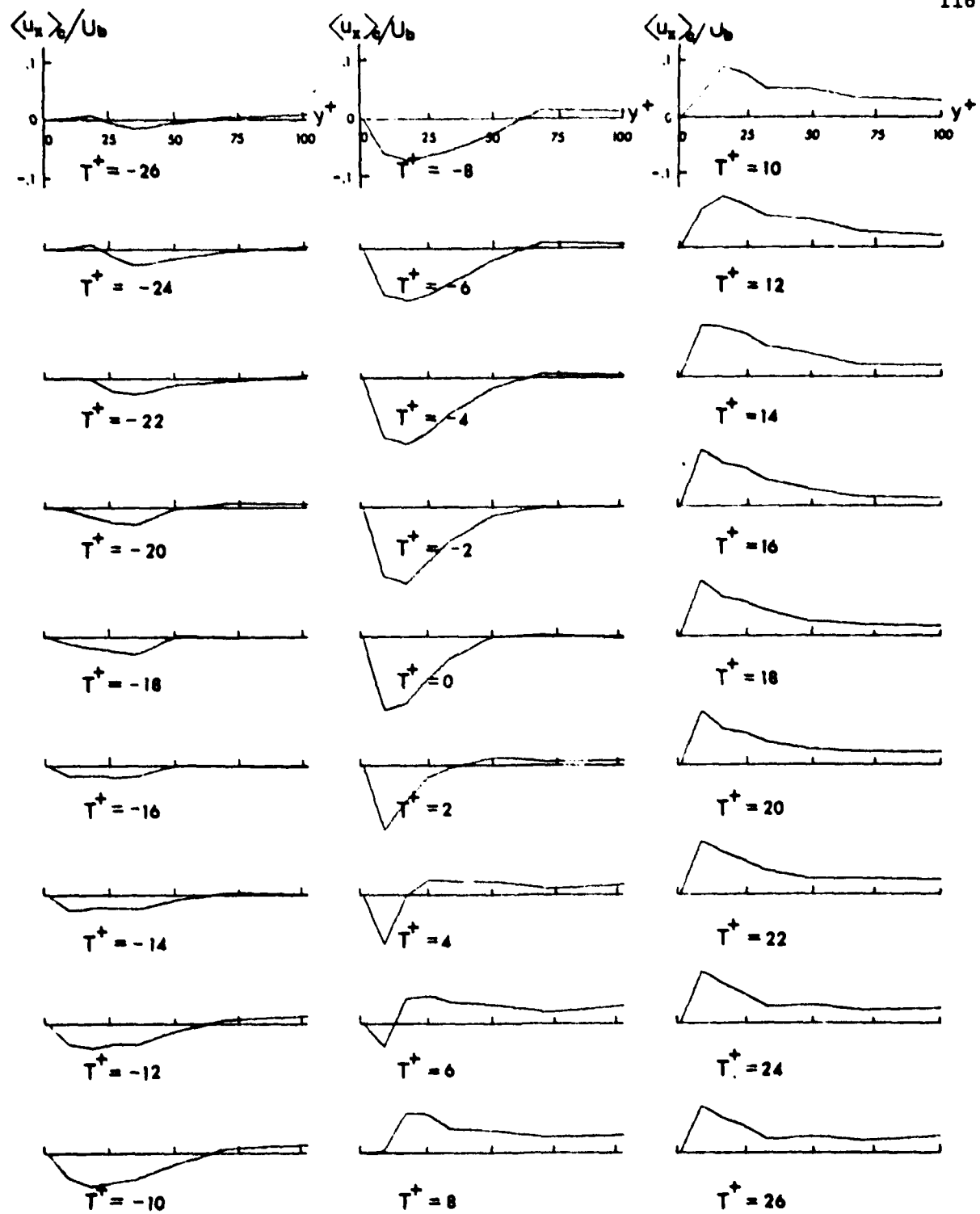


Figure 6-26. Conditionally averaged transitional outflow-inflow u_x patterns. Equation (3.4) applied to s_z gradients; $E_D = 70$; fluid probes at $\Delta x^+ = 60$.

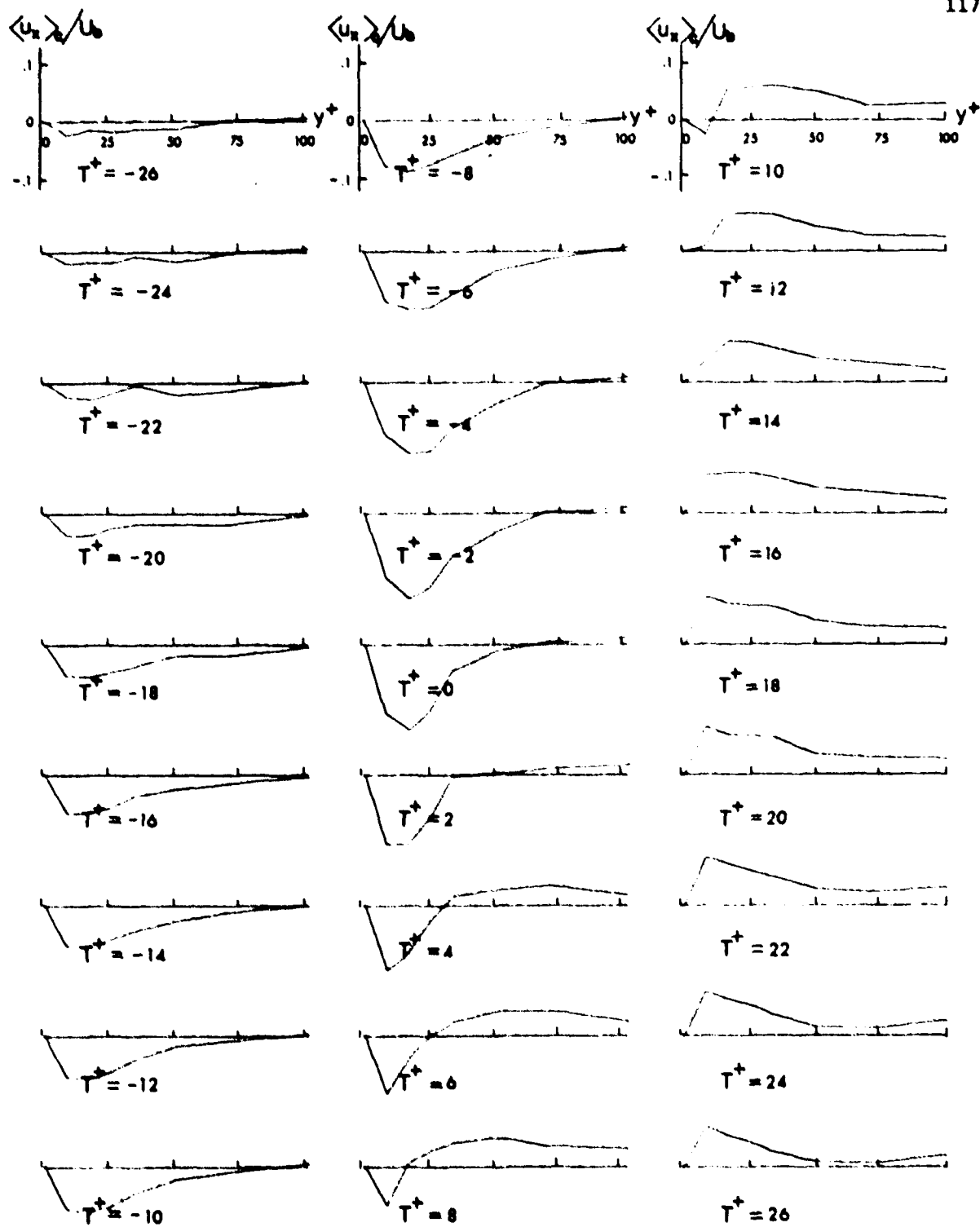


Figure 6-27. Conditionally averaged transitional outflow-inflow u_x patterns. Equation (3.4) applied to g_z gradients; $E_D = 78$; fluid probes at $\Delta x^+ = 90$.

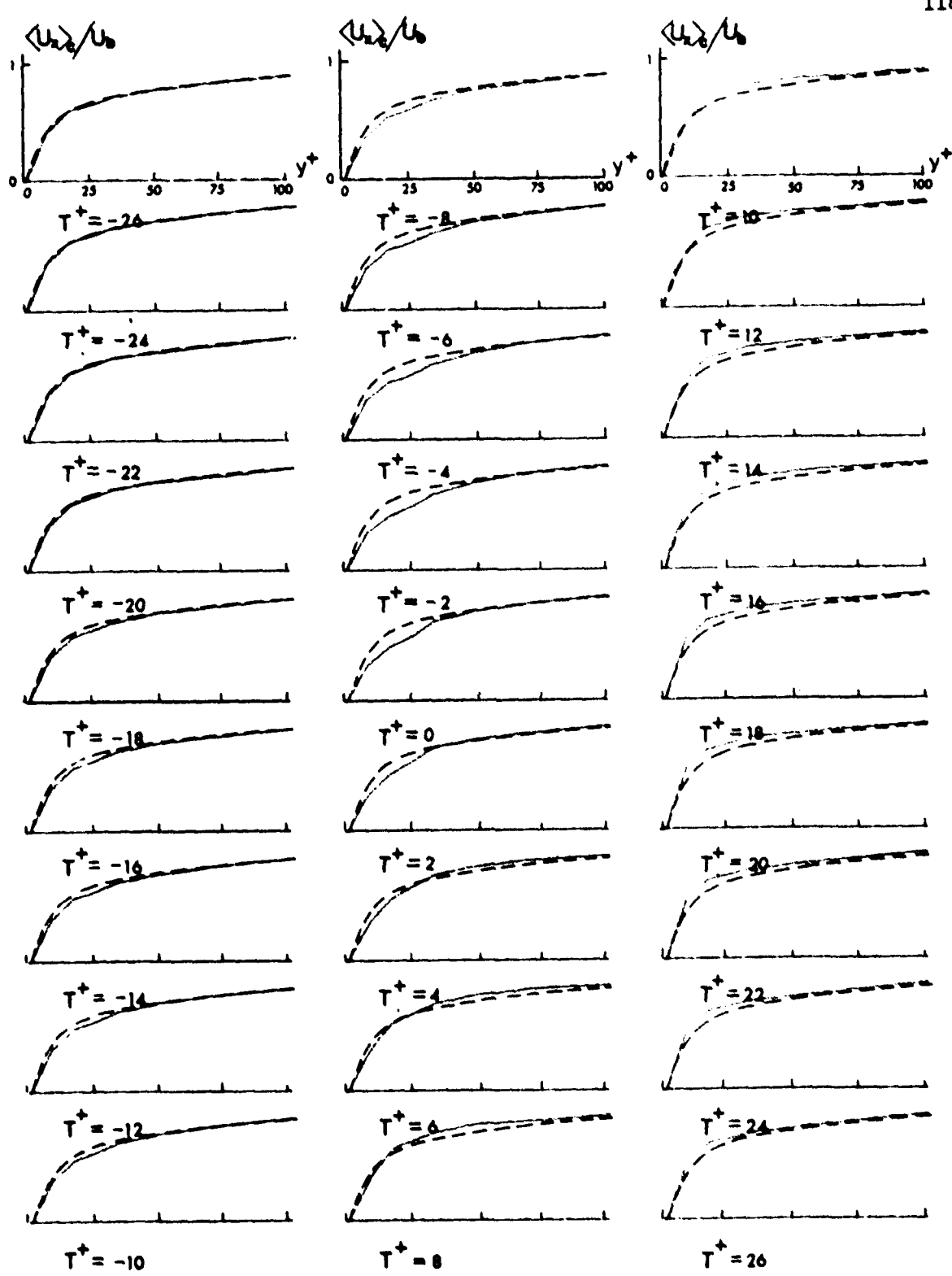


Figure 6-28. Conditionally averaged transitional outflow-inflow U_x patterns. Equation (3.4) applied to U_x gradients; $E_D = 78$; fluid probes at $\Delta x^+ = 90$; dashed line--mean velocity profile; solid line--conditionally averaged pattern.

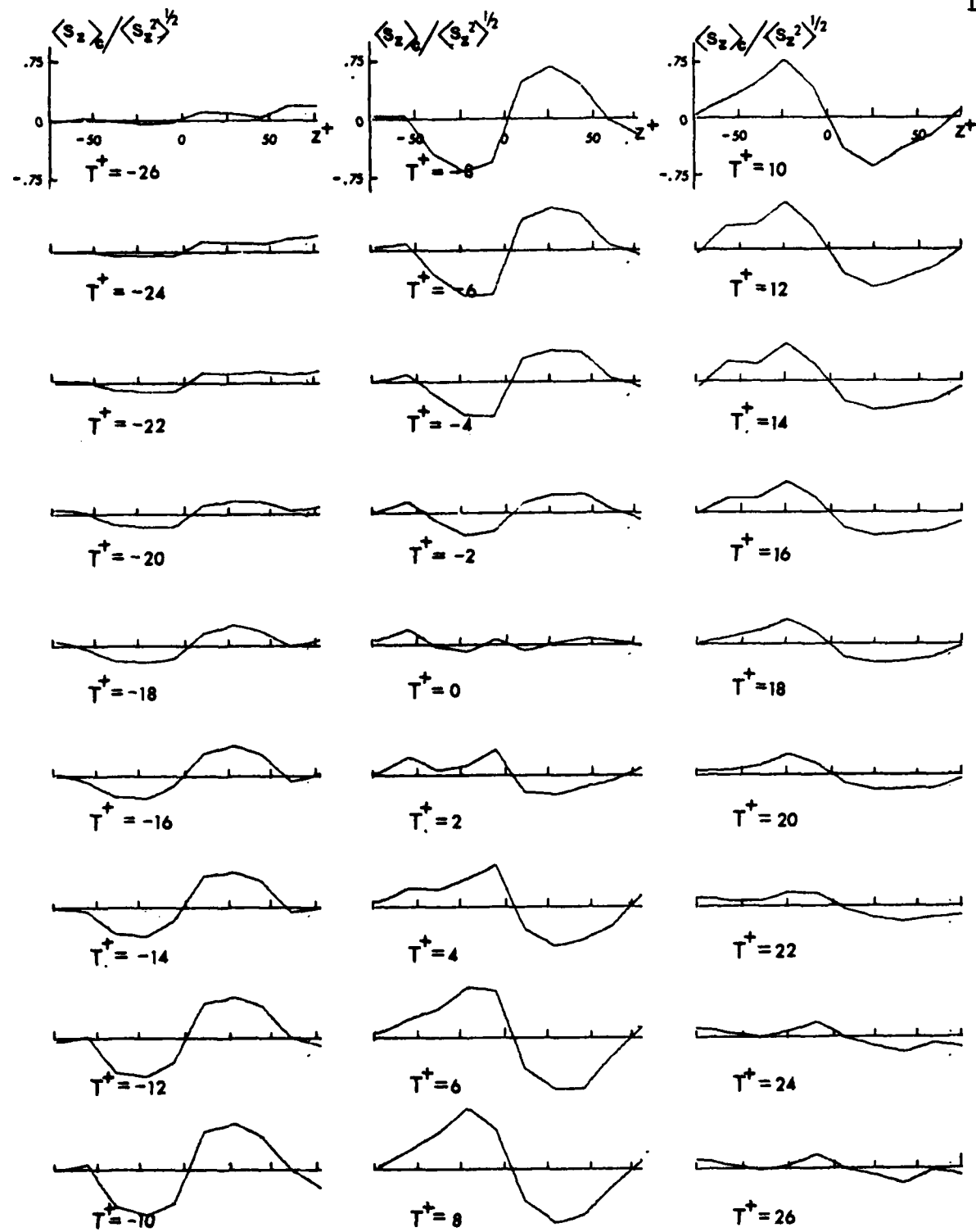


Figure 6-29. Conditionally averaged transitional inflow-outflow s_z patterns. Equation (3.4) applied to s_z gradients; $E_D^z = 66$.

$T^+=2$ reverses from an inflow to an outflow profile. The outflow profile (with negative slope) attains a maximum amplitude at $T^+=8$ after which it slowly decreases.

Associated with the inflow-outflow s_z pattern is the s_x pattern shown in Figure 6-30. An inflow profile is first evidenced at $T^+=-10$ and later at $T^+=2$ a large amplitude sine wave shaped s_x pattern with a wavelength of $\Delta z^+=100$ appears. The amplitude of this pattern is 40 percent of the axial turbulence intensity at the wall. Within a dimensionless time period of $\Delta T^+=8$ the inflow s_x pattern evolves into an outflow pattern, clearly established at $T^+=12$. The outflow pattern's amplitude grows until $T^+=20$ and then remains nearly constant until $T^+=26$.

Fluid probes were placed downstream from the wall probes at two positions, namely $\Delta x^+=60$ and $\Delta x^+=90$. Figures 6-31 and 6-32 exhibit the inflow-outflow sequence at the fluid probes. Both figures show the change from a profile with positive turbulence fluctuations to a profile with negative ones. The probes at $\Delta x^+=90$ detected a smaller excess of high momentum fluid than did the probes at $\Delta x^+=60$. In Figure 6-33 the conditionally averaged velocities (solid lines) and the mean velocities (dashed lines) are shown for the fluid probes at $\Delta x^+=90$. These plots show high momentum fluid in the viscous wall region starting at approximately $T^+=-10$. At $T^+=6$ the high momentum fluid is replaced by low momentum fluid apparent in the region close to the wall. During the rapid change of momentum small inflexions were formed in the conditionally averaged velocity profiles from $T^+=6$ to $T^+=12$. After $T^+=12$ this conditionally averaged profile returns slowly to the mean velocity profile.

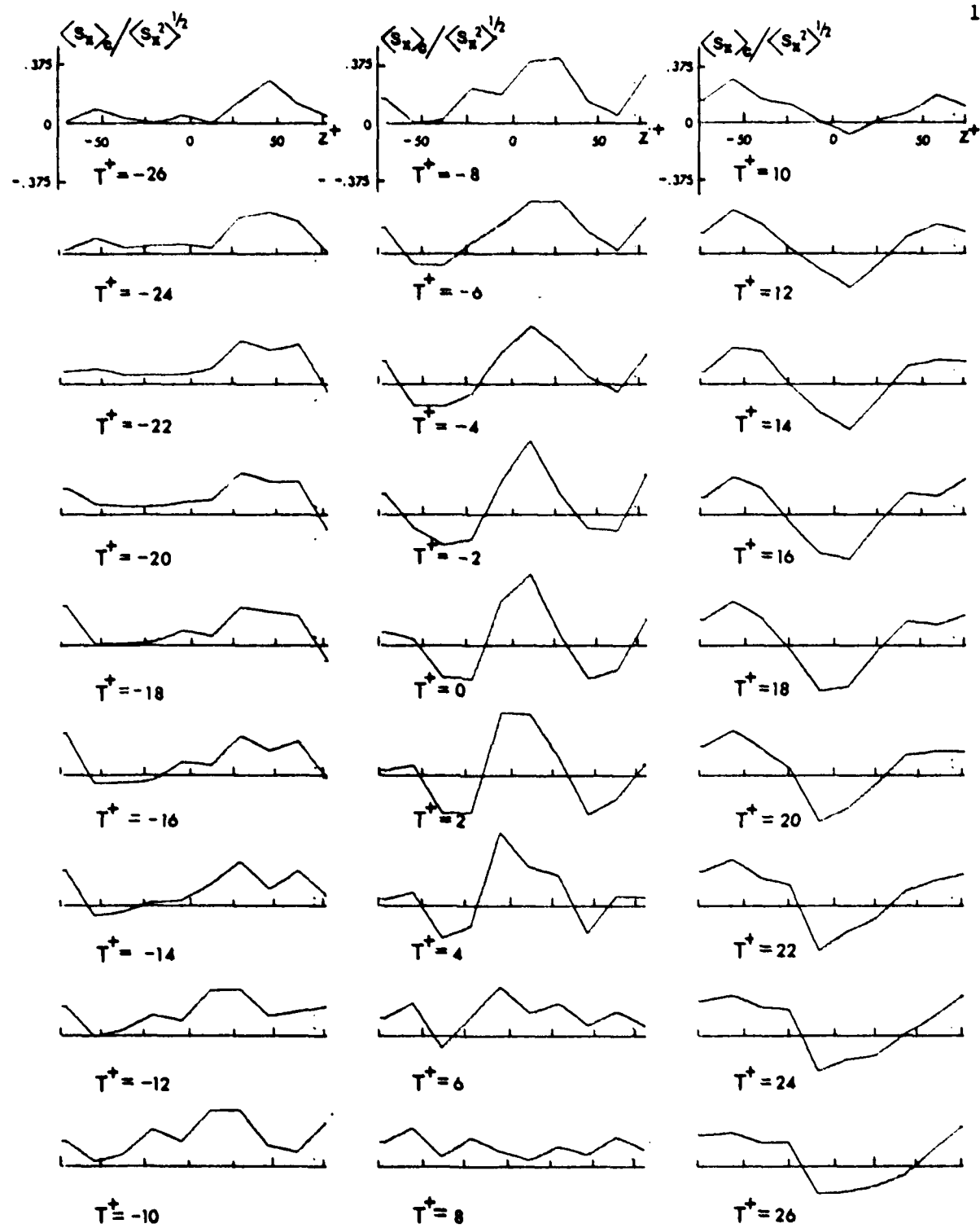


Figure 6-30. Conditionally averaged transitional inflow-outflow s_z patterns. Equation (3.4) applied to s_z gradients; $E_D^x = 66$.

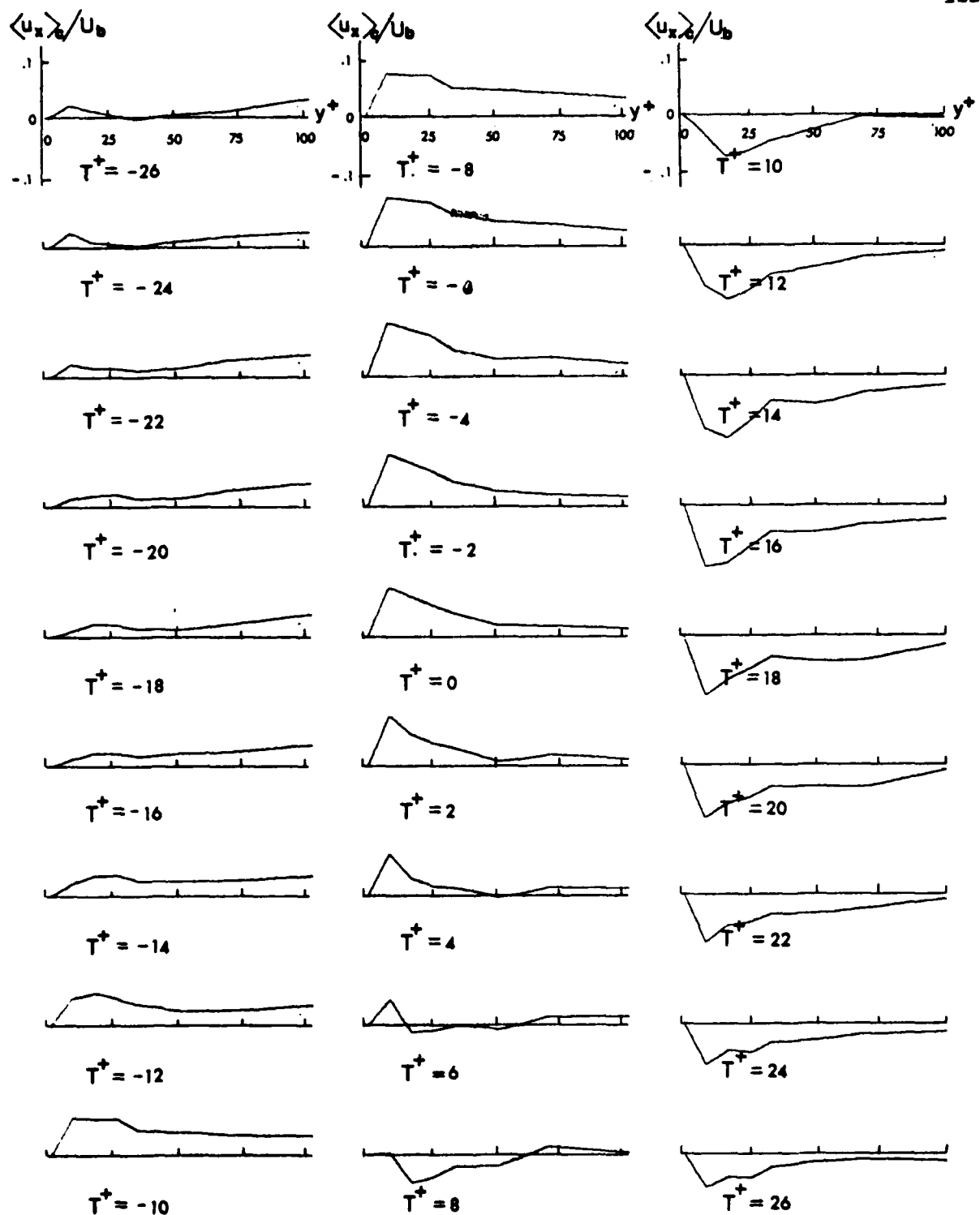


Figure 6-31. Conditionally averaged transitional inflow-outflow u_x patterns. Equation (3.4) applied to s_z gradients; $E_D = 66$; fluid probes at $\Delta x^+ = 60$.

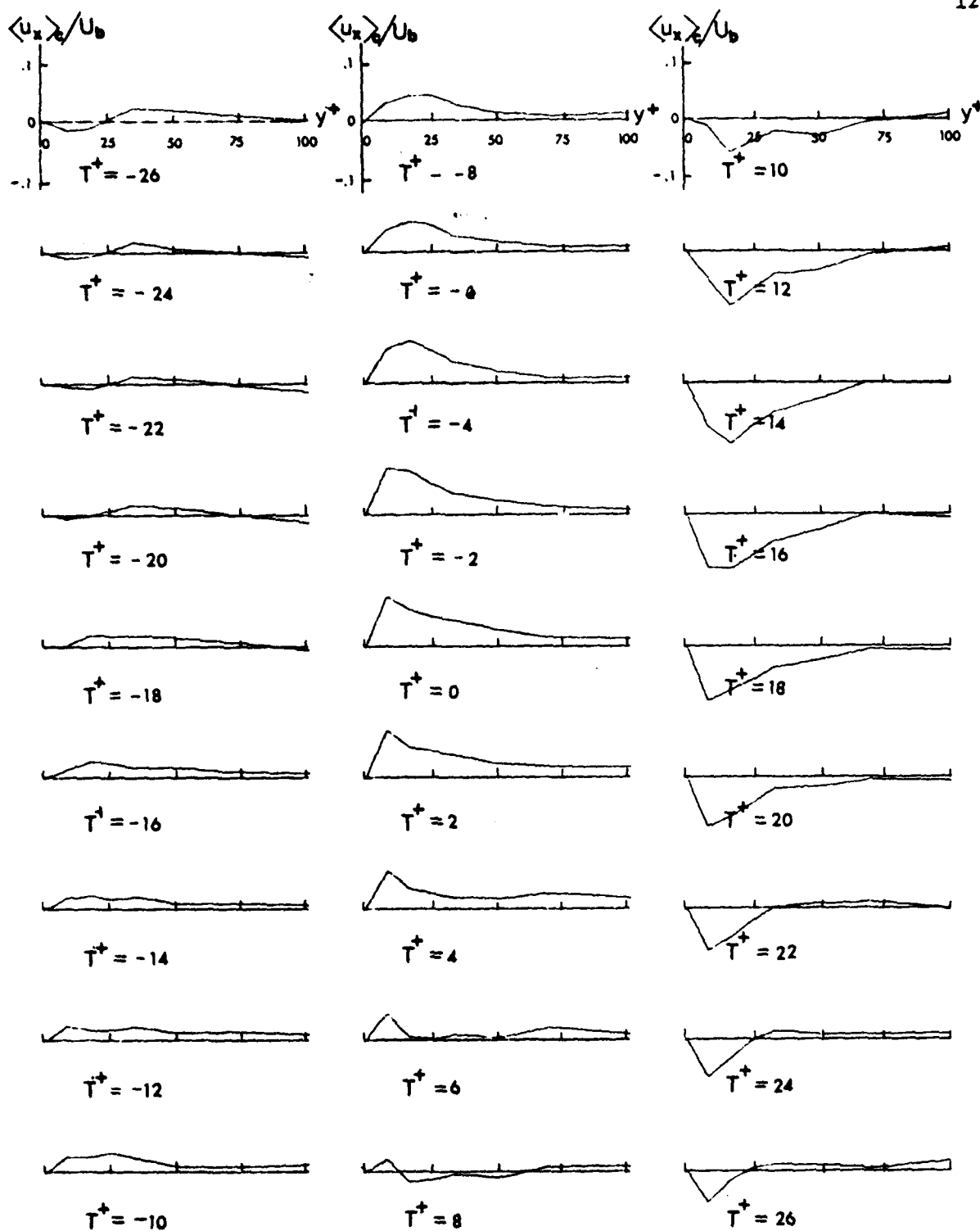


Figure 6-32. Conditionally averaged transitional inflow-outflow u_x patterns. Equation (3.4) applied to s_z gradients; $E_D = 68$; fluid probes at $\Delta x^+ = 90$.

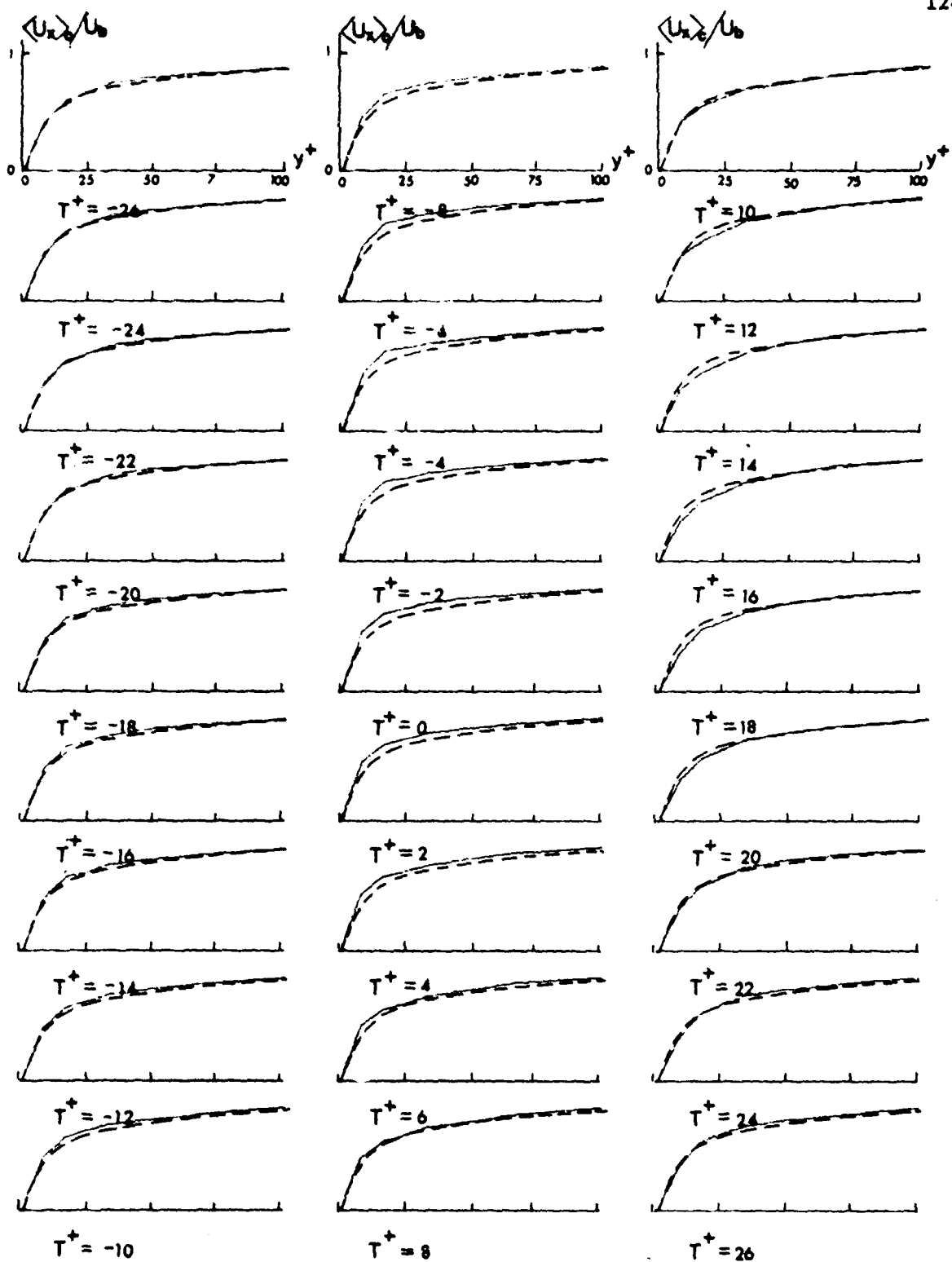


Figure 6-33. Conditionally averaged transitional inflow-outflow U_x patterns. Equation (3.4) applied to s_z gradients; $E_D = 68$; fluid probes at $\Delta x^+ = 90$; dashed line--mean velocity profile; solid line--conditionally averaged pattern.

C. Conditional Averaging Criteria Applied to the Axial Velocity

Fluctuations at the Fluid Probes

1. Detection of inflows with fluid probes at $y^+=8$ and 16.

Inflows were revealed by two fluid probes positioned in the viscous wall region ($y^+=8$ and 16) at a downstream distance from the wall probes of $\Delta x^+=90$. The velocity fluctuations at these probes were processed using equation (3.6) and 97 inflow events were selected from the data set. Conditionally averaged inflows for the fluctuating axial velocities at the event instants are shown in Figure 6-34 which illustrates a gradual inflow of high momentum fluid starting at $T^+=-26$. After the maximum inflow pattern is reached (at $T^+=0$) the high momentum fluid is replaced slowly by fluid with the mean velocity. The fluctuating axial velocity has at $y^+=8$ for $T^+=0$ a momentum excess of 25 percent of the bulk velocity. Figure 6-35 presents the conditionally averaged axial velocities for the 97 inflow events. These plots depict that around $T^+=0$ the high momentum fluid extends all the way to the wall. There the velocity profile is nearly flat resulting in a high shear stress in the viscous sublayer. For $T^+=-2$ to $T^+=4$ the velocity profiles show small inflexions in the range from $y^+=35$ to $y^+=50$.

Presented in Figures 6-36 and 6-37 are the conditionally averaged spanwise and axial velocity gradient patterns, respectively. These patterns were obtained at a distance of $\Delta x^+=90$ upstream from the fluid probes. The plots indicate that the maximum s_z pattern occurs a dimensionless time of $\Delta T^+=8$ before the maximum u_x profile is established (at $T^+=0$). At $T^+=-8$ the s_z pattern has a maximum amplitude equal to 60 percent of the spanwise turbulence intensity, but no well defined wavelength. Because the axial momentum associated with inflows have a broad and diffused nature, the fluid probes fail to

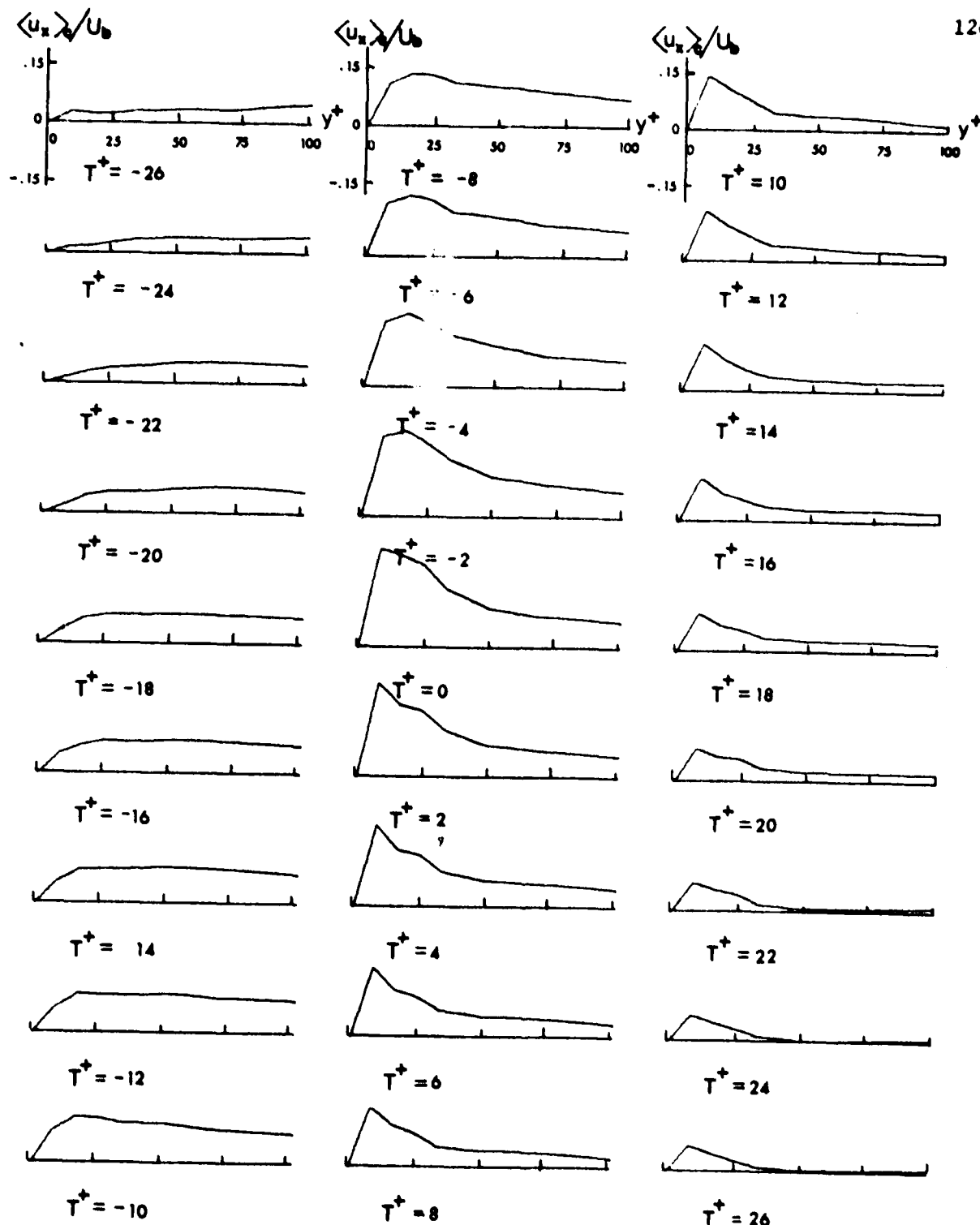


Figure 6-34. Conditionally averaged inflow u_x patterns. Equation (3.6) applied to u_x fluctuations at $y^+ = 8$ and 16 ; $E_D = 97$; fluid probes at $\Delta x^+ = 90$.

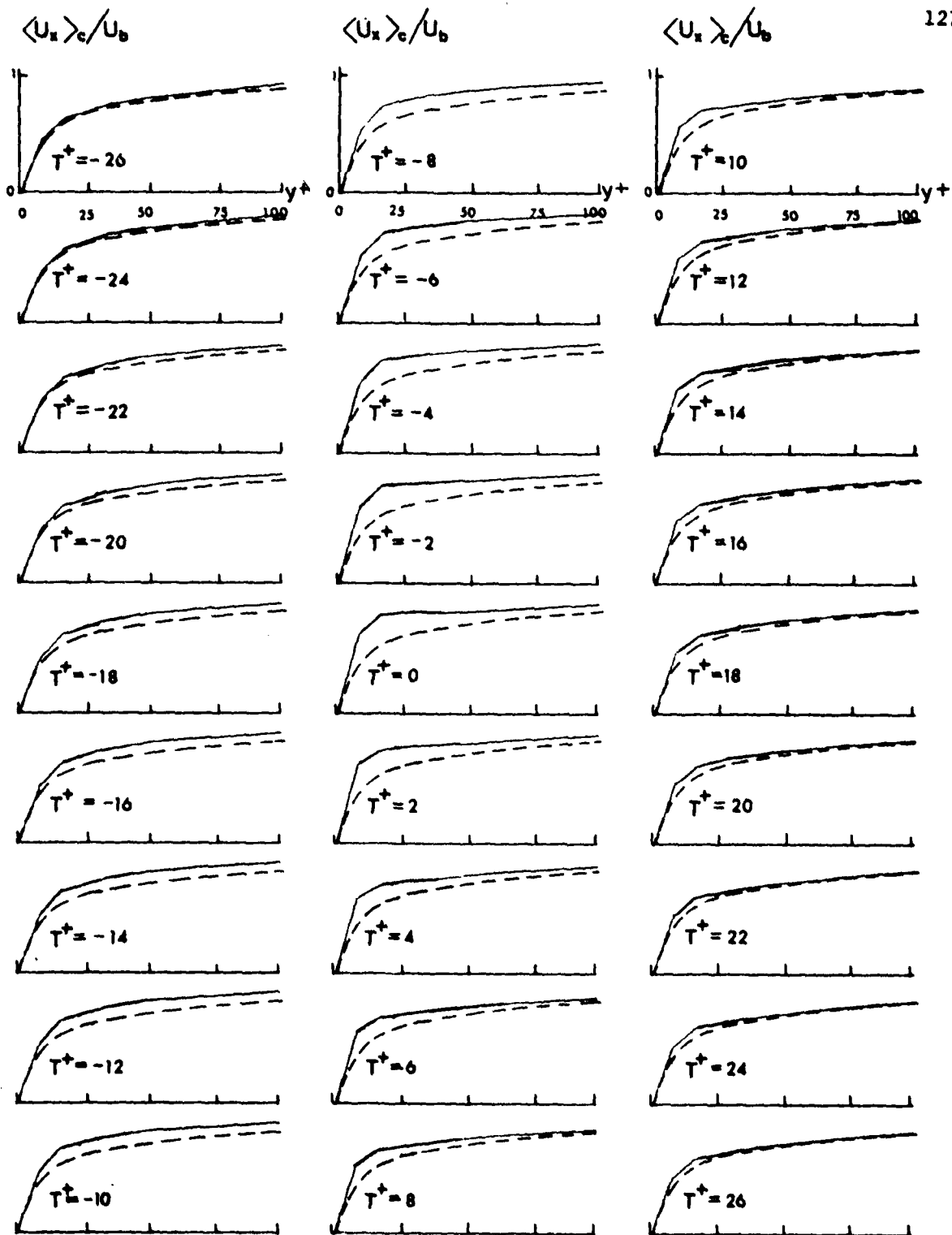


Figure 6-35. Conditionally averaged inflow U_x patterns. Equation (3.6) applied to u_x fluctuations at $y^+ = 8$ and 16; $E_D = 97$; fluid probes at $\Delta x^+ = 90$; dashed line--mean velocity profile; solid line--conditionally averaged pattern.

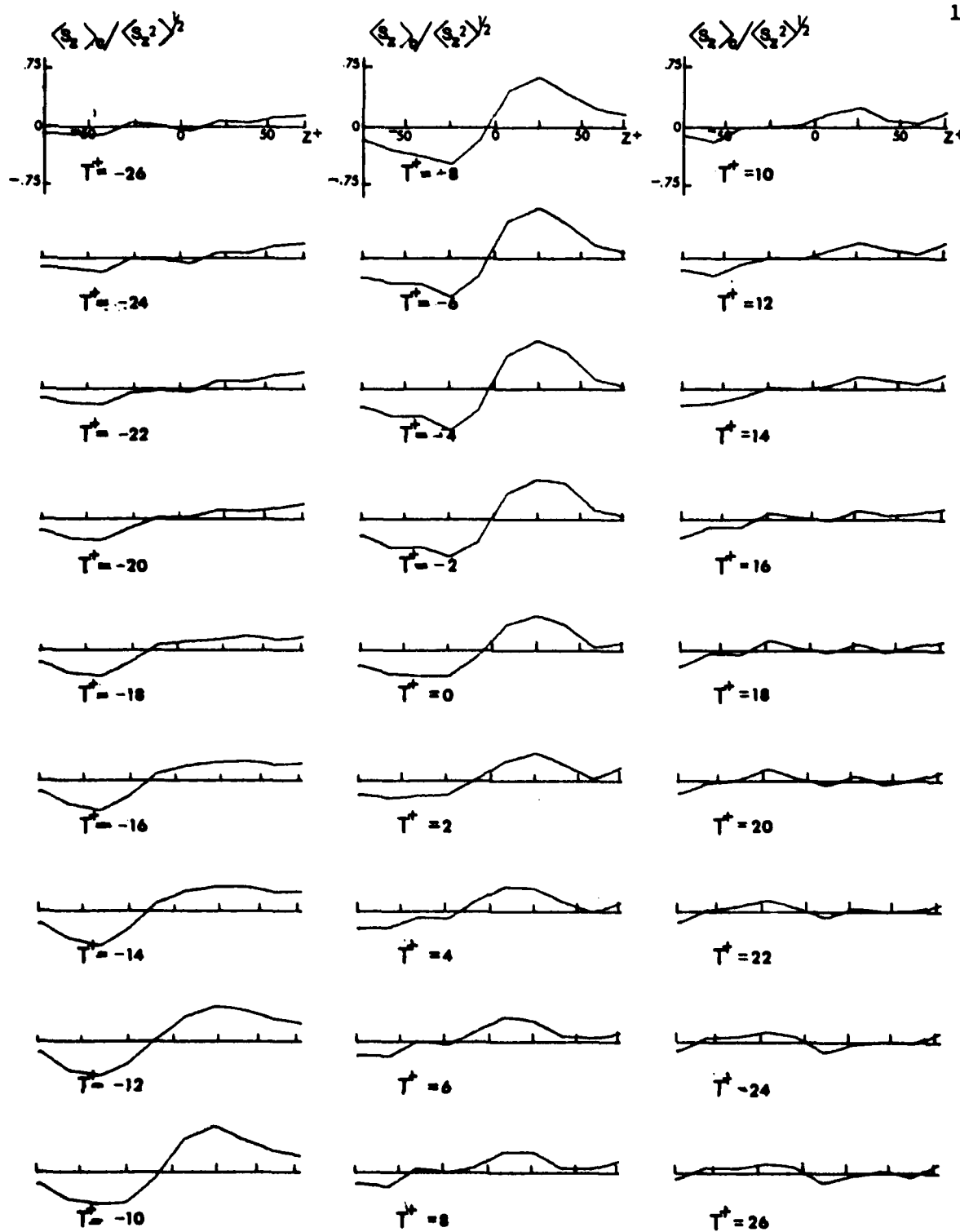


Figure 6-36. Conditionally averaged inflow s_z patterns. Equation (3.6) applied to u_x fluctuations at $y^+ = 8$ and 16; $E_D = 97$; fluid probes at $\Delta x^+ = 90$.

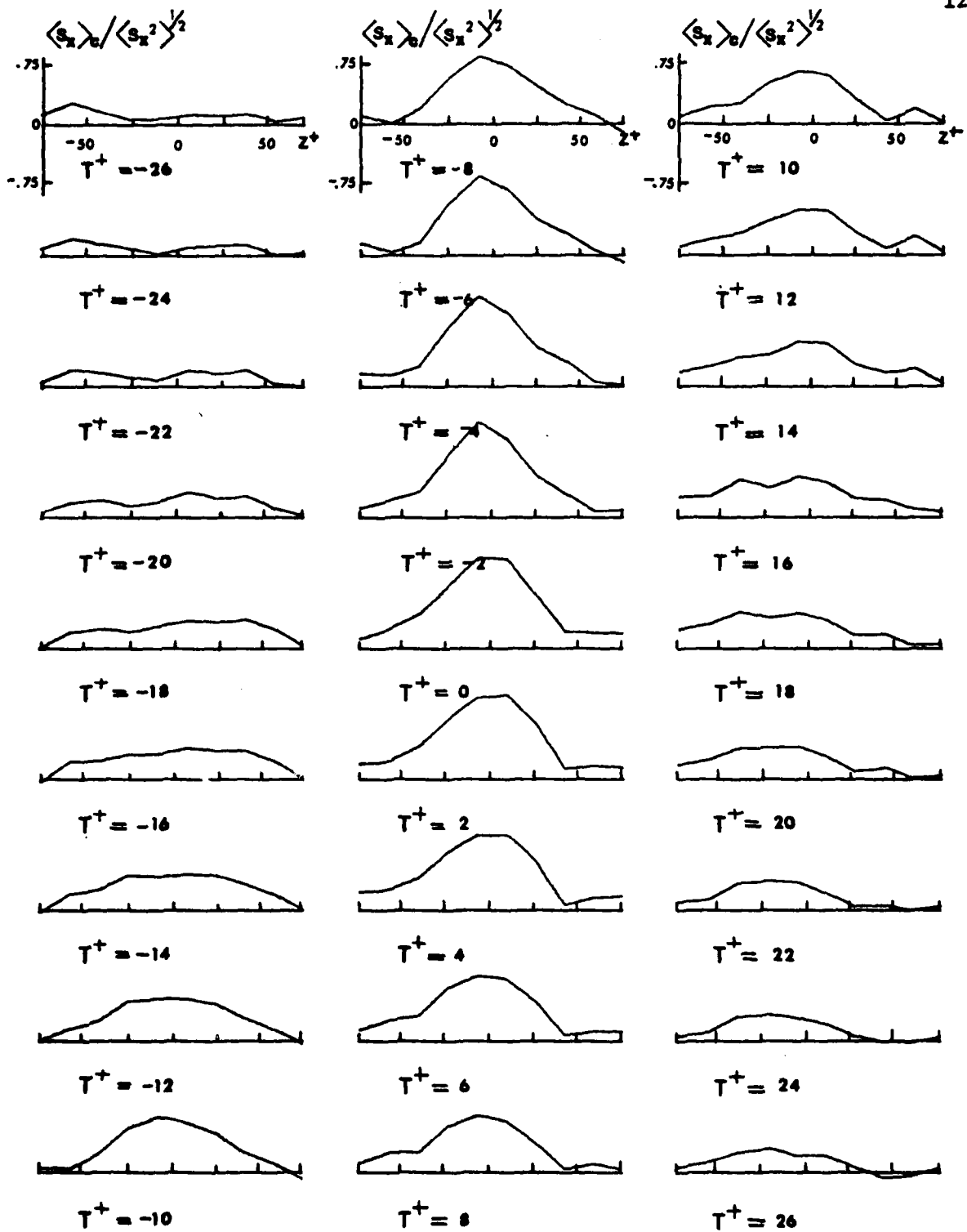


Figure 6-37. Conditionally averaged inflow s_x patterns. Equation (3.6) applied to u_x fluctuations at $y^+ = 8$ and 16; $E_D = 97$; fluid probes at $\Delta x^+ = 90$.

detect exactly the centre of the inflow event. As a consequence, sharp focussing upon a node of the s_z profile was not accomplished and so the s_z pattern's wavelength is poorly defined. The s_x patterns of Figure 6-37 also illustrate that use of the fluid probes was unsuccessful at focussing sharply upon a node. A high amplitude of 113 percent of the axial turbulence intensity was found for the s_x pattern at $T^+ = -2$ but no clear valleys appeared on the sides of the apex. Valleys failed to form because poor positioning with respect to the inflows results in wavering high momentum fluid which reduces the features of these valleys.

2. Detection of outflows with fluid probes at $y^+=8$ and 16.

Using equation (3.6) outflows were detected with two fluid probes ($y^+=8$ and 16) and strong 103 outflow events were selected. At the event instants conditionally averaged fluctuating velocity profiles were calculated which are shown in Figure 6-38. Beginning at $T^+ = -26$ low momentum fluid gradually emerged which seems to have been ejected from the wall because the largest momentum deficient contributions first appear in the viscous wall region. At $T^+ = 0$ a negative velocity fluctuation of 35 percent of the bulk velocity is present at $y^+=18$. Over time this momentum deficient fluid is gradually replaced by fluid with the mean velocity until $T^+ = 22$ when a fluctuating velocity profile with neither high nor low momentum fluid is established. Figure 6-39 presents the conditionally averaged velocities (solid lines) and the mean velocities (dashed lines). From $T^+ = -12$ to $T^+ = -4$ a large momentum deficiency develops in the viscous wall region. Several of these outflow profiles show signs of inflexions, particularly at time instants $T^+ = -12, -2, 0$ and 8.

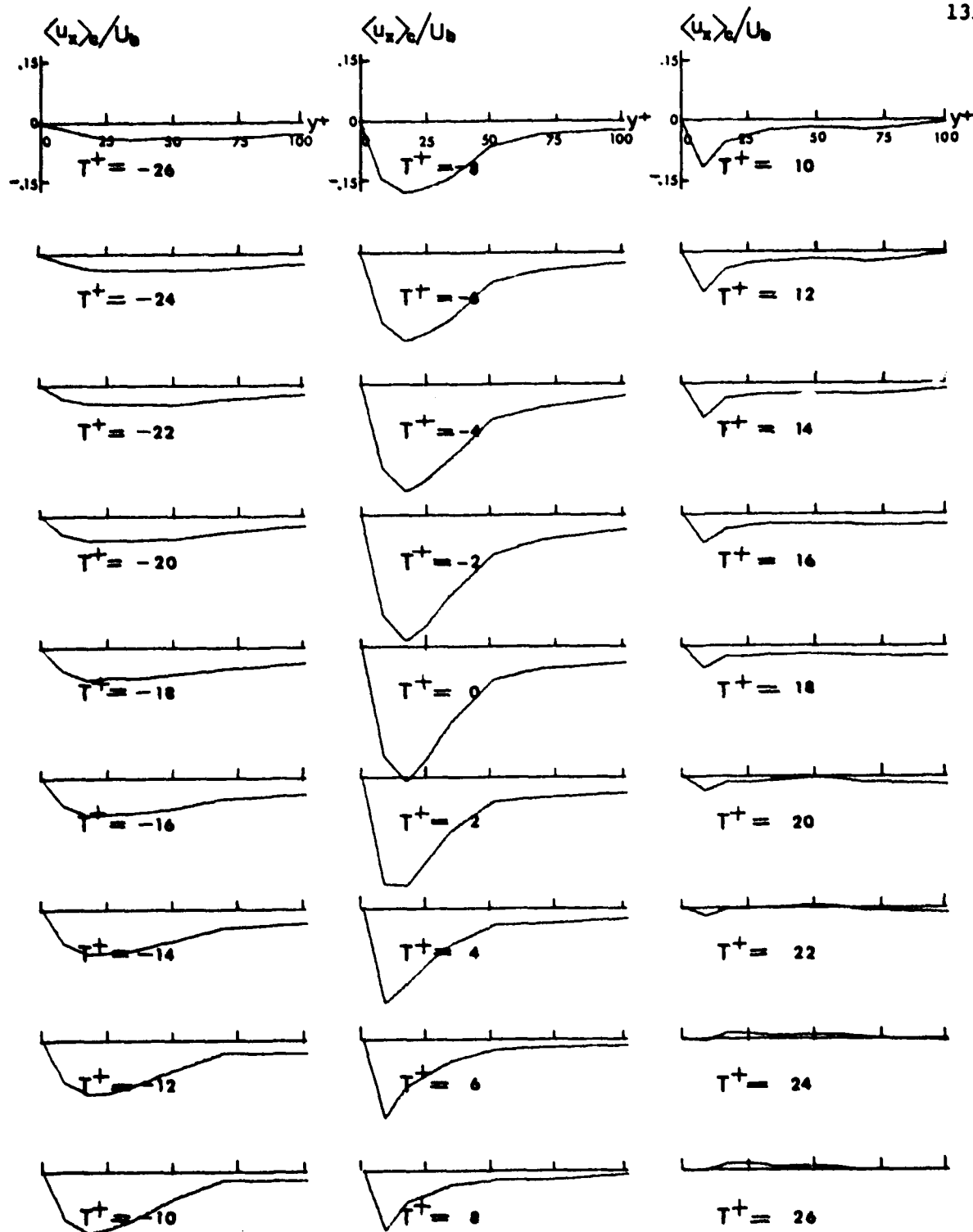


Figure 6-38. Conditionally averaged outflow u_x patterns. Equation (3.6) applied to u_x fluctuations at $y^+ = 8$ and 16 ; $E_D = 103$; fluid probes at $\Delta x^+ = 90$.

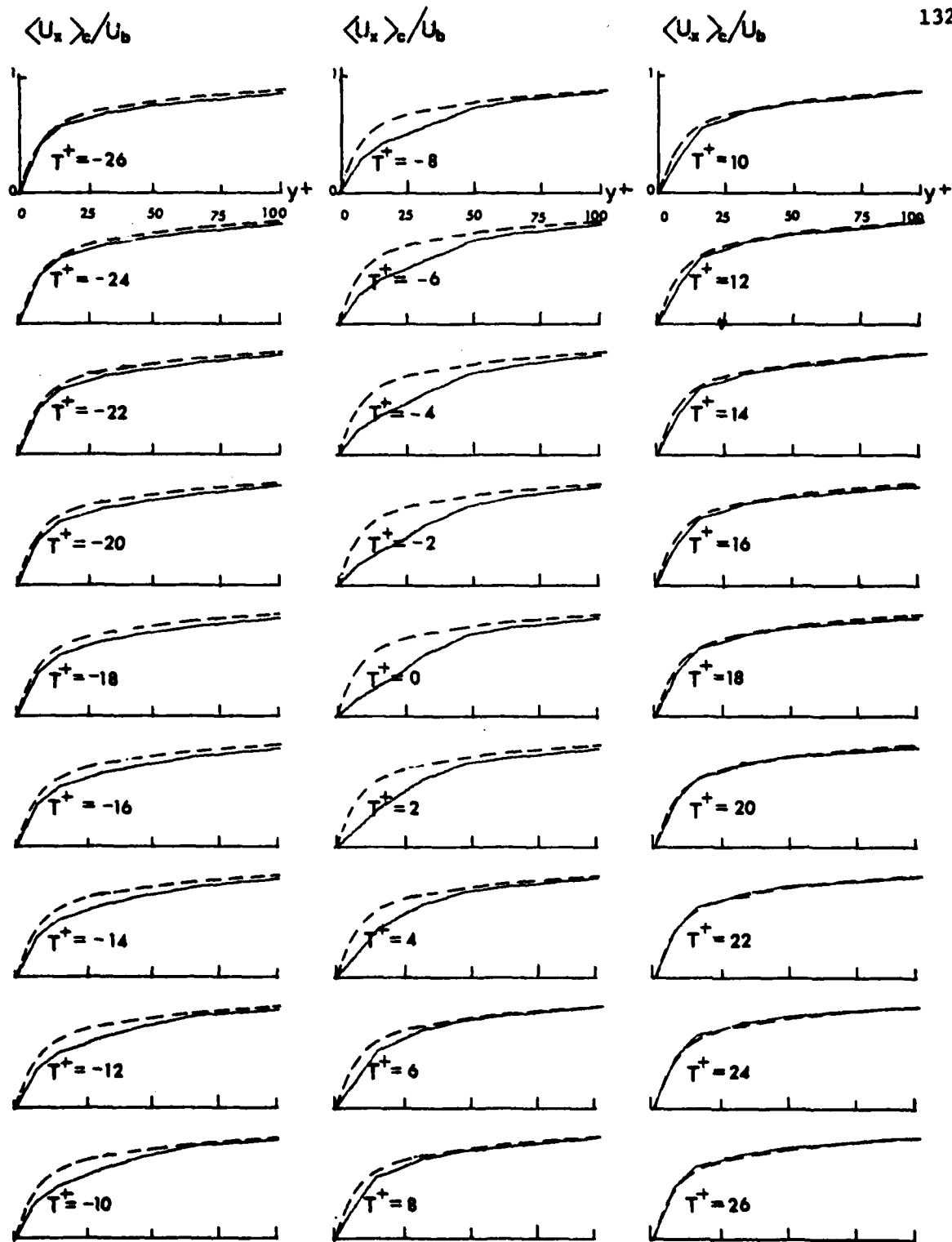


Figure 6-39. Conditionally averaged outflow U_x patterns. Equation (3.6) applied to u_x fluctuations at $y^+ = 8$ and 16 ; $E_D = 103$; fluid probes at $\Delta x^+ = 90$; dashed line--mean velocity profile; solid line--conditionally averaged pattern.

The conditionally averaged outflow s_z patterns are shown in Figure 6-40. The wall electrodes were positioned upstream from the fluid probes at a distance of $\Delta x^+ = 90$. The maximum s_z pattern exists at $T^+ = -8$ --constituting a dimensionless time of approximately $\Delta T^+ = 8$ before the maximum outflow profile was established at the fluid probes. This s_z pattern has large amplitudes equal to 75 percent of the spanwise turbulence intensity and an overall wavelength of approximately $\Delta z^+ = 125$. Apparently the axial momentum of outflows is narrower than that of inflows so detection of outflows via fluid probes is easier, resulting in more sharply defined s_z patterns. Axial outflow patterns are presented in Figure 6-41 which shows that they can be detected more easily than s_x inflows. The outflow plots presented for $T^+ = -8$ to $T^+ = 2$ illustrate the common characteristics, namely a valley in the centre and bulges on the sides of the valley. The maximum outflow profile is reached at $T^+ = -2$ --that is, a dimensionless time of $\Delta T^+ = 6$ after the maximum s_z pattern is established. This sine wave shaped s_x outflow pattern (at $T^+ = -2$) has a wavelength of $\Delta z^+ = 100$ and a large negative amplitude.

3. Rapid accelerations of fluctuating velocities in the fluid.

Velocity fluctuations in the fluid (at $y^+ = 8, 24$ and 50) were examined for rapid changes from large negative values to large positive ones. The velocity signals were studied by means of equation (3.8). The number of acceleration events selected were 106, 97 and 100 for the detection probes at $y^+ = 8, 24$ and 50 , respectively. For all cases the fluid probes were placed at a downstream distance of $\Delta x^+ = 90$ from the wall probes. Conditionally averaged fluctuating axial velocity profiles, calculated for the three sets of events are presented in Figures 6-42, 6-43 and 6-44. All three figures show negative momentum at the fluid

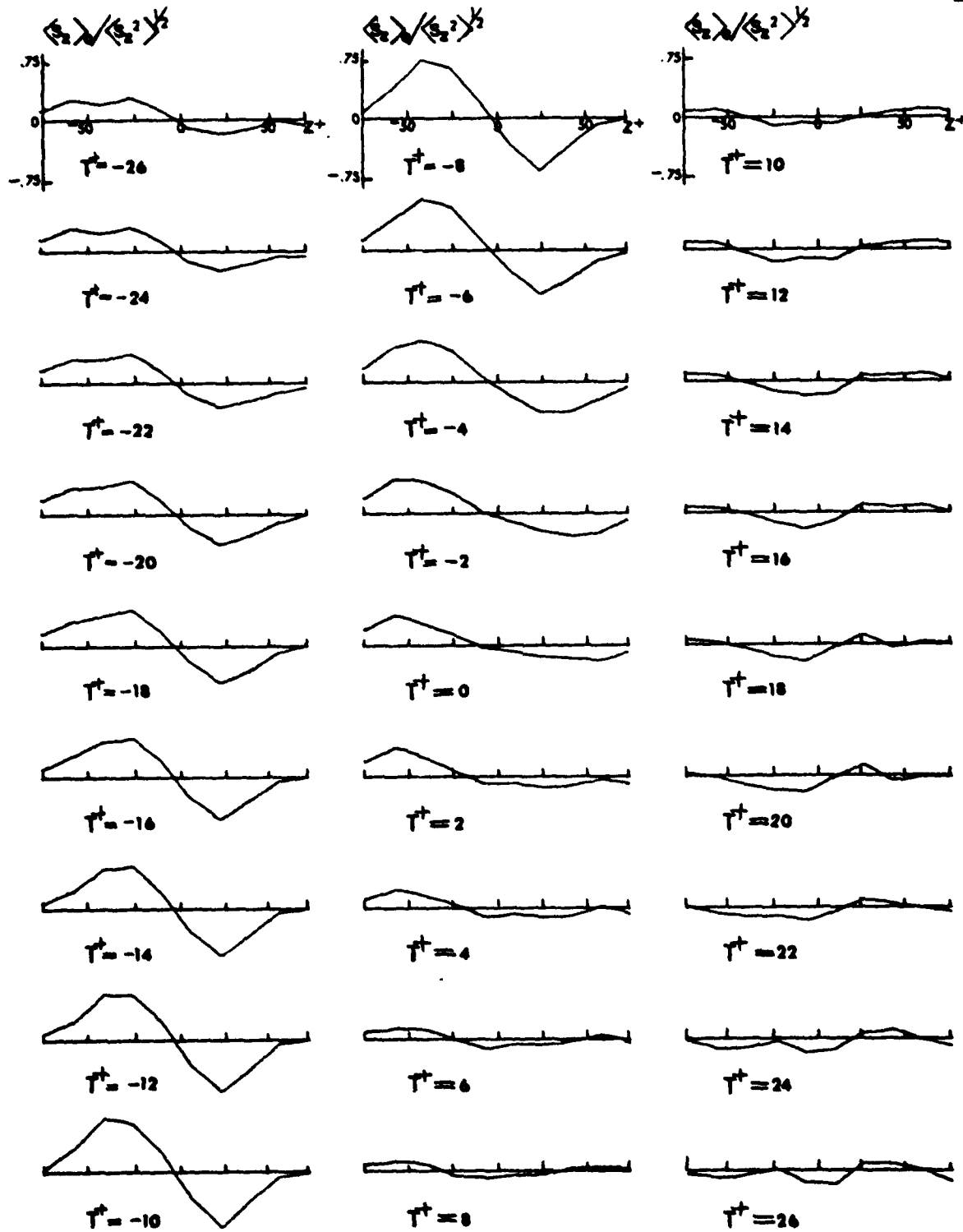


Figure 6-40. Conditionally averaged outflow s_z patterns. Equation (3.6) applied to u_x fluctuations at $y^+ = 8$ and 16; $E_D = 103$; fluid probes at $\Delta x^+ = 90$.

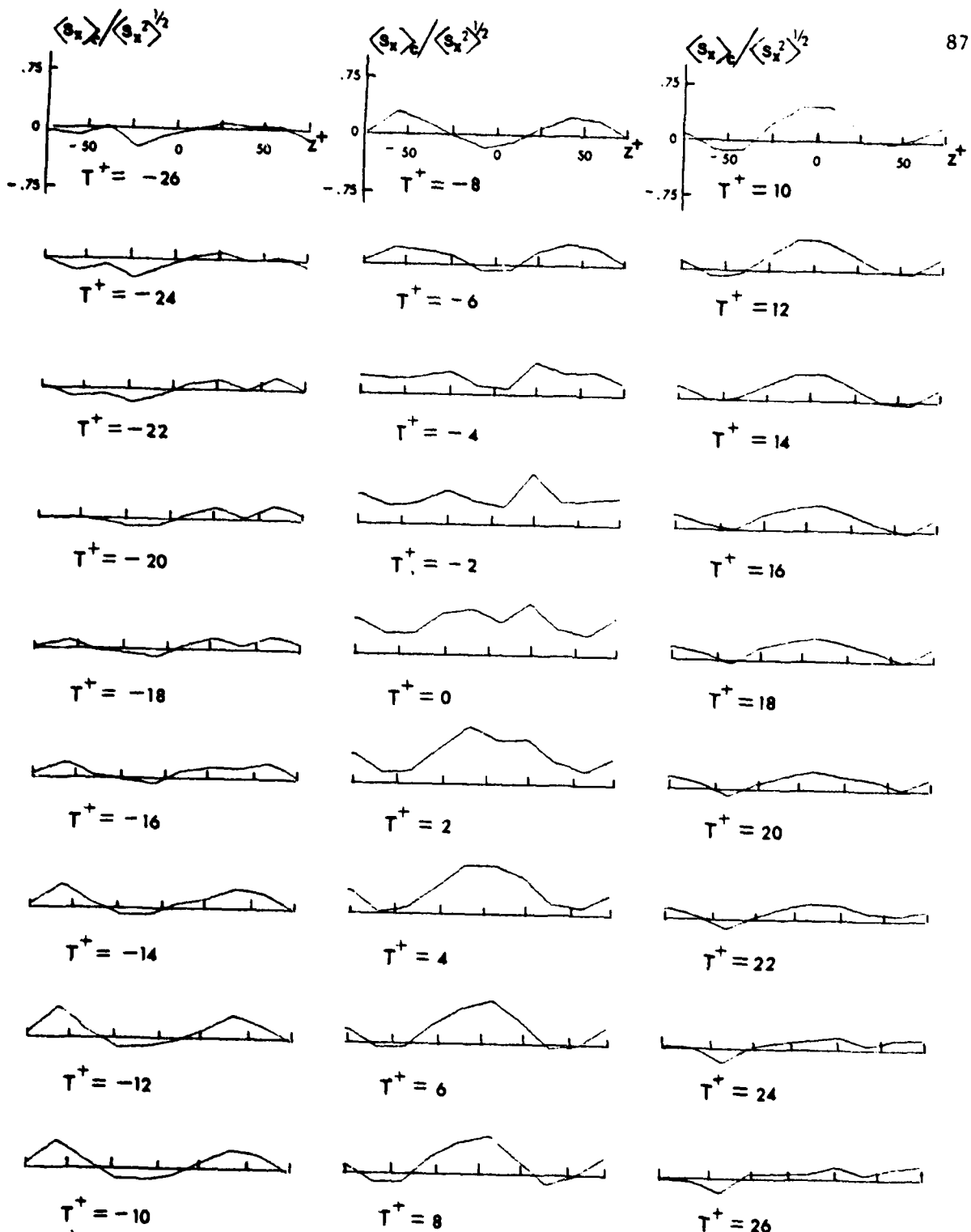


Figure 6-6. Conditionally averaged inflow s_x patterns. Equation (3.2) where $N = 5$ applied to s_z gradients; $E_D = 95$.

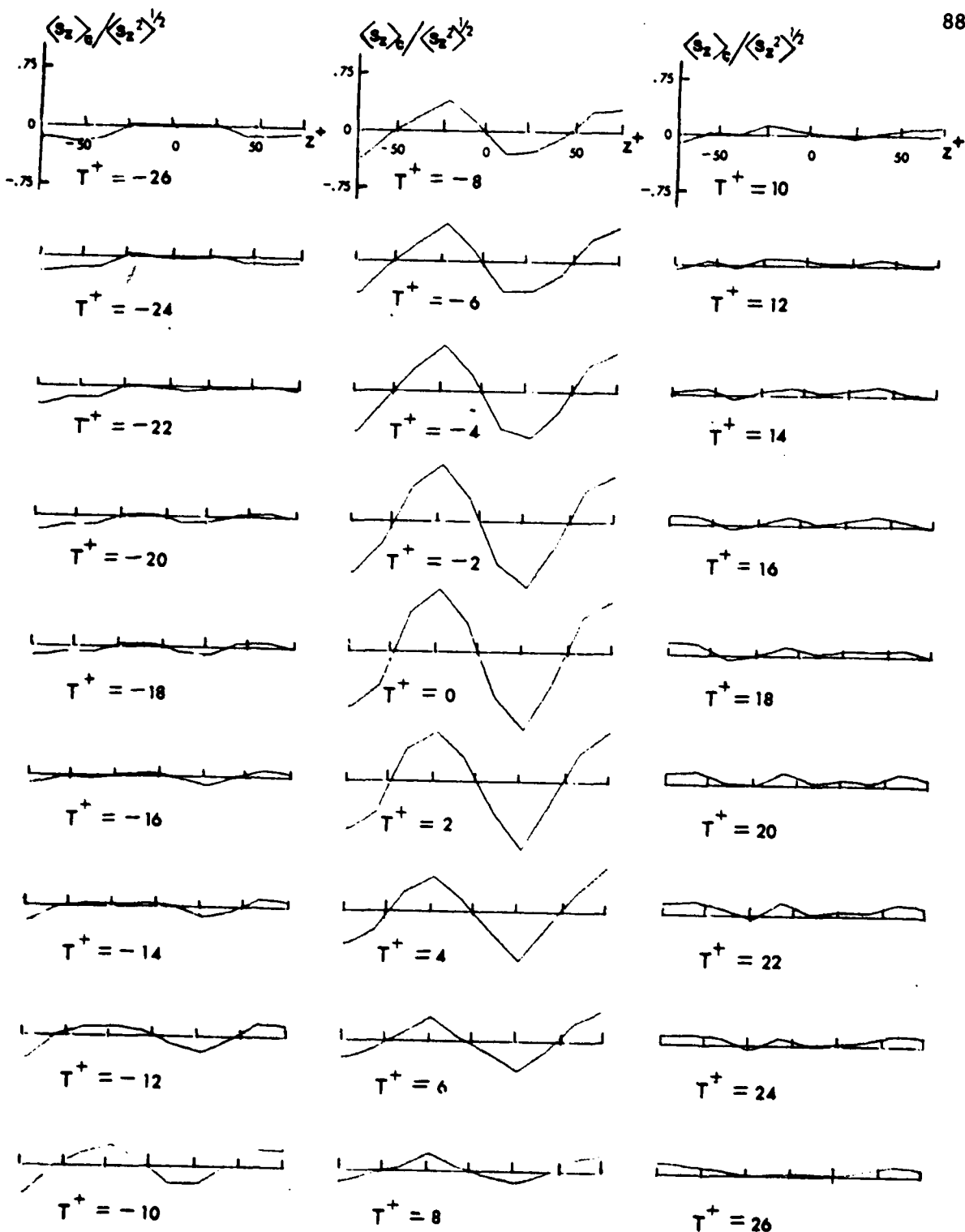


Figure 6-7. Conditionally averaged outflow s_z patterns. Equation (3.2) where $N = 5$ applied to s_z gradients; $E_D = 96$.

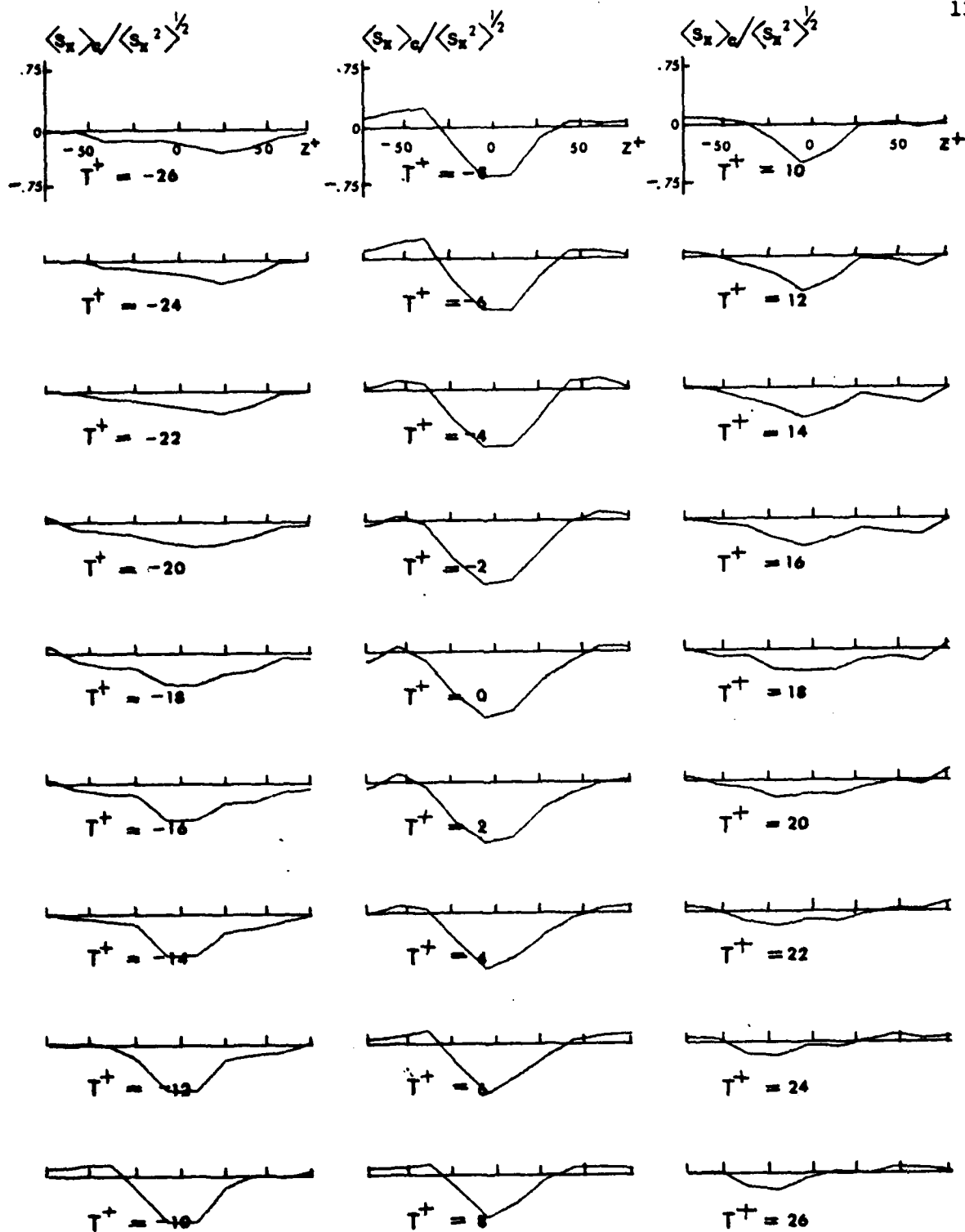


Figure 6-41. Conditionally averaged outflow s_x patterns. Equation (3.6) applied to u_x fluctuations at $y^+ = 8$ and 16; $E_D = 103$; fluid probes at $\Delta x^+ = 90$.

probes at $T^+ = -26$. This negative momentum increases in amplitude and extent until approximately $T^+ = -4$. Later, around $T^+ = 0$ the axial fluctuating velocities are accelerated. Figure 6-42 illustrates that low momentum fluid is confined to an area close to the wall while Figure 6-44 exhibits a concentration of low momentum fluid near $y^+ = 50$. It is suggested that the momentum deficient fluid of Figure 6-42 is ejected from the wall. The momentum deficient fluid present in Figure 6-44 does not originate from the wall; rather it is convected from an upstream position. Figure 6-43 constitutes a combination of both, ejected low momentum fluid from the wall and convected momentum deficient fluid from upstream. The latter type induces large negative amplitudes in the velocity fluctuations between $T^+ = -8$ and $T^+ = -2$ at distances from the wall of say $y^+ > 30$ (see Figures 6-43 and 6-44). Negative velocity fluctuations of approximately 18 percent of the bulk velocity are present at $T^+ = -4$ (Figures 6-42, 6-43 and 6-44). It is clear that from $T^+ = -4$ to $T^+ = 4$ high momentum fluid flows towards the wall from a dimensionless distance of $y^+ > 100$ because this high momentum fluid is first apparent in the axial fluctuating velocity profile for distances of $y^+ > 50$. This fluid pushes the low momentum fluid towards the wall and as a consequence a high shear layer develops in the viscous wall region between these two fluid streams of opposite axial momentum. In fact, the high momentum fluid constitutes an inflow as discussed in Sections B-1, B-3 and C-1. The figures also show that the larger the extent of the low momentum fluid in the wall region the longer is the time period before replacement of this fluid by high momentum fluid is complete. After $T^+ = 0$ fluid with a momentum excess dominates the wall region. At $T^+ = 4$ positive velocity fluctuations equal to 15 percent of the bulk velocity, occur while after this instant

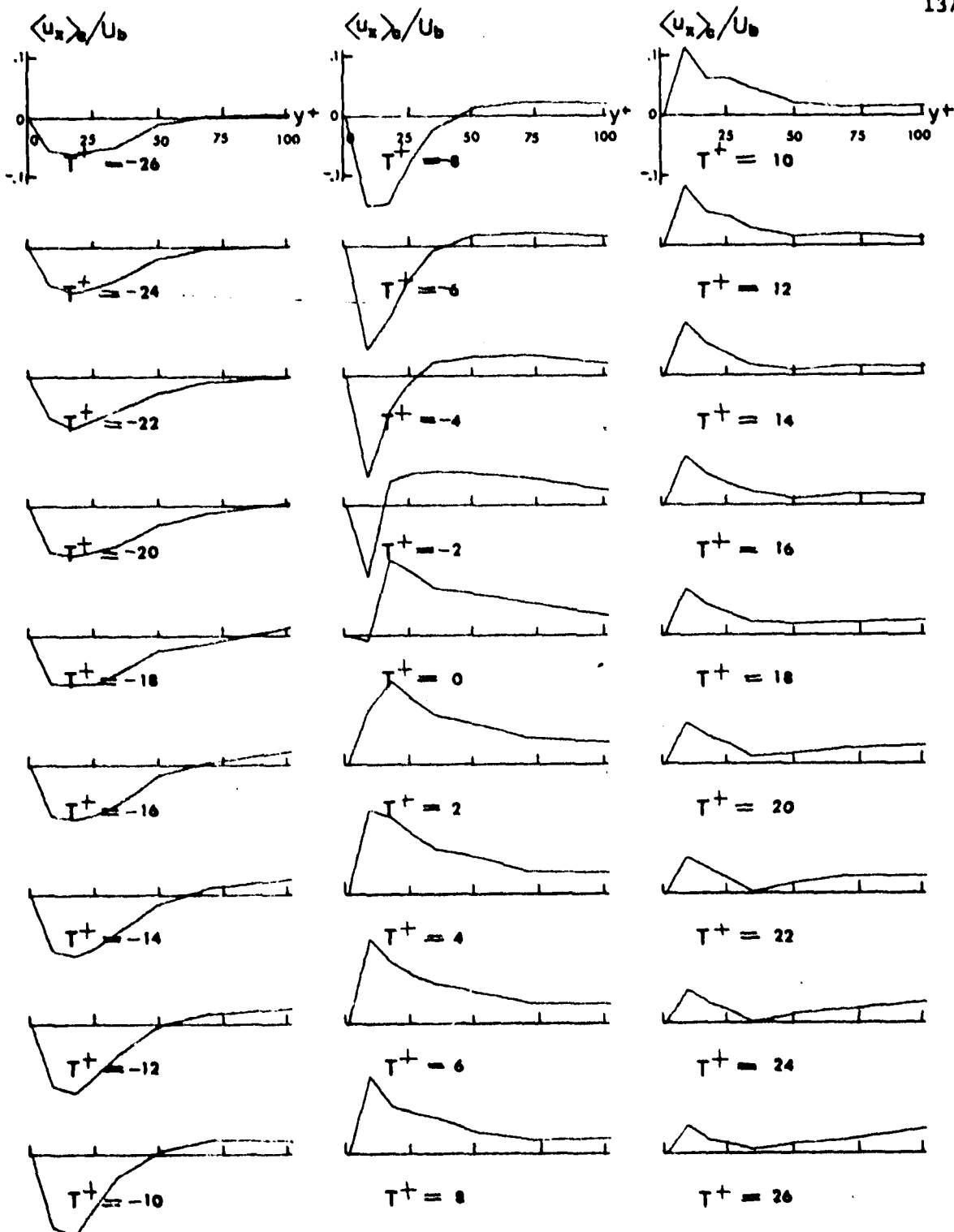


Figure 6-42. Conditionally averaged acceleration u_x patterns. Equation (3.8) applied to u_x fluctuations at $y^+ = 8$; $E_D = 106$; fluid probes at $\Delta x^+ = 90$.

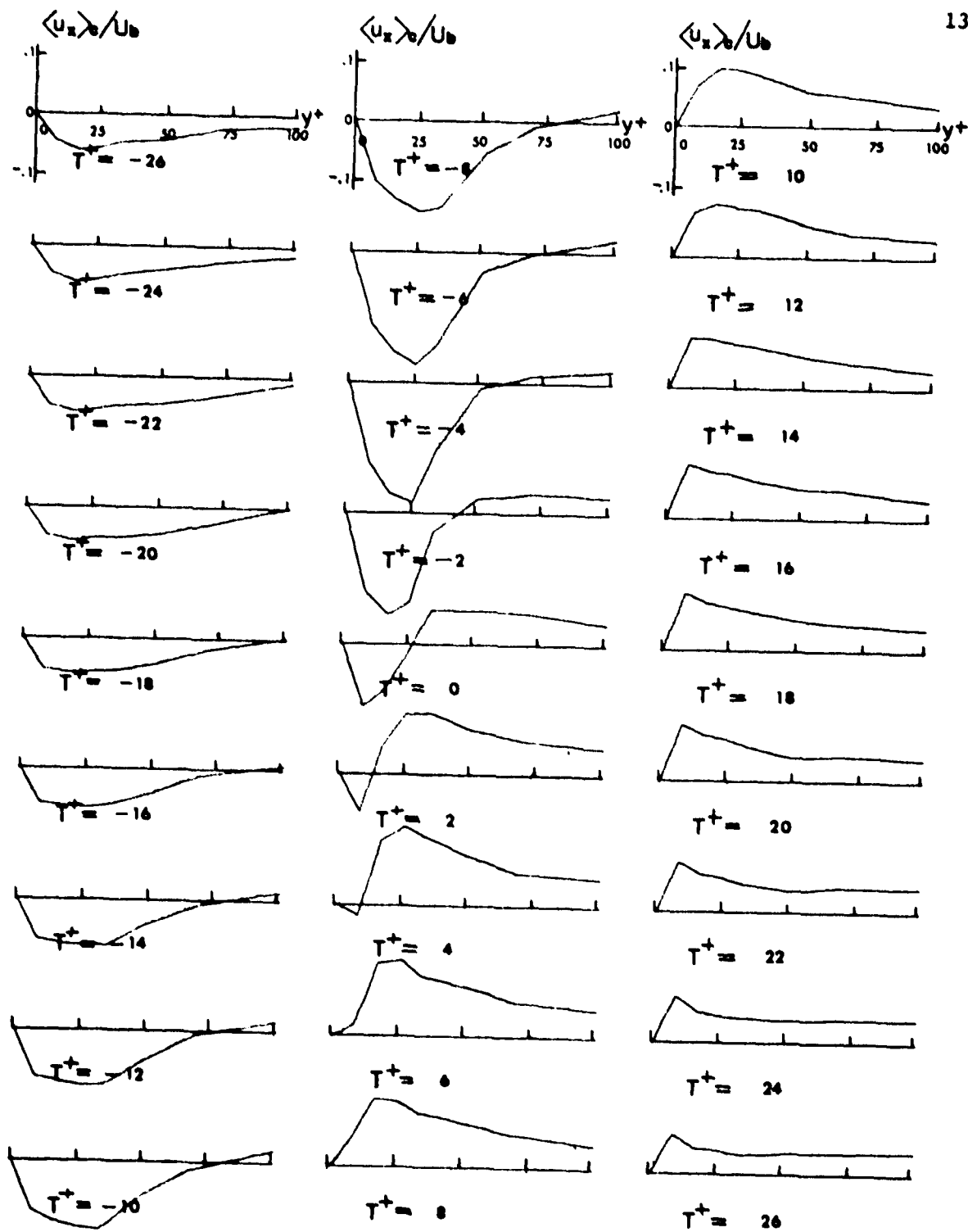


Figure 6-43. Conditionally averaged acceleration u_x patterns. Equation (3.8) applied to u_x fluctuations at $y^+ = 24$; $E_D = 97$; fluid probes at $\Delta x^+ = 90$.

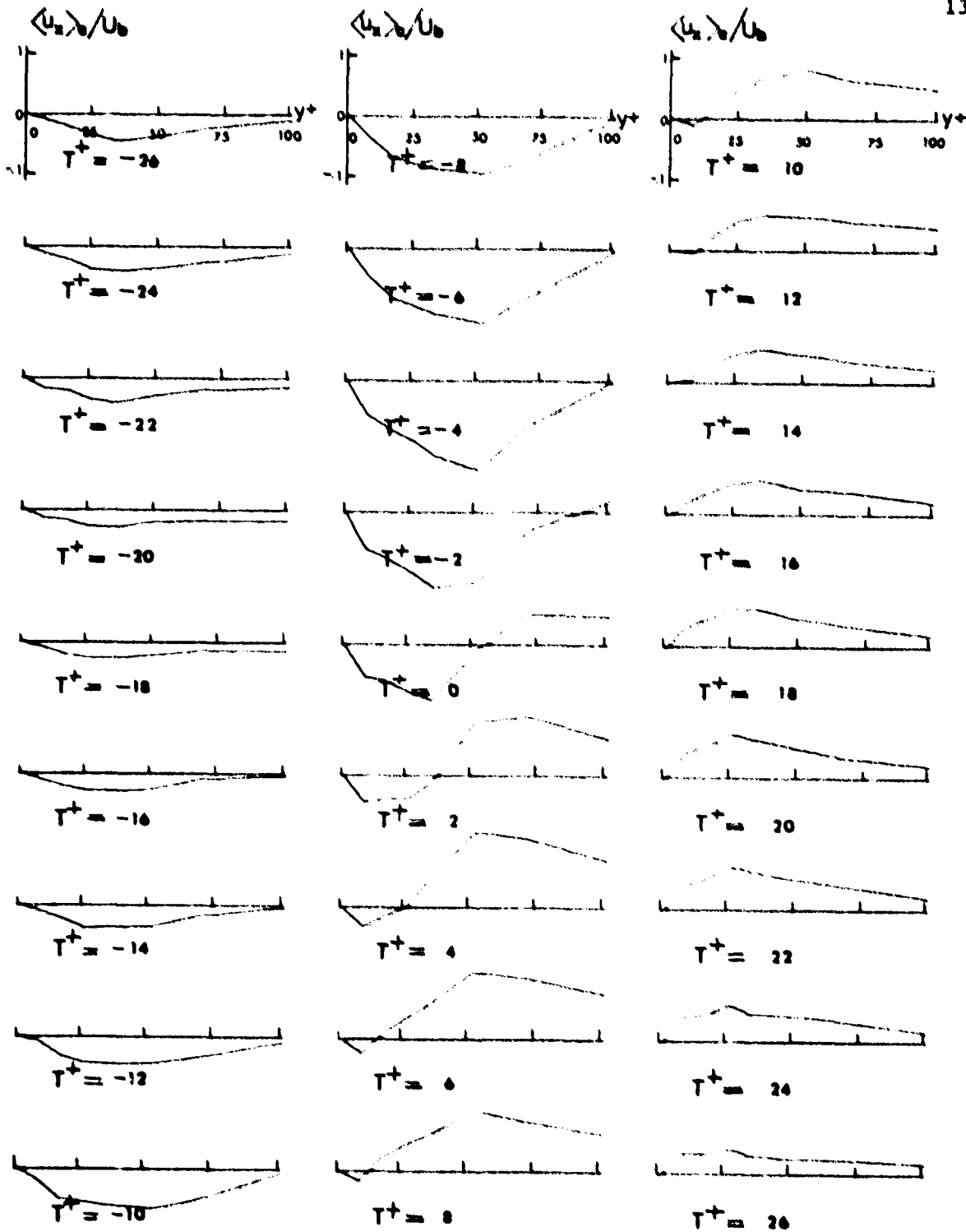


Figure 6-44. Conditionally averaged acceleration u_x patterns. Equation (3.8) applied to u_x fluctuations at $y^+ = 50$; $E_D = 100$; fluid probes at $\Delta x^+ = 90$.

the high momentum fluid decreases gradually. It is to be noted that the average velocity profile is still not attained at $T^+ = 26$.

Conditionally averaged velocity profiles for the detection probe positions of $y^+=8, 24$ and 50 are shown in Figures 6-45, 6-46 and 6-47.

The solid lines in these figures denote the conditionally averaged velocities and the dashed lines the mean velocities. In all the plots the wall regions contain low momentum fluid at $T^+=0$ but for different y^+ positions. By placing the detection probes at $y^+=8, 24$ and 50 , low momentum fluid was found to be present in the area around $y^+=50, 70$ and 100 , respectively. At approximately $T^+=-4$ high momentum fluid moves speedily wallward and the low momentum fluid is then trapped between this high speed front and the wall. During the inflow of high momentum fluid, inflexions are formed in the conditionally averaged velocity profiles. Figure 6-46 shows especially large inflexions from $T^+=-10$ to $T^+=0$ at a y^+ position of approximately 30 . In the case of Figure 6-47, where the detection probe was placed at $y^+=50$, inflexions appear near $y^+=50$. For times later than $T^+=0$ no inflexions are formed and the high momentum fluid extends all the way to the wall. Over time this high momentum fluid gradually is replaced by fluid with the mean velocity.

Conditionally averaged spanwise velocity gradient patterns were calculated at the instants of large velocity accelerations for the probe at $y^+=24$ and are shown in Figure 6-48. The slope of the s_z pattern at $T^+=-26$ is negative and so an outflow takes place which is consistent with the outflow profiles of Figure 6-43. Over time the s_z outflow pattern increases in amplitude and its form becomes sine wave shaped. At $T^+=-10$ the maximum s_z pattern is reached and within a time period of

$\langle U_x \rangle_c / U_b$ $\langle U_x \rangle_c / U_b$ $\langle U_x \rangle_c / U_b$

141

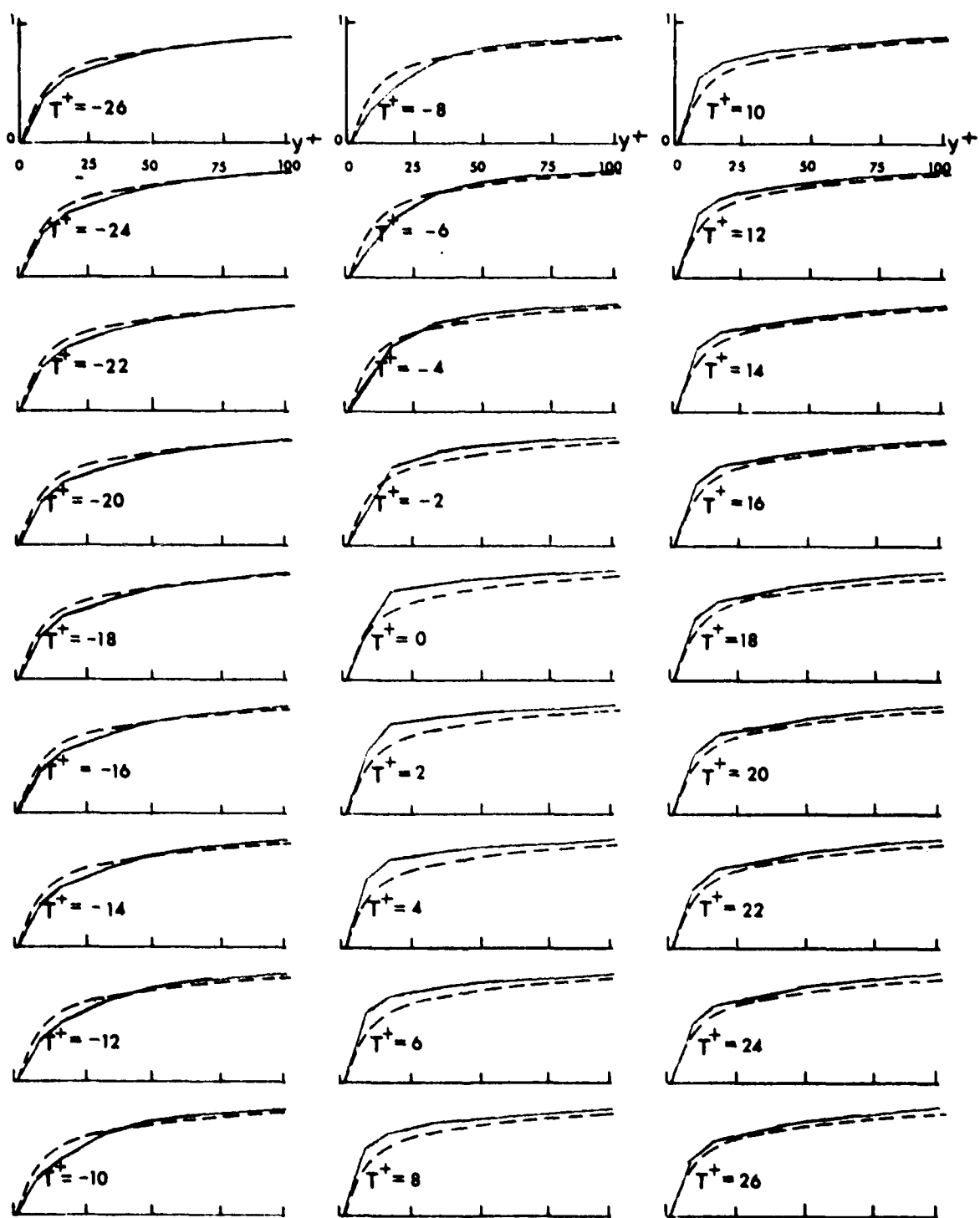


Figure 6-45. Conditionally averaged acceleration U_x patterns. Equation (3.8) applied to u_x fluctuations at $y^+ = 8$; $E_D = 106$; fluid probes at $\Delta x^+ = 90$; dashed line--mean velocity profile; solid line--conditionally averaged pattern.

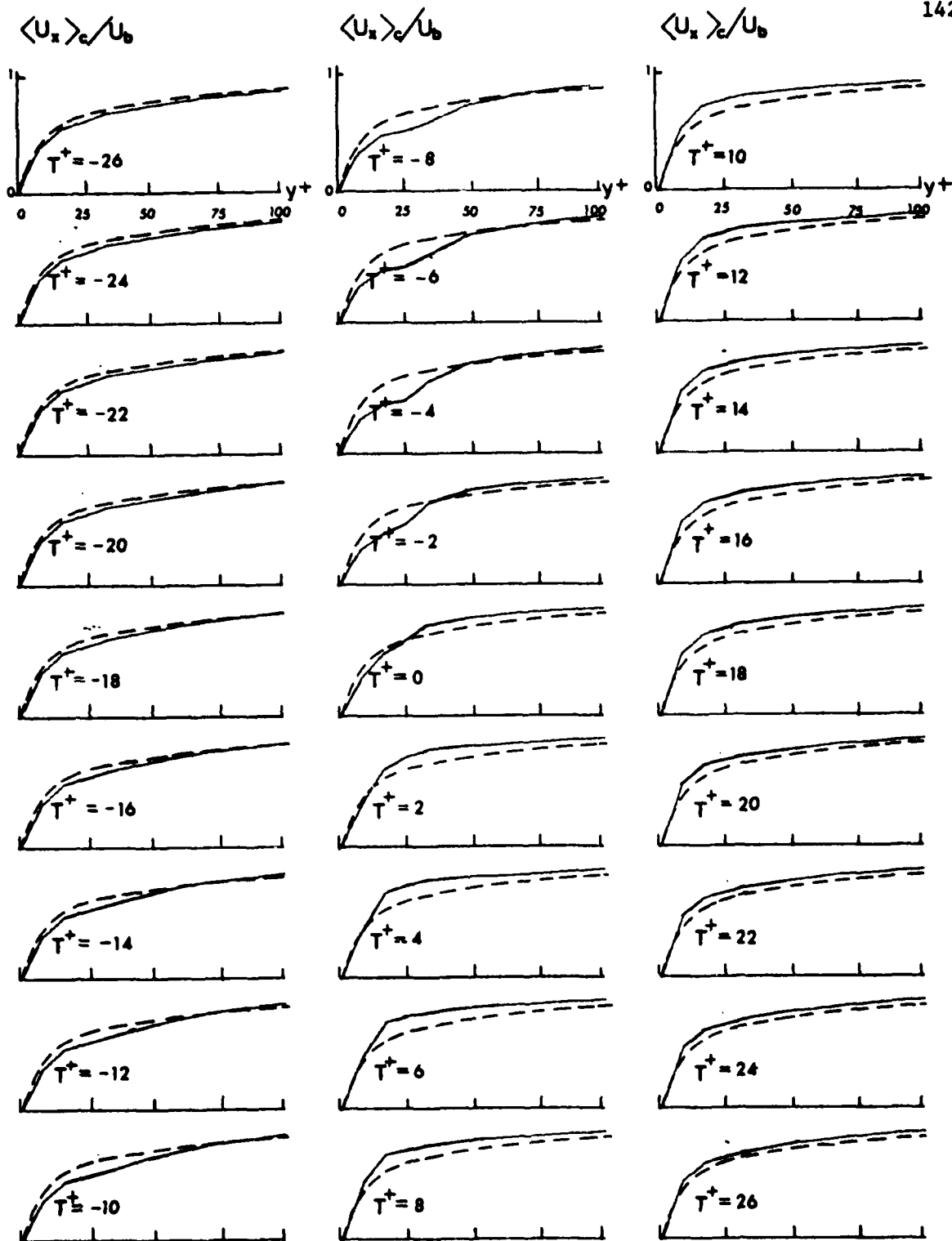


Figure 6-46. Conditionally averaged acceleration U_x patterns. Equation (3.8) applied to u_x fluctuations at $y^+ = 24$; $E_D = 97$; fluid probes at $\Delta x^+ = 90$; dashed line--mean velocity profile; solid line--conditionally averaged pattern.

$\langle U_x \rangle_c / U_b$ $\langle U_x \rangle_c / U_b$ $\langle U_x \rangle_c / U_b$

143

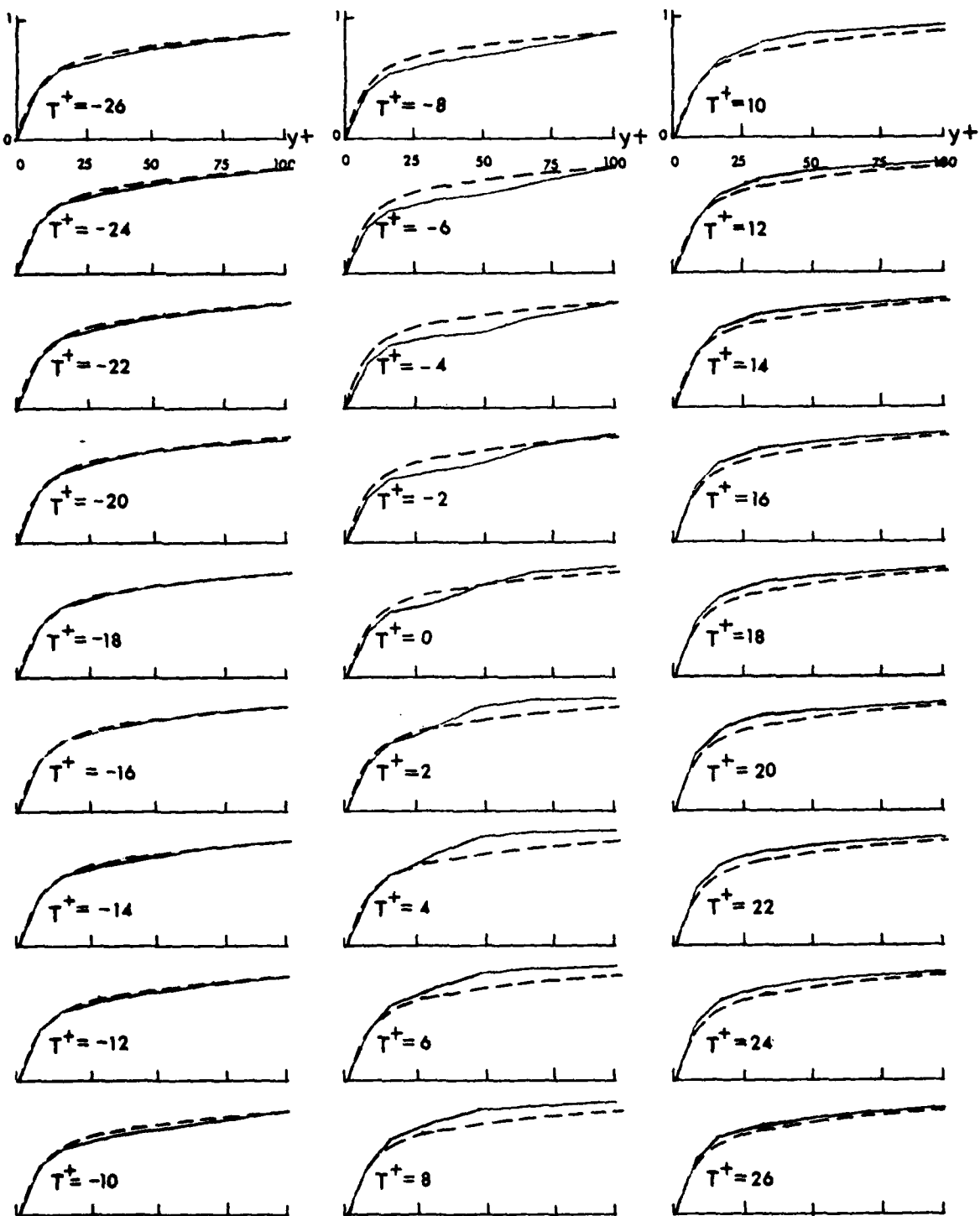


Figure 6-47. Conditionally averaged acceleration U_x patterns. Equation (3.8) applied to u_x fluctuations at $y^+ = 50$; $E_D = 100$; fluid probes at $\Delta x^+ = 90$; dashed line--mean velocity profile; solid line--conditionally averaged pattern.

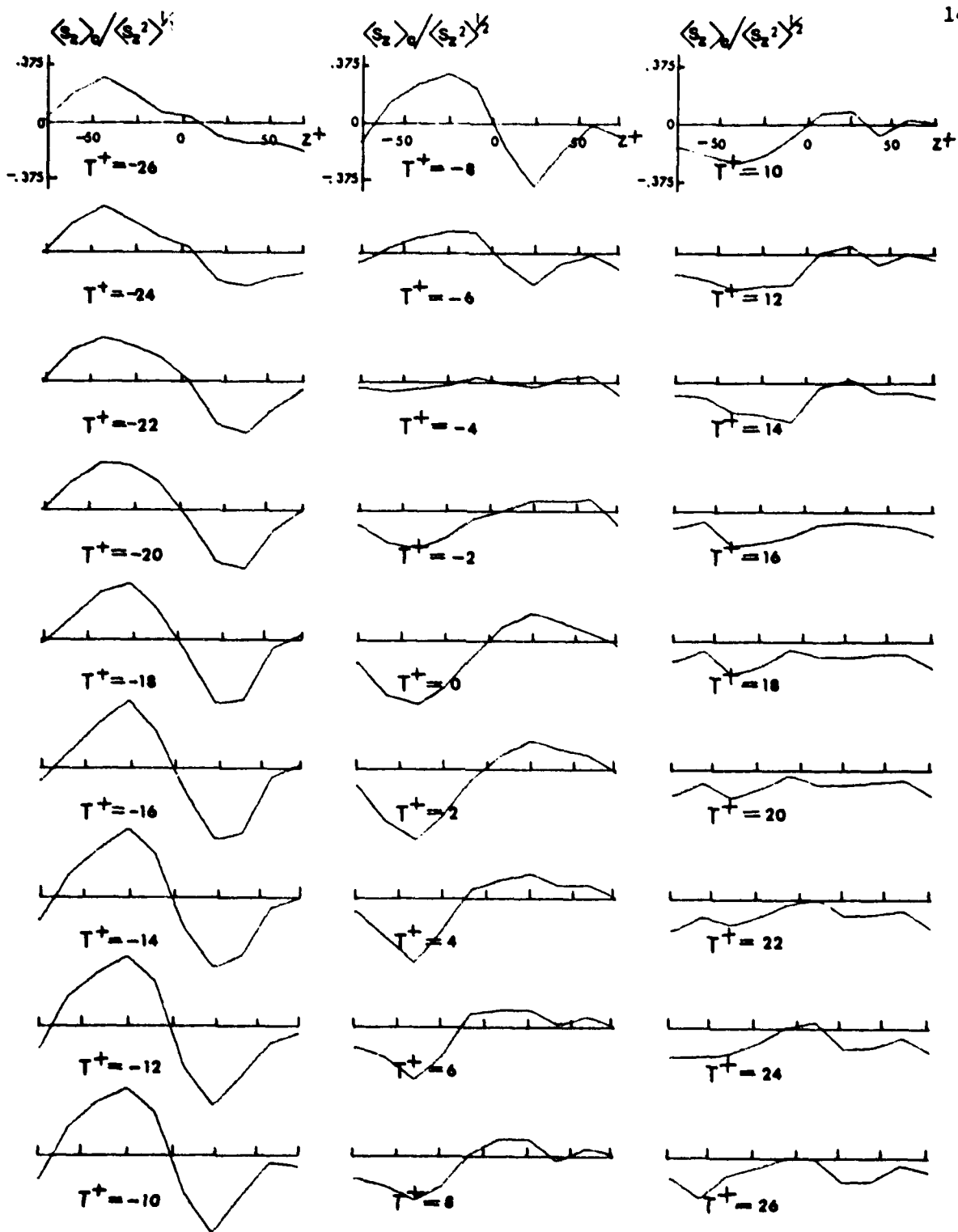


Figure 6-48. Conditionally averaged acceleration s_z patterns. Equation (3.8) applied to u_x^z fluctuations at $y^+ = 24$; $E_D = 97$; fluid probe at $\Delta x^+ = 90$.

$\Delta T^+ = 6$ this pattern reduces to a zero fluctuation profile after which a s_z pattern with a positive slope becomes apparent. This inflow pattern then increases in amplitude but its shape remains irregular. The maximum s_z inflow pattern is reached at $T^+ = 2$. For detection probes closer to the wall than $y^+ = 24$, the inflow and outflow s_z patterns have larger amplitudes and their forms become that of the sine wave shaped s_z pattern with a wavelength of $\Delta z^+ = 100$. (Their plots are not shown.) If the detection probe is placed far away from the wall (e.g. $y^+ > 24$) then the s_z patterns become still more irregular and their amplitudes smaller. (This plot also is not shown.) Apparently identification of an inflow-outflow sequence with the wall probes becomes increasingly more difficult as the detection probes are placed farther away from the wall.

The s_x patterns for the detection probe at $y^+ = 24$ are presented in Figure 6-49. Low momentum fluid is evidenced by the irregularly shaped axial velocity gradient pattern at $T^+ = -26$. Later in time this outflow pattern changes into a sine wave shaped s_x pattern (at $T^+ = -10$) with a large valley in the centre and an apex on each side. Its wavelength is $\Delta z^+ = 100$. A rapid change in this pattern takes place after $T^+ = -4$ and at $T^+ = 8$ the first signs of an inflow are visible. The inflow grows steadily and at $T^+ = 14$ a s_x inflow pattern with large amplitudes and a wavelength of approximately $\Delta z^+ = 100$ is established. Still later this inflow pattern decreases slowly in amplitude but high momentum fluid was yet observed at the wall electrodes at $T^+ = 26$.

4. Rapid decelerations of fluctuating velocities in the fluid.

Not only do accelerations occur in the fluid as discussed in Section C-3 but so do decelerations. For this work they were measured at three

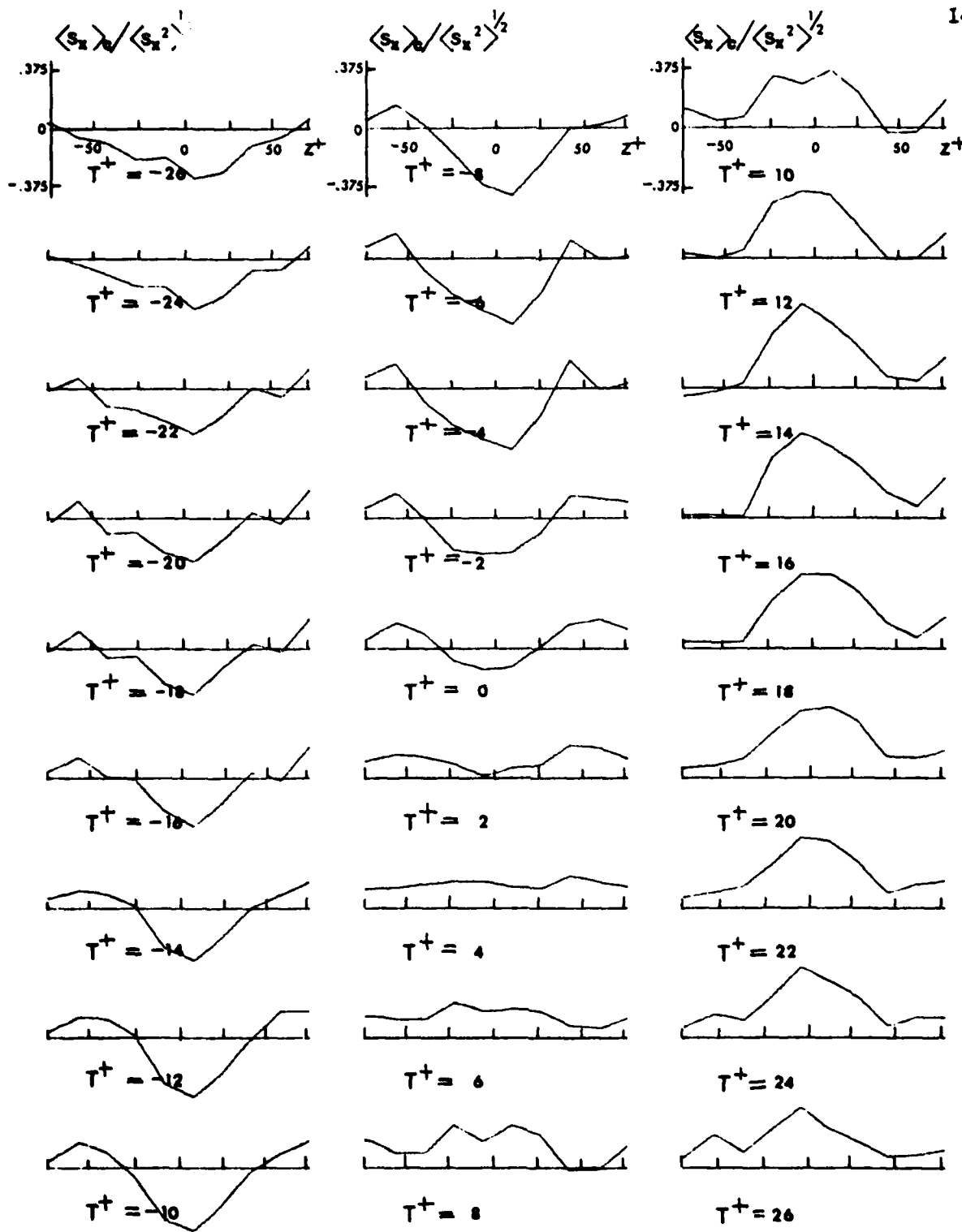


Figure 6-49. Conditionally averaged acceleration s_x patterns. Equation (3.8) applied to u_x fluctuations at $y^+ = 24$; $E_D = 97$; fluid probe at $\Delta x^+ = 90$.

positions in the fluid, namely at $y^+=8$, 24 and 50, at a downstream distance of $\Delta x^+=90$ from the wall electrodes. The decelerations were detected by applying equation (3.8) to the axial velocity fluctuations and approximately 100 deceleration events were selected for each position. The conditionally averaged fluctuating velocity profiles were calculated for the three event sets; the results are presented in Figures 6-50, 6-51 and 6-52. These three plots exhibit a common behaviour, specifically positive fluctuating velocity profiles for $T^+ < 0$ and negative fluctuating velocity profile for $T^+ > 0$. Figure 6-50 shows that the u_x profiles have a momentum excess which is confined mainly to the wall region (e.g. $y^+ < 30$) for $T^+ = -26$ to $T^+ = -4$. The maximum amplitude of the positive momentum is reached at approximately $T^+ = -6$. This momentum excess reduced rapidly during the strong deceleration from $T^+ = -4$ to $T^+ = 4$. A negative peak equal to 13 percent of the bulk velocity appeared in the u_x velocity profile at $T^+ = 4$. Later this momentum deficiency grew in extent and after $T^+ = 6$ the low momentum fluid was replaced gradually by fluid with the mean velocity. The u_x velocity profiles shown in Figure 6-51 were obtained with the detection probe at $y^+ = 24$. From $T^+ = -26$ to $T^+ = -2$ the u_x profiles all have a momentum excess. A maximum momentum excess with an amplitude of 11 percent of the bulk velocity was reached at $T^+ = -4$. From $T^+ = -2$ to $T^+ = 2$ an extremely fast deceleration took place resulting in a fluctuating axial velocity profile with a large momentum deficiency at $T^+ = 2$. The momentum deficient fluid reached a maximum negative value at time $T^+ = 4$ at a distance from the wall of $y^+ = 25$; later this pattern relaxed, turning into the zero fluctuation profile. In the case where decelerations were detected at $y^+ = 50$ a peak was found in the fluctuating velocity profile at $T^+ = -4$ as shown in Figure 6-52. Over time this profile

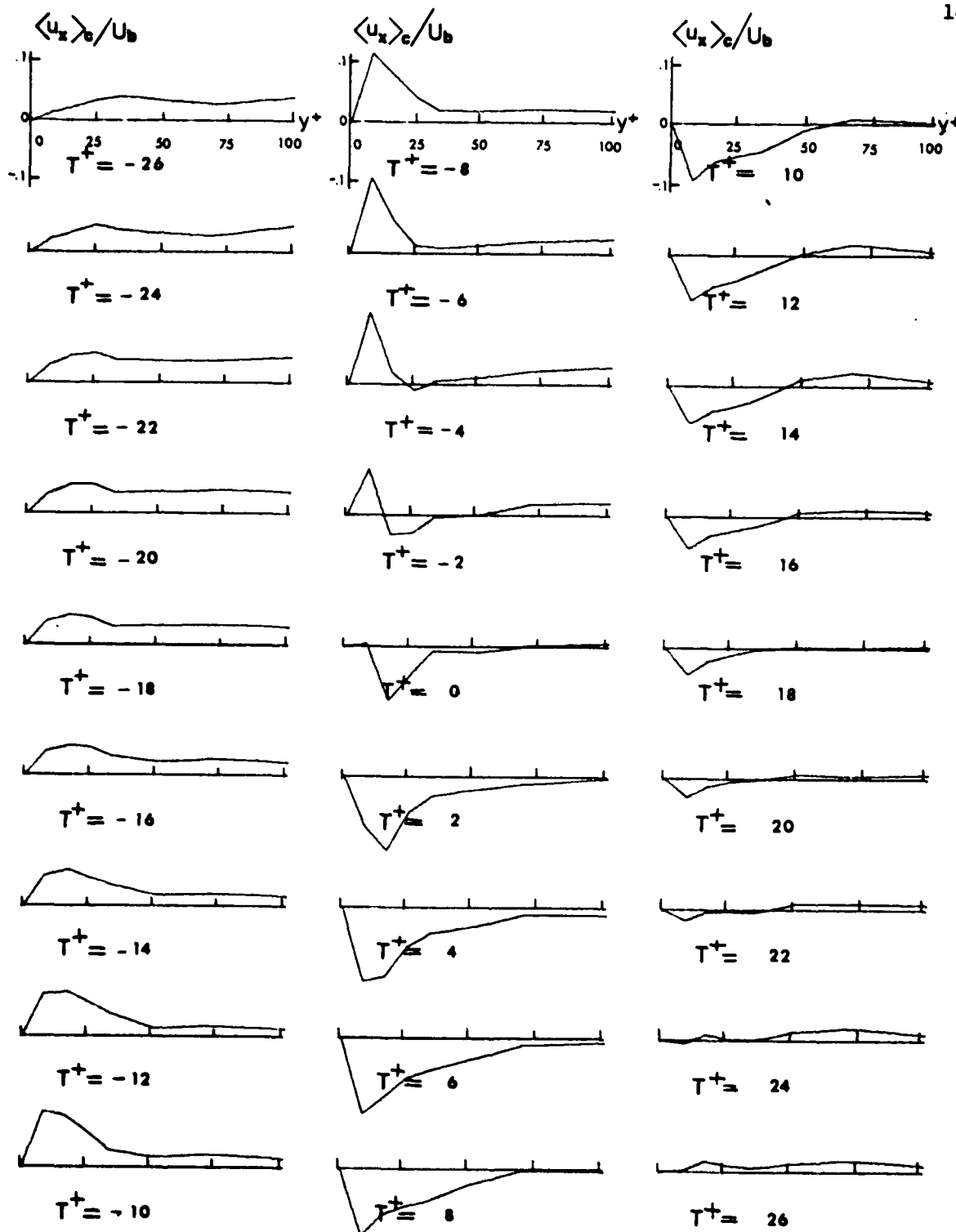


Figure 6-50. Conditionally averaged deceleration u_x patterns. Equation (3.8) applied to u_x fluctuations at $y^+ = 8$; $E_D = 96$; fluid probes at $\Delta x^+ = 90$.

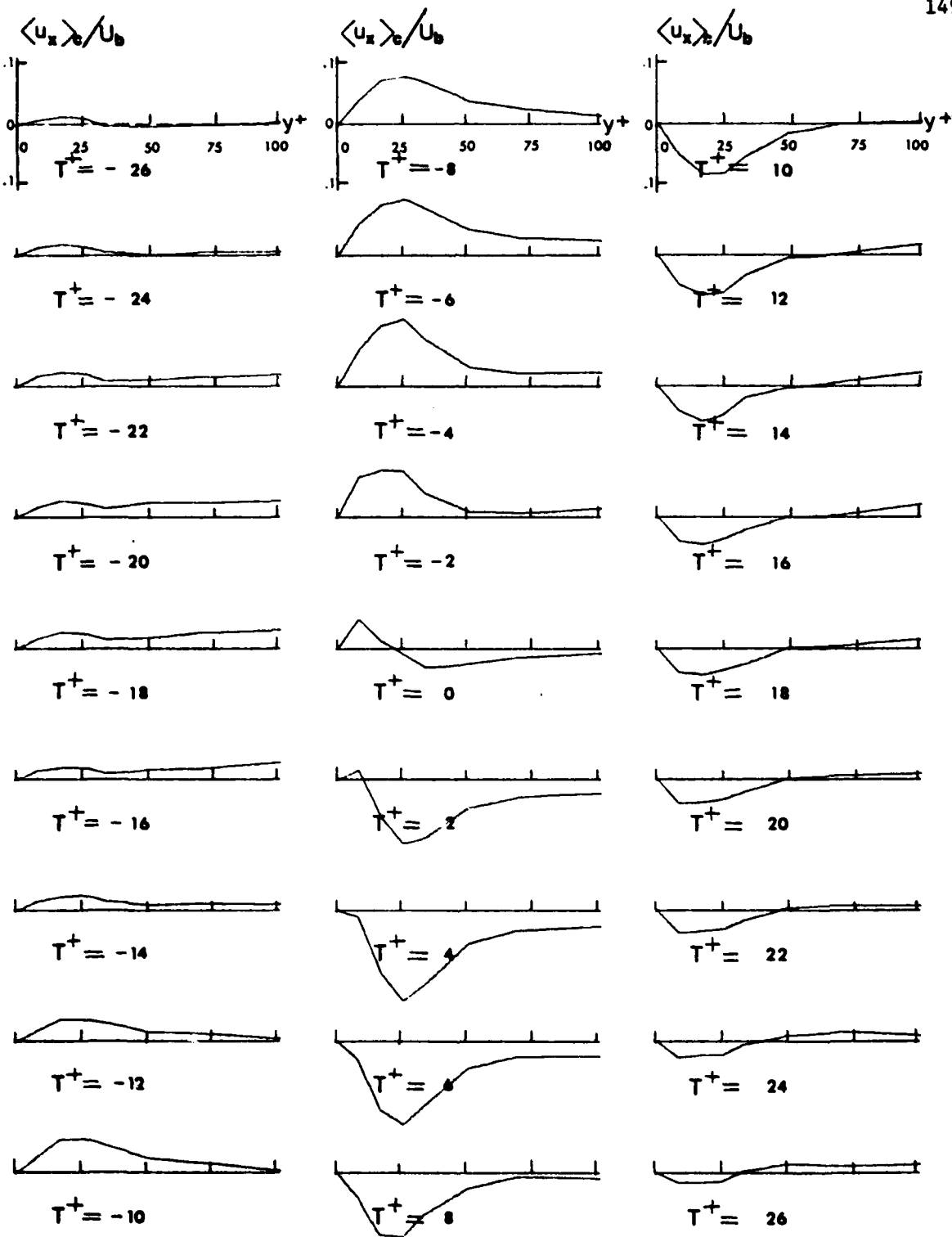


Figure 6-51. Conditionally averaged deceleration u_x patterns. Equation (3.8) applied to u_x fluctuations at $y^+ = 24$; $E_D = 100$; fluid probes at $\Delta x^+ = 90$.

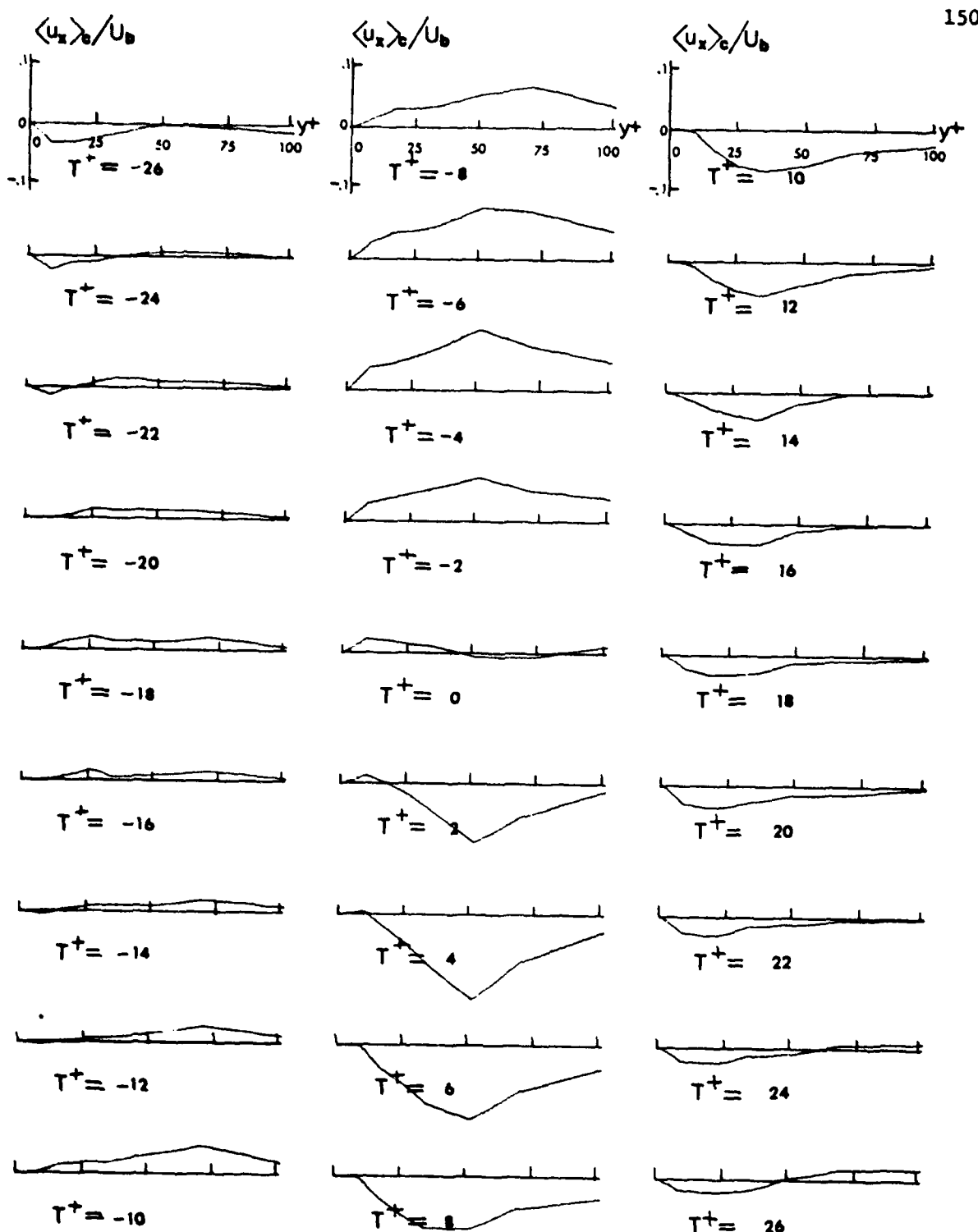


Figure 6-52. Conditionally averaged deceleration u_x patterns. Equation (3.8) applied to u_x fluctuations at $y^+ = 50$; $E_D = 101$; fluid probes at $\Delta x^+ = 90$.

changes rapidly from a momentum excess (at $T^+ = -2$) to a momentum deficient pattern (at $T^+ = 2$). This momentum deficient u_x profile exhibits a minimum at $y^+ = 50$. The location of the minimum suggests that this minimum is caused by downstream convected momentum deficient fluid, and not by a local ejection of momentum deficient fluid from the wall. The negative velocity peak increases in magnitude until $T^+ = 4$ at which an amplitude of 15 percent of the bulk velocity is found. Further in time this negative momentum slowly diminishes.

The conditionally averaged velocity profiles for the three positions of the fluid probes are presented in Figures 6-53, 6-54 and 6-55. The plots of Figure 6-53 show a momentum excess for velocity patterns from $T^+ = -26$ to $T^+ = -4$. Starting at time instant $T^+ = -6$ the high momentum fluid is decelerated at a distance from the wall of $y^+ = 20$. The combination of the presence of high momentum fluid near the wall and a deceleration of fluid farther away from the wall causes inflexions in the conditionally averaged velocity profile. The inflexions appear from $T^+ = -8$ to $T^+ = 0$ in the velocity patterns at a distance of approximately $y^+ = 20$. After $T^+ = 0$ momentum deficient fluid appears in the viscous wall region. In turn, this fluid is gradually replaced by fluid with the mean velocity. Figure 6-54 shows the conditionally averaged velocity patterns for the case where the detection probe was positioned at $y^+ = 24$. The plots exhibit high momentum fluid near the wall which is rapidly decelerated after $T^+ = -2$. Only fluid velocities at approximately $y^+ = 30$ were affected, leaving the high momentum fluid near the wall unchanged. Together high momentum fluid near the wall and low momentum fluid at $y^+ \approx 25$ create inflexions in the u_x velocity patterns from $T^+ = -2$ to $T^+ = 14$. The plots in Figure 6-55 were obtained from the probe signals at $y^+ = 50$.

$\langle U_x \rangle_c / U_b$ $\langle U_x \rangle_c / U_b$ $\langle U_x \rangle_c / U_b$

152

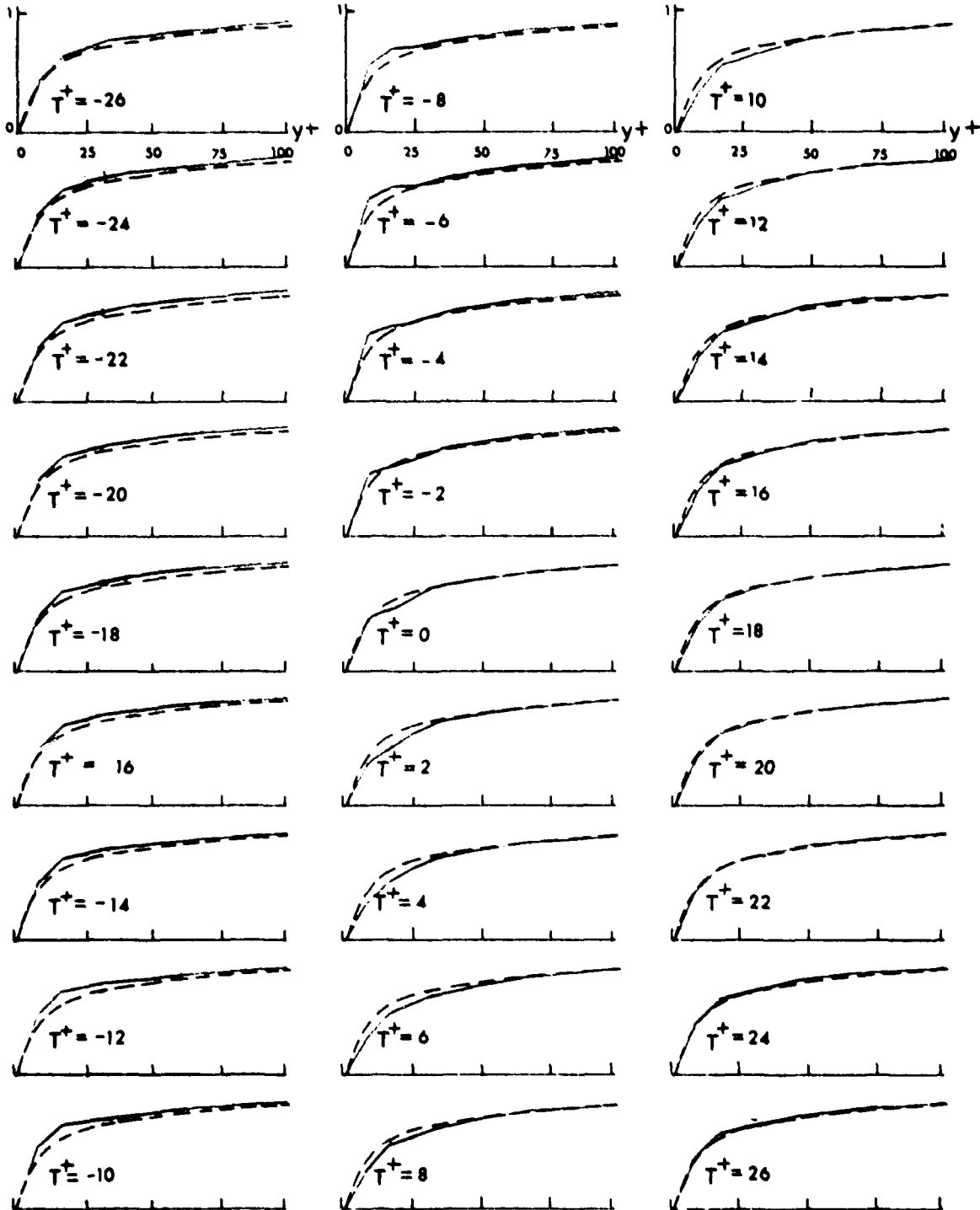


Figure 6-53. Conditionally averaged deceleration U_x patterns. Equation (3.8) applied to u_x fluctuations at $y^+ = 8$; $E_D = 96$; fluid probes at $\Delta x^+ = 90$; dashed line--mean velocity profile; solid line--conditionally averaged pattern.

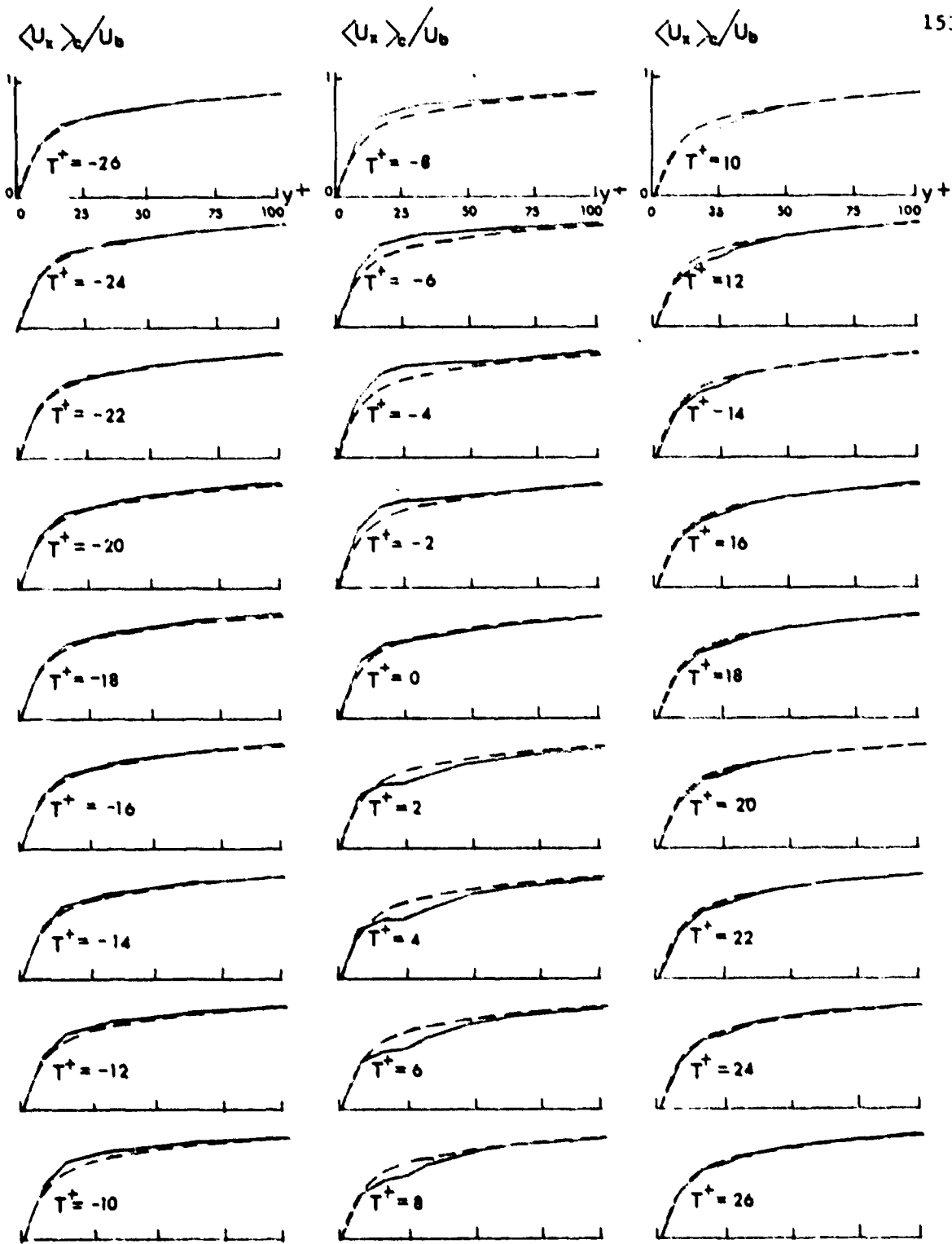


Figure 6-54. Conditionally averaged deceleration U_x patterns. Equation (3.8) applied to u_x fluctuations at $y^+ = 24$; $E_D = 100$; fluid probes at $\Delta x^+ = 90$; dashed line--mean velocity profile; solid line--conditionally averaged pattern.

$\langle U_x \rangle_c / U_b$ $\langle U_x \rangle_c / U_b$ $\langle U_x \rangle_c / U_b$

154

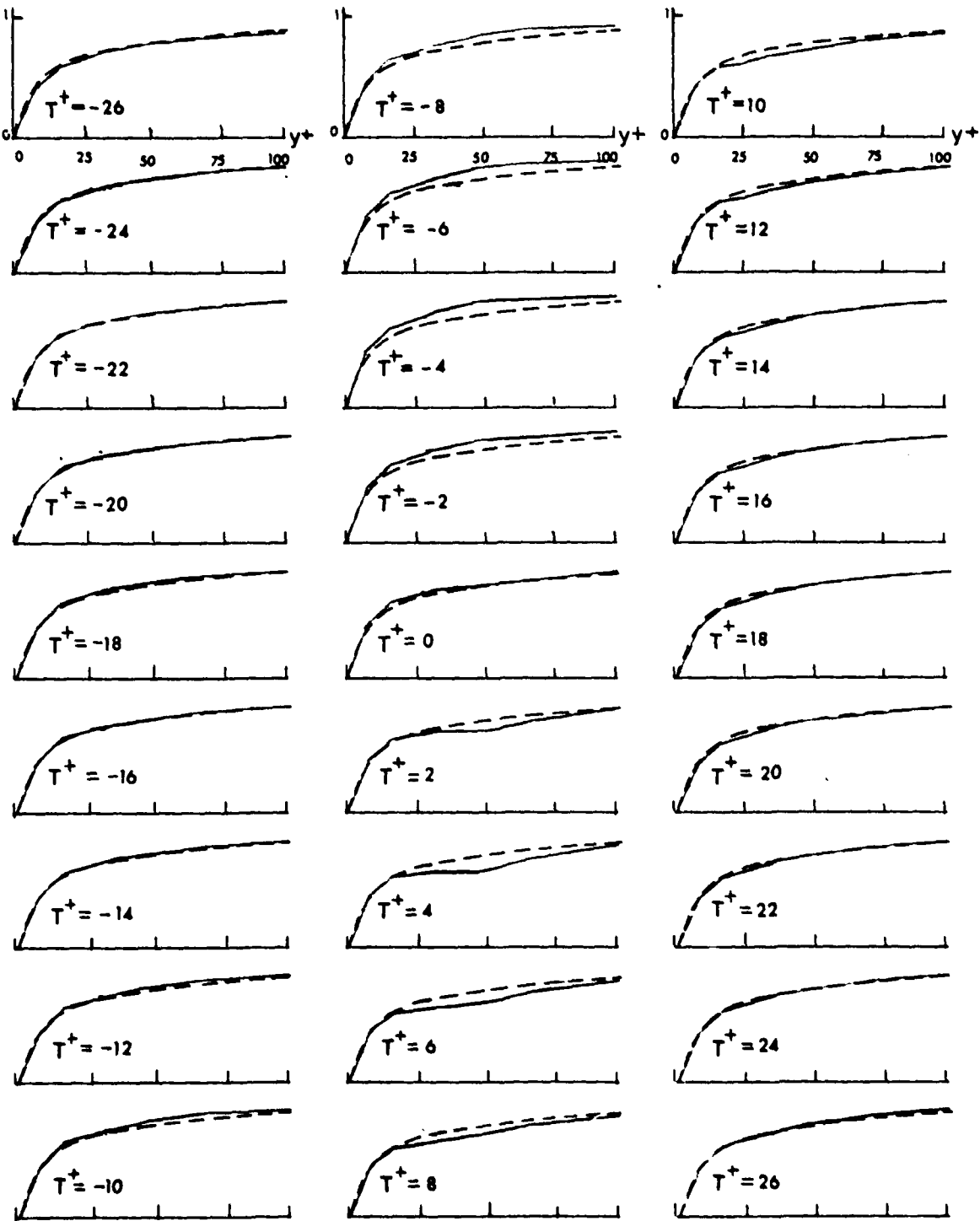


Figure 6-55. Conditionally averaged deceleration U_x patterns. Equation (3.8) applied to u_x fluctuations at $y^+ = 50$; $E_D = 101$; fluid probes at $\Delta x^+ = 90$; dashed line--mean velocity profile; solid line--conditionally averaged pattern.

They exhibit a similar behaviour as those of Figure 6-54. Before $T^+ = 0$ a momentum excess is present in the velocity profiles and beyond this time point a momentum deficiency appears in the range from $y^+ = 22$ to $y^+ = 90$. Again the combination of high momentum fluid near the wall and low momentum fluid at approximately $y^+ = 50$ induces inflexions at $y^+ = 50$ for the time period $T^+ = 2$ to $T^+ = 8$.

Deceleration s_z patterns for the detection probe positioned at $y^+ = 24$ are presented in Figure 6-56. From $T^+ = -26$ to $T^+ = -16$ no identifiable pattern can be observed but over time a very weak s_z inflow pattern develops which persists until $T^+ = -10$. This s_z inflow pattern is consistent with the axial velocity fluctuations (see Figure 6-51) which show an increase in high momentum fluid for the time period $T^+ = -14$ to $T^+ = -4$. At $T^+ = -6$ an outflow s_z pattern is present which grows in amplitude until approximately $T^+ = 2$ but its profile is irregular. Development of the outflow s_z pattern coincides with the first indication of low momentum in the axial velocity fluctuations. After $T^+ = 2$ the s_z pattern's amplitude decreases as does the magnitude of low momentum fluid at the fluid probes.

Figure 6-57 shows the s_x patterns for a deceleration. An inflow s_x pattern becomes apparent at $T^+ = -10$, a time period of $\Delta T^+ = 4$ after the first indication of an s_z inflow pattern. A maximum inflow is reached at $T^+ = -4$ followed by a transition period of $\Delta T^+ = 14$ after which an outflow s_x pattern appears. This outflow pattern increases in size and is still identifiable at $T^+ = 26$. If the detection probe is placed farther away from the wall than at $y^+ = 24$ then the s_z and s_x patterns at the wall become unidentifiable. (These plots are not shown.)

5. Positive slopes in the u_x profiles near the wall.

Spatial behaviour of the fluctuating velocities was studied by means of four fluid probes positioned at distances from the wall of

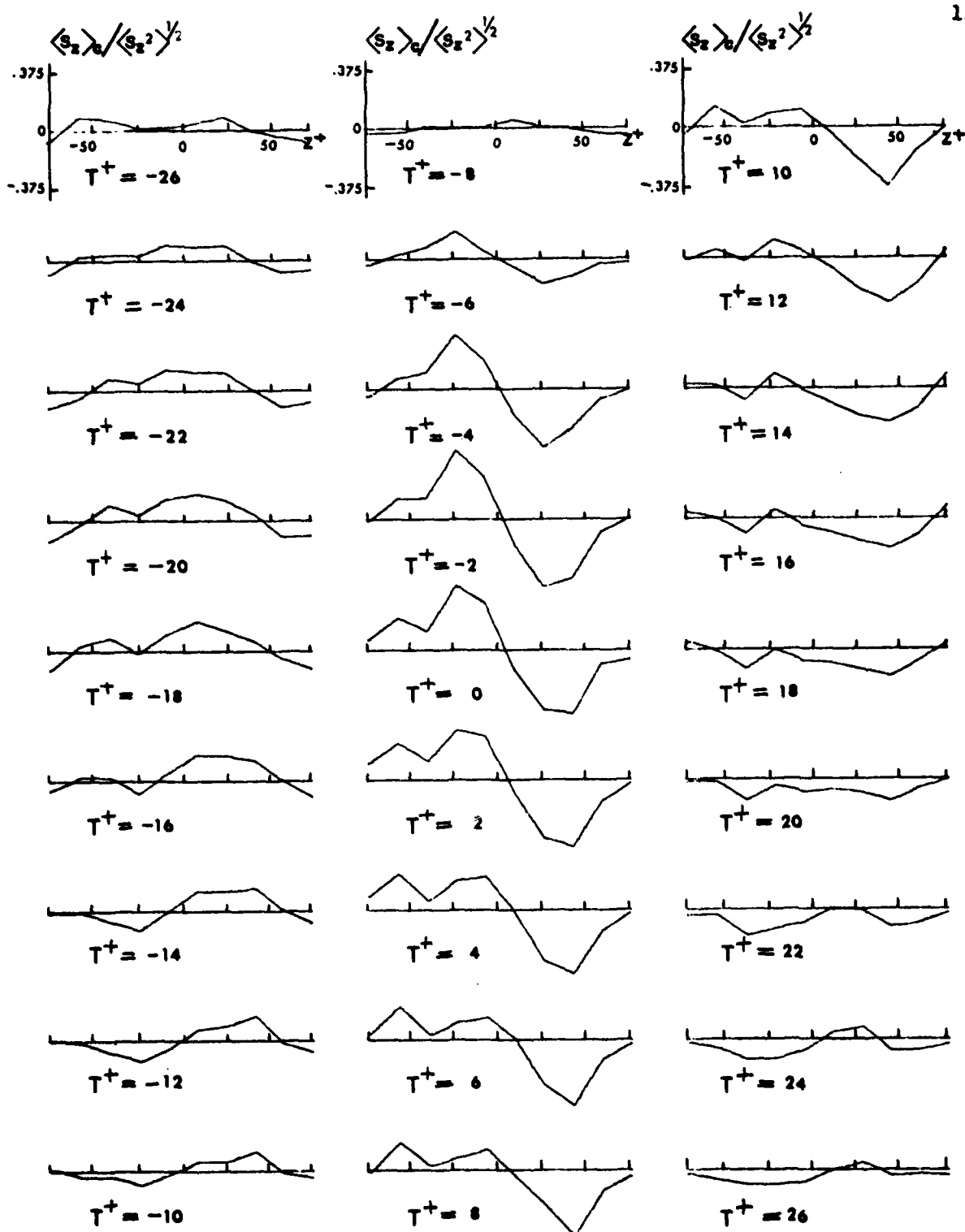


Figure 6-56. Conditionally averaged deceleration s_z patterns. Equation (3.8) applied to u_x fluctuations at $y^+ = 24$; $E_D = 100$; fluid probes at $\Delta x^+ = 90$.

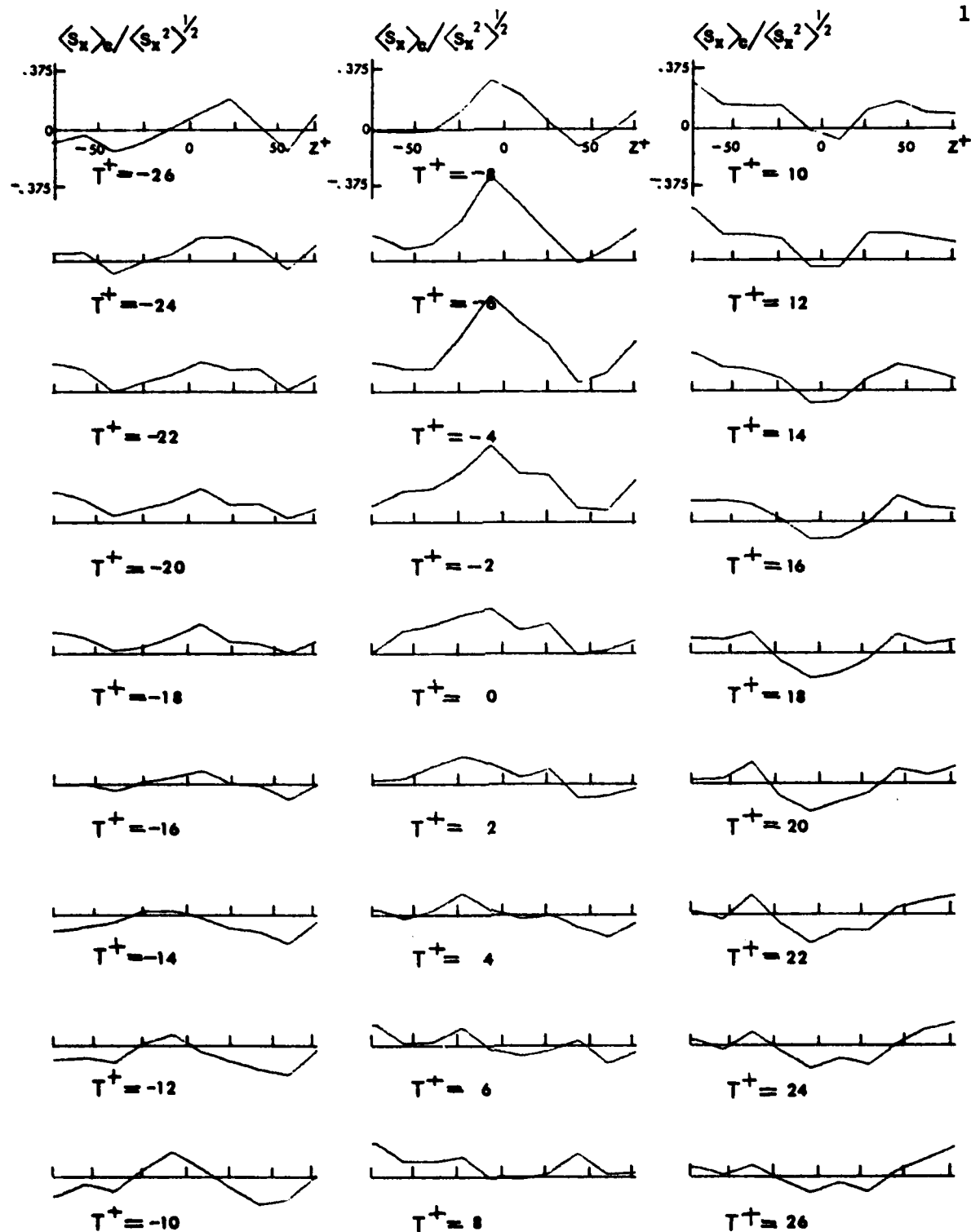


Figure 6-57. Conditionally averaged deceleration s_x patterns. Equation (3.8) applied to u_x fluctuations at $y^+ = 24$; $E_D = 100$; fluid probes at $\Delta x^+ = 90$.

$y^+=8, 16, 24$ and 33 . The probes were placed at a downstream distance of $\Delta x^+=90$ from the wall electrodes. The condition described by equation (3.7) was applied to the probe signals in order to search for instants in the data set which show fluctuations with deficient momentum at $y^+=8$ and 16 and fluctuations with excess momentum at $y^+=24$ and 33 . Totally 98 of these events were selected from the data set and then used to calculate the conditionally averaged u_x velocity profiles (shown in Figure 6-58). From $T^+=-26$ to $T^+=-8$ negative momentum fluid extended from the wall to $y^+=50$. Suddenly at $T^+=-6$ high momentum fluid entered at $y^+=60$ from upstream at an angle towards the wall. This high momentum fluid pushed the momentum deficient fluid towards the wall, creating both large amplitude low momentum fluid at $y^+=8$ and large amplitude high momentum fluid at $y^+=30$ with maxima of 17 and 13 percent of the bulk velocity, respectively. Later both the high and low momentum fluctuations reduced in amplitude and at $T^+=-8$ only high momentum fluid was present in the u_x profile, and over time this fluid diminished slowly. Figure 6-59 shows the conditionally averaged velocity patterns. These plots exhibit an increase in momentum deficiency of the fluid near the wall from $T^+=-26$ to $T^+=-8$. High momentum fluid began moving towards the wall at $T^+=-12$; inflexions arise from this instant to $T^+=-6$. After $T^+=-6$ the rapidly inmoving high momentum fluid replaces the momentum deficient fluid and then the inflexions disappear.

The events were also used to calculate the conditionally averaged s_z and s_x patterns. The wall electrodes were positioned upstream from the fluid probes at $\Delta x^+=90$. The s_z plots are shown in Figure 6-60. A s_z outflow pattern with a large amplitude is present from $T^+=-18$ to

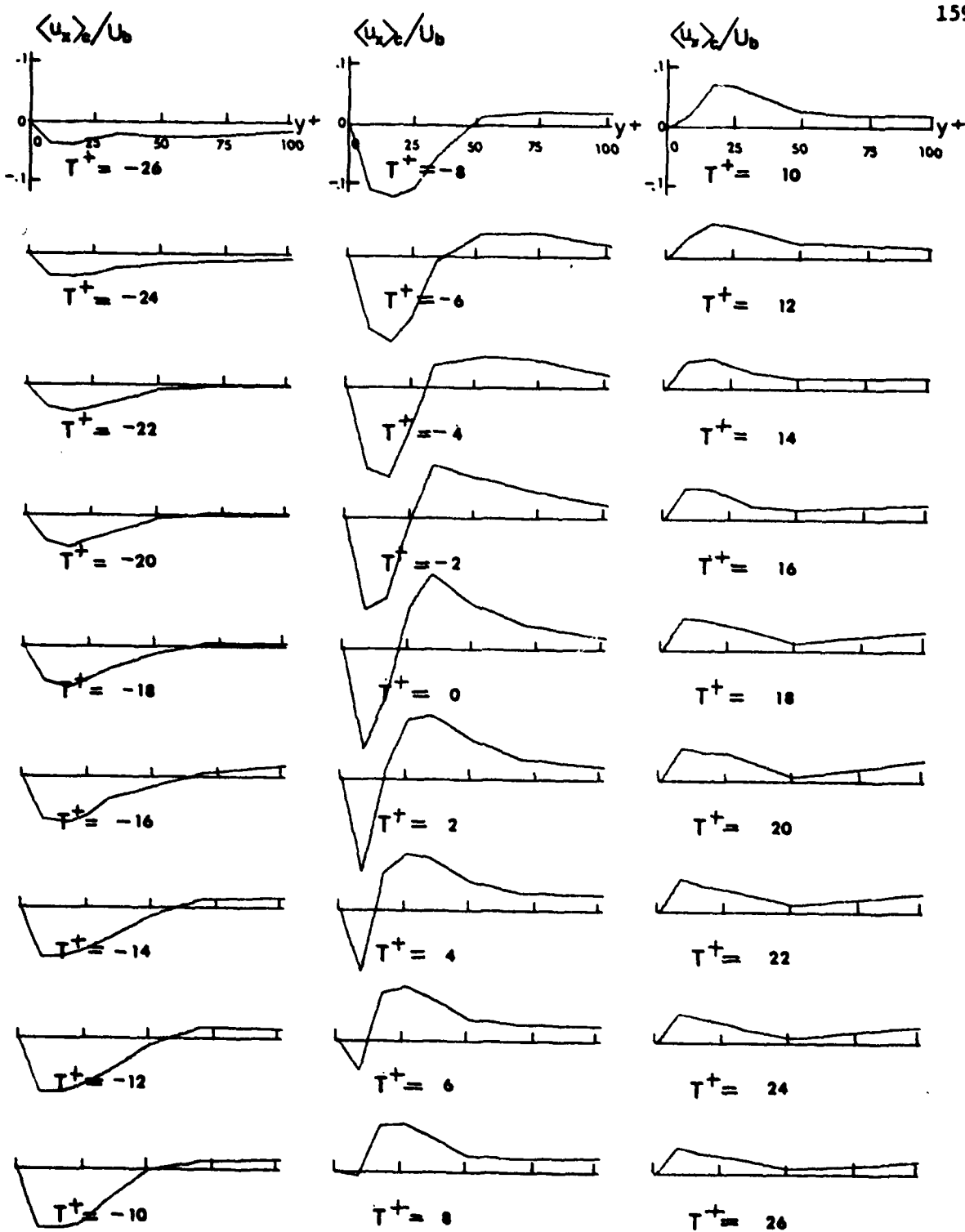


Figure 6-58. Conditionally averaged u_x patterns--positively sloped u_x profile. Equation (3.7) applied to u_x fluctuations at $y^+ = 8, 16, 24$ and 30 ; $E_D = 98$; fluid probes at $\Delta x^+ = 90$.

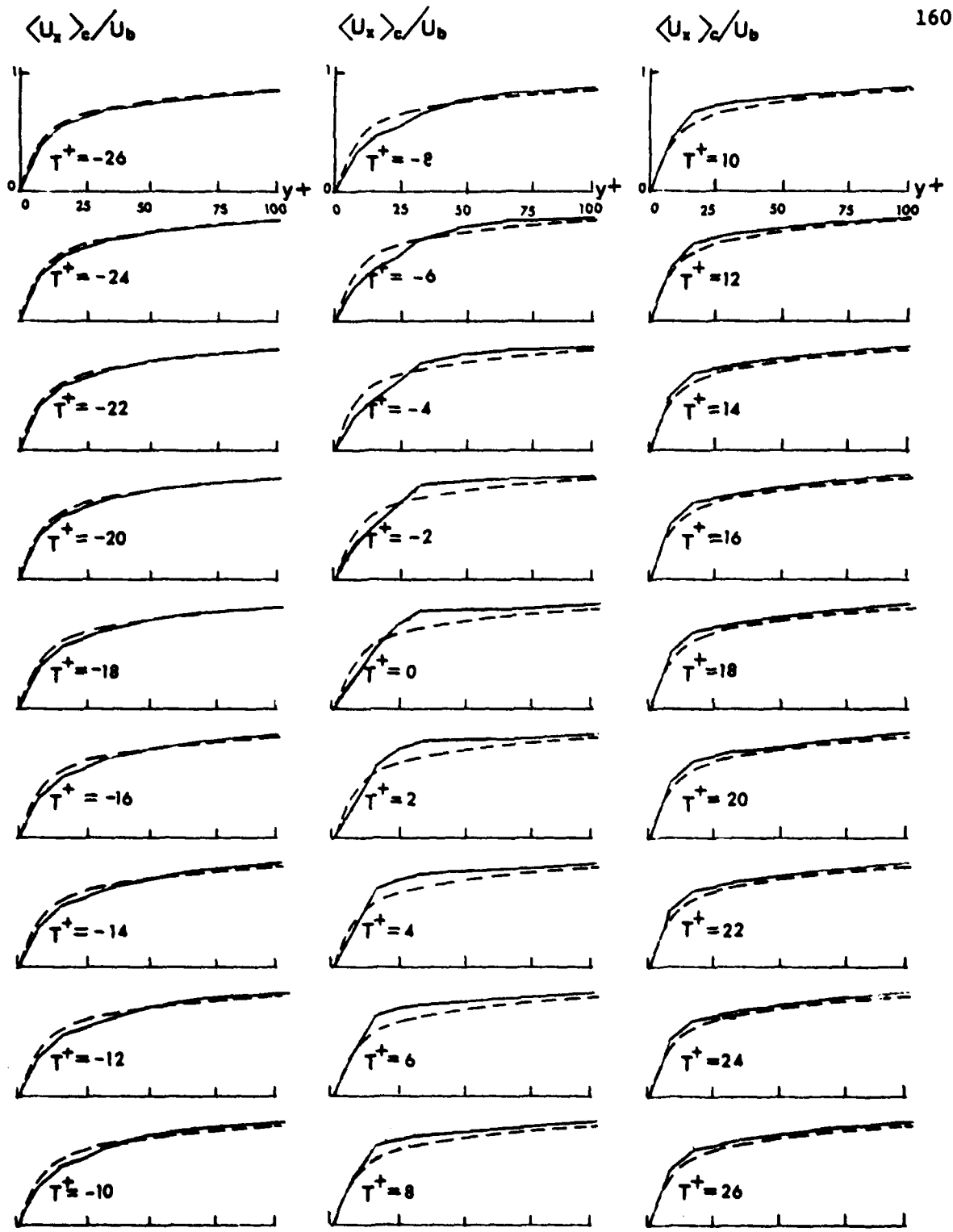


Figure 6-59. Conditionally averaged U_x patterns--positively sloped u_x profile. Equation (3.7) applied to u_x fluctuations at $y^+ = 8, 16, 24$ and 30 ; $E_D = 98$; fluid probes at $\Delta x^+ = 90$; dashed line--mean velocity profile; solid line--conditionally averaged pattern.

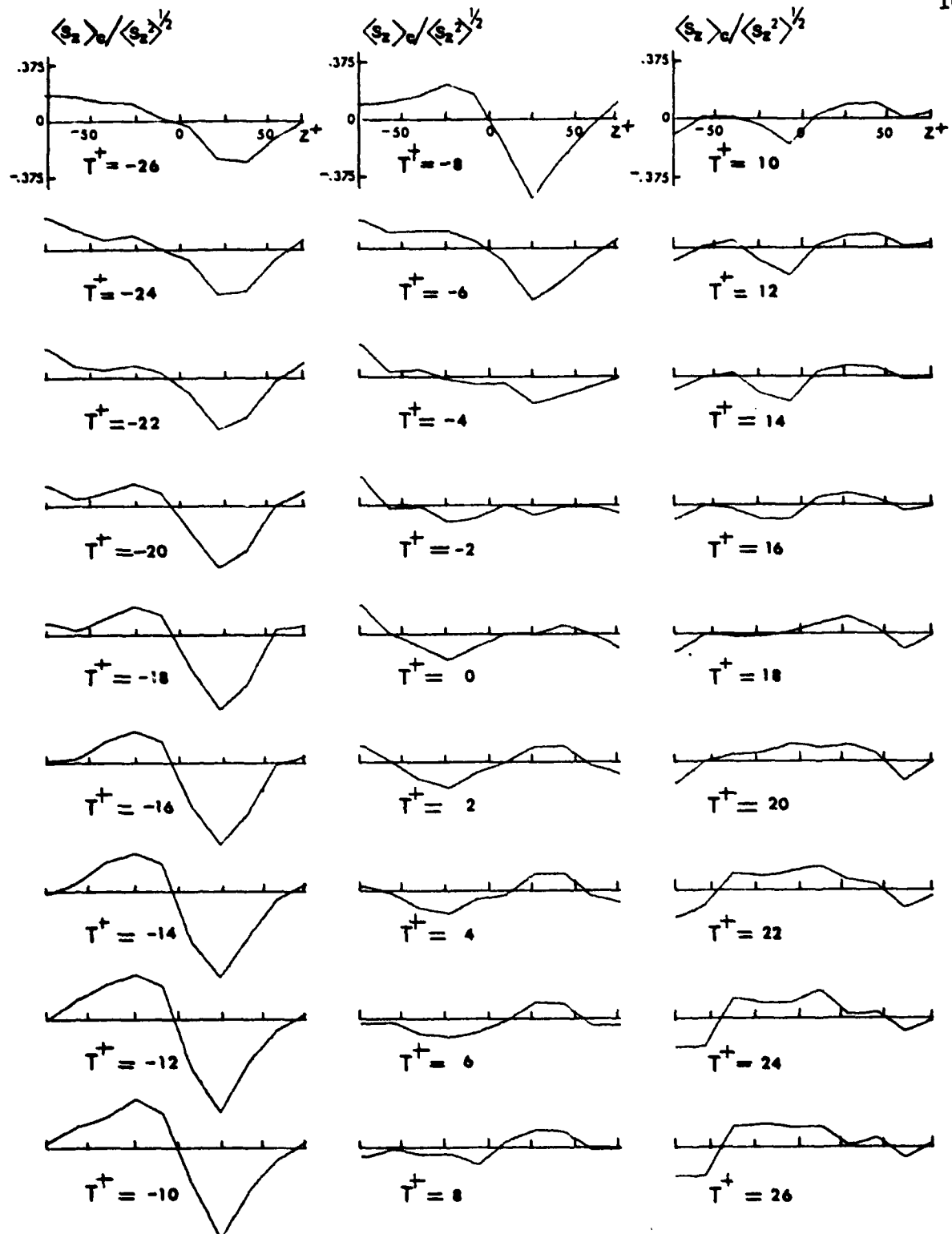


Figure 6-60. Conditionally averaged s_z patterns--positively sloped u_x profile. Equation (3.7) applied to u_x fluctuations at $y^+ = 8, 16, 24$ and 30 ; $E_D = 98$; fluid probes at $\Delta x^+ = 90$.

$T^+ = -8$ which is consistent with the presence of momentum deficient fluid detected by the fluid probes. Later, hardly any pattern is identifiable except for the range from $T^+ = 2$ to $T^+ = 8$ where a small s_z inflow pattern can be observed. As concluded from the fluid probes' signals, the high momentum fluid is convected downstream at a slight angle towards the wall. This fluid does not reach the wall; consequently the fluid's influence cannot be detected with the wall probes. The s_x patterns presented in Figure 6-61 exhibit a small outflow profile from $T^+ = -26$ to $T^+ = 2$. These profiles agree with the axial velocity fluctuation patterns which indicate momentum deficient fluid for the same time period. Further in time a slight momentum excess is present in the s_x profiles from $T^+ = 8$ to $T^+ = 22$ which is consistent with the small s_z inflow pattern observed.

6. Negative slopes in the u_x profiles near the wall.

Not only were positive slopes found in the u_x profiles near the wall but so were negative slopes. To detect u_x profiles with negative slopes, again equation (3.7) was used. With 98 events selected in the data set, the conditionally averaged profiles of the fluctuating velocities were determined as presented in Figure 6-62. Only positive momentum is exhibited in the plots from $T^+ = -20$ to $T^+ = -10$. Negative momentum appeared (at $T^+ = -8$) in the u_x profiles at a distance from the wall of $y^+ = 45$. This negative momentum fluid, wallward moving, increased in extent and amplitude. Apparently the fluid was not locally ejected from the wall but was downstream convected. Both the high and low momentum fluids have maximum amplitudes of approximately 15 percent of the bulk velocity at $T^+ = 0$. Over time the amplitudes of these two fluids of opposite fluctuating momentum reduced. The conditionally averaged velocity profiles are presented in Figure 6-63. The plots show the

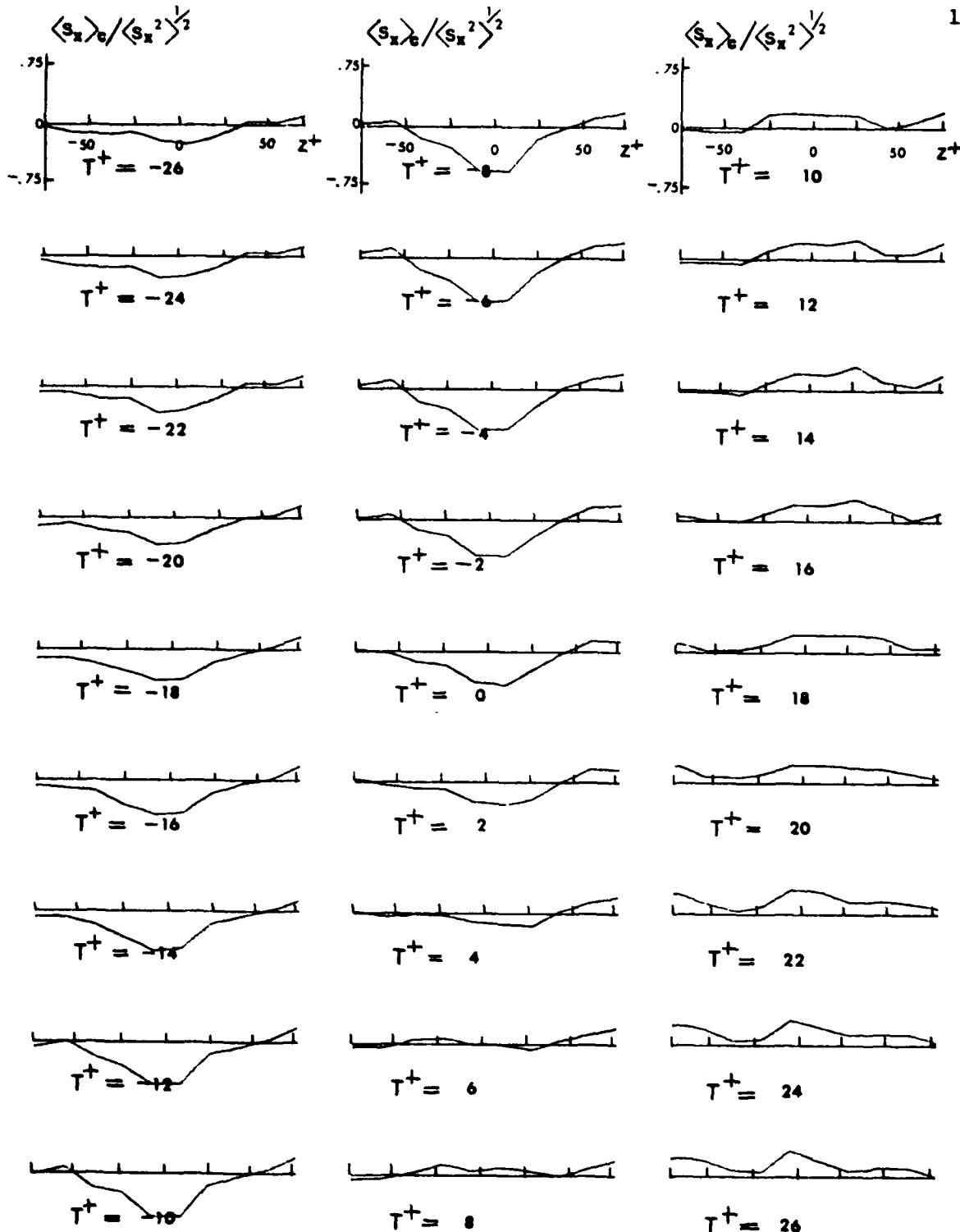


Figure 6-61. Conditionally averaged s_x patterns--positively sloped u_x profile. Equation (3.7) applied to u_x fluctuations at $y^+ = 8, 16, 24$ and 30 ; $E_D = 98$; fluid probes at $\Delta x^+ = 90$.

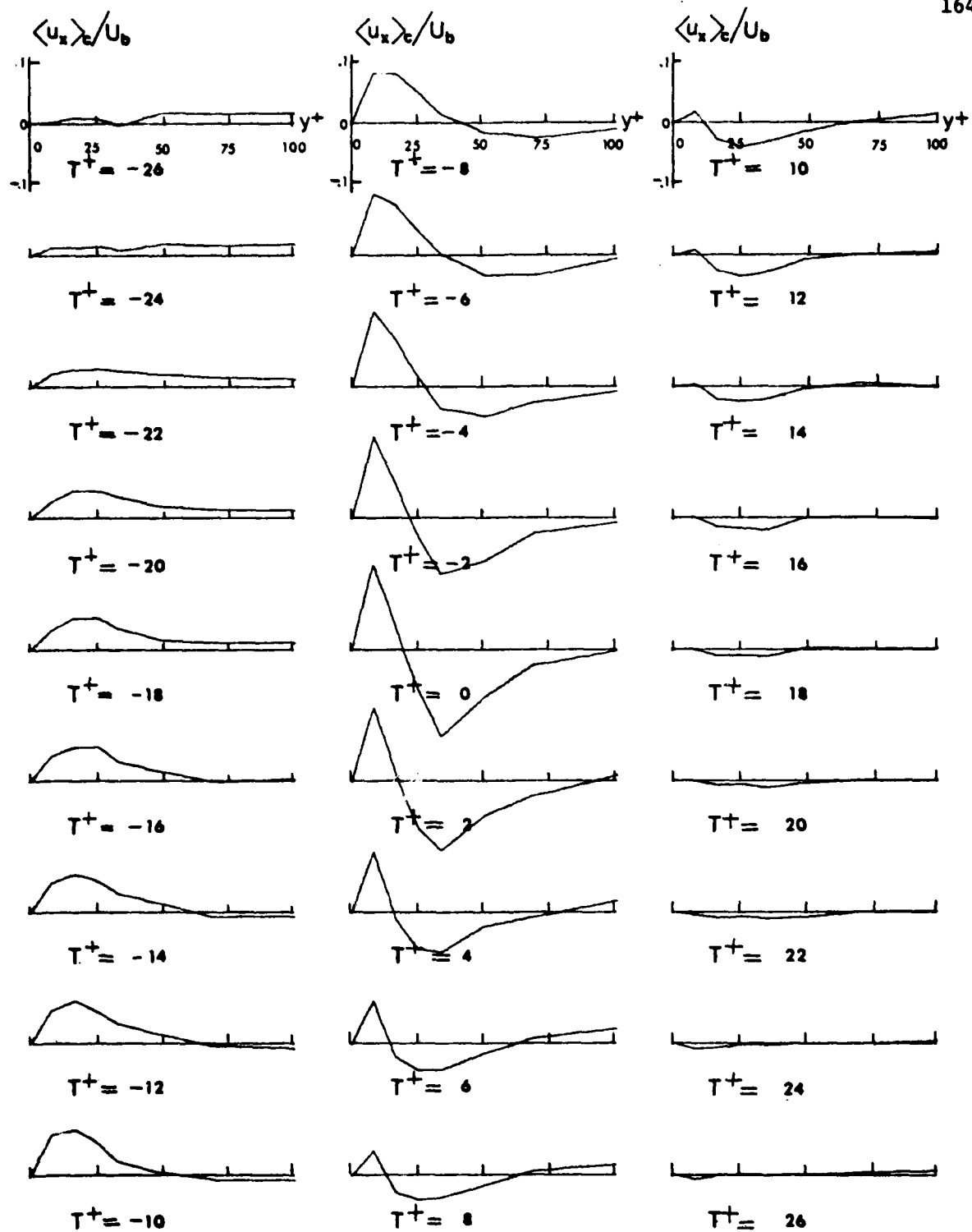


Figure 6-62. Conditionally averaged u_x patterns--negatively sloped u_x profile. Equation (3.7) applied to u_x fluctuations at $y^+ = 8, 16, 24$ and 30 ; $E_D = 98$; fluid probes at $\Delta x^+ = 90$.

$\langle U_x \rangle_c / U_a$ $\langle U_x \rangle_c / U_b$ $\langle U_x \rangle_c / U_b$

165

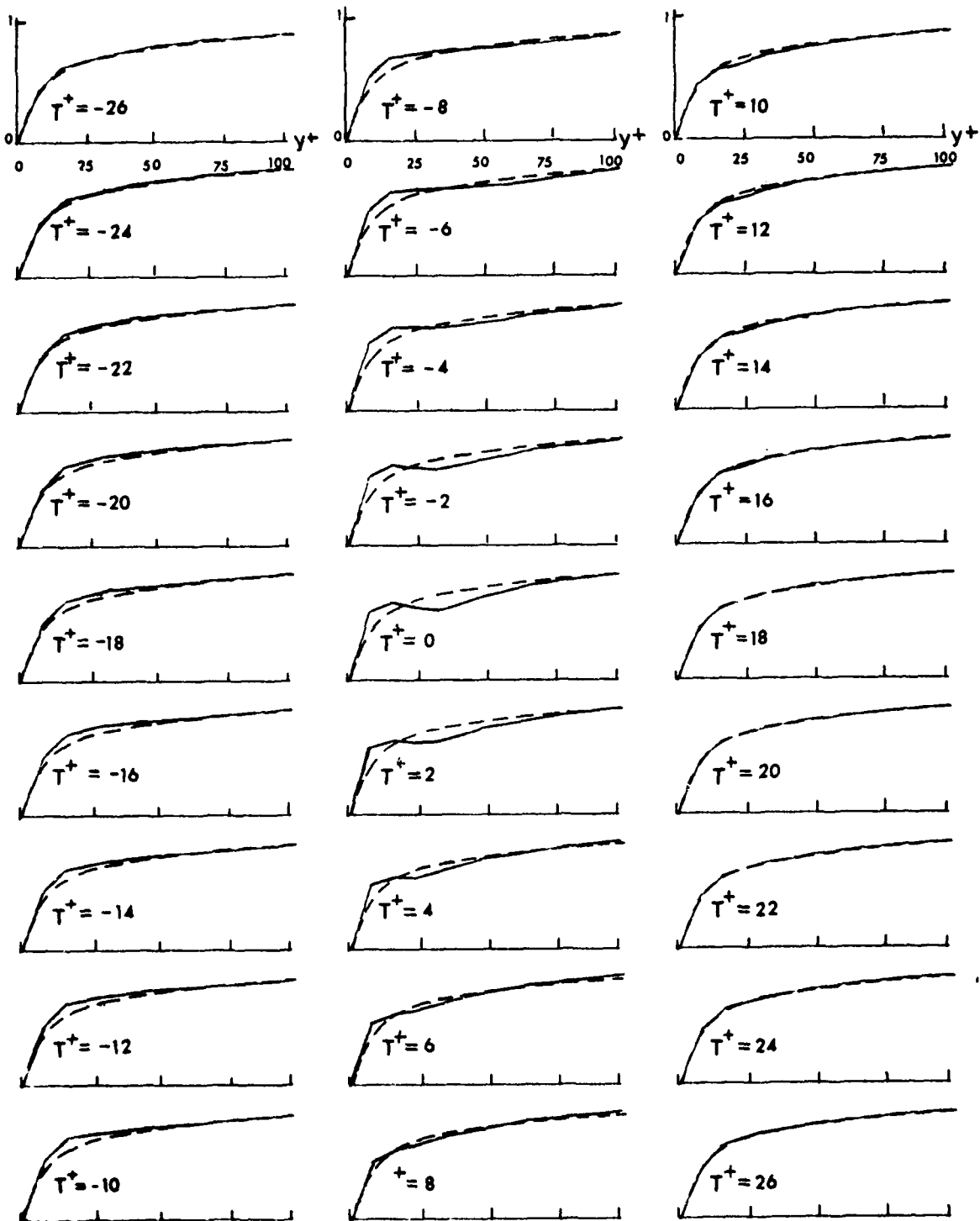


Figure 6-63. Conditionally averaged U_x patterns--negatively sloped U_x profile. Equation (3.7) applied to U_x fluctuations at $y^+ = 8, 16, 24$ and 30 ; $E_p = 98$; fluid probes at $\Delta x^+ = 90$; dashed line--mean velocity profile; solid line--conditionally averaged velocity pattern.

influence of the low momentum fluid starting at $T^+ = -8$. At this instant a small valley forms in the conditionally averaged velocity profile. Over time the trough of this valley appears closer to the wall. The low momentum fluid which caused the valleys induced inflexions in the conditionally averaged profiles and persisted from $T^+ = -6$ to $T^+ = 10$.

The conditionally averaged s_z and s_x patterns are presented in Figures 6-64 and 6-65. Inflow s_z patterns are observed from $T^+ = -18$ to $T^+ = -8$. At $T^+ = -10$ the maximum sine wave shaped s_z pattern is reached with a wavelength of $\Delta z^+ = 100$. After the inflow pattern disappears no identifiable s_z outflow pattern forms because the momentum deficient fluid was not locally ejected from the wall but downstream convected so it could not be detected with the wall electrodes. Figure 6-65 presents the s_x patterns which exhibit the inflow of high momentum fluid with the maximum inflow profile at $T^+ = -6$. At this instant the inflow pattern has a maximum amplitude of 80 percent of the axial turbulence intensity. The pattern at $T^+ = -6$ also shows valleys on each side of the maximum. Further in time the inflow pattern reduces in amplitude and after $T^+ = -6$ no pattern is identifiable. The low momentum fluid present in the u_x profiles does not appear in the s_x patterns as discussed above.

7. Time correlations between temporal and spatial u_x fluctuations.

Time correlations between the spatial derivative and the temporal derivative of the axial velocity fluctuations were studied with the following equation.

$$R_{uy} u_t(\tau) = \frac{\frac{du(y,t)}{dy} \cdot \frac{du(y,t+\tau)}{dt}}{\sqrt{\frac{du(y,t)^2}{dy}}} \sqrt{\frac{du(y,t+\tau)^2}{dt}} \quad (6.1)$$

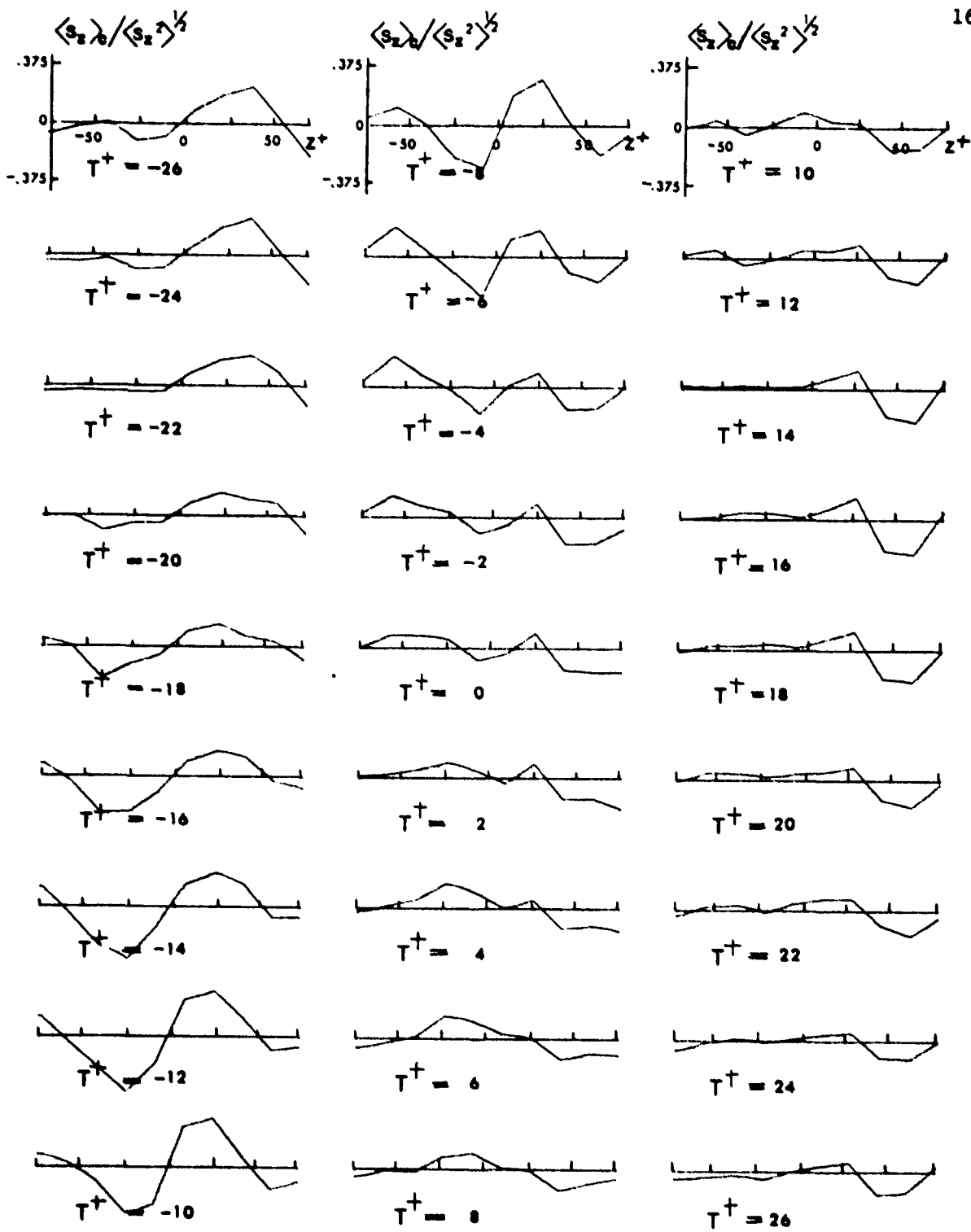


Figure 6-64. Conditionally averaged s_z patterns--negatively sloped u_x profile. Equation (3.7) applied to u_x fluctuations at $y^+ = 8, 16, 24$ and 30 ; $E_D = 98$; fluid probes at $\Delta x^+ = 90$.

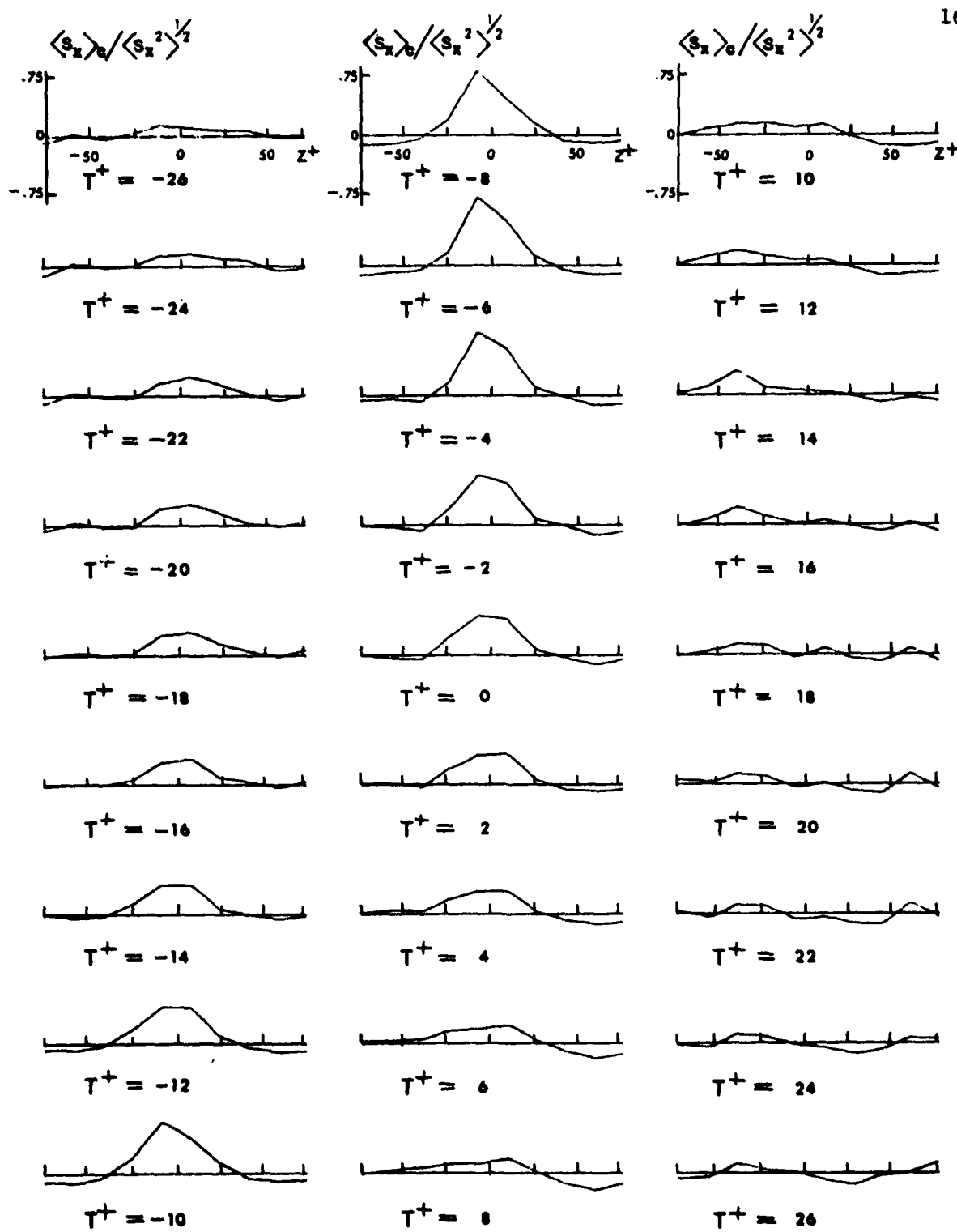


Figure 6-65. Conditionally averaged s_x patterns--negatively sloped u_x profile. Equation (3.7) applied to u_x fluctuations at $y^+ = 8, 16, 24$ and 30 ; $E_D = 98$; fluid probes at $\Delta x^+ = 90$.

For positive time delays the spatial derivatives of the u_x fluctuations were delayed with respect to its temporal derivative. Five correlations were calculated at distances from the wall between $y^+=12$ and $y^+=60$ as shown in Figure 6-66. A maximum correlation value of .52 is reached for approximately zero time delay at $y^+=12$. For distances from the wall between $y^+=20$ and $y^+=40$ the correlation value is approximately .25. Figure 6-66 shows that the correlation values diminish rapidly outside the viscous wall region. A high correlation value indicates that velocity accelerations (discussed in Section C-3) and positive slopes in the u_x profiles (discussed in Section C-6) represent essentially the same phenomenon. Thus Figures 6-42, 6-43 and 6-44 are comparable to Figure 6-58.

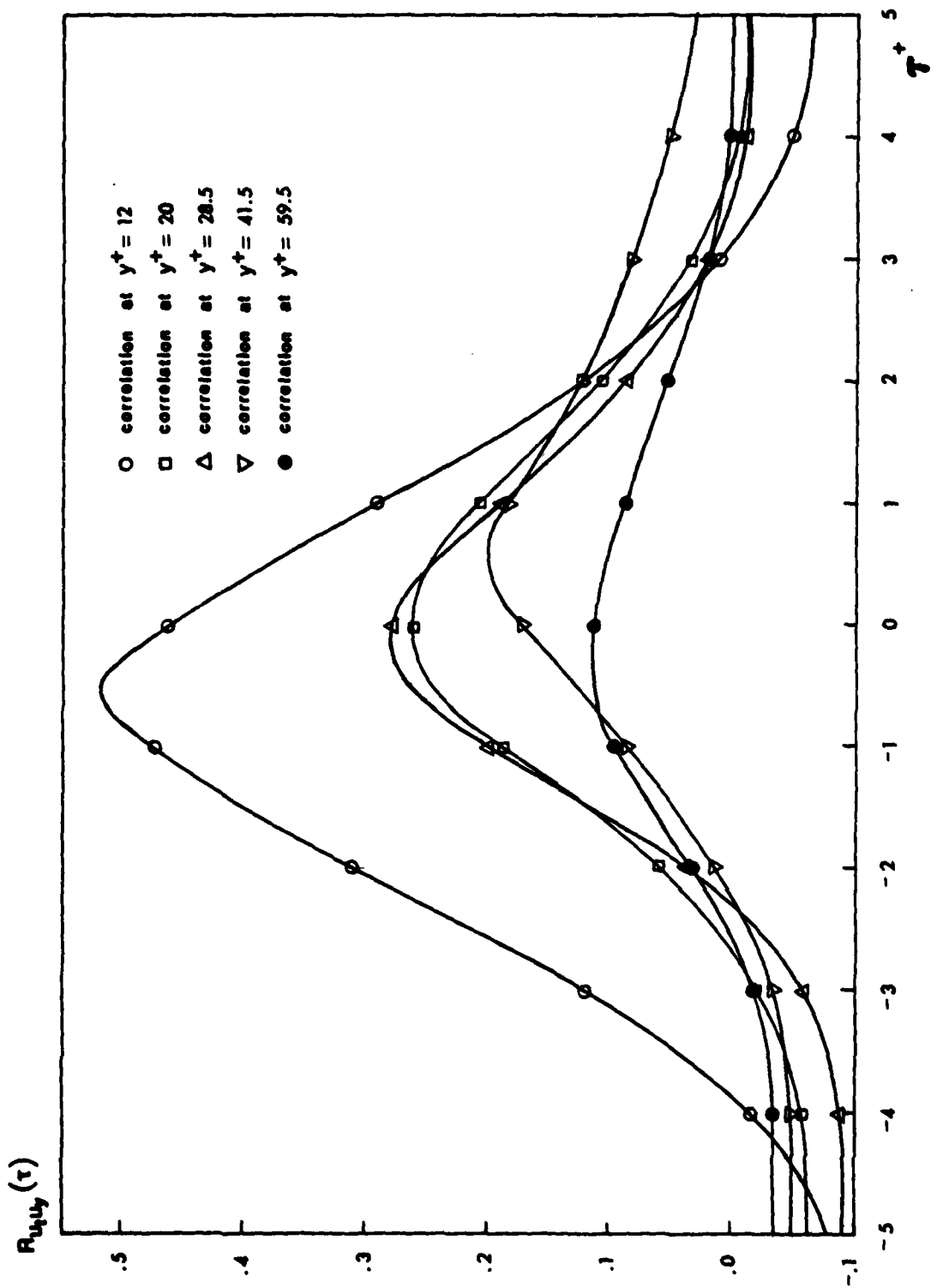


Figure 6-66. Time correlations between spatial derivative and temporal derivative of the axial velocity fluctuations.

VII. CONCLUSION

The dominant flow structure in the viscous wall region was found to be a combination of fluid of high axial momentum flowing towards the wall and fluid of low axial momentum flowing away from the wall. This structure was substantiated by means of conditional averaging using the idealized coherent eddy structure as the basis for applying the conditions to the fluctuating velocities. A premise of the open eddy structure is that in the s_z pattern, inflows occur at locations of positive slope and outflows at locations of negative slope. Conditionally averaged s_z profiles reveal that inflows and outflows occur in the viscous wall region and further, that these fluid flows are coupled in the spanwise direction, separated by a distance of $\Delta z^+=100$. Spanwise spacing between the high and low speed streaks has been investigated by many researchers and this work concurs with their findings with respect to the spacing observed. Also, a relation between inflows and outflows was indicated by the observations of Kim et al (1971), Offen and Kline (1974) and Corino and Brodkey (1969). During inflows the axial velocity gradient (s_x) patterns exhibit a momentum excess while the outflow s_x patterns show a momentum deficiency which is consistent with the open coherent eddy structure. The cause of the inflows and outflows could not be determined but it is likely that they are initiated by disturbances in the outer flow field.

The nature of turbulence implies that inflows and outflows are distributed randomly in space and time, inducing outflow-inflow sequences over time. Such sequences were studied using wall electrodes as well as fluid probes. The common feature shared by these sequences is a

rapid acceleration of the axial velocity fluctuations at a certain instant in the viscous wall region. Only if an acceleration effects a sloped u_x profile with large amplitudes does an inflexional velocity profile form. Profile inflexions are a flow phenomenon; they are a consequence of the outflow-inflow sequence, not its impetus. The case where an inflow succeeds an outflow is commonly called the bursting phenomenon as discussed by Blackwelder and Kaplan (1976), Kline et al (1967) and Corino and Brodkey (1969).

Secondly it was found that inflows can be succeeded by outflows or by downstream convected low momentum fluid and if so, again inflexions form in the conditionally averaged axial velocity profile. Concluded from this work is that the bursting phenomenon is just one of four possible flow modes. The others are inflows, outflows, and inflow-outflow sequences. Radial velocity fluctuations were measured at $y^+=70$ which is too far from the wall to gain insight into the relation between the flow modes and the Reynolds stress production, and so further research is needed.

LIST OF REFERENCES

- Abramowitz, M., J. Math. Phys., 20, 162 (1951)
- Acrivos, A., Phys. Fluids, 3, 657 (1960)
- Bakewell, H. P., Lumley, J. L., Phys. Fluids, 10, 1880 (1967)
- Bieg, K. W., M. S. Thesis, University of Illinois, Urbana, Illinois (1974)
- Blackwelder, R. F., Phys. Fluids, 20, S232 (1977)
- Blackwelder, R. F., Eckelmann, H., Structure and Mechanisms of Turbulence I, Lecture Notes in Physics Vol. 75, Springer Verlag (1978)
- Blackwelder, R. F., Kaplan, R. E., NATO-AGARD Conf. Proc. No. 93., London: Technical Editing and Reproduction Ltd. (1972)
- Blackwelder, R. F., Kaplan, R. E., J. Fluid Mech., 76, 89 (1976)
- Brown, G. L., Thomas, A. S. W., Phys. Fluids, 20, S243 (1977)
- Chorn, L. G., Ph.D. Thesis, University of Illinois, Urbana, Illinois (1978)
- Corino, E. R., Brodkey, R. S., J. Fluid Mech., 37, 1 (1969)
- Corrsin, S., NACA Rep. W-94 (1943)
- Corrsin, S., Symp. on Naval Hydrodyn., 373 (1956)
- Corrsin, S., Kistler, A. L., NACA Tech. Note N. 3133 (1954)
- Davies, P. O. A. L., Yule, A. J., J. Fluid Mech., 69, 513 (1975)
- Dimopoulos, H. G., Hanratty, T. J., J. Fluid Mech., 33, 303 (1968)
- Eckelman, L. D., Ph.D. Thesis, University of Illinois, Urbana, Illinois (1971)
- Falco, R. E., Phys. Fluids, 20, S124 (1977)
- Falco, R. E., Workshop on Coherent Structure of Turbulent Boundary Layer, Smith, C. R., Abbott, D. E., Lehigh University, 448 (1978)
- Favre, A., Gaviglio, J., Dumas, R., J. Fluid Mech., 3, 334 (1958)
- Fortuna, G., Ph.D. Thesis, University of Illinois, Urbana, Illinois (1971)
- Fortuna, G., Hanratty, T. J., J. Heat Mass Transfer, 14, 1499 (1971)

- Grass, A. J., J. Fluid Mech., 50, 233 (1971)
- Gupta, A. K., Ph.D. Thesis, University of Southern California, Los Angeles, California (1970)
- Gupta, A. K., Laufer, J., Kaplan, R. E., J. Fluid Mech., 50, 493 (1971)
- Gurkham, A. A., Kader, B. A., Paris Heat Transfer Conf., FC 2.5 (1970)
- Hanratty, T. J., Phys. Fluids, S126 (1967)
- Hanratty, T. J., Chorn, L. G., Hatzivramidis, D. T., Phys. Fluids, 20, S112 (1977)
- Hatzivramidis, D. T., Ph.D. Thesis, University of Illinois, Urbana, Illinois (1978)
- Hinze, J. O., Turbulence, McGraw Hill (1975)
- Isakoff, S. E., Drew, T. B., Proc. Gen. Disc. on Heat Transfer, I. M. E., London (1951)
- Kaplan, R. E., Laufer, J., Proc. 12th Int. Cong. Appl. Mech., Stanford, Springer, 236 (1969)
- Kim, H. T., Kline, S. J., Reynolds, W. C., J. Fluid Mech., 50, 133 (1971)
- Kline, S. J., Reynolds, W. C., Schraub, F. A., Runstadtler, P. W., J. Fluid Mech., 30, 741 (1967)
- Kovasznay, L. S. G., Kibens, V., Blackwelder, R. F., J. Fluid Mech., 41, 283 (1970)
- Kreplin, H. P., Eckelmann, H., Max-Planck-Institut für Strömungsforschung, Bericht 119 (1978)
- Lau, K. K., M.S. Thesis, University of Illinois, Urbana, Illinois (1977)
- Laufer, J., NACA Rep. 1174 (1954)
- Laufer, J., Annual Review of Fluid Mech., 7, 307 (1975)
- Laufer, J., Badri Narayanan, M. A., Phys. Fluids, 14, 182 (1971)
- Lee, M. K., Ph.D. Thesis, University of Illinois, Urbana, Illinois (1975)
- Lee, M. K., Eckelman, L. D., Hanratty, T. J., J. Fluid Mech., 66, 17 (1974)
- Levi, E., J. Hydraulic Res., 16, 107 (1978)

- Lighthill, M. J., Laminar Boundary Layers, Chap. II, see Rosenhead, L. (1963)
- Lu, S. S., Willmarth, W. W., Phys. Fluids, 16, 2012 (1973)
- Lumley, J. L., Stochastic Tools in Turbulence, Academic (1970)
- McConaghy, G. A., Ph.D. Thesis, University of Illinois, Urbana, Illinois (1974)
- Mitchell, J. E., Hanratty, T. J., J. Fluid Mech., 26, 199 (1966)
- Mollo-Christensen, E., Annual Review of Fluid Mech., 101 (1973)
- Nychas, S. G., Hershey, H. C., Brodkey, R. S., J. Fluid Mech., 61, 513 (1973)
- Offen, G. R., Kline, S. J., J. Fluid Mech., 62, 223 (1974)
- Offen, G. R., Kline, S. J., J. Fluid Mech., 70, 209 (1975)
- Oldaker, D. K., Tiederman, W. G., Phys. Fluids, 20, S133 (1977)
- Praturi, A. K., Brodkey, R. S., J. Fluid Mech., 89, 251 (1978)
- Rao, K. N., Narasimha, R., Badri Narayanan, M. A., J. Fluid Mech., 48, 339 (1971)
- Reiss, L. P., Hanratty, T. J., A.I.Ch.E.J., 8, 245 (1962)
- Reiss, L. P., Hanratty, T. J., A.I.Ch.E.J., 9, 154 (1963)
- Rice, S. O. Bell System Tech. J., 23, 282 (1944)
- Rosenhead, L., Laminar Boundary Layers, Oxford University Press (1963)
- Schubert, G., Corcos, G. M., J. Fluid Mech., 29, 113 (1967)
- Shaw, D. A., Ph.D. Thesis, University of Illinois, Urbana, Illinois (1976)
- Sirkar, K. K., Hanratty, T. J., Ind. Eng. Chem. Fund., 8, 189 (1969)
- Sirkar, K. K., Ph.D. Thesis, University of Illinois, Urbana, Illinois (1969)
- Sirkar, K. K., Hanratty, T. J., J. Fluid Mech., 44, 605 (1970)
- Sternberg, J., J. Fluid Mech., 13, 241 (1962)
- Tani, I., Phys. Fluids, S11 (1967)

- Tani, I., Hama, F. R., J. Aero. Sci., 20, 289 (1953)
- Taylor, G. I., Proc. Roy. Soc. A156, 307 (1936)
- Theodorsen, T., 50 Jahre Grenzschichtforschung, Görtler, H., Tollmien, W., Vieweg, 55 (1955)
- Townsend, A. A., The Structure of Turbulent Shear Flow, Cambridge University Press (1976)
- Ueda, H., Hinze, J. O., J. Fluid Mech., 67, 125 (1975)
- Uzkan, T., Reynolds, W. C., J. Fluid Mech., 28, 803 (1967)
- Wallace, J. M., Eckelmann, H., Brodkey, R. S., J. Fluid Mech., 54, 39 (1972)
- Wallace, J. M., Brodkey, R. S., Eckelmann, H., J. Fluid Mech., 83, 673 (1977)
- Willmarth, W. W., Annual Review of Fluid Mech., 7, 13 (1975)
- Willmarth, W. W., Bogar, T. J., Phys. Fluids, 20, S9 (1977)
- Willmarth, W. W., Lu, S. S., J. Fluid Mech., 55, 65 (1972)
- Zilker, D. P. Jr., Private communication (1977)

NOMENCLATURE

Symbol	Description	Units
A_e	Surface area of the wall electrode	cm ²
B	Calibration constant defined in equation (4.12)	
C	Concentration	moles/cm ³
C_b	Bulk concentration of reactant species	moles/cm ³
C_w	Concentration of reactant species at electrode surface	moles/cm ³
$C_i(t)$	Defined in equations (3.2) to (3.7)	
D	Internal diameter of the test section	cm
d	Diameter of the probe wire	cm
d_p	Distance between the probe wires	cm
\mathfrak{D}	Diffusivity	cm ² /sec
E	Voltage defined in equation (4.12)	volts
E_D	Number of events in the data set	
F	Faraday's constant, (F=96500)	coulombs equivalent
f_s	Sample frequency	sec ⁻¹
f_i	Defined in equation (4.26) where i = 1, 2, 3 and 4	
$g(R_d)$	Defined in equation (4.10)	
$h(\theta)$	Defined in equation (4.10)	
I	Current	amps
K	Mass transfer coefficient	cm/sec
K_1, K_2	Mass transfer coefficients for an electrode pair	cm/sec
K_w	Mass transfer for electrode with effective path length w	cm/sec

Symbol	Description	Units
k	Fluctuating mass transfer coefficient	cm/sec
L	Electrode length	cm
M_a, M_b	Effective velocity for probe wire a and b	cm/sec
N	Mass flux per unit area	moles/cm ² sec
N_D	Number of data per run per channel	
n	Frequency Parameter defined in equation (4.14) Calibration constant defined in equation (4.12)	sec ⁻¹
n_e	Number of electrons transferred in the reaction	
P	Pressure	dyne/cm ²
p	Fluctuating component of pressure	dyne/cm ²
R_D	Reynolds number based upon ID test section, DU_b/v	
R_d	Reynolds number based upon wire diameter, dU_b/v	
R_f	Feedback resistance	ohms
R_h	Reynolds number based upon channel height, hU_∞/v	
R_θ	Reynolds number based upon momentum thickness, $\theta U_\infty/v$	
r	Coordinate in radial direction	cm
S	Shear rate vector at the wall Parameter defined in equation (4.7)	sec ⁻¹
S_a, S_b	Probe wires a and b	
S_c	Schmidt number, v/λ	
S_h	Sherwood number, $\langle K \rangle d/\lambda$	
S_w	Shear rate for electrode with effective path length w	sec ⁻¹
S_x	Axial shear rate at the wall	sec ⁻¹

AD-A080 855

ILLINOIS UNIV AT URBANA-CHAMPAIGN DEPT OF CHEMICAL EN--ETC F/0 20/4
IDENTIFICATION OF THE DOMINANT FLOW STRUCTURE IN THE VISCOUS WA--ETC(U)

AUG 79 J H HOGENES, T J HANRATTY N00014-76-C-1034

NL

UNCLASSIFIED

TR-2

3 OF 3
4
309424.3

END
DATE
3-80
nmr

Symbol	Description	Units
$s_x(z,t)$	Fluctuating component of the axial shear rate at the wall	sec^{-1}
$s_z(z,t)$	Fluctuating component of the spanwise shear rate at the wall	sec^{-1}
T	Time	sec
	Transference number, ($T=.001$)	
T_D	Time for which signals were digitalized	sec
T_E	Duration of an event	sec
t	Time	sec
U	Velocity vector Axial velocity	cm/sec cm/sec
U_b	Bulk velocity	cm/sec
U_i	Velocity vector at fluid probes	cm/sec
U_m	Maximum axial velocity	cm/sec
U_x	Axial velocity	cm/sec
u	Fluctuating axial velocity	cm/sec
u_x	Fluctuating axial velocity	cm/sec
u_y	Fluctuating radial velocity	cm/sec
u^*	Wall friction velocity, $\sqrt{\tau_w/\rho}$	cm/sec
v	Radial velocity	cm/sec
v_i	Input voltage	volts
v_o	Output voltage	volts
v	Fluctuating radial velocity	cm/sec
w	Spanwise velocity Electrode width	cm/sec cm
w	Fluctuating spanwise velocity Effective instantaneous electrode width	cm/sec cm
x	Coordinate in the mean flow direction	cm

Symbol	Description	Units
y	Coordinate in the radial direction	cm
y_c	Concentration boundary layer thickness defined in equation (4.4)	cm
z	Coordinate in the spanwise direction	cm
α	Angle Probability	degrees
β	Angle Streamwise wall velocity gradient defined in equation (4.8)	degrees
$\Gamma(\frac{4}{3})$	Gamma function, ($\Gamma(\frac{4}{3}) = .893$)	
γ	Euler's constant, ($\gamma = .5772$)	
Δ	Prefix for time and length increments	
η	Defined in equation (4.21)	
θ	Cylindrical coordinate Angle to the direction of mean flow	degrees degrees
λ	Spanwise streak spacing	cm
ν	Kinematic viscosity	cm^2/sec
ρ	Density	g/cm^3
σ	Defined in equation (4.22)	
Σ	Summation sign	
τ	Defined in equation (4.24)	
τ_w	Shear stress at the wall	dyne/cm^2
ϕ	Angle to the direction of mean flow, ($\phi = 15^\circ$)	degrees
ψ	Stream function defined in equation (4.7)	
$\langle \rangle$	Time averaged quantity	
$\langle \rangle_c$	Conditionally averaged quantity	
\cdot	Quantity made dimension less with wall parameters, u^* and v	
\cdot	Root-mean-squared quantity	